School of Electrical Engineering, Computing and
Mathematical Sciences

Theory of Ion-Atom Collisions for Stopping Power Calculations

Jackson Bailey

This thesis is presented for the Degree of
Doctor of Philosophy
of
Curtin University

August 2018

Declaration

To the best of my knowledge and belief this thesis contains no material previously published by any other person except where due acknowledgment has been made.

This thesis contains no material which has been accepted for the award of any other degree or diploma in any university.

Jackson Bailey

1st August, 2018

Acknowledgments

First of all I wish to acknowledge my supervisor Professor Alisher Kadyrov. I am truely grateful for his mentorship and guidance during my studies, as well as his constant encouragement and support. In fact, during my undergraduate studies, it was Professor Kadyrov's lectures that inspired me to pursue research in theoretical physics. I am also incredibly grateful to my co-supervisor Dr Ilkhom Abdurakhmanov for his invaluable expertise and assistance. I also wish to acknowledge my co-supervisor Professor Igor Bray for his invaluable advice; his passion for science is uplifting. Without these three people this thesis would not have been possible.

I would like to thank all members of the Theoretical Physics Group for creating a pleasant and enjoyable research environment. Furthermore, I must acknowledge members of the Physics Department whose friendly conversations and bouts of table tennis offered welcome breaks from my work.

My deepest gratitude goes to my family and friends. In particular my parents and brother for their tremendous support and encouragement from the very beginning. Finally, my love goes to my beautiful wife Tania, I could not have done this without her.

It is with great pleasure that I acknowledge these people.

Contents

Summary

This thesis is devoted to the application of the convergent close-coupling method to the study of energy-loss processes in ion-atom collisions. The method is applied to the calculation of the stopping cross section, which is directly related to the stopping power, for various atomic and molecular targets.

To start with, the single-centre convergent close-coupling method is applied to the calculation of stopping cross sections in antiproton collisions with hydrogen, helium, neon, argon, krypton, and xenon. The scattering wave function is expanded in a basis of target pseudostates that are constructed from the orthonormal Laguere functions. The semiclassical impact-parameter approximation is used to derive a set of coupled-channel differential equations for the expansion coefficients, which is solved with the condition that the target is initially in the ground state. For the helium target a multiconfiguration approach is used, which fully accounts for the electron-electron correlation. Double-ionisation and ionisation-with-excitation processes are taken into account using an independent-event model. The wave functions for the Ne, Ar, Kr, and Xe atoms are described in a model of six p-shell electrons above a frozen Hartree-Fock core with only one-electron excitations from the outer p shell allowed.

The single-centre convergent close-coupling method is also applied to the calculation of stopping cross sections in antiproton collisions with the hydrogen and water molecules. The H_2 target is described using a two-centre molecular

structure model, which fully accounts for the electron-electron correlation. An analytic orientation-averaging technique is used to account for all possible orientations of the target molecule. Double-ionisation and dissociative-ionisation processes are included via an independent-event model. Energy loss through vibrational excitations is also taken into account. For H_2O, a multi-centre problem is reduced to a central one by describing the water molecule as a pseudo-spherical neon-like atom.

The stopping cross section for protons passing through hydrogen is also calculated. Both the positive and neutral charge-states of the projectile are accounted for. The two-centre convergent close-coupling method is used to model proton collisions with hydrogen. In this approach electron-capture channels are explicitly included by expanding the scattering wave function in a basis of both target and projectile pseudostates. The standard two-centre coupled-channel scattering equations are derived without the introduction of electron translation factors. To model hydrogen collisions with hydrogen, the single-centre convergent close-coupling approach is used for the calculation of one-electron processes, while two-electron processes are calculated using the Born approximation. The aforementioned approaches are also applied to the calculation of the charge-state fractions. These are then used to combine the proton-hydrogen and hydrogen-hydrogen stopping cross sections to yield the total stopping cross section for protons passing through hydrogen.

Main results

- The convergent close-coupling method has been applied to the calculation of stopping cross sections for the first time.

- Results for the antiproton-hydrogen stopping cross section are found to be in good agreement with existing theories, validating our approach.

- Calculations for the antiproton-helium stopping cross section are the first to fully account for the electron-electron correlation in the target structure. The results improve upon previous calculations that use hydrogen-like models which don't take into account electron correlation effects.

- Results for antiproton stopping in the noble gasses neon, argon, krypton, and xeon are the first for these targets.

- An accurate molecular structure model has been used in the calculation of the antiproton-H_2 stopping cross section for the first time. A significant reduction in the stopping cross section is seen in the low to intermediate energy region compared to previous theories that use an atomic model for the hydrogen molecule.

- The use of an analytic orientation-averaging technique for the H_2 molecule has resulted in an improved stopping cross section compared to the often-used technique of averaging over three perpendicular orientations. Also, it was found that energy losses due to vibrational excitation make only a small contribution to the stopping cross section at low energies.

- Comparison of antiproton-H and antiproton-H_2 stopping cross sections demonstrate that Bragg's additivity rule is not satisfied at low and intermediate incident energies. There is also slight deviation from the rule in the high-energy region.

- Calculation of the stopping cross section for antiproton collisions with the water molecule are the first for this system.

- For the first time, a two-centre coupled-channel approach, which accurately models electron-capture processes, has been used to calculate the proton-hydrogen stopping cross section over a wide energy range. The results demonstrate that single-centre approaches do not give the correct stopping cross section in the low to intermediate energy region.

- The two-centre coupled-channel equations are derived without the introduction of electron translation factors.

- The Barkas effect is demonstrated based on calculations for the antiproton-hydrogen and proton-hydrogen stopping cross sections.

- The convergent close-coupling method has been extended to model the collision of two hydrogen atoms for the first time. The results demonstrate that the coupling between channels significantly increases the stopping cross section associated with one-electron processes at low and intermediate incident energies in comparison to a perturbative theory.

- Two-electron processes are shown to make a significant contribution to the hydrogen-hydrogen stopping cross section in the intermediate to high energy region.

- Experimental data for the proton-atomic hydrogen stopping cross section is deduced by scaling proton-molecular hydrogen data using the ratio between the proton-H and proton-H_2 total ionisation cross sections. The present calculations are in excellent agreement with this data.

The thesis is organised in the following way:

The motivation behind this work and a brief overview of existing theories are discussed in Chapter 1. The theory of the single-centre convergent close-coupling method and its application to stopping cross section calculations in

ion-atom collisions are detailed in Chapter 2. In Chapter 3 results for antiproton stopping in hydrogen, helium, neon, argon, krypton, and xenon are presented. The theory and results of antiproton stopping cross section calculations for the hydrogen and water molecules are presented in Chapters 4 and 5, respectively. The two-centre convergent close-coupling approach to calculating the proton-hydrogen stopping cross section is described in Chapter 6. In Chapter 7 the theory for modelling hydrogen collisions with hydrogen is detailed. Results of stopping cross section calculations for protons passing through hydrogen are presented in Chapter 8. In Chapter 9 conclusions from the present study are drawn and future directions of this work are discussed.

List of publications

During my studies I have coauthored 12 peer-reviewed papers. They are listed below in reverse-chronological order.

1. J. J. Bailey, I. B. Abdurakhmanov, A. S. Kadyrov, and I. Bray, "The stopping power of hydrogen for protons and antiprotons" in *Recent developments in ion-atom and ion-molecule collisions: experiment, theory and applications*, edited by Dž. Belkić (accepted for publication).

2. I. B. Abdurakhmanov, Sh. U. Alladustov, J. J. Bailey, A. S. Kadyrov, and I. Bray, "Proton scattering from excited states of atomic hydrogen", Plasma Phys. Control. Fusion **60**, 095009 (2018).

3. I. B. Abdurakhmanov, J. J. Bailey, A. S. Kadyrov, and I. Bray, "Wave-packet continuum-discretisation approach to ion-atom collisions including rearrangement: Application to differential proton-hydrogen scattering", Phys. Rev. A **97**, 032707 (2018).

4. I. Bray, I. B. Abdurakhmanov, J. J. Bailey, A. W. Bray, D. V. Fursa, A. S. Kadyrov, C. M. Rawlins, J. S. Savage, A. T. Stelbovics, and M. C. Zammit, "Convergent close-coupling approach to light and heavy projectile scattering on atomic and molecular hydrogen", J. Phys. B **50**, 202001 (2017).

5. J. J. Bailey, A. S. Kadyrov, I. B. Abdurakhmanov, and I. Bray, "Hybrid approach to calculating proton stopping power in hydrogen", J. Phys. Conf. Ser. **777**, 012010 (2017).

6. J. J. Bailey, A. S. Kadyrov, I. B. Abdurakhmanov, D. V. Fursa, and I. Bray, "Antiproton stopping power data for radiation therapy simulations", Phys. Med. **32**, 1827 (2016).

7. I. Bray, J. J. Bailey, D. V. Fursa, A. S. Kadyrov, and R. Utamuratov, "Internal consistency in the close-coupling approach to positron collisions with atoms", Eur. Phys. J. D **70**, 6 (2016).

8. J. J. Bailey, A. S. Kadyrov, I. B. Abdurakhmanov, D. V. Fursa, and I. Bray, "Antiproton stopping in H_2 and H_2O", Phys. Rev. A **92**, 052711 (2015).

9. J. J. Bailey, A. S. Kadyrov, I. B. Abdurakhmanov, D. V. Fursa, and I. Bray, "Antiproton stopping in atomic targets", Phys. Rev. A **92**, 022707 (2015).

10. I. B. Abdurakhmanov, A. S. Kadyrov, D. V. Fursa, S. K. Avazbaev, J. J. Bailey, and I. Bray, "Antiproton-impact ionization of Ne, Ar, Kr, Xe, and H_2O", Phys. Rev. A **91**, 022712 (2015).

11. J. J. Bailey, A. S. Kadyrov, and I. Bray, "Internal consistency in positron-hydrogen-scattering calculations", Phys. Rev. A **91**, 012712 (2015).

12. A. S. Kadyrov, J. J. Bailey, I. Bray, and A. T. Stelbovics, "Two-center approach to fully differential positron-impact ionization of hydrogen", Phys. Rev. A **89**, 012706 (2014).

Chapter 1

Introduction

The study of ion-atom collisions has led to some of the most significant discoveries in physics that have revolutionised our understanding of not only our world, but the entire universe. The first of these discoveries was made in 1911 by Ernest Rutherford [1], who, via the study of alpha particles colliding with a gold foil established the nuclear model of the atom. This discovery, along with many others that have followed, have either directly or indirectly led to the development of technologies that currently underpin our day-to-day life.

The stopping power of matter is one of the most fundamental concepts in the field of ion-atom collisions. Essentially, the stopping power is the kinetic-energy loss of an ion travelling through a medium of atoms. Although the notion of stopping power is simple, theoretical calculations of the quantity can be extremely challenging. This thesis is devoted to the extension of the convergent close-coupling method to the study of energy-loss processes in ion-atom collisions. Before we dive into the details of the aforementioned method, a brief discussion of the importance of stopping power calculations is necessary to set the scene.

1.1 Importance of stopping power calculations

Any application of ion transport through matter is dependent on knowledge of energy losses during ion-atom collisions. This means stopping power data is of fundamental importance in a great number of fields including astrophysics, radiation protection, fusion research, materials analysis, space exploration, medical physics, etc. [2] For example, NASA uses stopping power data in the development of radiation shielding technology that protects astronauts from the highly energetic ions penetrating space as a result of solar winds and solar flares [3]. Another example is the use of stopping power data in the development of effective cancer treatment techniques, specifically, hadron therapy [4]. In fact, the work presented in this thesis is the beginning of a larger project that aims to provide accurate data on the stopping power of biologically relevant molecules for use in hadron therapy. Therefore, below we provide a short summary of hadron therapy and discuss the importance of stopping power calculations in this type of radiation therapy.

In 1904 William Henry Bragg [5] discovered that the energy loss by heavy ions travelling through matter tremendously increases and reaches its maximum (known as a Bragg peak) immediately before the ions come to rest. In fact, it was this fundamental discovery that in 1946 allowed Robert R. Wilson [6] to first propose the use of heavy ions as a potential radiation therapy tool for the treatment of cancer. Fast forward to 2018 and hadron therapy has developed into a cutting-edge cancer treatment technique.

Although X-rays are traditionally used when it comes to radiation therapy, heavy charged particles offer significant benefits over photons due to the existence of the aforementioned Bragg peak. Namely, heavy ions deposit most of their energy in a very small region, whereas the energy deposited by X-rays

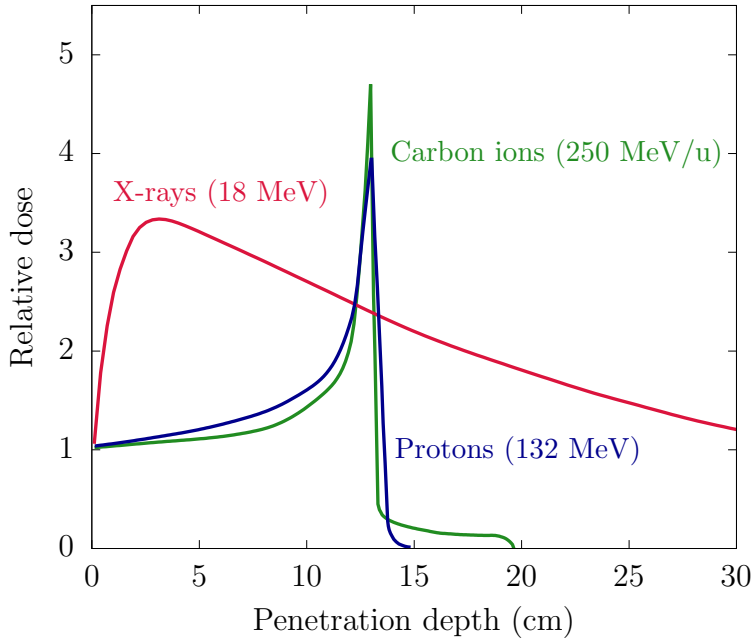

Figure 1.1: Radiation dose rates for X-rays, protons and carbon ions passing through matter. The doses are normalised to 1 at entry. Figure is taken from Ref. [7].

peaks near the entrance point and then linearly decays. This is illustrated in Figure 1.1, which shows the difference in radiation dose from X-rays, protons, and carbon ions as a function of penetration depth. It can be seen that for protons and carbon ions the radiation dose is relatively small at the beginning of their pathways before dramatically increasing at the end. As a result, when using hadrons for radiation therapy purposes, if the Bragg peak is aligned with the site of the tumour a significant dose of radiation can be delivered to the cancerous cells, while minimising damage to the surrounding healthy tissue. On the other hand, X-rays deliver a maximum dose of radiation to healthy cells at the surface, with only a small fraction of the overall dose reaching the tumour. There is also a significant exit dose in X-ray therapy, as illustrated in Figure 1.2, which compares proton therapy to conventional X-ray therapy.

Treatment planning for hadron therapy relies on Monte Carlo simulations

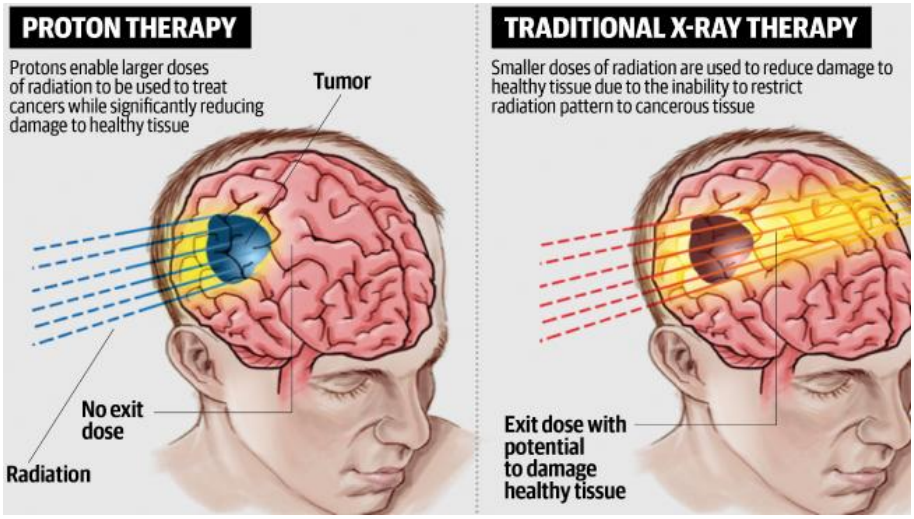

Figure 1.2: Benefits of proton therapy. Figure is taken from Ref. [8].

of ion beam passage through biological matter, which can be done with codes such as Geant4 [9–11], FLUKA [12, 13], and SHIELD-HIT12A [14, 15]. The precision of these simulations is paramount in ensuring the dose of radiation is delivered accurately. However, the limiting factor in the accuracy of these Monte Carlo codes is the underlying physics (stopping powers) that drive the simulations. Therefore, the theoretical models on which these codes are based need to be of sufficient accuracy to ensure the reliability of their output. That is, the success of hadron therapy for the treatment of cancer relies heavily on the accuracy of stopping power data.

What's more, a significant part of the present work focuses on stopping power calculations involving antiprotons, therefore, their application to radiation therapy will also be discussed. Although it is well known that hadrons, like protons and carbon ions, provide a significant benefit over photons when used for radiation therapy purposes, in terms of antiprotons the picture is not yet complete. Antiprotons were first proposed as a potential radiation therapy tool in 1984 by Gray and Kalogeropoulos [16] based on Monte Carlo simulations that showed an enhancement of the physical dose in the Bragg-peak region. As with

other hadrons, antiprotons deposit most of their kinetic energy before coming to rest. Additionally, as they come to rest they annihilate producing π-mesons. These π-mesons will in turn be absorbed by the nucleus on which the antiprotons annihilate resulting in the emission of nuclear fragments with high linear energy transfer (LET). These high-LET secondary particles cause an enhancement of the physical dose and relative biological effectiveness. However, the contribution to the background dose from secondary neutrons must also be considered.

The ACE collaboration has been conducting experiments using the AD facility at CERN to fully assess the effectiveness of antiprotons for use in radiation therapy. They have shown that the peak to plateau dose ratio for antiprotons is two-fold higher than for protons [17, 18]. Additionally, due to the limited capabilities of the experiment further investigation is carried out using Monte Carlo codes, such as those mentioned above. Again, these codes rely on accurate antiproton stopping power calculations.

1.2 Overview of existing theories

Now a brief description of existing theoretical approaches to calculating the stopping power in ion-atom collisions will be given. They will be separated into perturbative and non-perturbative methods. Also, we will focus on methods that have been applied to the systems considered in this work.

1.2.1 Perturbative methods

Bethe theory

The first quantum-mechanical formulation of energy loss per unit path length, or stopping power, was developed by Bethe [19]. He applied the dipole approxima-

tion and showed that the stopping power for heavy projectiles travelling through matter at non-relativistic velocity v is given by

$$-\frac{dE}{dx} = N_{\mathrm{a}} \frac{4\pi k_{\mathrm{c}}^2 e^4 Z_{\mathrm{P}}^2 Z_{\mathrm{T}}^2}{m_e v^2} \ln\left(\frac{2m_e v^2}{\bar{E}}\right), \tag{1.1}$$

where N_{a} is the number of target atoms per unit volume, k_{c} is the Coulomb constant, e is the elementary charge, m_e is the electron mass, Z_{T} is the atomic number of the target, Z_{P} is the charge of the incident particle in units of e, and $\bar{E}$ is the mean excitation energy of the target. However, due to the approximations made by Bethe the above formula is applicable only at sufficiently high projectile velocities, as the dipole approximation is a further simplification of the first Born approximation[1] (FBA). Additionally, when the Bethe theory is applied to molecules Bragg's additivity rule [20] is usually used. According to this rule the stopping power of a molecule is simply the sum of stopping powers for its constituent atoms. A benefit of Bethe's theory is that it provides a single stopping power formula that is applicable to any atomic target as long as $\bar{E}$ is known. For this reason a tremendous amount of work has gone into improving the accuracy of the Bethe formula via the introduction of correction factors such as the Bloch [21], Barkas [22], and shell [23] corrections.

Born approximation

The FBA was first applied to the calculation of stopping powers by Dalgarno and Griffing [24]. In this work the cross sections calculated by Bates and Dalgarno [25, 26] and Bates and Griffing [27–29] were used. The Born approximation is a perturbative approach, which neglects the coupling between channels. It is based on the assumption that the scattering wave function can be expanded in a rapidly convergent series. The initial-state wave function is the product of the

[1] Hereafter, the first Born approximation may simply be referred to as the Born approximation.

target ground-state wave function and a plane wave describing the projectile. While the final-state wave function is the product of a plane wave describing the projectile and any bound or continuum target wave function. The Born approximation is justifiable only when the scattering potential is small compared to the incident energy, i.e. it is applicable only at high energies. It also fails in the study of charge effects, as calculations involving projectiles with the same mass but opposite charge yield the same result. On the other hand, an advantageous aspect of the Born approximation is that the scattering amplitude can be determined completely analytically for hydrogen-like atoms, which makes calculations relatively simple.

Continuum-distorted-wave eikonal-initial-state approach

The continuum-distorted-wave eikonal-initial-state (CDW-EIS) method [30, 31] is another perturbative approach applicable at sufficiently high energies. However, unlike the Born approximation it takes into account the distortion of the wave function due to the infinite range of the Coulomb potential. These distortions are accounted for with the introduction of a multiplicative factor. In the initial channel this is achieved via the eikonal approximation and in the final channel by the continuum distorted-wave approximation. The CDW-EIS approach has been applied to the calculation of stopping powers by Fainstein *et al.* [32].

1.2.2 Non-perturbative methods

Electron-nuclear dynamics approach

The electron-nuclear dynamics (END) method [33] has been applied to the calculation of stopping powers by Cabrera-Trujillo *et al.* [34–37]. This approach

is non-perturbative and based on the application of the time-dependent variational principle to the Schrödinger equation. The wave function is described in a coherent-state representation, which results in a set of coupled first-order differential equations for the time evolution of the parameters representing the wave function.

Coupled-channel approach

The most sophisticated and accurate technique for calculating the stopping power is the coupled-channel approach, sometimes referred to as the close-coupling approach. In this method the scattering wave function is expanded in terms of a set of target states (or target and projectile states in the case of a two-centre approach) and after substitution into the Schrödinger equation a set of coupled equations for the expansion coefficients is obtained. The solution of these coupled equations provides all information about the scattering process. However, a sufficient number of target states must be used in the expansion of the scattering wave function to ensure the accuracy of calculations. The difficulty associated with the coupled-channel approach is two-fold: (i) the approach requires significant computational resources due to a large number of basis states required, which leads to a large set of coupled equations that need to be solved, and (ii) the treatment of the continuum via a suitable discretisation as the use of true-continuum functions is not possible within the coupled-channel method. Coupled-channel approaches to ion-atom collisions have a long history [38], however, they have rarely been applied to the calculation of stopping powers.

To fill this gap Schiwietz [39] developed a coupled-channel atomic-orbital method and applied it to the calculation of stopping powers. In this method eigenstates were used for the bound target states, while wave-packets were used for the continuum target states. The wave-packet approach involves discretising

the continuum into a number of energy intervals, then for each interval a continuum wave packet is constructed via integration of the true-continuum wave functions over this region. These states decay to zero at large distances. This coupled-channel approach was further refined and applied to the calculation of stopping powers by Schiwietz and Grande [40], Grande and Schiwietz [41–43], and Schiwietz *et al.* [44, 45].

Lühr and Saenz [46–49] also developed a coupled-channel approach, which was then applied to the calculation of stopping powers [50]. In their approach the pseudostates are constructed from a basis of B-spline functions that diagonalise the target Hamiltonian. The approach is based on box discretisation and, hence, selects states that possess a node at the box boundary.

Lastly, the convergent close-coupling method has recently been applied to the calculation of stopping powers [51–54]. These works form a large part of this thesis and will be described in detail in the appropriate chapters. In the following section we first give a brief history and description of the convergent close-coupling method.

1.3 Convergent close-coupling method

The convergent close-coupling (CCC) method was first developed for the problem of electron-hydrogen scattering by Bray and Stelbovics [55, 56] as a way of solving the momentum-space Lippmann-Schwinger equation without any approximation. The power behind the approach is the fact that target states are constructed from a basis of orthonormal Laguerre functions. This allows for the modelling of the whole spectrum of the target, both bound and continuum. The term "convergent" refers to the fact that an increasing number of basis functions was used until the solution converged to the final result. Calculations for this

system were in excellent agreement with most, but not all, experimental measurements. However, when Bray [57] applied the theory to electron collisions with the hydrogen-like target of sodium excellent agreement with all experimental measurements was obtained. Later, when the electron-hydrogen experiments that were in disagreement were repeated, it was found that there were problems with the initial measurements and the new experiments were in agreement with the CCC theory.

Due to its success in describing electron collisions with hydrogen and hydrogen-like targets the CCC method would continue to be developed for application to light-projectile scattering. It was extended to two-electron targets by Fursa and Bray [58] and applied to electron collisions with helium. At this point in time the CCC method was a purely single-centre approach and, therefore, its application to systems that included electron-capture processes was limited. However, the next advancement would come from Kadyrov and Bray [59] with the development of the two-centre CCC approach to position-hydrogen scattering. This allowed for the accurate calculation of positronium formation in positron collisions with various atomic and molecular targets [60] and has also been applied to antihydrogen formation in collisions of antiprotons with positronium [61].

In more recent times the ideas behind the CCC method have been applied to the field of ion-atom collisions with great success. First, it was applied to the calculation of scattering cross sections in antiproton-hydrogen collisions by Abdurakhmanov *et al.* [62, 63]. Further work in this field proceeded and resulted in calculations for antiproton scattering on helium [64], molecular hydrogen [65, 66], and noble gasses and H_2O [67]. Antiproton projectiles were initially chosen as the entry point into the field of ion-atom collision physics as calculations are simpler than those involving protons due to the lack of electron-capture processes. However, very recently a two-centre CCC approach to ion-atom collisions, which

accurately models electron capture, has been developed and applied to proton-hydrogen scattering [68–70]. Additionally, some CCC calculations focusing on differential cross sections for antiproton [71, 72] and proton [73] scattering have used wave packets instead of Laguerre-based pseudostates in the expansion of the scattering wave function. This is because wave-packets allow for better control over the distribution of the continuum states.

The CCC method has recently been applied to the calculation of stopping powers for the first time, and this work is the subject of the present thesis. In Chapter 2 we detail the theory behind the single-centre CCC approach to ion-atom collisions and its application to stopping power calculations. Specifically, the approach is applied to the calculation of antiproton stopping in hydrogen, helium, neon, argon, krypton, and xenon. Then in Chapter 3 the results of these calculations are presented and discussed alongside existing theories and experiments. In Chapters 4 and 5 we present the theory and results, respectively, for the calculation of antiproton stopping in molecules, the latter being H_2 and H_2O. Next, we shift our attention to calculating the stopping power of hydrogen for protons. This requires the modelling proton-hydrogen and hydrogen-hydrogen collisions. To model proton-hydrogen collisions we use the two-centre CCC approach, which is detailed in Chapter 6. Following this, in Chapter 7 our approach to modelling hydrogen collisions with hydrogen is described. In Chapter 8 we present and discuss the results of our stopping power calculations for protons passing through hydrogen alongside other theories and experiments. Conclusions are drawn in Chapter 9.

Atomic units are used throughout unless stated otherwise.

Chapter 2

Single-centre coupled-channel approach to ion-atom collisions

2.1 Introduction

In this chapter we will present details of our single-centre approach to modelling the collisions of ions with atoms for the purpose of calculating the stopping power. We will use the semiclassical approximation in deriving a set of coupled-channel differential equations, whose solutions give the probability of a scattering event occurring. As such, the method is referred to as the single-centre semiclassical convergent close-coupling approach, or single-centre CCC. Since it is a single-centre method it does not explicitly include electron-capture channels. This is an issue when considering collisions involving positive ions where electron-capture channels dominate at low incident energies (approximately less than 50 keV/amu). For collisions requiring explicit charge-transfer channels we use a two-centre approach (see Chapter 6). Therefore the single-centre approach will primarily be used to model antiproton collision with atoms, specifically hydrogen, helium, and the noble gasses neon, argon, krypton, and xenon at energies where the probability of protonium formation is negligible.

As stated we will be using the semiclassical approximation meaning the projectile is treated classically while the target electrons are treated fully quantum-mechanically. The semiclassical approximation has been shown to be equivalent to the exact quantum theory if the following conditions are met [74]:

1) The initial and final projectile-target relative momenta are approximately equal, i.e $k_i \approx k_f$, and $k_i^2/2\mu \gg \Delta E$, where ΔE is the energy lost during the collision and μ is the reduced mass of the system,

2) The scattering is confined to small angles, i.e $\arccos(\hat{\boldsymbol{k}}_i \cdot \hat{\boldsymbol{k}}_f) \ll 1$,

3) The de Broglie wavelength of the relative motion $\lambda = \hbar/k_i$ is small compared with atomic dimensions.

All calculations in this thesis are performed at energies where the semiclassical approximation is valid.

The coordinate system that will be used is illustrated in Figure 2.1. The target nucleus (T) is at the origin and the projectile (P) is assumed to be moving with constant velocity $\boldsymbol{v}$ along a straight line toward the target at an impact parameter $\boldsymbol{b}$. The position of the projectile with respect to the target nucleus is then given by

$$\boldsymbol{R}(t) = \boldsymbol{b} + \boldsymbol{v}t, \tag{2.1}$$

where t is time and $t = 0$ corresponds to the distance of closest approach. The velocity of the projectile is taken to be along the z-axis and the impact parameter is taken to be along the x-axis. The position of the projectile along the z-axis is hence $z = vt$.

In what follows we will be considering the collisions of antiprotons with target atoms of atomic number Z_T. For positive ions the appropriate changes

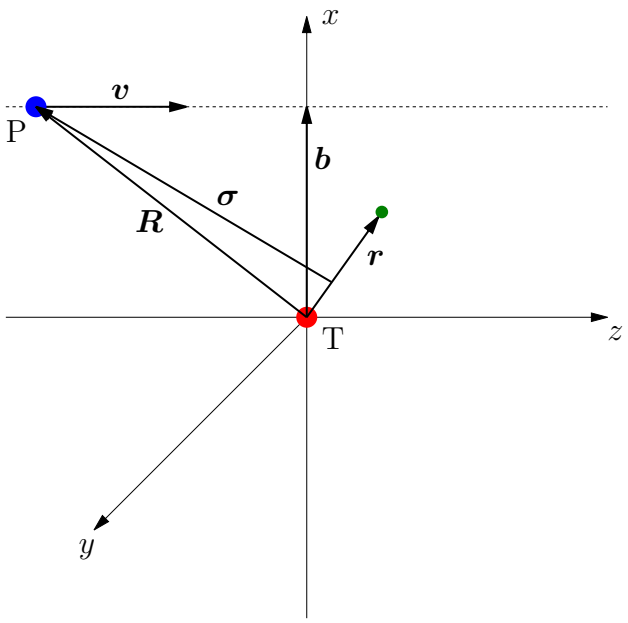

Figure 2.1: Coordinates used for the collision of a projectile ion (P) with a target atom. The target nucleus (T) is at the origin, with the projectile's velocity directed along the z-axis. The position of P relative to the centre-of-mass of the target atom is given by $\boldsymbol{\sigma}$, while $\boldsymbol{r}$ is the position of the target electron.

to the potentials must be made. First we will formulate the coupled-channel equations whose solution describes the scattering event. Then details of target structure calculations for hydrogen, helium, neon, argon, krypton, and xenon will be given. Lastly we will discuss the calculation of the stopping power in the semiclassical coupled-channel formalism.

2.2 Formulation of scattering equations

In this section, starting from Schrödinger's equation, we formulate a set of coupled-channel differential equations that describe our scattering system. The standard approach widely used in the literature starts from the approximate time-dependent Schrödinger equation for the electronic part of the scattering

wave function. This time-dependent Schrödinger equation follows from the full Schrödinger equation when the semi-classical approximation is used. However, we will present a different derivation that starts from the full time-independent Schrödinger equation and employ a general expansion of the total scattering wave function. The reason for this is to be consistent with our formalism in Chapter 6, where we derive a set of two-centre coupled-channel equations using an expansion of the scattering wave function that does not rely on the introduction of the so-called "electron translation factors" commonly used in the literature (see Chapter 6 for details).

The nonrelativistic time-independent Schrödinger equation for the total scattering wave function Ψ is

$$H\Psi(\boldsymbol{r},\boldsymbol{\sigma}) = E\Psi(\boldsymbol{r},\boldsymbol{\sigma}), \tag{2.2}$$

where $\boldsymbol{\sigma}$ is the position vector of the antiproton relative to the centre-of-mass of the target atom, $\boldsymbol{r}$ collectively denotes the position vectors of all N_e target electrons ($\boldsymbol{r} = \{\boldsymbol{r}_1, ..., \boldsymbol{r}_{N_\mathrm{e}}\}$), E is the total energy of the system, and H is the full three-body Hamiltonian

$$H = -\frac{1}{2\mu}\nabla^2_{\boldsymbol{\sigma}} + V + H_\mathrm{T}. \tag{2.3}$$

Here V is the projectile-target interaction

$$V = -\frac{Z_\mathrm{T}}{R} + \sum_{i=1}^{N_\mathrm{e}} \frac{1}{|\boldsymbol{R} - \boldsymbol{r}_i|}, \tag{2.4}$$

and H_T is the target Hamiltonian

$$H_\mathrm{T} = \sum_{i=1}^{N_\mathrm{e}} \left(-\frac{1}{2}\nabla^2_{\boldsymbol{r}_i} - \frac{Z_\mathrm{T}}{r_i} + \sum_{j>i}^{N_\mathrm{e}} \frac{1}{|\boldsymbol{r}_i - \boldsymbol{r}_j|} \right). \tag{2.5}$$

The total scattering wave function is expanded in terms of a complete set of N target pseudostates ψ_α according to

$$\Psi(\boldsymbol{r},\boldsymbol{\sigma}) = \sum_{\alpha=1}^{N} A_\alpha(\boldsymbol{\sigma})\psi_\alpha(\boldsymbol{r})e^{i\boldsymbol{k}_\alpha\cdot\boldsymbol{\sigma}}, \tag{2.6}$$

where α denotes a target electronic state, $\boldsymbol{k}_\alpha$ is the projectile-target relative momentum in channel α, and A_α are the expansion coefficients that contain all information about the scattering process. Hence the total energy of the system is

$$E = \frac{k_\alpha^2}{2\mu} + \epsilon_\alpha, \tag{2.7}$$

where ϵ_α is the energy of the state α and μ is the reduced mass of the projectile-target system. Pseudostates are square-integrable functions that approximate the true eigenstates of a particular target, both bound and continuum. Details of pseudostates for each target considered are given in Section 2.3. In general they are constructed to satisfy the conditions

$$\langle \psi_{\alpha'} | \psi_\alpha \rangle = \delta_{\alpha'\alpha}, \tag{2.8}$$

and

$$\langle \psi_{\alpha'} | H_\mathrm{T} | \psi_\alpha \rangle = \epsilon_\alpha \delta_{\alpha'\alpha}. \tag{2.9}$$

Substituting our expression for the total scattering wave function (2.6) into the Schrödinger equation (2.2) yields

$$\begin{aligned} &-\sum_{\alpha=1}^{N} \frac{1}{2\mu} A_\alpha(\boldsymbol{\sigma}) \psi_\alpha(\boldsymbol{r}) \nabla_{\boldsymbol{\sigma}}^2 e^{i\boldsymbol{k}_\alpha\cdot\boldsymbol{\sigma}} - \sum_{\alpha=1}^{N} \frac{1}{\mu} \psi_\alpha(\boldsymbol{r}) \big(\nabla_{\boldsymbol{\sigma}} e^{i\boldsymbol{k}_\alpha\cdot\boldsymbol{\sigma}}\big)\cdot\big(\nabla_{\boldsymbol{\sigma}} A_\alpha(\boldsymbol{\sigma})\big) \\ &+\sum_{\alpha=1}^{N} (H_\mathrm{T} + V) A_\alpha(\boldsymbol{\sigma}) \psi_\alpha(\boldsymbol{r}) e^{i\boldsymbol{k}_\alpha\cdot\boldsymbol{\sigma}} = E \sum_{\alpha=1}^{N} A_\alpha(\boldsymbol{\sigma}) \psi_\alpha(\boldsymbol{r}) e^{i\boldsymbol{k}_\alpha\cdot\boldsymbol{\sigma}}. \end{aligned} \tag{2.10}$$

In order to obtain Eq. (2.10) we take into account that $\nabla^2 = \nabla\cdot\nabla$ and write

$$\begin{aligned} \nabla_{\boldsymbol{\sigma}}^2 \left(A_\alpha(\boldsymbol{\sigma}) e^{i\boldsymbol{k}_\alpha\cdot\boldsymbol{\sigma}}\right) =& A_\alpha(\boldsymbol{\sigma}) \nabla_{\boldsymbol{\sigma}}^2 e^{i\boldsymbol{k}_\alpha\cdot\boldsymbol{\sigma}} + e^{i\boldsymbol{k}_\alpha\cdot\boldsymbol{\sigma}} \nabla_{\boldsymbol{\sigma}}^2 A_\alpha(\boldsymbol{\sigma}) \\ &+ \big(\nabla_{\boldsymbol{\sigma}} e^{i\boldsymbol{k}_\alpha\cdot\boldsymbol{\sigma}}\big)\cdot\big(\nabla_{\boldsymbol{\sigma}} A_\alpha(\boldsymbol{\sigma})\big). \end{aligned} \tag{2.11}$$

Then we use the semiclassical approximation by neglecting the term containing $\nabla_{\boldsymbol{\sigma}}^2 A_\alpha(\boldsymbol{\sigma})$ assuming that the expansion coefficients A_α vary slowly with $\boldsymbol{\sigma}$. This

is indeed the case since

$$\nabla^2_{\boldsymbol{\sigma}} A_\alpha(\boldsymbol{\sigma}) \ll \nabla^2_{\boldsymbol{\sigma}} e^{i\boldsymbol{k}_\alpha\cdot\boldsymbol{\sigma}}. \tag{2.12}$$

The action of the gradient and Laplacian operators on the plane wave results in

$$\nabla_{\boldsymbol{\sigma}} e^{i\boldsymbol{k}_\alpha\cdot\boldsymbol{\sigma}} = i\boldsymbol{k}_\alpha e^{i\boldsymbol{k}_\alpha\cdot\boldsymbol{\sigma}}, \tag{2.13}$$

and

$$\nabla^2_{\boldsymbol{\sigma}} e^{i\boldsymbol{k}_\alpha\cdot\boldsymbol{\sigma}} = -k^2_\alpha e^{i\boldsymbol{k}_\alpha\cdot\boldsymbol{\sigma}}. \tag{2.14}$$

Therefore, Eq. (2.10) becomes

$$\begin{aligned}&\sum_{\alpha=1}^{N} \frac{k^2_\alpha}{2\mu} A_\alpha(\boldsymbol{\sigma})\psi_\alpha(\boldsymbol{r}) e^{i\boldsymbol{k}_\alpha\cdot\boldsymbol{\sigma}} - i\sum_{\alpha=1}^{N} \frac{1}{\mu} e^{i\boldsymbol{k}_\alpha\cdot\boldsymbol{\sigma}} \big(\boldsymbol{k}_\alpha\cdot\nabla_{\boldsymbol{\sigma}} A_\alpha(\boldsymbol{\sigma})\big)\psi_\alpha(\boldsymbol{r}) \\ &+ \sum_{\alpha=1}^{N} (H_{\mathrm{T}} + V) A_\alpha(\boldsymbol{\sigma})\psi_\alpha(\boldsymbol{r}) e^{i\boldsymbol{k}_\alpha\cdot\boldsymbol{\sigma}} = E\sum_{\alpha=1}^{N} A_\alpha(\boldsymbol{\sigma})\psi_\alpha(\boldsymbol{r}) e^{i\boldsymbol{k}_\alpha\cdot\boldsymbol{\sigma}}.\end{aligned} \tag{2.15}$$

Now, to relate the motion of the nuclei to time we replace $\nabla_{\boldsymbol{\sigma}}$ with the time derivative using

$$\frac{\boldsymbol{k}_\alpha}{\mu}\cdot\nabla_{\boldsymbol{\sigma}} = \boldsymbol{v}\cdot\nabla_{\boldsymbol{\sigma}} = \frac{d}{dt} \tag{2.16}$$

and considering Eq. (2.7) we arrive at

$$i\sum_{\alpha=1}^{N} \frac{dA_\alpha(\boldsymbol{\sigma})}{dt}\psi_\alpha(\boldsymbol{r}) e^{i\boldsymbol{k}_\alpha\cdot\boldsymbol{\sigma}} = \sum_{\alpha=1}^{N} A_\alpha(\boldsymbol{\sigma})(H_{\mathrm{T}} + V - \epsilon_\alpha)\psi_\alpha(\boldsymbol{r}) e^{i\boldsymbol{k}_\alpha\cdot\boldsymbol{\sigma}}. \tag{2.17}$$

Multiplying Eq. (2.17) on the left by $\psi^*_{\alpha'}(\boldsymbol{r}) e^{-i\boldsymbol{k}_{\alpha'}\cdot\boldsymbol{\sigma}}$ and integrating over $\boldsymbol{r}$ we obtain

$$i\sum_{\alpha=1}^{N} \frac{dA_\alpha(\boldsymbol{\sigma})}{dt}\langle\psi_{\alpha'}|\psi_\alpha\rangle e^{i(\boldsymbol{k}_\alpha - \boldsymbol{k}_{\alpha'})\cdot\boldsymbol{\sigma}} = \sum_{\alpha=1}^{N} A_\alpha(\boldsymbol{\sigma})\langle\psi_{\alpha'}|H_{\mathrm{T}} + V - \epsilon_\alpha|\psi_\alpha\rangle e^{i(\boldsymbol{k}_\alpha - \boldsymbol{k}_{\alpha'})\cdot\boldsymbol{\sigma}}. \tag{2.18}$$

At this point we need to look at the term in the exponential factors that contains the momentum transfer vector $\boldsymbol{q} = \boldsymbol{k}_\alpha - \boldsymbol{k}_{\alpha'}$. First we make the approximation $\boldsymbol{\sigma} \approx \boldsymbol{R}$, that is

$$(\boldsymbol{k}_\alpha - \boldsymbol{k}_{\alpha'})\cdot\boldsymbol{\sigma} \approx (\boldsymbol{k}_\alpha - \boldsymbol{k}_{\alpha'})\cdot\boldsymbol{R} = q_\parallel z + \boldsymbol{q}_\perp\cdot\boldsymbol{b}, \tag{2.19}$$

where $q_\parallel$ and $q_\perp$ are the components of momentum transfer parallel and perpendicular to the z-axis, respectively. Furthermore we can express $q_\parallel$ (see Appendix A for details) as

$$q_\parallel = (\epsilon_{\alpha'} - \epsilon_\alpha)/v \tag{2.20}$$

and write Eq. (2.18) as

$$\begin{aligned} & ie^{i\boldsymbol{q}_\perp\cdot\boldsymbol{b}} \sum_{\alpha=1}^{N} \frac{dA_\alpha(t,\boldsymbol{b})}{dt} \langle\psi_{\alpha'}|\psi_\alpha\rangle e^{i(\epsilon_{\alpha'}-\epsilon_\alpha)t} \\ & = e^{i\boldsymbol{q}_\perp\cdot\boldsymbol{b}} \sum_{\alpha=1}^{N} A_\alpha(t,\boldsymbol{b}) \langle\psi_{\alpha'}|H_\mathrm{T} + V - \epsilon_\alpha|\psi_\alpha\rangle e^{i(\epsilon_{\alpha'}-\epsilon_\alpha)t}. \end{aligned} \tag{2.21}$$

Finally, taking into account Eqs. (2.8) and (2.9) we arrive at the final set of coupled-channel differential equations

$$i\frac{dA_{\alpha'}(t,\boldsymbol{b})}{dt} = \sum_{\alpha=1}^{N} A_\alpha(t,\boldsymbol{b}) \langle\psi_{\alpha'}|V(\boldsymbol{r},\boldsymbol{R})|\psi_\alpha\rangle e^{i(\epsilon_{\alpha'}-\epsilon_\alpha)t}; \quad \alpha' = 1,\ldots,N. \tag{2.22}$$

Equation (2.22) is solved with the initial condition $A_{\alpha'}(t=-\infty,\boldsymbol{b}) = \delta_{\alpha' i}$, where i corresponds to the initial state of the target. For all calculations presented in this thesis we take $i = 1$, i.e. the target is initially in the ground state. The angular dependence of $A_{\alpha'}$ on $\boldsymbol{b}$ can be factored out according to

$$A_{\alpha'}(t,\boldsymbol{b}) = e^{i(m_{\alpha'}-m_\alpha)\phi_b} A_{\alpha'}(t,b). \tag{2.23}$$

The probability for transition into some final state f is then

$$p_f(b) = |A_f(t=+\infty,b)|^2, \tag{2.24}$$

where $A_f(t=+\infty,b)$ is the probability amplitude. We solve Eq. (2.22) within the region $[-z_\mathrm{max}, z_\mathrm{max}]$ using the standard Runge-Kutta method. Parameter z_max is increased to give convergent results.

2.3 Details of target structure calculations

In this section we present the details of how target pseudostates ψ_α are constructed for hydrogen, helium, and noble gasses neon, argon, krypton, and xenon.

2.3.1 Structure of hydrogen

For target structure calculations of atomic hydrogen we follow the ideas of Bray and Stelbovics [55]. The target pseudostates ψ_α in Eq. (2.6) are written as

$$\psi_\alpha \equiv \psi_{nlm}(\boldsymbol{r}) = \phi_{nl}(r) Y_{lm}(\hat{\boldsymbol{r}}), \tag{2.25}$$

where

$$\phi_{nl}(r) = \frac{1}{r} \sum_{k=1}^{N_l} B^l_{nk} \xi_{kl}(r), \tag{2.26}$$

and n, l, and m are the principal, orbital, and magnetic quantum numbers of target electronic state α, and N_l is the number of basis functions for a given l.

In Eq. (2.26), ξ_{kl} is a complete set of basis functions that we choose to be the orthonormal Laguerre functions

$$\xi_{kl}(r) = \left(\frac{\lambda_l (k-1)!}{(2l+1+k)!} \right)^{1/2} (\lambda_l r)^{l+1} \exp(-\lambda_l r/2) L^{2l+2}_{k-1}(\lambda_l r), \tag{2.27}$$

where $L^{2l+2}_{k-1}(\lambda_l r)$ are the associated Laguerre polynomials and λ_l is an exponential fall-off parameter. Typically we choose λ_l to give the most accurate ground state of the target with a minimum number of basis functions. Choice of λ_l does not affect the final result, however it does affect the speed of convergence. Specific values of λ_l will be given in Chapter 3. Also, the expansion coefficients B^l_{nk} are found by diagonalisation of the target Hamiltonian in the Laguerre basis. In other words, the states ψ_α satisfy $\langle \psi_{\alpha'} | H_{\rm T} | \psi_\alpha \rangle = \epsilon_\alpha \delta_{\alpha'\alpha}$ and $\langle \psi_{\alpha'} | \psi_\alpha \rangle = \delta_{\alpha'\alpha}$.

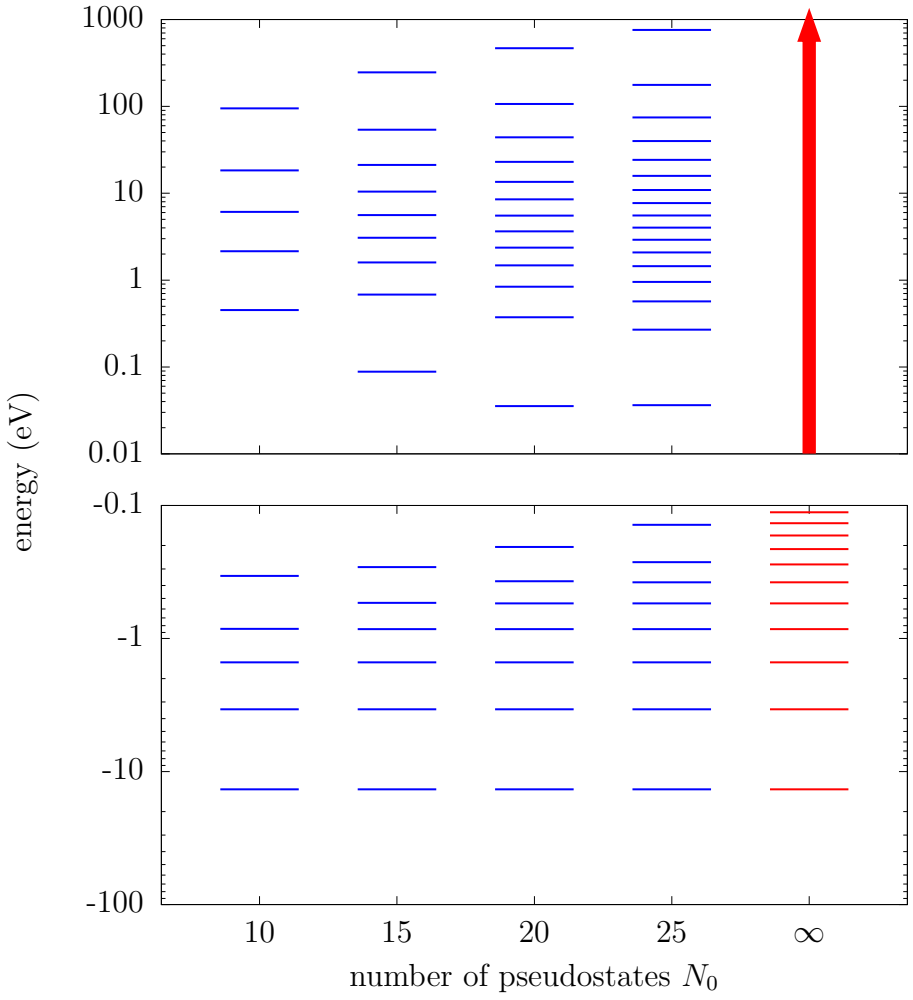

Figure 2.2: Energy levels of atomic hydrogen obtained from a Laguerre basis with N_0 functions for $l = 0$. Also shown is a part of the true spectrum of the hydrogen atom, which corresponds to a Laguerre basis with $N_0 = \infty$ functions.

An important feature of the CCC approach is the choice of the basis as a set of orthogonal Laguerre functions. This choice of basis allows us to model the whole spectrum of the target atom. As the size of the one-electron basis increases the low-lying states will converge to the bound states of the target, while the remaining (pseudo) states will provide an effective representation of the high-lying bound states of the target atom and an increasingly dense square-integrable representation of the target continuum. This is illustrated in Figure 2.2, where

the pseudostate energies obtained from a Laguere basis with N_0 functions for $l = 0$ is plotted against the eigenenergies of the hydrogen atom. Higher orbital angular momentum states are distributed similarly.

2.3.2 Structure of helium

For target structure calculations of helium we use the configuration-interaction (CI) approach of Fursa and Bray [58]. Generating pseudostates for the two-electron helium atom is much more complicated than for atomic hydrogen. Here we state the main ideas and formulae in order to facilitate calculations of the transition matrix elements.

Within a nonrelativistic formulation the target orbital angular momentum l, spin s, and parity π are conserved quantum numbers. Therefore it is convenient to use the L-S coupling scheme. For each target symmetry $\alpha = \{l, s, \pi\}$ the target states are obtained via the configuration-interaction expansion

$$\Phi_\alpha(x_1, x_2) = \sum_{k=1}^{N} B_k^\alpha \tilde{\Phi}_k^{ls\pi}(x_1, x_2), \tag{2.28}$$

where x denotes spatial and spin coordinates. Each configuration $\tilde{\Phi}_k^{ls\pi}$ is simply an antisymmetrised two-electron function that is built by orbital angular momentum and spin coupling of one-electron orbitals $\varphi_a(x)$ given by

$$|\tilde{\Phi}_k^{ls\pi}\rangle = \frac{1}{\sqrt{2}}(1 - P_{12})|\varphi_a(x_1), \varphi_b(x_2) : ls\pi\rangle, \tag{2.29}$$

where P_{12} is the permutation operator. Also, the CI coefficients B_k^n are obtained by diagonalisation of the target Hamiltonian in the basis of configurations $\{\tilde{\Phi}_k^{ls\pi}\}$.

The one electron orbitals in Eq. (2.29) are the product of a radial function, spherical harmonic, and spin function, that is

$$\varphi_\alpha(x) = \phi_\alpha(r) Y_{l_\alpha m_\alpha}(\hat{\boldsymbol{r}}) \chi(\sigma). \tag{2.30}$$

Again we choose the radial functions in the form of the orthogonal Laguerre functions ξ_{kl} (2.27), such that

$$\phi_\alpha(r) = \frac{1}{r}\xi_{k_\alpha l_\alpha}(r). \tag{2.31}$$

Therefore, we can write the two-electron functions as

$$|\varphi_a(x_1), \varphi_b(x_2) : ls\pi\rangle = \phi_a(r_1)\phi_b(r_2)\left\{Y_{l_a}(\hat{\boldsymbol{r}}_1) \otimes Y_{l_b}(\hat{\boldsymbol{r}}_2)\right\}_{l_\alpha m_\alpha} X(s), \tag{2.32}$$

where $X(s)$ is a two-electron spin function and the bipolar harmonics are defined through the spherical harmonics Y_{lm} as

$$\left\{Y_{l_a}(\hat{\boldsymbol{r}}_1) \otimes Y_{l_b}(\hat{\boldsymbol{r}}_2)\right\}_{l_\alpha m_\alpha} = \sum_{m_a m_b} C^{l_\alpha m_\alpha}_{l_a m_a l_b m_b} Y_{l_a m_a}(\hat{\boldsymbol{r}}_1) Y_{l_b m_b}(\hat{\boldsymbol{r}}_2). \tag{2.33}$$

During the collision the total electronic spin of the helium atom is always conserved. Therefore, only the spatial part of the target wave function ψ_α needs to be considered. Additionally, since we only consider scattering on the ground state ($s = 0$) only states with $s = 0$ can be excited. The spatial part of the target wave function is given by

$$\psi_\alpha(\boldsymbol{r}_1, \boldsymbol{r}_2) = \sum_{a,b} B^\alpha_{a,b}\phi_a(r_1)\phi_b(r_2)\left\{Y_{l_a}(\hat{\boldsymbol{r}}_1) \otimes Y_{l_b}(\hat{\boldsymbol{r}}_2)\right\}_{l_\alpha m_\alpha}, \tag{2.34}$$

where, to ensure antisymmetry of the two-electron target states, the CI coefficients satisfy the symmetry property

$$B^\alpha_{a,b} = (-1)^{l_a + l_b - l_\alpha} B^\alpha_{b,a}. \tag{2.35}$$

As only one electron can be excited, we may use the hydrogenic notation nlm to label the quantum state α. Equation (2.34) defines our pseudostates that will be used in the evaluation of transition matrix elements.

Limiting the set of two-electron configurations to those where one of the electrons only occupies the $\mathrm{He}^+(1s)$ orbital is referred to as a frozen-core model of

helium. Excited states of helium are well described within the frozen-core model. However, the ground state benefits from a more accurate description, which can be readily achieved by allowing for a more general choice of the configurations. When several inner orbitals are allowed we have a multiconfiguration description. We emphasise here that both frozen-core and multiconfiguration descriptions of the target explicitly account for the electron correlation effects. The number of inner-electron orbitals included in Eq. (2.34) will be discussed in Chapter 3.

2.3.3 Structure of noble gasses

For target structure calculations of the noble gasses neon, argon, krypton, and xeon we use the approach of Fursa and Bray [75]. The method is very similar to that of helium. Here we state the main ideas and formulae in order to facilitate calculations of the transition matrix elements.

For noble gases, it is not practical to include all target electrons and so we adopt a model of six p electrons above an inert Hartree-Fock core. Excited states of noble gases are obtained by allowing one-electron excitations from the outer p-shell. Therefore, with $N_\mathrm{e} = 6$ and the remaining electrons treated as an inert core the target Hamiltonian becomes

$$H_\mathrm{T} = \sum_{i=1}^{N_\mathrm{e}} \left(H_i + \sum_{j>i}^{N_\mathrm{e}} \frac{1}{|\boldsymbol{r}_i - \boldsymbol{r}_j|} \right), \tag{2.36}$$

where H_i is Hamiltonian of the inert-core+one electron system, discussed further below.

This structure model is implemented in a number of steps, in what follows we will use neon for example. First, we perform self-consistent Hartree-Fock calculations for the Ne^+ ion and obtain a set of orbitals: $1s, 2s, 2p$. We will refer to $1s$ and $2s$ orbitals as inert core orbitals and to the $2p$ orbital as the frozen-

core orbital. Next, using a set of Laguerre functions ξ_{kl} (2.27) we diagonalise the Hamiltonian of the Ne^{5+} ion H_i, which in our model is given by

$$H_i = -\frac{1}{2}\nabla^2_{\boldsymbol{r}_i} + V_i^{\mathrm{HF}}, \tag{2.37}$$

where V^{HF} is a non-local Hartree-Fock potential that is constructed using inert core orbitals φ_c ($1s$ and $2s$ for Ne) according to

$$\begin{aligned} V^{\mathrm{HF}}\xi(\boldsymbol{r}) = &-\frac{N_{\mathrm{e}}}{r}\xi(\boldsymbol{r}) + \sum_{\varphi_c}\left(\int d\boldsymbol{r}'\frac{|\varphi_c(\boldsymbol{r}')|^2}{|\boldsymbol{r}'-\boldsymbol{r}|} - \frac{1}{r}\right)\xi(\boldsymbol{r}) \\ &- \sum_{\varphi_c}\int d\boldsymbol{r}'\frac{\varphi_c(\boldsymbol{r}')\xi(\boldsymbol{r}')}{|\boldsymbol{r}'-\boldsymbol{r}|}\varphi_c(\boldsymbol{r}). \end{aligned} \tag{2.38}$$

The result is a set of one-electron functions $\{\varphi_a\}$ that satisfy

$$\langle\varphi_b|H_i|\varphi_a\rangle = \epsilon_a\delta_{ba}, \tag{2.39}$$

where ϵ_a is the one-electron energy.

The $2p$ orbital in the $\{\varphi_a\}$ basis differs substantially from the Hartree-Fock $2p$ orbital. In order to build a one-electron basis suitable for the description of a neutral Ne atom we replace the former orbital with the Hartree-Fock one. The basis is then orthogonalised by the Gram-Schmidt procedure. The resulting orthonormal basis is denoted as $\{\phi_a\}$ and satisfies

$$\langle\phi_b|H_i|\phi_a\rangle = e_{b,a}. \tag{2.40}$$

The coefficients $e_{b,a}$ can be trivially obtained from the one-electron energies ϵ_a and overlap coefficients between the Hartree-Fock $2p$ orbital and the $\{\varphi_a\}$ basis.

The target states $\{\Phi_\alpha\}$ of Ne are then described via the CI expansion

$$\Phi_\alpha = \sum_a C_a^\alpha\,\tilde{\Phi}_a. \tag{2.41}$$

The set of configurations $\{\tilde{\Phi}_a\}$ is built by angular momentum coupling of the wave function of $2p^5$ electrons and one-electron functions from the $\{\phi_a\}$ basis. We will refer to the former wave function as the frozen-core wave function

$\psi_c(l_0^{4l+1})$, and to the latter one as the active electron wave function. The frozen-core wave function has angular momentum $l_0 = 1$ and spin 1/2, and when coupled with the active electron wave function ϕ_a leads to configurations with spin $s = 0, 1$, orbital angular momentum l ($|l_a - l_0| \leq l \leq l_a + l_0$), and parity $\pi = (-1)^{l_0+l_a}$

$$|\tilde{\Phi}_a\rangle = \mathcal{A}\,|\psi_c(l_0^{4l+1}), \phi_a : ls\pi\rangle. \tag{2.42}$$

The antisymmetrisation operator $\mathcal{A}$ is given by

$$\mathcal{A} = \frac{1}{\sqrt{N_\mathrm{e}}}\left(1 - \sum_{i=1}^{N_\mathrm{e}-1} P_{iN_\mathrm{e}}\right), \tag{2.43}$$

where P_{ij} is a permutation operator.

The coefficients C_a^α in the CI expansion (2.41) are obtained by diagonalisation of the target Hamiltonian (2.36) in the basis of configurations (2.42). The target orbital angular momentum l, spin s, and parity π are conserved quantum numbers and diagonalisation of the target Hamiltonian is performed separately for each target symmetry $\{l, s, \pi\}$. The resulting set of target states satisfy

$$\langle\Phi_{\alpha'}|H_\mathrm{T}|\Phi_\alpha\rangle = \epsilon_\alpha \delta_{\alpha'\alpha}, \tag{2.44}$$

where ϵ_α is the target state energy. Additionally, for scattering from the ground state ($s = 0$) of a noble gas atom only target states with $s = 0$ can be excited. As for hydrogen and helium, the size of the calculations can be increased by simply increasing the number of Laguerre functions (N_l). The low-lying states will converge to bound states of the target, while the remaining pseudostates will provide an increasingly accurate representation of the high-lying bound states of the target atom and an increasingly dense square-integrable representation of the target continuum.

2.4 Evaluation of transition matrix elements

In this section we show how the transition matrix elements $\langle\psi_{\alpha'}|V(\boldsymbol{r},\boldsymbol{R})|\psi_\alpha\rangle$ are calculated for hydrogen, helium, and noble gasses neon, argon, krypton, and xenon.

2.4.1 Transition matrix elements for hydrogen

For the hydrogen target, the transition matrix elements are defined as

$$V_{\alpha'\alpha}(\boldsymbol{R}) \equiv \langle\psi_{\alpha'}|V(\boldsymbol{r},\boldsymbol{R})|\psi_\alpha\rangle = \int d\boldsymbol{r}\psi^*_{\alpha'}(\boldsymbol{r})\left(-\frac{1}{R}+\frac{1}{|\boldsymbol{R}-\boldsymbol{r}|}\right)\psi_\alpha(\boldsymbol{r}). \quad (2.45)$$

We start by expanding the Coulomb potential in the following form [76]

$$-\frac{1}{R}+\frac{1}{|\boldsymbol{R}-\boldsymbol{r}|} = 4\pi\sum_{\lambda\mu}\frac{1}{2\lambda+1}\mathcal{U}_\lambda(R,r)Y^*_{\lambda\mu}(\hat{\boldsymbol{R}})Y_{\lambda\mu}(\hat{\boldsymbol{r}}), \quad (2.46)$$

where

$$\mathcal{U}_\lambda(R,r) = \begin{cases} -\dfrac{\delta_{\lambda0}}{R}+\dfrac{R^\lambda}{r^{\lambda+1}} & \text{if} \quad R\le r, \\ -\dfrac{\delta_{\lambda0}}{R}+\dfrac{r^\lambda}{R^{\lambda+1}} & \text{if} \quad R>r. \end{cases} \quad (2.47)$$

Inserting our expression for the hydrogen wave functions (2.25) and expansion (2.46) into Eq. (2.45) we obtain

$$\begin{aligned} V_{\alpha'\alpha}(\boldsymbol{R}) =& 4\pi\sum_{\lambda\mu}\frac{Y^*_{\lambda\mu}(\hat{\boldsymbol{R}})}{2\lambda+1}\int_0^\infty dr r^2\phi_{n_{\alpha'}l_{\alpha'}}(r)\phi_{n_\alpha l_\alpha}(r)\mathcal{U}_\lambda(R,r) \\ &\times\int d\hat{\boldsymbol{r}}Y^*_{l_{\alpha'}m_{\alpha'}}(\hat{\boldsymbol{r}})Y_{l_\alpha m_\alpha}(\hat{\boldsymbol{r}})Y_{\lambda\mu}(\hat{\boldsymbol{r}}). \end{aligned} \quad (2.48)$$

The angular integration can be taken if we use the following relation for spherical harmonics [76]

$$\int d\hat{\boldsymbol{r}}\, Y^*_{l_{\alpha'}m_{\alpha'}}(\hat{\boldsymbol{r}})Y_{l_\alpha m_\alpha}(\hat{\boldsymbol{r}})Y_{\lambda\mu}(\hat{\boldsymbol{r}}) = \sqrt{\frac{(2l_\alpha+1)(2\lambda+1)}{4\pi(2l_{\alpha'}+1)}}\,C^{l_{\alpha'}0}_{l_\alpha0\,\lambda0}C^{l_{\alpha'}m_{\alpha'}}_{l_\alpha m_\alpha\,\lambda\mu}, \quad (2.49)$$

where $C^{LM}_{lml'm'}$ are the Clebsch-Gordan coefficients. Therefore, Eq. (2.48) reduces to

$$V_{\alpha'\alpha}(\boldsymbol{R}) = \sum_{\lambda\mu} \sqrt{\frac{4\pi(2l_\alpha+1)}{(2l_{\alpha'}+1)(2\lambda+1)}}\, C^{l_{\alpha'}0}_{l_\alpha 0\,\lambda 0} C^{l_{\alpha'}m_{\alpha'}}_{l_\alpha m_\alpha\,\lambda\mu} Y^*_{\lambda\mu}(\hat{\boldsymbol{R}}) \times \int_0^\infty dr r^2 \phi_{n_{\alpha'}l_{\alpha'}}(r)\phi_{n_\alpha l_\alpha}(r)\mathcal{U}_\lambda(R,r). \tag{2.50}$$

The remaining radial integral is evaluated using Simpson's rule and λ and μ are limited by the Clebsch-Gordan coefficients.

2.4.2 Transition matrix elements for helium

For the helium target, the transition matrix elements read as

$$\begin{aligned} V_{\alpha'\alpha}(\boldsymbol{R}) &\equiv \langle\psi_{\alpha'}|V(\boldsymbol{r},\boldsymbol{R})|\psi_\alpha\rangle \\ &= \int d\boldsymbol{r}_1 d\boldsymbol{r}_2 \psi^*_{\alpha'}(\boldsymbol{r}_1,\boldsymbol{r}_2)\left(-\frac{2}{R}+\frac{1}{|\boldsymbol{R}-\boldsymbol{r}_1|}+\frac{1}{|\boldsymbol{R}-\boldsymbol{r}_2|}\right)\psi_\alpha(\boldsymbol{r}_1,\boldsymbol{r}_2). \end{aligned} \tag{2.51}$$

Considering the symmetry with respect to interchanging $\boldsymbol{r}_1$ and $\boldsymbol{r}_2$ we can write

$$V_{\alpha'\alpha}(\boldsymbol{R}) = 2\int d\boldsymbol{r}_1 d\boldsymbol{r}_2 \psi^*_{\alpha'}(\boldsymbol{r}_1,\boldsymbol{r}_2)\left(-\frac{1}{R}+\frac{1}{|\boldsymbol{R}-\boldsymbol{r}_1|}\right)\psi_\alpha(\boldsymbol{r}_1,\boldsymbol{r}_2). \tag{2.52}$$

Now inserting our expression for the helium wave functions (2.34) into Eq. (2.52) we obtain

$$\begin{aligned} V_{\alpha'\alpha}(\boldsymbol{R}) =& 2\sum_{a,b} B^{\alpha'}_{a,b} \sum_{m_a m_b} C^{l_{\alpha'}m_{\alpha'}}_{l_a m_a l_b m_b} \sum_{c,d} B^{\alpha}_{c,d} \sum_{m_c m_d} C^{l_\alpha m_\alpha}_{l_c m_c l_d m_d} \\ &\times \int d\boldsymbol{r}_1 d\boldsymbol{r}_2 \phi_a(r_1)\phi_b(r_2) Y^*_{l_a m_a}(\hat{\boldsymbol{r}}_1) Y^*_{l_b m_b}(\hat{\boldsymbol{r}}_2) \\ &\times \left(-\frac{1}{R}+\frac{1}{|\boldsymbol{R}-\boldsymbol{r}_1|}\right)\phi_c(r_1)\phi_d(r_2) Y_{l_c m_c}(\hat{\boldsymbol{r}}_1) Y_{l_d m_d}(\hat{\boldsymbol{r}}_2). \end{aligned} \tag{2.53}$$

Taking into account the orthogonality of spherical harmonics

$$\int d\hat{\boldsymbol{r}}_2\, Y^*_{l_b m_b}(\hat{\boldsymbol{r}}_2)\, Y_{l_d m_d}(\hat{\boldsymbol{r}}_2) = \delta_{l_b l_d}\delta_{m_b m_d}, \tag{2.54}$$

integration over $\hat{\boldsymbol{r}}_2$ can be performed, leading to

$$V_{\alpha'\alpha}(\boldsymbol{R}) = 2\sum_{a,b} B^{\alpha'}_{a,b} \sum_{c,d} B^{\alpha}_{c,d} \sum_{m_a m_b m_c} C^{l_{\alpha'} m_{\alpha'}}_{l_a m_a l_b m_b} C^{l_\alpha m_\alpha}_{l_c m_c l_b m_b} \langle \phi_b | \phi_d \rangle \times \int d\boldsymbol{r}_1 \phi_a(r_1) Y^*_{l_a m_a}(\hat{\boldsymbol{r}}_1) \left(-\frac{1}{R} + \frac{1}{|\boldsymbol{R} - \boldsymbol{r}_1|} \right) \phi_c(r_1) Y_{l_c m_c}(\hat{\boldsymbol{r}}_1). \quad (2.55)$$

Here $\langle \phi_b | \phi_d \rangle$ is the overlap of two radial functions,

$$\langle \phi_b | \phi_d \rangle = \int_0^\infty dr_2 r_2^2 \phi_b(r_2) \phi_d(r_2). \quad (2.56)$$

Now, following the ideas of Section 2.4.1 integration over $\hat{\boldsymbol{r}}_1$ can be performed. First, we expand the Coulomb potential using Eq. (2.46), then we utilise Eq. (2.49) to get

$$V_{\alpha'\alpha}(\boldsymbol{R}) = 2 \sum_{a,b,c,d,\lambda,\mu} \sqrt{\frac{4\pi(2l_c+1)}{(2\lambda+1)(2l_a+1)}} B^{\alpha'}_{a,b} B^{\alpha}_{c,d} C^{l_a 0}_{l_c 0 \lambda 0} Y^*_{\lambda\mu}(\hat{\boldsymbol{R}}) \langle \phi_b | \phi_d \rangle \times \sum_{m_a m_b m_c} C^{l_{\alpha'} m_{\alpha'}}_{l_a m_a l_b m_b} C^{l_\alpha m_\alpha}_{l_c m_c l_b m_b} C^{l_a m_a}_{l_c m_c \lambda \mu} \int_0^\infty dr_1 r_1^2 \phi_a(r_1) \phi_c(r_1) \mathcal{U}_\lambda(R, r_1). \quad (2.57)$$

Finally, we utilise the following expression for the summation over Clebsch-Gordan coefficients [76],

$$\sum_{m_a m_b m_c} C^{l_{\alpha'} m_{\alpha'}}_{l_a m_a l_b m_b} C^{l_\alpha m_\alpha}_{l_c m_c l_b m_b} C^{l_a m_a}_{l_c m_c \lambda \mu} = (-1)^{l_a + l_b + l_\alpha + \lambda} \sqrt{(2l_\alpha+1)(2l_a+1)} C^{l_{\alpha'} m_{\alpha'}}_{l_\alpha m_\alpha \lambda \mu} \begin{Bmatrix} l_b & l_a & l_{\alpha'} \\ \lambda & l_\alpha & l_c \end{Bmatrix}, \quad (2.58)$$

where the braces denote the $6j$ symbol of the first kind, to arrive at

$$V_{\alpha'\alpha}(\boldsymbol{R}) = 2 \sum_{a,b,c,d,\lambda,\mu} \sqrt{\frac{4\pi(2l_\alpha+1)(2l_c+1)}{(2\lambda+1)}} B^{\alpha'}_{a,b} B^{\alpha}_{c,d} C^{l_{\alpha'} m_{\alpha'}}_{l_\alpha m_\alpha \lambda \mu} C^{l_a 0}_{l_c 0 \lambda 0} Y^*_{\lambda\mu}(\hat{\boldsymbol{R}}) \langle \phi_b | \phi_d \rangle \times (-1)^{l_a + l_b + l_\alpha + \lambda} \begin{Bmatrix} l_b & l_a & l_{\alpha'} \\ \lambda & l_\alpha & l_c \end{Bmatrix} \int_0^\infty dr_1 r_1^2 \mathcal{U}_\lambda(R, r_1) \phi_a(r_1) \phi_c(r_1). \quad (2.59)$$

2.4.3 Transition matrix elements for noble gasses

For the noble gas targets, as the first step we use the CI expansion (2.41) to express the transition matrix elements via matrix elements for configurations $\{\tilde{\Phi}_a\}$,

$$\langle \Phi_{\alpha'} | V(\boldsymbol{r}, \boldsymbol{R}) | \Phi_\alpha \rangle = \sum_{a,b} C_a^\alpha C_b^{\alpha'} \langle \tilde{\Phi}_b | V(\boldsymbol{r}, \boldsymbol{R}) | \tilde{\Phi}_a \rangle. \tag{2.60}$$

With our model of $N_\mathrm{e} = 6$ p-shell electron above an inert core the projectile-target interaction (2.4) becomes

$$V(\boldsymbol{r}, \boldsymbol{R}) = V_0 + \sum_{i=1}^{N_\mathrm{e}} \frac{1}{|\boldsymbol{R} - \boldsymbol{r}_i|}, \tag{2.61}$$

where V_0 is the interaction of the projectile with the inert core. The potential V_0 is defined as

$$V_0(\boldsymbol{R}) = -\frac{N_\mathrm{e}}{R} + U_0(\boldsymbol{R}), \tag{2.62}$$

where

$$U_0(\boldsymbol{R}) = \sum_{\varphi_c} \left(-\frac{1}{R} + \int d\boldsymbol{r}' \frac{|\varphi_c(\boldsymbol{r}')|^2}{|\boldsymbol{r}' - \boldsymbol{R}|} \right). \tag{2.63}$$

For noble gasses we are only interested in calculating the electronic stopping cross section (see Section 2.5), therefore we will neglect the V_0 interaction. Neglecting this interaction will result in an incorrect elastic-scattering cross section, however elastic scattering does not contribute to the electronic stopping power.

In order to perform the angular integration in Eq. (2.60) analytically we use the following multipole expansion of the potential

$$V(\boldsymbol{r}, \boldsymbol{R}) = 4\pi \sum_{i=1}^{N_\mathrm{e}} \sum_{\lambda\mu} \frac{1}{2\lambda + 1} \mathcal{U}_\lambda(R, r_i) Y^*_{\lambda\mu}(\hat{\boldsymbol{R}}) Y_{\lambda\mu}(\hat{\boldsymbol{r}}), \tag{2.64}$$

where

$$\mathcal{U}_\lambda(R, r_i) = \begin{cases} \dfrac{R^\lambda}{r_i^{\lambda+1}} & \text{if} \quad R \le r_i, \\ \dfrac{r_i^\lambda}{R^{\lambda+1}} & \text{if} \quad R > r_i. \end{cases} \tag{2.65}$$

With this and also using the properties of antisymmetric configurations (2.42) the final expression for the matrix elements for configurations $\{\tilde{\Phi}_a\}$ can be written as

$$\langle\tilde{\Phi}_b|V(\boldsymbol{r},\boldsymbol{R})|\tilde{\Phi}_a\rangle = \sum_\lambda (-1)^{l_\alpha}\frac{1}{\sqrt{2l_\alpha+1}}Y_{\lambda\mu}(\hat{\boldsymbol{R}})^* C^{l_{\alpha'}m_{\alpha'}}_{l_\alpha m_\alpha \lambda\mu} \times (I_1(a,b,\lambda,R)+I_2(a,b,\lambda,R)), \tag{2.66}$$

where

$$I_1(a,b,\lambda,R) = (-1)^{\lambda+l_0+l_b+l_\alpha}\sqrt{(2l_a+1)(2l_\alpha+1)}C^{l_b0}_{l_a0\lambda0}\begin{Bmatrix} l_a & l_0 & l_\alpha \\ l_{\alpha'} & \lambda & l_b \end{Bmatrix} \times \int_0^\infty dr_c r_c^2\phi_c(r_c)\phi_c(r_c)\int_0^\infty dr_6 r_6^2\phi_b(r_6)\mathcal{U}_\lambda(R,r_6)\phi_a(r_6), \tag{2.67}$$

and

$$I_2(a,b,\lambda,R) = \delta_{l_b l_a}\delta_{m_b m_a}(-1)^{\lambda+l_b+l_{\alpha'}+l_0}\sqrt{(2l_0+1)(2l_\alpha+1)}C^{l_00}_{l_00\lambda0}\begin{Bmatrix} l_0 & l_b & l_\alpha \\ l_{\alpha'} & \lambda & l_0 \end{Bmatrix} \times \int_0^\infty dr_6 r_6^2\phi_b(r_6)\phi_a(r_6)\int_0^\infty dr_c r_c^2\phi_c(r_c)\mathcal{U}_\lambda(R,r_c)\phi_c(r_c) \tag{2.68}$$

with $\boldsymbol{R}$, $\boldsymbol{r}_6$ and $\boldsymbol{r}_c$ being the position vectors of the incoming antiproton and the active and core electrons, respectively.

2.5 Stopping power

In this section we discuss the stopping power formula and how it should appear in a coupled-channel approach. Since our calculations are for a closed system the energy lost by the projectile is equal to the energy gained by the target.

The stopping power is the energy loss per unit path length and in general is defined as

$$-\frac{dE}{dx} = N_\mathrm{a}S(E_0), \tag{2.69}$$

where $S(E_0)$ is referred to as the stopping cross section. It depends on the incident energy of the projectile E_0, and is related to the stopping power through the

density of target atoms in the stopping medium N_{a}. For heavy projectiles it can be assumed that the total stopping cross section is the sum of two contributions, the nuclear and the electronic stopping cross sections, i.e.

$$S = S_{\mathrm{e}} + S_{\mathrm{n}}. \tag{2.70}$$

The electronic stopping cross section S_{e} is due to energy losses associated with all possible events of excitation and ionisation of the target electrons. Considering only single-electron processes the electronic stopping cross section is written as

$$S_{\mathrm{e}}(E_0) = \sum_{f=1}^{\infty}(\epsilon_f - \epsilon_i)\sigma_{fi} + \int_0^{E_0+\epsilon_i}(\epsilon - \epsilon_i)\frac{d\sigma}{d\epsilon}d\epsilon, \tag{2.71}$$

where ϵ_i is the energy of the initial state of the target i, σ_{fi} is the cross section for excitation to a state f of energy ϵ_f, and $d\sigma/d\epsilon$ is the single-differential cross section for ionisation of the electron with energy ϵ. Hence one sums over all possible energy losses due to excitation to bound states and integrates over all possible energy losses due to ionisation to the continuum states.

In the coupled-channel approach used in this thesis we discretise the continuum as described in Section 2.3. Therefore the sum and integral in Eq. (2.71) becomes a single sum over the total number N of negative- and positive-energy pseudostates. The electronic stopping cross section is hence written as

$$S_{\mathrm{e}}(E_0) \approx \sum_{f=1}^{N}(\epsilon_f - \epsilon_i)\sigma_{fi}, \tag{2.72}$$

where the cross section for transition of the target σ_{fi} is obtained by integration of the transition probability (2.24) over the impact parameter, that is

$$\sigma_{fi}(E_0) = 2\pi\int_0^{\infty} p_{fi}(b)bdb. \tag{2.73}$$

When dealing with a multi-electron target, such as helium, it is possible to include the contribution of two-electron processes to the electronic stopping

cross section. This is done by using an independent-event model to calculate ionisation with excitation (IE) and double ionisation (DI). In this model IE and DI are considered in a two-step approximation. The first step is single ionisation of the target and the second is ionisation or excitation of the residual ion. When the two-electron processes are included the electronic stopping cross section (2.72) gains an extra term and becomes

$$S_{\mathrm{e}}(E_0) \approx \sum_{f=1}^{N}(\epsilon_f - \epsilon_i)\sigma_{fi} + \sum_{k=1}^{N^+}(\epsilon_k^+ - \epsilon_1^+)\sigma_k^+, \tag{2.74}$$

where N^+ is the number of pseudostates used to represent the singly-ionised target, ϵ_1^+ is the ground-state energy of the target ion, and σ_k^+ is the IE/DI cross section for which the second electron transitions to a state k of energy ϵ_k^+ of the target ion.

As stated, the cross section σ_k^+ is calculated using an independent-event model, where IE and DI are considered in a two-step approximation. Therefore the cross section is defined by the product of the total single-ionisation probability, p_{ion}, and the probability of the residual ion transitioning from its ground state to some final state k, p_k^+. Hence

$$\sigma_k^+ = 2\pi \int_0^\infty p_{\mathrm{ion}}(b) p_k^+(b) b db. \tag{2.75}$$

Here p_{ion} is given by the sum of all probabilities (2.24) for transitions to positive energy states

$$p_{\mathrm{ion}}(b) = \sum_{f,\epsilon_f>0}^{N} p_f(b), \tag{2.76}$$

and p_k^+ is obtained by performing scattering calculations involving a singly ionised target.

The nuclear stopping cross section S_{n} is due to energy losses associated with momentum transfer to the target during elastic and inelastic scattering. It is

useful to be able to calculate the nuclear stopping cross section when comparing to experiments that measure all energy-loss contributions at once. The nuclear stopping cross section is given by

$$S_{\mathrm{n}}(E_0) = \sum_f \int \frac{q_f^2}{2M_T} \left(\frac{d\sigma_f}{d\Omega} \right) d\Omega, \tag{2.77}$$

where M_T is the mass of the target, q_f is the magnitude of momentum transfer to the target which depends on the scattering angle of the projectile, and $d\sigma_f/d\Omega$ is the angular-differential cross section. The angular-differential cross section is constructed from the amplitudes in the impact-parameter representation via the Bessel transformation,

$$\frac{d\sigma_f}{d\Omega} = (\mu v)^2 \left| \int_0^\infty A_f(t = +\infty, b) J_{m_f}(2\mu v b \sin(\theta/2)) b db \right|^2, \tag{2.78}$$

where μ is the reduced mass of the projectile-target system, v is the lab-frame incident velocity, J is the Bessel function of the first kind, m_f is the magnetic quantum number of electronic state f, and θ is the scattering angle of the projectile.

2.6 Chapter summary

The single-centre semiclassical convergent close-coupling method has been presented. The semiclassical impact-parameter approximation is used to derive a set of coupled-channel differential equations for the expansion coefficients of the total scattering wave function, which are solved with the condition that the target is initially in the ground state. Hydrogen, helium, and noble gas target pseudostates are constructed from Laguerre basis functions. This allows us to model the whole spectrum of the target, both discrete and continuum. Details of the electronic and nuclear stopping power in a coupled-channel approach has been presented.

In the following chapter results of calculations for the stopping cross section in antiproton collisions with hydrogen, helium, neon, argon, krypton, and xenon will be presented.

Chapter 3

Antiproton stopping in atomic targets

3.1 Introduction

In this chapter calculations of the stopping cross section for antiproton collisions with hydrogen, helium, neon, argon, krypton, and xenon will be presented and compared with existing theoretical and experimental data.

With the development of the low-energy antiproton ring (LEAR) facility at CERN stopping cross section measurements for antiprotons in He were performed by Agnello *et al.* [77]. They simultaneously measured the spacial coordinates and times of annihilation. Then they solved an inverse problem to obtain the stopping cross section. Resulting equations were solved numerically using parameters to obtain the best fit to the data. Measurements were performed between 0.5 keV and 1.1 MeV. This data was later reanalysed by Lodi Rizzini *et al.* [78] with emphasis on the Barkas effect [22].

With experimental data available to compare with, Schiwietz *et al.* [44, 45] performed the first theoretical calculations of the stopping cross section for antiprotons in H and He. They performed calculations using atomic-orbital (AO)

close coupling, distorted-wave (DW) Born, and generalised adiabatic-ionisation (AI) methods. It was found that the first order contribution to the stopping cross section dominates at high velocities with higher order effects becoming important at intermediate velocities, while near-adiabatic dynamics prevailed in the low velocity limit. The AO and DW calculations were in mutual agreement above the stopping maximum. The He calculations of Schiwietz *et al.* [44, 45] were in general not within the experimental uncertainty of Agnello *et al.* [77].

Cabrera-Trujillo *et al.* [36] were the next to contribute from a theoretical perspective. They used the electron-nuclear dynamics formalism to calculate the antiproton-hydrogen stopping cross section up to 300 keV. The results showed reasonable agreement with the AO method of Schiwietz *et al.* [44, 45].

The latest development in solving the problem comes from Lühr and Saenz [50] who calculated the stopping cross sections for antiprotons in H and He between 1 keV and 6.4 MeV. They used a semiclassical close-coupling approach to the solution of the time-dependent Schrödinger equation. The radial wave function was expanded in a B-spline basis with the He target described using an effective one-electron treatment. For H, Lühr and Saenz [50] obtained good agreement with the calculations of Schiwietz *et al.* [44, 45] and there was reasonable agreement with the calculations of Cabrera-Trujillo *et al.* [36] as well. For He, there was good agreement with the data of Agnello *et al.* [77] above 2 MeV, but disagreement at intermediate and low energies. Lühr and Saenz [50] concluded that this is due to using a one-electron model.

In this chapter we present stopping cross section calculations for antiproton collisions with H, He, Ne, Ar, Kr, and Xe using the semiclassical time-dependent CCC method, described in Chapter 2. The results presented in this chapter for helium improve upon the current theories of Schiwietz *et al.* [44, 45] and Lühr and

Saenz [50] by employing a multiconfiguration treatment of the target, which fully accounts for the electron-electron correlation, and taking into account double ionisation and ionisation with excitation via the independent-event model.

3.2 Hydrogen

In this section we present calculations of the stopping cross section for antiproton-hydrogen collisions. Convergence of the stopping cross section with increasing basis size is investigated. Then we present our final calculations compared to existing theories.

3.2.1 Convergence studies

When using a coupled-channel approach where the scattering wave function is expanded in a set of target pseudostates it is important to establish convergence of the stopping cross section with increasing the size of the underlying basis. This is done to ensure the target space is well represented and the addition of more basis functions will not change the final result. Here we investigate convergence of the electronic stopping cross section in terms of the basis parameters $l_{\max}$, the maximum value of orbital angular momentum included in the expansion, and $n_{\max}$, the maximum number of basis functions for $l = 0$. The number of basis functions for each l is $N_l = n_{\max} - l$. Then the total number of pseudostates N used to expand the scattering wave function is given by $N = \sum_{l=0}^{l_{\max}} N_l(2l+1)$.

As previously stated the final result should not depend on the basis exponential fall-off parameter λ_l, however the rate of convergence does. Typically we choose λ_l to give the most accurate ground state energy with the minimum number of basis functions, therefore in all calculations presented in this section we will set $\lambda_l = 2$.

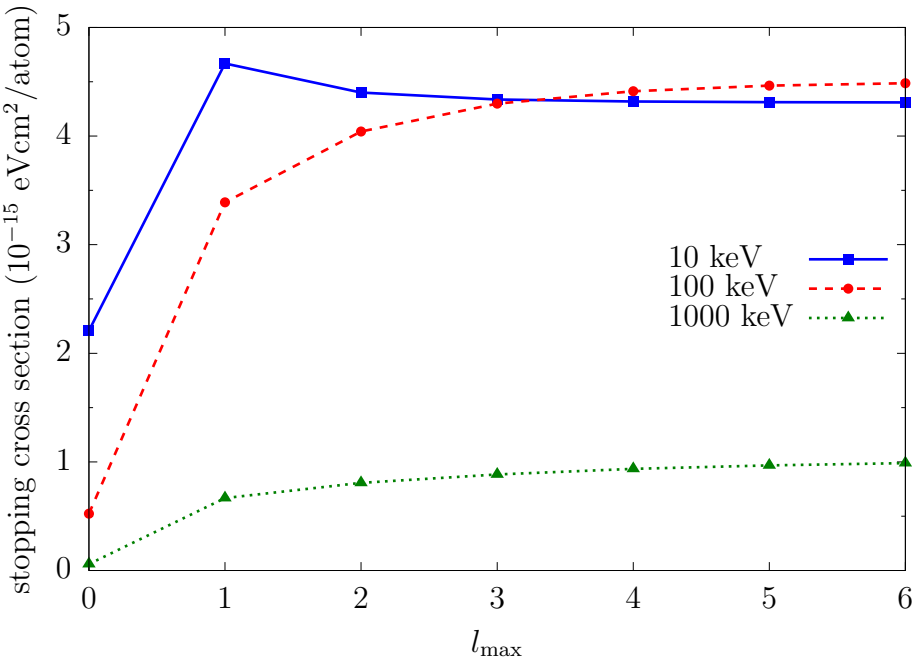

Figure 3.1: Convergence of the electronic stopping cross section for antiprotons incident on hydrogen with increasing $l_{\max}$ for $n_{\max} = 30$ at incident energies of 10 keV, 100 keV, and 1000 keV.

Convergence of the electronic stopping cross section has been studied over the whole energy region considered in this work. Here we will give typical examples at antiproton incident energies of 10 keV, 100 keV, and 1000 keV, i.e. low, intermediate, and high incident energies. First, we fix the basis parameter $n_{\max}$ at some large value and systematically increase $l_{\max}$. Figure 3.1 shows the convergence of the electronic stopping cross section for antiproton-hydrogen collisions with increasing $l_{\max}$, while $n_{\max}$ is fixed at 30. From this figure we can see that at lower incident energies the results converge faster with $l_{\max}$. For instance, at 10 keV, $l_{\max}$ of 4 appears to give sufficient convergence, whereas $l_{\max} = 6$ is required to achieve convergent results at 1000 keV incident energy. Specifically, the difference between stopping cross section with $l_{\max} = 5$ and $l_{\max} = 6$ at 10 keV, 100 keV, and 1000 keV is 0.06%, 0.49%, and 1.9%, respectively. Next we take a look at convergence of the electronic stopping cross

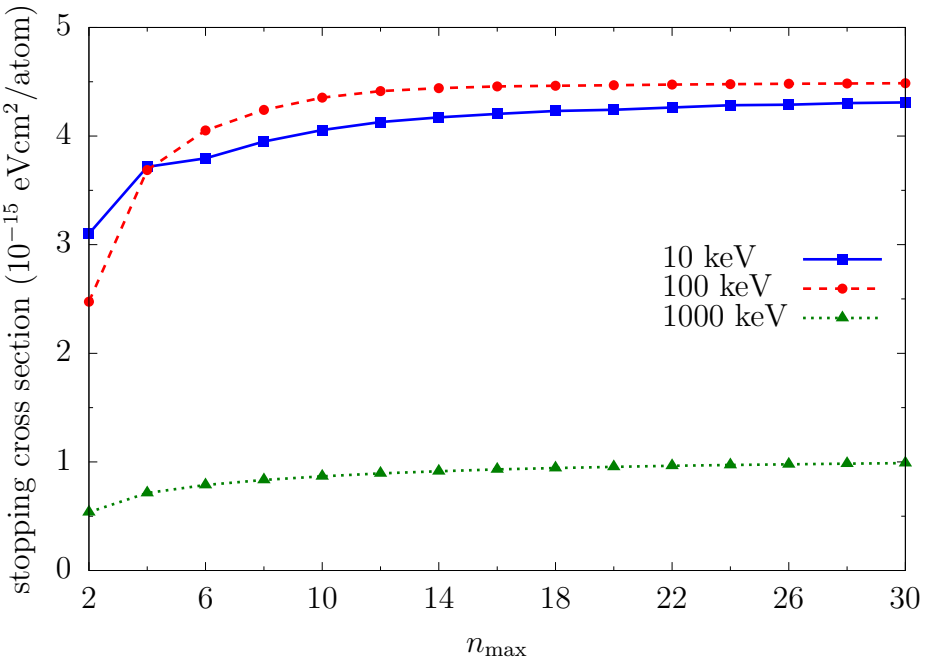

Figure 3.2: Convergence of the electronic stopping cross section for antiprotons incident on hydrogen with increasing $n_{\max}$ for $l_{\max} = 6$ at incident energies of 10 keV, 100 keV, and 1000 keV.

section with increasing $n_{\max}$.

Figure 3.2 shows the convergence of the electronic stopping cross section with increasing $n_{\max}$, while $l_{\max}$ is fixed at 6. From the figure we can see that convergence with $n_{\max}$ is similar for all incident energies, i.e. the cross section gradually increases before reaching convergence. The difference between stopping cross section when $n_{\max}$ changes from 28 to 30 at 10 keV, 100 keV, and 1000 keV is 0.29%, 0.06%, and 0.48%, respectively. From Figures 3.1 and 3.2 it can be concluded that a basis with $n_{\max} = 30$ and $l_{\max} = 6$ produces sufficiently convergent results for the electronic stopping cross section. This shows that the stopping cross section requires a larger basis to reach convergence when compared to the total ionisation cross section, which required $n_{\max} = 20$ and $l_{\max} = 5$ [62].

3.2.2 Results of calculations

Here we present our final calculations of the antiproton-hydrogen stopping cross section. The convergent basis parameters discussed above result in a total of 1267 states to be used in the solution of the coupled-channel differential equations (2.22). In Figure 3.3 we present our result for the antiproton-hydrogen electronic stopping cross section together with the theoretical calculations of Schiwietz *et al.* [44, 45] (AO, DW, and AI), Lühr and Saenz [50], and Cabrera-Trujillo *et al.* [36]. Also shown is the result obtained using Bethe's formula (1.1). The CCC results are in good agreement with the AO calculations of Schiwietz *et al.* [44, 45] and the results of Lühr and Saenz [50] over the whole energy range. Also, good agreement with the calculations of Cabrera-Trujillo *et al.* [36] and the DW calculations by Schiwietz *et al.* [44, 45] is seen above 30 keV and

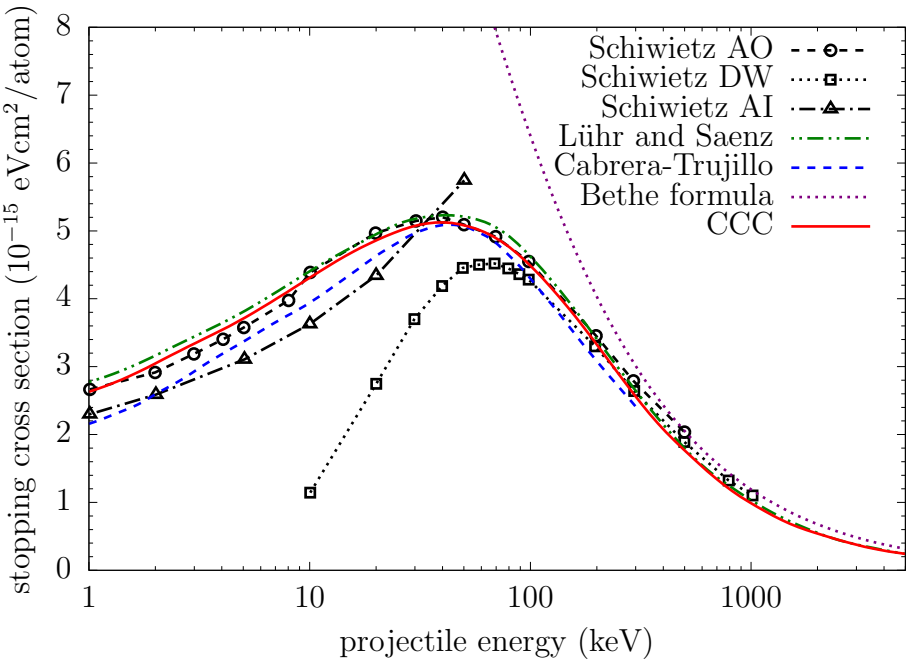

Figure 3.3: Electronic stopping cross section for antiprotons incident on hydrogen. The CCC calculations are compared with calculations of Schiwietz *et al.* [44, 45] (obtained using the AO, DW, and AI methods), Lühr and Saenz [50], and Cabrera-Trujillo *et al.* [36].

100 keV, respectively. Additionally, the CCC calculations tend toward those from Bethe's formula at high energies where the latter is applicable. There is currently no experiment to compare with, however good agreement with other theories validates our method and the associated computer code.

3.3 Helium

In this section we present calculations of the stopping cross section for antiproton-helium collisions. Convergence of the stopping cross section with increasing basis size and increasing number of inner-electron orbitals included in a multiconfiguration calculation is investigated. Then we present our final calculations and compare them with the existing theories and experiment. Our final calculations include the nuclear stopping cross section and contributions to the electronic stopping cross section from double ionisation and ionisation with excitation.

3.3.1 Convergence studies

Convergence of the antiproton-helium stopping cross section is investigated in much the same way as for hydrogen in Section 3.2.1, however we add consideration of how many inner-electron orbitals to include in a multiconfiguration approach. To this end we will first investigate convergence of the electronic stopping cross section in terms of the basis parameters $l_{\max}$ and $n_{\max}$ in the frozen-core approximation. Once convergence in terms of these parameters is established we can investigate convergence in terms of the number of inner-electron orbitals included in the multiconfiguration approach. For all calculations the basis function exponential fall-off parameter λ_l is chosen to be 2.

As done previously, we will give typical examples at antiproton incident energies of 10 keV, 100 keV, and 1000 keV. First, in the frozen-core approxi-

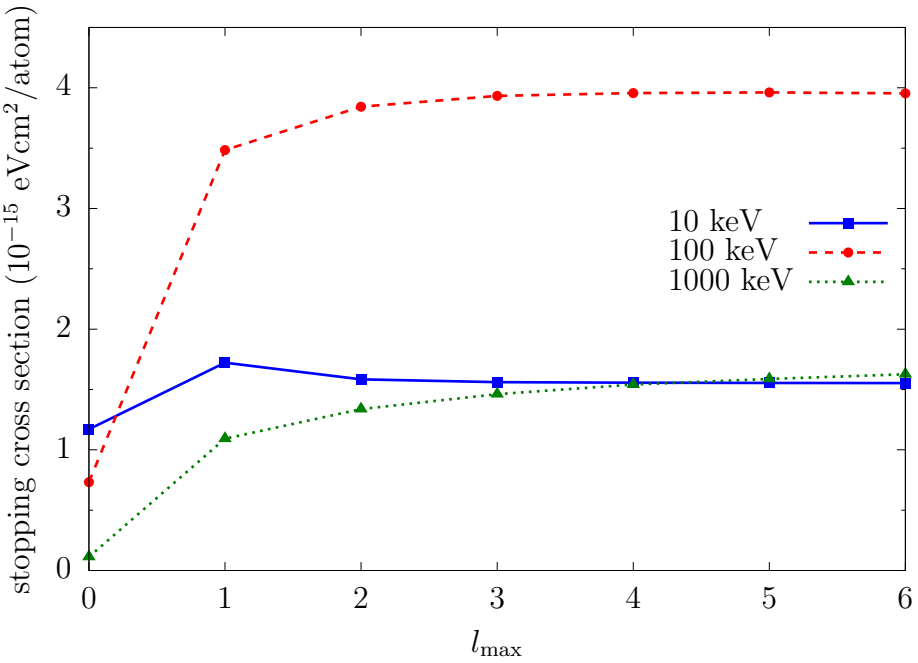

Figure 3.4: Convergence of the electronic stopping cross section for antiprotons incident on helium with increasing $l_{\max}$ for $n_{\max} = 20$ at incident energies of 10 keV, 100 keV, and 1000 keV. Calculations presented here were performed in the frozen-core approximation.

mation, we fix the basis parameter $n_{\max}$ at some large value and systematically increase $l_{\max}$. Figure 3.4 shows the convergence of the electronic stopping cross section for antiproton-helium collisions with increasing $l_{\max}$, while $n_{\max}$ is fixed at 20. From this figure we can see that at lower incident energies the results converge faster with $l_{\max}$. For instance, at 10 keV an $l_{\max}$ of 3 appears to give sufficient convergence, whereas $l_{\max} = 6$ is required to achieve convergent results at 1000 keV incident energy. Specifically, the difference between stopping cross section with $l_{\max} = 5$ and $l_{\max} = 6$ at 10 keV, 100 keV, and 1000 keV is 0.08%, 0.19%, and 2.4%, respectively. Next we take a look at convergence of the stopping cross section with increasing $n_{\max}$, while still in the frozen-core approximation.

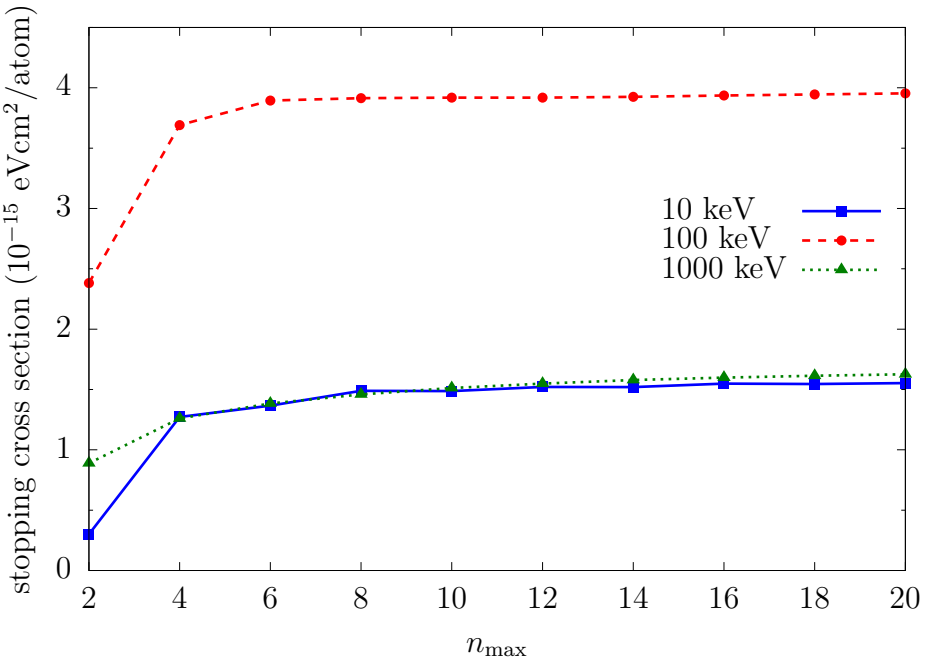

Figure 3.5: Convergence of the electronic stopping cross section for antiprotons incident on helium with increasing $n_{\max}$ for $l_{\max} = 6$ at incident energies of 10 keV, 100 keV, and 1000 keV. Calculations presented here were performed in the frozen-core approximation.

Figure 3.5 shows the convergence of the electronic stopping cross section with increasing $n_{\max}$, while $l_{\max}$ is fixed at 6. From the figure we can see that convergence with $n_{\max}$ is similar for all incident energies. The difference between stopping cross section when $n_{\max}$ changes from 18 to 20 at 10 keV, 100 keV, and 1000 keV is 0.55%, 0.21%, and 0.79%, respectively. From Figures 3.4 and 3.5 it can be concluded that a basis with $n_{\max} = 20$ and $l_{\max} = 6$ produces sufficiently convergent results for the electronic stopping cross section. Again, this shows that the stopping cross section requires a larger basis to reach convergence when compared to the total ionisation cross section, which required $n_{\max} = 20$ and $l_{\max} = 5$ [64].

Now that convergence in terms of $l_{\max}$ and $n_{\max}$ in the frozen-core approximation has been established we can investigate convergence in the mulitconfig-

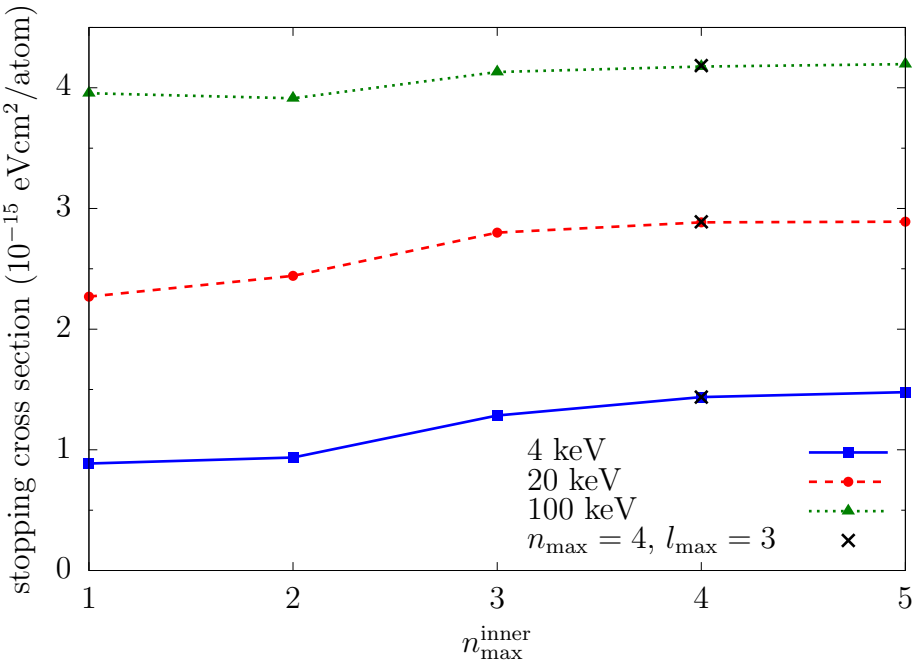

Figure 3.6: Convergence of the electronic stopping cross section for antiprotons incident on helium with increasing number of inner-electron orbitals in the multiconfiguration approach at incident energies of 4 keV, 20 keV, and 100 keV. The active-electron basis was constructed with $n_{\max} = 20$ and $l_{\max} = 6$.

urational approach. It was found that inclusion of inner-electron orbitals only effects the stopping cross section below the stopping maximum, therefore typical examples of convergence will be shown for 4 keV, 20 keV, and 100 keV antiproton incident energies. Figure 3.6 shows the convergence of the electronic stopping cross section with increasing number of the inner-electron orbitals in the multiconfiguration approach. The active-electron basis is kept constant with $n_{\max} = 20$ and $l_{\max} = 6$ while the number of inner-electron orbitals included in the expansion (2.34) is gradually increased. Here orbitals are added in entire shells, that is $n_{\max}^{\text{inner}}$ is increased and all possible l^{inner} are included. At $n_{\max}^{\text{inner}} = 4$ this changes such that $l_{\max}$ of the inner-electron orbitals is limited to 2 to reduce the computational time required for calculations. This limitation on l^{inner} should not affect the electronic stopping cross section as it was found that the inner-

electron orbitals with l of 3 or greater did not contribute. This is illustrated in Figure 3.6 with black crosses representing calculations with $n_{\max}^{\text{inner}} = 4$ and $l_{\max}^{\text{inner}} = 3$ for the inner electron that are on top of the points representing calculations with $n_{\max}^{\text{inner}} = 4$ and $l_{\max}^{\text{inner}} = 2$. From Figure 3.6 it can be concluded that the inclusion of the $1s$, $2s$, $2p$, $3s$, $3p$, $3d$, $4s$, $4p$, $4d$, $5s$, $5p$, and $5d$ orbitals for the inner electron are enough to give convergent results in a multiconfiguration approach with $n_{\max} = 20$ and $l_{\max} = 6$.

As described in Section 2.5 calculation of the stopping cross section associated with double ionisation and ionisation with excitation requires calculation of antiproton-He^+ collisions. Of course such calculations are checked for convergence as well. It was found that basis parameters of $n_{\max} = 20$ and $l_{\max} = 4$ were sufficient to give convergent results. This reduction in the required maximum orbital angular momentum for He^+ is due to the increase in the binding energy of the target electron.

3.3.2 Results of calculations

Here we present our final calculations of the antiproton-helium stopping cross section. The convergent basis parameters discussed above result in a total of 1288 states to be used in the solution of the coupled-channel differential equations (2.22) in the multiconfigruation approach. One of the major benefits of the multiconfiguration structure model is that it improves the ground state. In the frozen-core approximation the ionisation energy of the helium ground state was obtained to be 23.741 eV, however in the multiconfiguration calculations we obtain a ground state ionisation energy of 24.540 eV. This is very close to the experimentally measured value of 24.586 eV.

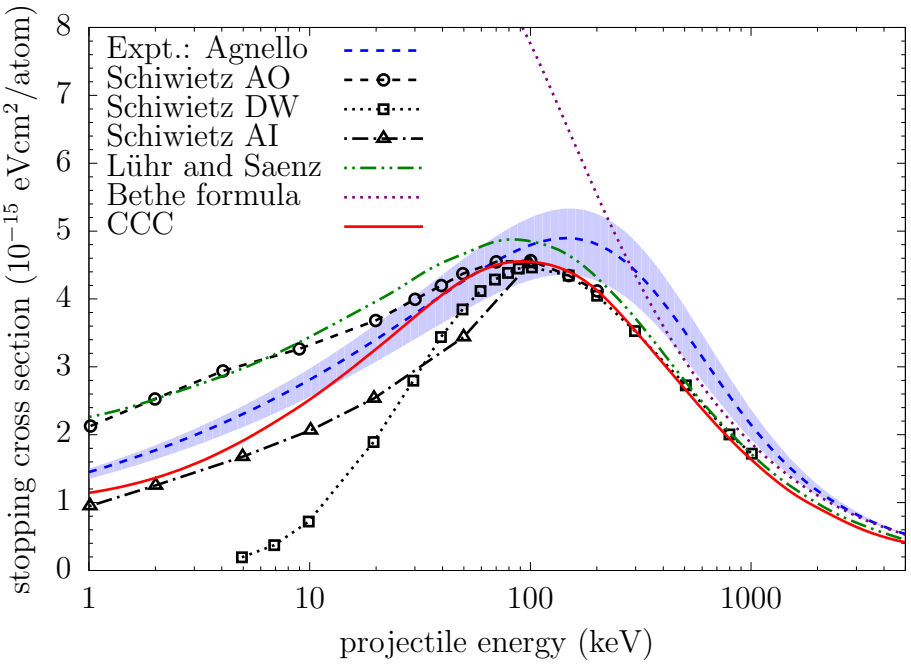

Figure 3.7: Total stopping cross section for antiprotons incident on helium. Included is the experiment of Agnello *et al.* [77], with the shaded region representing the experimental uncertainty. Electronic stopping cross sections of Lühr and Saenz [50], and Schiwietz *et al.* [44, 45] (obtained using the AO, DW, and AI methods) are also presented.

In Figure 3.7 we present result for the antiproton-helium stopping cross section together with the calculations of Lühr and Saenz [50] and Schiwietz *et al.* [44, 45], and the experimental results of Agnello *et al.* [77]. We use the multi-configuration representation of helium, which when compared to the frozen-core approach, significantly increases the stopping cross section below the stopping maximum. We also take into account double ionisation and ionisation with excitation via the independent-event model. The nuclear contribution is also added, which makes a noticeable contribution below 5 keV, as discussed later. Our calculations are in agreement with those of Lühr and Saenz [50] above 250 keV and the AO and DW calculations of Schiwietz *et al.* [44, 45] above 80 keV, but our results appear to systematically underestimate the experiment (except the region from 10 keV and 150 keV).

To better understand the reason for the small systematic disagreement a comment about the experimental data and associated uncertainties is warranted. The experiment of Agnello *et al.* [77] measures the mean annihilation time $\langle t_a \rangle$ and path length R of antiprotons in helium and then simultaneously solves the following two relationships for the total stopping cross section; (i)

$$R = \int_{E_{\rm cap}}^{E_0} \frac{dE}{S(E)}, \tag{3.1}$$

and (ii)

$$t(E_0) = \int_{E_{\rm cap}}^{E_0} \frac{dE}{vS(E)} = \langle t_a \rangle - \langle t_{\rm cas} \rangle, \tag{3.2}$$

where v is the antiproton instantaneous velocity, $E_{\rm cap}$ is the antiproton capture energy by the target atom, and $\langle t_{\rm cas} \rangle$ is the mean cascade time. To solve these equations they make use of a parameterised function for S presented by Andersen and Ziegler [79]. At low energies S is based on the Thomas-Fermi statistical model and is given by $S_l = \alpha E^{\beta}$, and at high energies it is based on Bethe's formula and is given by $S_h = [(243 - 0.375Z_2)Z_2/E] \ln(1 + \gamma/E + 4m_e E/m_{\bar{p}}\bar{E})$. In the intermediate energy range an interpolation formula originally proposed by Varelas and Biersack [80] is used, where $1/S = 1/S_l + 1/S_h$. In this formula α, β, and γ are determined by fitting to their experimentally measured data and were found to be 1.45, 0.29, and 2×10^5, respectively. According to Andersen and Ziegler [79] this particular fitting function has an accuracy of around 10% at 10 keV and 5% at 500 keV. However the accuracy of the interpolation method in the intermediate energy range is said to be approximately 20%. This uncertainty is in addition to the shaded region in Figure 3.7, which is the limiting behaviour determined by the uncertainty in the experimental measurements. The constraints of using a fitting function may be one possible explanation for the small systematic disagreement between our calculations and the experimental data. In terms of uncertainties in our calculations it must be pointed out that the independent-event model tends to overestimate the double-ionisation cross

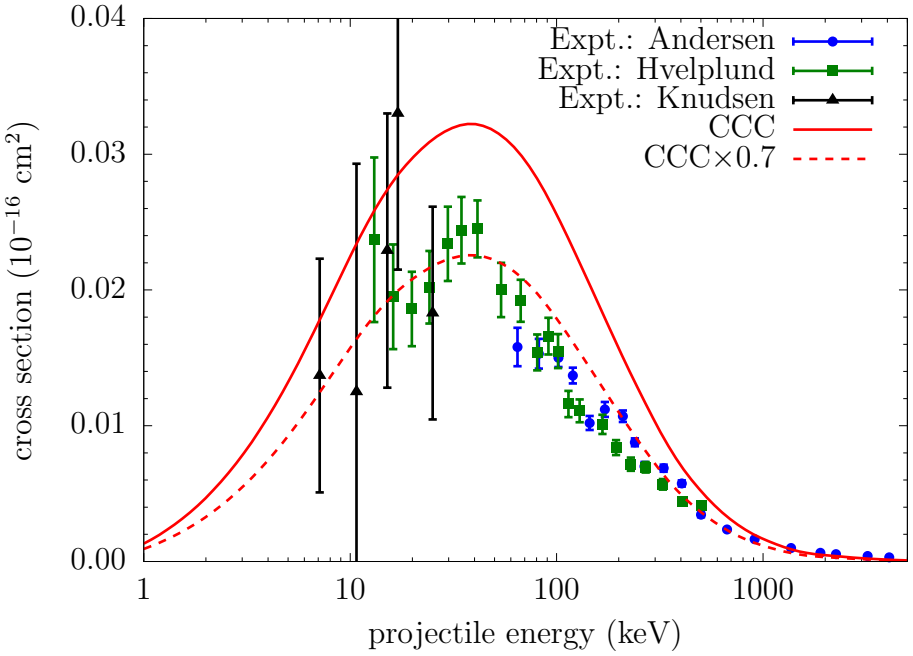

Figure 3.8: Cross section for double ionisation of helium by antiproton impact calculated using the independent-event model. Calculations are compared to the experiments of Andersen *et al.* [81], Hvelplund *et al.* [82], and Knudsen *et al.* [83]. Also shown is the CCC cross section reduced by 30%.

section by approximately 30%. This is illustrated in Figure 3.8, where the cross section for double ionisation of helium calculated using the independent-event model is compared to the experimental data of Andersen *et al.* [81], Hvelplund *et al.* [82], and Knudsen *et al.* [83][1]. However, since the contribution of double ionisation and ionisation with excitation to the total stopping cross section is small this leads to only about 2% overestimation at the stopping maximum.

The AO calculations of Schiwietz *et al.* [44, 45] and the calculations of Lühr and Saenz [50], shown in Figure 3.7, are for the electronic stopping cross section. These calculations are in good agreement with each other, however they significantly overestimate the experimental data below 15 keV. Adding the nuclear stopping cross section would make the disagreement even worse. This overesti-

[1] double ionisation data from [81] is presented in [83].

mation can be attributed to their use of a hydrogen-like description for helium that does not take into account electron correlation effects. The stopping cross section obtained from this model is multiplied by two in order to account for the contribution from both electrons. This demonstrates the importance of using a more detailed structure model if one wishes to obtain more accurate results. The structural improvements over existing theories have allowed us to obtain better agreement with experiment. It is important to emphasise that the CCC results shown in Figure 3.7 are based on the cross section for single antiproton-impact ionisation of helium that is in excellent agreement with the corresponding experimental measurements [64].

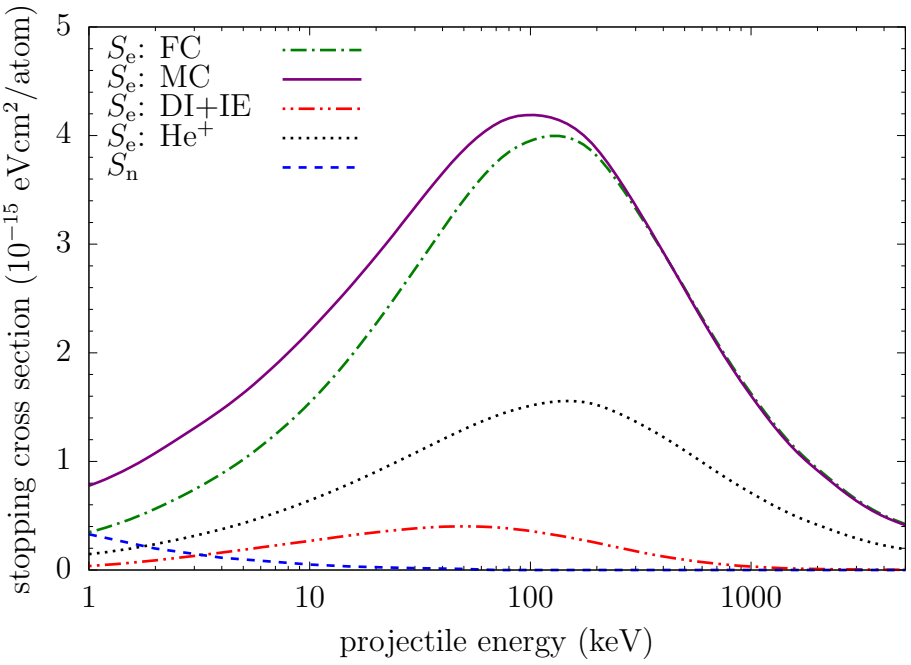

Figure 3.9: Individual contributions to the antiproton-helium total stopping cross section. FC is the stopping cross section for the primary electron in the frozen-core approximation. Similarly, MC is for the multiconfiguration approximation. DI+IE is the stopping cross section associated with double ionisation and ionisation with excitation (obtained using the MC treatment). S_n is the nuclear stopping cross section. The stopping cross section for antiprotons in He^+ is also shown.

Individual contributions to the total stopping cross section are presented in Figure 3.9. This figure demonstrates the improvement the multiconfiguration description of the target provides over the frozen-core description at low and intermediate energies. It also shows that energy losses associated with double ionisation and ionisation with excitation make a substantial contribution around the maximum. So does the nuclear stopping cross section below 5 keV. The stopping cross section for antiprotons in He^+ is also shown.

3.4 Noble gasses

Here we present calculations of the electronic stopping cross section for antiproton collisions with the more complex noble gasses of neon, argon, krypton, and xenon using a model of 6 p-shell electrons above a frozen Hartree-Fock core, described in Section 2.3.3. Calculations were performed with basis parameters $N_l = 20 - l$ and λ_l chosen to be 2, 2, 2.5, and 3 for the Ne, Ar, Kr, and Xe targets, respectively. For neon and argon the maximum orbital angular momentum $l_{\max}$ of target states used in calculations were 3 and 5, respectively. For krypton and xenon the maximum orbital angular momentum of target states was 9. This resulted in the total number of coupled differential equations for the different targets being 803, 1276 and 3475, respectively. To quantitatively assess the accuracy of our structure model for noble gasses we can compare our calculated ionisation energies to measured ones. With our frozen-core approximation for neon, argon, krypton, and xenon we obtained ionisation energies of 20.57 eV, 14.95 eV, 13.38 eV and 11.73 eV, respectively, which agree reasonably well with the measured data of 21.56 eV, 16.76 eV, 14.00 eV and 12.13 eV.

The calculations for neon, argon, krypton, and xenon are shown in Figure 3.10. Stopping cross sections of antiprotons in these targets have been cal-

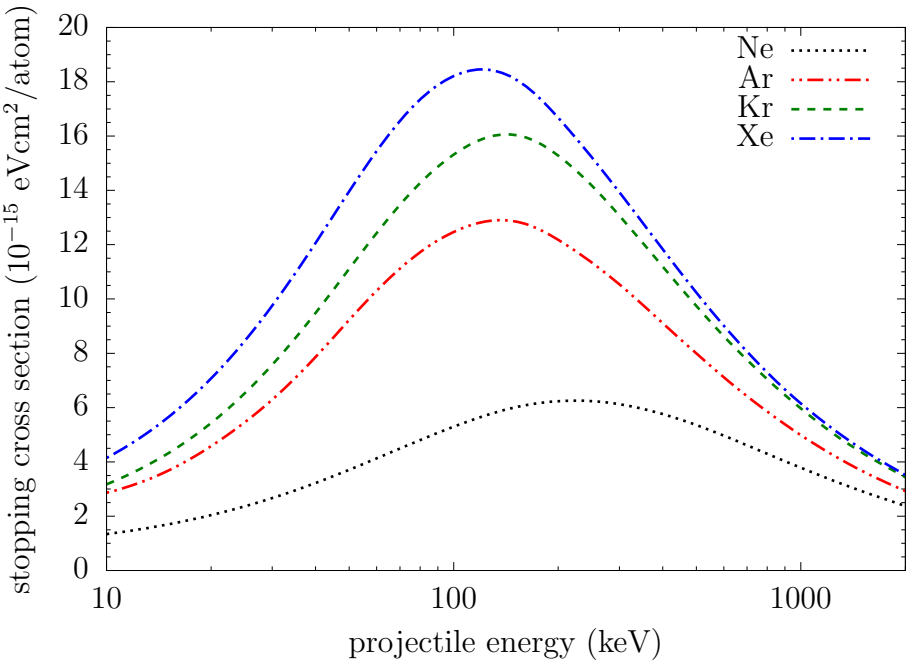

Figure 3.10: Electronic stopping cross sections due to one-electron transitions from the outer p-shell for antiproton collisions with neon, argon, krypton, and xenon.

culated for the first time. The peak of the stopping cross section increases with the atomic number of the target. This is expected since the ionisation energies decrease with the atomic number of the target and hence the active electron is less tightly bound. We note that these results represent the stopping cross sections associated with the energy losses due to single-electron transitions from the outer p-shell only.

3.5 Chapter summary

We have applied the semiclassical CCC method to the calculation of stopping cross sections for antiprotons in hydrogen, helium, neon, argon, krypton, and xenon. We have obtained excellent agreement with existing theories for hydrogen and use this as a validation of our approach. For He we obtain generally better

agreement with the experiment of Agnello *et al.* [77] than the other theories in the intermediate to low energy region. This is achieved due to the use of a multiconfiguration description of the He atom that fully accounts for electron-electron correlations and taking into account double ionisation and ionisation with excitation via an independent-event model. We also presented the first calculations of stopping cross sections for antiprotons in Ne, Ar, Kr, and Xe. For these targets we used a model of six p-shell electrons above a frozen Hartree-Fock core with only one-electron excitations from the outer p-shell allowed.

In the following chapter we shall turn our attention to molecules. We will present the theoretical framework used for the calculation of the stopping cross section in antiproton-H_2 and antiproton-H_2O collisions.

Chapter 4

Single-centre coupled-channel approach to ion-molecule collisions

4.1 Introduction

In this chapter we will present details of our single-centre coupled-channel approach to modelling the collisions of ions with molecules for the purpose of calculating the stopping power. Specifically, we consider the collisions of antiprotons with molecular hydrogen and the water molecule. As for the atomic targets, we will be using the single-centre semiclassical convergent close-coupling approach. This essentially reduces to solving a set of coupled-channel differential equations, whose solutions gives the probability of a scattering event occurring. The target electrons are treated fully quantum-mechanically while the motion of the incident antiproton is treated classically.

Let us first consider antiproton collisions with H_2. The laboratory-frame coordinate system is shown in Figure 4.1. Here the origin is at the midpoint of the target nuclei with the molecular axis $\boldsymbol{d}$ specifying the distance between the two protons and their orientation in the laboratory frame. Furthermore,

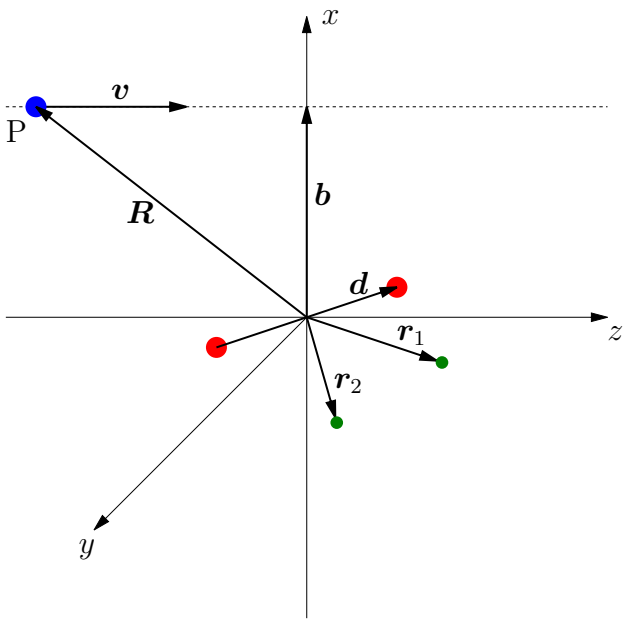

Figure 4.1: Laboratory-frame coordinates used for the collision of an antiproton with H_2. The midpoint of the target nuclei is at the origin, with the projectile's velocity directed along the z-axis.

the position vectors of the target electrons are denoted $\boldsymbol{r}_1$ and $\boldsymbol{r}_2$. The incident antiproton is assumed to be moving with constant velocity $\boldsymbol{v}$ along a straight line toward the target at an impact parameter $\boldsymbol{b}$. The velocity and impact parameter are taken to be along the z-axis and x-axis, respectively. The position of the antiproton is given by $\boldsymbol{R}(t) = \boldsymbol{b} + \boldsymbol{v}t$.

For molecular hydrogen the target Hamiltonian H_T is the sum of nuclear and electronic parts, that is

$$H_\mathrm{T} = H_\mathrm{n} + H_\mathrm{e}. \tag{4.1}$$

The nuclear and electronic parts are given by

$$H_\mathrm{n} = -\frac{1}{2M}\nabla^2_{\boldsymbol{R}_1} - \frac{1}{2M}\nabla^2_{\boldsymbol{R}_2} + \frac{1}{d}, \tag{4.2}$$

and

$$H_{\rm e} = \sum_{i=1}^{2}\left(-\frac{1}{2}\nabla^2_{\boldsymbol{r}_i} - \sum_{n=1}^{2}\frac{1}{|\boldsymbol{r}_i - \boldsymbol{R}_n|} + \sum_{j>i}^{2}\frac{1}{|\boldsymbol{r}_i - \boldsymbol{r}_j|}\right), \tag{4.3}$$

where $\boldsymbol{R}_1$ and $\boldsymbol{R}_2$ are the position vectors of the two protons and M is the mass of a proton. The reader is reminded that atomic units are used, and therefore the electron mass is unity. The many degrees of freedom associated with nuclear and electronic motions of the target makes solving Schrödinger's equation directly very difficult. However, the problem can be simplified if we invoke the Born-Oppenheimer approximation. This assumes that the electrons can almost immediately adjust their positions to a changed nuclear configuration as the nuclei are much heavier and slower than the electrons. With this approximation the target wave function can be expressed as the product of an electronic part and a nuclear part according to

$$\tilde{\psi}_\alpha(\boldsymbol{r}, \boldsymbol{d}) \approx \psi_\alpha(\boldsymbol{r}, \boldsymbol{d})\chi_{\nu jm}(\boldsymbol{d}), \tag{4.4}$$

where ψ_α is the electronic wave function that depends parametrically on $\boldsymbol{d}$, $\boldsymbol{r}$ collectively denotes the position of both electrons, and $\chi_{\nu jm}$ is the nuclear wave function. In addition, if we assume that the rate of the molecular oscillations is much smaller than the speed of an incoming antiproton $\boldsymbol{v}$, then the nuclei can be approximated as fixed at a given distance and orientation during a collision event. Under these assumptions the total scattering wave function can also be written in a form with the target nuclear part separated as

$$\tilde{\Psi}(t, \boldsymbol{r}, \boldsymbol{b}, \boldsymbol{d}) \approx \Psi(t, \boldsymbol{r}, \boldsymbol{b}, \boldsymbol{d})\chi_{\nu jm}(\boldsymbol{d}). \tag{4.5}$$

The scattering wave function for fixed-nuclei Ψ can be expanded according to Eq. (2.6), which leads to the set of coupled-channel differential equations

$$i\frac{dA_{\alpha'}(t, \boldsymbol{b}, \boldsymbol{d})}{dt} = \sum_{\alpha=1}^{N} A_\alpha(t, \boldsymbol{b}, \boldsymbol{d})\langle\psi_{\alpha'}|V(\boldsymbol{r}, \boldsymbol{R}, \boldsymbol{d})|\psi_\alpha\rangle e^{i(\epsilon_{\alpha'} - \epsilon_\alpha)t}; \quad \alpha' = 1, \ldots, N. \tag{4.6}$$

Here V is the projectile-target interaction and is given by

$$V = -\frac{1}{|\boldsymbol{R} - \boldsymbol{d}/2|} - \frac{1}{|\boldsymbol{R} + \boldsymbol{d}/2|} + \frac{1}{|\boldsymbol{R} - \boldsymbol{r}_1|} + \frac{1}{|\boldsymbol{R} - \boldsymbol{r}_2|}. \tag{4.7}$$

As it stands, the solutions of Eq. (4.6) are for a particular molecular orientation. However, a comprehensive solution of the problem requires the calculation of orientation-averaged transition probabilities. Solving Eq. (4.6) for many orientations to allow accurate orientation averaging of the H_2 molecule is computationally expensive. Alternatively, it will be shown below in Section 4.4 that molecular-orientation dependence can be factored out of Eq. (4.6), which allows orientation averaging to be performed analytically. Hence, all possible orientations of the hydrogen molecule will be accounted for. Furthermore, although the internuclear distance is assumed fixed during the collision, the target nuclear motion will be considered when calculating the stopping power as described in Section 4.5.

Moving from H_2 to H_2O the complexity of the problem significantly increases. Therefore, we will employ an approach that allows us to model the water molecule as an atom-like target, with the laboratory frame coordinates given in Figure 2.1. With a multi-centre problem reduced to a central one, meaning molecular-orientation dependence is removed, we can solve the coupled-channel differential equations for a spherically symmetric target simply given by Eq. (2.22). However, now the projectile-target interaction V and target pseudostates $\psi_{\alpha'}$ are determined by the atom-like model employed, which is described in section 4.2.2 below.

In what follows we will present the theoretical details that allow us to model the collisions of antiprotons with molecular hydrogen and the water molecule by solving Eqs. (4.6) and (2.22), respectively. First we will discuss target structure calculations for H_2 and H_2O. Then we will show how molecular-orientation

dependence can be factored out of Eq. (4.6) to obtain orientation-independent coupled-channel equations. This allows orientation averaging to be performed analytically. Finally we will discuss the calculation of the stopping powers for H_2 and H_2O.

4.2 Details of target structure calculations

In this section we present the details of how target pseudostates ψ_α are constructed for molecular hydrogen and the water molecule.

4.2.1 Structure of molecular hydrogen

In target structure calculations for molecular hydrogen we follow the ideas of Abdurakhmanov *et al.* [65, 66]. Here we state the main ideas and formulae.

The electronic wave function of the H_2 molecule is symmetric around the molecular axis. Therefore, it is best to utilise the body-frame (BF) coordinate system for the purpose of target structure calculations. Coordinates in the body frame are denoted with primed variables, as shown in Figure 4.2. The origin is at the midpoint between the two protons and the z' axis is aligned with molecular axis $\boldsymbol{d}$.

Body-frame H_2 wave functions are constructed via a CI expansion around the midpoint of the internuclear axis, that is

$$\psi_\alpha^{\mathrm{BF}}(\boldsymbol{r}_1', \boldsymbol{r}_2', d) = \sum_{a,b} B_{a,b}^\alpha(d)\varphi_a(\boldsymbol{r}_1')\varphi_b(\boldsymbol{r}_2'), \tag{4.8}$$

where $B_{a,b}^\alpha$ are the CI expansion coefficients found by diagonalisation of the target Hamiltonian (4.1) for each target symmetry α characterised by the projection of the total orbital angular momentum m, parity π, and spin s. For

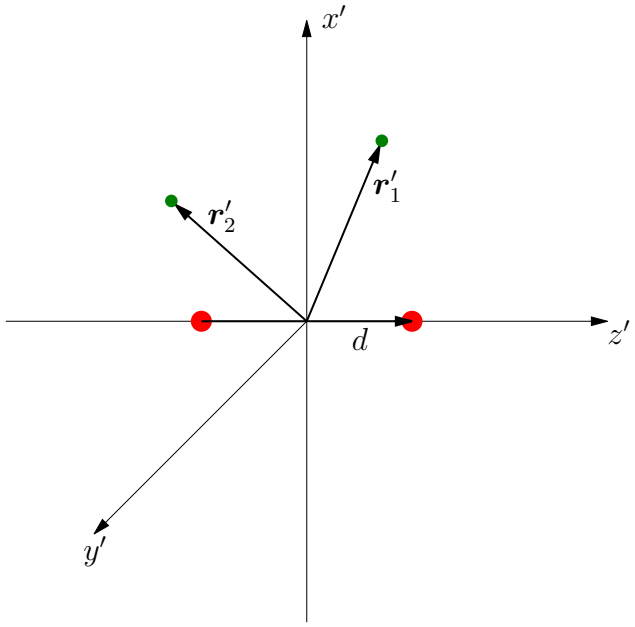

Figure 4.2: Body-frame coordinate system of the hydrogen molecule. The internuclear axis is directed along the z'-axis.

scattering from the ground state, only states with $s = 0$ are required. The one electron orbitals φ_a are defined as the product of a radial function and spherical harmonic according to

$$\varphi_a(\boldsymbol{r}) = \phi_a(r) Y_{l_a m_a}(\hat{\boldsymbol{r}}). \tag{4.9}$$

The radial functions are written in the form $\phi_a(r) = \xi_{kl}^{(\lambda_l)}(r)/r$, where $\xi_{kl}^{(\lambda_l)}$ are the Laguerre functions

$$\xi_{kl}^{(\lambda_l)}(r) = \left(\frac{\lambda_l r (k-1)!}{2(k+l)(k+2l)!} \right)^{1/2} (\lambda_l r)^{l+1} \exp\left(-\lambda_l r/2\right) L_{k-1}^{2l+1}(\lambda_l r). \tag{4.10}$$

Note, Eq. (4.10) is very similar to the Laguerre functions used for atomic targets (2.27). However, the associated Laguerre polynomials L_{k-1}^{2l+1} in Eq. (4.10) are of order $2l+1$, whereas in Eq. (2.27) they are of order $2l+2$. Again, λ_l is an exponential fall-off parameter, which is typically chosen to give the most accurate ground state with a minimum number of one-electron orbitals. As we did for helium, we use a multiconfiguration approach by allowing several inner electron

orbitals in the CI expansion. This results in a more accurate description of the H_2 ground state. The number of inner electron orbitals included in Eq. (4.8) will be discussed in Chapter 5.

Calculations involving the hydrogen molecular ion are also performed for the purpose of including two-electron processes in the stopping power, as to be discussed in Section 4.5. The one-electron H_2^+ molecule wave functions are constructed via the simpler expression

$$\psi_\alpha^{\mathrm{BF}}(\boldsymbol{r}_1', d) = \sum_a B_a^\alpha \varphi_a(\boldsymbol{r}_1'). \tag{4.11}$$

Laboratory-frame pseudostates $\psi_\alpha(\boldsymbol{r}, \boldsymbol{d})$ can be generated from the body-frame pseudostates (4.8) and (4.11) by rotating the latter into the laboratory frame according to

$$\psi_\alpha(\boldsymbol{r}, \boldsymbol{d}) = \hat{D}\psi_\alpha^{\mathrm{BF}}(\boldsymbol{r}', d), \tag{4.12}$$

where $\hat{D}$ is the rotation operator.

4.2.2 Structure of the water molecule

The structure of the water molecule is treated using a "neonisation" idea proposed by Montanari and Miraglia [84]. According to the idea the water molecule is described as a dressed pseudo-spherical atom. Following Ref. [84] the multi-centre potential of H_2O is approximated with a spherical potential given by

$$V_{\mathrm{H_2O}} = -\frac{8}{r} - \frac{2(1-\eta)\Theta(R_{\mathrm{H}} - r)}{R_{\mathrm{H}}} - \frac{2(1-\eta e^{1-r/R_{\mathrm{H}}})\Theta(r - R_{\mathrm{H}})}{r}, \tag{4.13}$$

where R_H is the distance between the oxygen atom and either of the two hydrogen atoms, Θ is the Heaviside step function, and η is introduced to account for the fact that the target is not spherically symmetry, i.e. it adjusts the energy levels. With the multi-centre problem now reduced to a central one we can apply

the techniques used to determine the structure of the Ne atom described in Section 2.3.3. This requires replacing the electron-nucleus term N_e/r in Eq. (2.37) with the potential (4.13). In addition, the $1s$, $2s$, and $2p$ core wave functions for the Ne atom are replaced by corresponding core wave functions for the water molecule. The latter are taken from the Slater basis representation presented in Ref. [84]. Finally, the parameter η of the potential (4.13) is varied to match the experimentally measured value for the ground-state energy of the target. As a result the H_2O molecule is represented by the same model that has been used for Ne: six p-shell electrons above a frozen Hartree-Fock core with only one-electron excitations from the outer p shell allowed.

4.3 Evaluation of transition matrix elements for molecular hydrogen

Having defined our H_2 pseudostates in section 4.2.1 we can turn our attention to the evaluation of transition matrix elements

$$V_{\alpha'\alpha}(\boldsymbol{R},\boldsymbol{d}) \equiv \langle\psi_{\alpha'}|V(\boldsymbol{r},\boldsymbol{R},\boldsymbol{d})|\psi_\alpha\rangle. \tag{4.14}$$

It will prove computationally efficient to use the available body-frame target pseudostates (4.8) in the evaluation of Eq. (4.14), instead of rotating them into the laboratory frame before taking integrals. This can be achieved if we factor out the molecular-orientation-dependent part from the projectile-target interaction (4.7). Then it will be irrelevant whether the body frame or laboratory frame is used for taking the integrals over the coordinates of the electrons.

The transition matrix elements are defined as

$$V_{\alpha'\alpha}(\boldsymbol{R},\boldsymbol{d}) = \int d\boldsymbol{r}_1' d\boldsymbol{r}_2' \psi_{\alpha'}^{\mathrm{BF}*}(\boldsymbol{r}_1',\boldsymbol{r}_2',d)\left(-\frac{1}{|\boldsymbol{R}-\boldsymbol{d}/2|}-\frac{1}{|\boldsymbol{R}+\boldsymbol{d}/2|}\right.$$
$$\left.+\frac{1}{|\boldsymbol{R}-\boldsymbol{r}_1|}+\frac{1}{|\boldsymbol{R}-\boldsymbol{r}_2|}\right)\psi_\alpha^{\mathrm{BF}}(\boldsymbol{r}_1',\boldsymbol{r}_2',d), \tag{4.15}$$

where the primed coordinates are relative to the body frame. We split Eq. (4.15) into two parts: I_1 and I_2, where I_1 contains the interaction of the antiproton with the target protons and I_2 contains the interaction of the antiproton with the target electrons. Evaluation of I_1 is trivial due to the orthogonality of the target pseudostates, that is

$$\begin{aligned} I_1 =& \int d\boldsymbol{r}_1' d\boldsymbol{r}_2' \psi_{\alpha'}^{\mathrm{BF}*}(\boldsymbol{r}_1', \boldsymbol{r}_2', d) \left(-\frac{1}{|\boldsymbol{R} - \boldsymbol{d}/2|} - \frac{1}{|\boldsymbol{R} + \boldsymbol{d}/2|} \right) \psi_{\alpha}^{\mathrm{BF}}(\boldsymbol{r}_1', \boldsymbol{r}_2', d) \\ =& -\delta_{\alpha'\alpha} \left(\frac{1}{|\boldsymbol{R} - \boldsymbol{d}/2|} + \frac{1}{|\boldsymbol{R} + \boldsymbol{d}/2|} \right). \end{aligned} \tag{4.16}$$

Evaluation of I_2 is more involved. First, considering the symmetry with respect to interchanging $\boldsymbol{r}_1$ and $\boldsymbol{r}_2$, we can write

$$I_2 = 2 \int d\boldsymbol{r}_1' d\boldsymbol{r}_2' \psi_{\alpha'}^{\mathrm{BF}*}(\boldsymbol{r}_1', \boldsymbol{r}_2', d) \frac{1}{|\boldsymbol{R} - \boldsymbol{r}_1|} \psi_{\alpha}^{\mathrm{BF}}(\boldsymbol{r}_1', \boldsymbol{r}_2', d). \tag{4.17}$$

Now inserting our expression for the H_2 wave functions (4.8) into Eq. (4.17) we obtain

$$\begin{aligned} I_2 =& 2 \sum_{a,b,g,h} B_{a,b}^{\alpha'} B_{g,h}^{\alpha} \int d\boldsymbol{r}_1' d\boldsymbol{r}_2' \phi_a(r_1') \phi_b(r_2') Y_{l_a m_a}^*(\hat{\boldsymbol{r}}_1') Y_{l_b m_b}^*(\hat{\boldsymbol{r}}_2') \\ & \times \frac{1}{|\boldsymbol{R} - \boldsymbol{r}_1'|} \phi_g(r_1') \phi_h(r_2') Y_{l_g m_g}(\hat{\boldsymbol{r}}_1') Y_{l_h m_h}(\hat{\boldsymbol{r}}_2') \end{aligned} \tag{4.18}$$

Taking into account the orthogonality of spherical harmonics (2.54), integration over $\hat{\boldsymbol{r}}_2'$ can be performed, which gives

$$I_2 = 2 \sum_{a,b,g,h} B_{a,b}^{\alpha'} B_{g,h}^{\alpha} \langle \phi_b | \phi_h \rangle \int d\boldsymbol{r}_1' d\phi_a(r_1') Y_{l_a m_a}^*(\hat{\boldsymbol{r}}_1') \frac{1}{|\boldsymbol{R} - \boldsymbol{r}_1'|} \phi_g(r_1') Y_{l_g m_g}(\hat{\boldsymbol{r}}_1'). \tag{4.19}$$

Here $\langle \phi_b | \phi_h \rangle$ is the overlap of two radial functions,

$$\langle \phi_b | \phi_h \rangle = \int_0^\infty dr_2 r_2^2 \phi_b(r_2) \phi_h(r_2). \tag{4.20}$$

Now expanding the Coulomb potential in a similar manner to Eq. (2.46) and

considering the fact that $|\boldsymbol{r}_1'| = |\boldsymbol{r}_1|$, we get

$$I_2 = 8\pi \sum_{\lambda\mu} \sum_{a,b,g,h} \frac{1}{2\lambda+1} B_{a,b}^{\alpha'} B_{g,h}^{\alpha} Y_{\lambda\mu}^*(\hat{\boldsymbol{R}}) \langle \phi_b | \phi_h \rangle \int_0^\infty dr_1 r_1^2 \phi_a(r_1) \phi_g(r_1) \mathcal{U}_\lambda(R, r_1) \times \int d\hat{\boldsymbol{r}}_1' Y_{l_a m_a}^*(\hat{\boldsymbol{r}}_1') Y_{l_g m_g}(\hat{\boldsymbol{r}}_1') Y_{\lambda\mu}(\hat{\boldsymbol{r}}_1), \tag{4.21}$$

where

$$\mathcal{U}_\lambda(R, r_1) = \begin{cases} \dfrac{R^\lambda}{r_1^{\lambda+1}} & \text{if } R \leq r_1, \\ \dfrac{r_1^\lambda}{R^{\lambda+1}} & \text{if } R > r_1. \end{cases} \tag{4.22}$$

To evaluate the integral over $\hat{\boldsymbol{r}}_1'$ we need to transform $Y_{\lambda\mu}(\hat{\boldsymbol{r}}_1)$ into the body frame. For this we utilise the Wigner rotation matrix (Wigner D-function) $D_{\mu m}^{\lambda *}(\phi_d, \theta_d, 0)$ to write [76]

$$Y_{\lambda\mu}(\hat{\boldsymbol{r}}_1) = \sum_m Y_{\lambda m}(\hat{\boldsymbol{r}}_1') D_{\mu m}^{\lambda *}(\phi_d, \theta_d, 0), \tag{4.23}$$

where ϕ_d and θ_d are the azimuthal and polar angles of the internuclear axis $\boldsymbol{d}$, respectively. Substituting Eq. (4.23) into (4.21) and utilising Eq. (2.49), integration over $\hat{\boldsymbol{r}}_1'$ can now be performed, and I_2 becomes

$$I_2 = 4\sqrt{\pi} \sum_{\lambda\mu} D_{\mu(m_a - m_g)}^{\lambda *}(\phi_d, \theta_d, 0) Y_{\lambda\mu}^*(\hat{\boldsymbol{R}}) \sum_{a,b,g,h} B_{a,b}^{\alpha'} B_{g,h}^{\alpha} \sqrt{\frac{2l_g+1}{(2\lambda+1)(2l_a+1)}} \times C_{l_g 0 \lambda 0}^{l_a 0} C_{l_g m_g \lambda (m_a - m_g)}^{l_a m_a} \langle \phi_b | \phi_h \rangle \int_0^\infty dr_1 r_1^2 \phi_a(r_1) \phi_g(r_1) \mathcal{U}_\lambda(R, r_1), \tag{4.24}$$

where the sum over m disappears due to the condition $m = m_a - m_g$ that comes from the Clebsch-Gordan coefficient.

We now want to combine I_1 and I_2. To do this we first expand the Coulomb potential in I_1 in a similar manner to Eq. (2.46). By considering the fact that $Y_{lm}(-\hat{\boldsymbol{r}}) = (-1)^l Y_{lm}(\hat{\boldsymbol{r}})$ we can write

$$\frac{1}{|\boldsymbol{R} - \boldsymbol{d}/2|} + \frac{1}{|\boldsymbol{R} + \boldsymbol{d}/2|} = 4\pi \sum_{\lambda\mu} \frac{(1 + (-1)^\lambda)}{2\lambda+1} \mathcal{U}_\lambda(R, d/2) Y_{\lambda\mu}^*(\hat{\boldsymbol{R}}) Y_{\lambda\mu}(\hat{\boldsymbol{d}}), \tag{4.25}$$

where $\mathcal{U}_\lambda$ is given by Eq. (4.22). Then expressing $Y_{\lambda\mu}(\hat{\boldsymbol{d}})$ in terms of a Wigner rotation matrix using the relation

$$D^{\lambda *}_{\mu 0}(\phi_d, \theta_d, 0) = \sqrt{\frac{4\pi}{2\lambda+1}} Y^*_{\lambda\mu}(\hat{\boldsymbol{d}}), \tag{4.26}$$

I_1 becomes

$$I_1 = -\delta_{\alpha'\alpha} 2\sqrt{\pi} \sum_{\lambda\mu} D^{\lambda *}_{\mu 0}(\phi_d, \theta_d, 0) Y^*_{\lambda\mu}(\hat{\boldsymbol{R}}) \frac{(1+(-1)^\lambda)}{\sqrt{2\lambda+1}} \mathcal{U}_\lambda(R, d/2). \tag{4.27}$$

Finally, combining equations (4.24) and (4.27) the transition matrix elements $V_{\alpha'\alpha}(\boldsymbol{R}, \boldsymbol{d})$ can be written as

$$V_{\alpha'\alpha}(\boldsymbol{R}, \boldsymbol{d}) = \sum_{\lambda\mu} \mathcal{V}^{\alpha'\alpha}_{\lambda\mu}(\boldsymbol{R}, d) D^{\lambda *}_{\mu(m_{\alpha'} - m_\alpha)}(\phi_d, \theta_d, 0), \tag{4.28}$$

where the molecular-orientation-independent parts $\mathcal{V}^{\alpha'\alpha}_{\lambda\mu}(\boldsymbol{R}, d)$ are defined as

$$\begin{aligned} \mathcal{V}^{\alpha'\alpha}_{\lambda\mu}(\boldsymbol{R}, d) = & \frac{4\sqrt{\pi} Y^*_{\lambda\mu}(\hat{\boldsymbol{R}})}{\sqrt{2\lambda+1}} \Bigg(-\delta_{\alpha'\alpha} \mathrm{mod}(\lambda, 2) \mathcal{U}_\lambda(R, d/2) + \sum_{a,b,g,h} B^{\alpha'}_{a,b} B^{\alpha}_{g,h} \sqrt{\frac{2l_g+1}{2l_a+1}} \\ & \times C^{l_a 0}_{l_g 0 \lambda 0} C^{l_a m_a}_{l_g m_g \lambda m} \langle \phi_b | \phi_h \rangle \int_0^\infty dr_1 r_1^2 \phi_a(r_1) \phi_g(r_1) \mathcal{U}_\lambda(R, r_1) \Bigg). \end{aligned} \tag{4.29}$$

Here $\mathrm{mod}(\lambda, 2)$ is the remainder function since $(1+(-1)^\lambda) = 2\mathrm{mod}(\lambda, 2)$.

4.4 Orientation-independent scattering equations and analytic orientation averaging

In this section we derive a set of coupled-channel differential equations for the orientation-independent parts of the expansion coefficients A_α in the antiproton-H_2 scattering problem. Furthermore, we demonstrate that from the solution of these differential equations we can obtain analytic orientation-averaged transition probabilities that account for all possible orientations of the H_2 molecule.

First, we express the time-dependent expansion coefficients in Eq. (4.6) in a form similar to Eq. (4.28) as

$$A_{\alpha'}(t,\boldsymbol{b},\boldsymbol{d}) = \sum_{\lambda\mu} \mathcal{A}^{\alpha'}_{\lambda\mu}(t,b,d) D^{\lambda *}_{\mu,m_{\alpha'}}(\phi_d,\theta_d,0), \tag{4.30}$$

where $\mathcal{A}^{\alpha'}_{\lambda\mu}$ is the molecular-orientation-independent part of the expansion coefficients. The expansion indices are limited by the maximum allowed total orbital angular momentum. Now, substituting Eqs. (4.30) and (4.28) into Eq. (4.6) we obtain

$$\begin{aligned} & i \sum_{\lambda_3\mu_3} \frac{d\mathcal{A}^{\alpha'}_{\lambda_3\mu_3}(t,b,d)}{dt} D^{\lambda_3 *}_{\mu_3,m_{\alpha'}}(\phi_d,\theta_d,0) \\ & = \sum_{\alpha} e^{i(\epsilon_{\alpha'}-\epsilon_\alpha)t} \sum_{\lambda_1\mu_1} \mathcal{A}^{\alpha}_{\lambda_1\mu_1}(t,b,d) D^{\lambda_1 *}_{\mu_1,m_\alpha}(\phi_d,\theta_d,0) \\ & \quad \times \sum_{\lambda_2\mu_2} \mathcal{V}^{\alpha'\alpha}_{\lambda_2\mu_2}(\boldsymbol{R},d) D^{\lambda_2 *}_{\mu_2(m_{\alpha'}-m_\alpha)}(\phi_d,\theta_d,0). \end{aligned} \tag{4.31}$$

Multiplying both sides of Eq. (4.31) by $D^{\lambda'}_{\mu' m_{\alpha'}}(\phi_d,\theta_d,0)$ and integrating over θ_d and ϕ_d, we obtain

$$\begin{aligned} & i \sum_{\lambda_3\mu_3} \frac{d\mathcal{A}^{\alpha'}_{\lambda_3\mu_3}(t,b,d)}{dt} \int_0^{2\pi} d\phi_d \int_0^{\pi} d\theta_d \sin\theta_d D^{\lambda_3 *}_{\mu_3,m_{\alpha'}}(\phi_d,\theta_d,0) D^{\lambda'}_{\mu' m_{\alpha'}}(\phi_d,\theta_d,0) \\ & = \sum_{\alpha} e^{i(\epsilon_{\alpha'}-\epsilon_\alpha)t} \sum_{\lambda_1\mu_1} \mathcal{A}^{\alpha}_{\lambda_1\mu_1}(t,b,d) \sum_{\lambda_2\mu_2} \mathcal{V}^{\alpha'\alpha}_{\lambda_2\mu_2}(\boldsymbol{R},d) \\ & \quad \times \int_0^{2\pi} d\phi_d \int_0^{\pi} d\theta_d \sin\theta_d D^{\lambda_1 *}_{\mu_1,m_\alpha}(\phi_d,\theta_d,0) D^{\lambda'}_{\mu' m_{\alpha'}}(\phi_d,\theta_d,0) D^{\lambda_2 *}_{\mu_2(m_{\alpha'}-m_\alpha)}(\phi_d,\theta_d,0). \end{aligned} \tag{4.32}$$

Using the following identities for the Wigner D-functions [76],

$$\int_0^{2\pi} d\phi \int_0^{\pi} d\theta \sin\theta D^{J_1 *}_{M_1 M_1'}(\phi,\theta,0) D^{J_2}_{M_2 M_2'}(\phi,\theta,0) = \frac{4\pi}{2J_1+1} \delta_{J_1 J_2} \delta_{M_1 M_2} \delta_{M_1' M_2'}, \tag{4.33}$$

and

$$\begin{aligned} & \int_0^{2\pi} d\phi \int_0^{\pi} d\theta \sin\theta D^{J_1 *}_{M_1 M_1'}(\phi,\theta,0) D^{J_2}_{M_2 M_2'} D^{J_3 *}_{M_3 M_3'}(\phi,\theta,0)(\phi,\theta,0) \\ & = \frac{4\pi}{2J_1+1} C^{J_1 M_1}_{J_2 M_2 J_3 M_3} C^{J_1 M_1'}_{J_2 M_2' J_3 M_3'}, \end{aligned} \tag{4.34}$$

we can reduce Eq. (4.32) to the final set of coupled differential equations for the molecular-orientation-independent parts of the expansion coefficients

$$i\frac{d\mathcal{A}^{\alpha'}_{\lambda'\mu'}(t,b,d)}{dt} = \sum_{\alpha} e^{i(\epsilon_{\alpha'}-\epsilon_{\alpha})t} \sum_{\lambda_1\mu_1} \frac{2\lambda'+1}{2\lambda_1+1} \mathcal{A}^{\alpha}_{\lambda_1\mu_1}(t,b,d) \times \sum_{\lambda_2\mu_2} C^{\lambda_1\mu_1}_{\lambda'\mu'\lambda_2\mu_2} C^{\lambda_1 m_\alpha}_{\lambda' m_{\alpha'}\lambda_2 m_\alpha - m_{\alpha'}} \mathcal{V}^{\alpha'\alpha}_{\lambda_2\mu_2}(t,b,d). \tag{4.35}$$

This set of equations is solved subject to the initial conditions $\mathcal{A}^{\alpha'}_{\lambda'\mu'}(t=-\infty,b,d) = \delta_{\alpha'1}\delta_{\lambda'0}\delta_{\mu'0}$. These boundary conditions imply that the target is initially in the ground state ($\alpha'=1$) and that at infinite distance the antiproton does not feel the anisotropic nature of the molecular target.

From the solution of Eq. (4.35) we can analytically determine the probability for transition of the H_2 molecule into some final electronic state f that takes into account all possible orientations of the molecule. The orientation-averaged probability is given by

$$p_f^{\mathrm{av}}(b) = \int_0^{2\pi} d\phi_d \int_0^{\pi} d\theta_d \sin\theta_d |A_f(t=+\infty,b,\boldsymbol{d})|^2. \tag{4.36}$$

To evaluate Eq. (4.36) analytically we first substitute in Eq. (4.30) to obtain

$$p_f^{\mathrm{av}}(b) = \frac{1}{4\pi} \int_0^{2\pi} d\phi_d \int_0^{\pi} d\theta_d \sin\theta_d \sum_{\lambda'\mu'} \mathcal{A}^{f*}_{\lambda'\mu'}(t=+\infty,b,d) D^{\lambda'}_{\mu',m_f}(\phi_d,\theta_d,0) \times \sum_{\lambda\mu} \mathcal{A}^{f}_{\lambda\mu}(t=+\infty,b,d) D^{\lambda*}_{\mu,m_f}(\phi_d,\theta_d,0). \tag{4.37}$$

Now using Eq. (4.33) we arrive at the final expression for the analytic orientation-averaged transition probability

$$p_f^{\mathrm{av}}(b) = \sum_{\lambda\mu} \frac{1}{2\lambda+1} |\mathcal{A}^{f}_{\lambda\mu}(t=+\infty,b,d)|^2. \tag{4.38}$$

4.5 Stopping power

In this section we discuss the stopping cross section formula for H_2 and H_2O and how it should appear in the coupled-channel approach presented in this chapter.

The stopping cross section is related to the stopping power by the density of target molecules in the stopping medium as shown in Eq. (2.69).

For the H_2 molecule we include both the electronic and nuclear contributions when calculating the stopping cross section. Additionally, being a molecular target it is important to consider the energy losses associated with vibrational excitations. Rotational excitation is not included as its contribution is insignificant in the energy region considered. Therefore we write the total stopping cross section S as the sum of the electronic S_e, nuclear S_n, and vibrational S_vib stopping cross sections, i.e.

$$S = S_\mathrm{e} + S_\mathrm{n} + S_\mathrm{vib}. \tag{4.39}$$

For the electronic stopping cross section it is important to include energy losses due to one- and two-electron processes. Therefore, we use Eq. (2.74) described in Section 2.5, that is

$$S_\mathrm{e}(E_0) \approx \sum_{f=1}^{N}(\epsilon_f - \epsilon_i)\sigma_{fi} + \sum_{k=1}^{N^+}(\epsilon_k^+ - \epsilon_1^+)\sigma_k^+. \tag{4.40}$$

Here the first sum accounts for energy losses due to single nondissociative ionisation and excitation, while the second sum accounts for energy losses due to double ionisation and dissociative ionisation. Dissociative ionisation takes place through single ionisation followed by dissociation of the residual H_2^+ molecule. As described in Section 2.5, σ_k^+ is calculated using an independent-event model, which requires the calculation of antiproton scattering on H_2^+. Antiproton collisions with H_2^+ are modelled in much the same way as for H_2. However, in this case H_2^+ pseudostates (4.11) and the appropriate interaction potential are used. It must be emphasised that we use the same internuclear distance for H_2^+ calculations as we do for H_2, which is a requirement of the independent-event model. The cross sections corresponding to the positive-energy states of H_2^+ represent

double ionisation, while those corresponding to the negative energies contribute towards dissociative ionisation due to the antibonding nature of the H_2^+ excited states. The cross sections σ_{fi} and σ_k^+ are both calculated using the analytic orientation-averaged probabilities (4.38).

The nuclear stopping cross section is calculated according to Eq. (2.77), that is

$$S_{\mathrm{n}}(E_0) = \sum_f \int \frac{q_f^2}{2M_{\mathrm{T}}} \left(\frac{d\sigma_f^{\mathrm{av}}}{d\Omega} \right) d\Omega. \tag{4.41}$$

Here we use averaging over three perpendicular orientations to calculate the differential cross section $d\sigma_f^{\mathrm{av}}/d\Omega$ independent of the target orientation. Orientation-dependent differential cross sections are calculated according to Eq. (2.78). As demonstrated in Chapter 5, averaging over three orientations is sufficiently accurate at energies below 30 keV where the nuclear stopping cross section makes a significant contribution.

Collisions between antiprotons and molecular hydrogen can also lead to changes in vibrational energy levels of the target. These processes lead to an additional loss of the projectile's energy. Their contribution to the stopping cross section can be accounted for if we write the total scattering wave function in a form where the target nuclear part is separated according to Eq. (4.5). Since we do not consider rotational motion we may write $\chi_{f\nu jm}(\boldsymbol{d}) = \chi_{f\nu}(\boldsymbol{d})$, where $\chi_{f\nu}(\boldsymbol{d})$ is the molecular vibrational wave function that depends on the internuclear distance of the target in the electronic state f. As discussed above this kind of separation is possible under the assumption that the electrons can almost immediately adjust their positions to a changed nuclear configuration. The wave functions and corresponding energies for the vibrational motion of the molecular target, $\chi_{f\nu}(\boldsymbol{d})$ and $\varepsilon_{f\nu}$, satisfy the Schrödinger equation

$$(H_{\mathrm{n}} + \epsilon_f)\chi_{f\nu}(\boldsymbol{d}) = \varepsilon_{f\nu}\chi_{f\nu}(\boldsymbol{d}), \tag{4.42}$$

where $H_{\rm n}$ is the target Hamiltonian representing nuclear motion given by Eq. (4.2). The stopping cross section associated with the vibrational transitions from the electronic ground state i into all the vibrational levels of the electronic state f can be calculated as

$$S_{\rm vib,f}(E_0) = \frac{1}{4\pi} \sum_{\nu=0}^{N_{{\rm vib},f}} (\varepsilon_{f\nu} - \varepsilon_{i0}) \left| \langle \chi_{f\nu}(\boldsymbol{d}) | A_f(t, \boldsymbol{b}, \boldsymbol{d}) \exp(-i\epsilon_f t) | \chi_{i0}(\boldsymbol{d}) \rangle \right|^2 , \quad (4.43)$$

where $N_{\rm vib,f}$ is the total number of molecular vibrational eigenstates in the electronic state f. Among all vibrational transitions, those within the electronic ground state give the most dominant contribution to the stopping cross section. Thus, in the present work we consider vibrational transitions only within the electronic ground state. To avoid doing averaging over molecular orientations numerically we write Eq. (4.43) in the following approximate form

$$S_{\rm vib}(E_0) \approx \sum_{\nu=0}^{N_{{\rm vib},i}} (\varepsilon_{i\nu} - \varepsilon_{i0}) \langle \chi_{i\nu}(d) | \sqrt{\sigma_{\rm el}^{\rm av}(d)} | \chi_{i0}(d) \rangle, \quad (4.44)$$

where $\sigma_{\rm el}^{\rm av}(d)$ is the elastic cross section analytically averaged over molecular orientations. Using $\sqrt{\sigma_{\rm el}^{\rm av}(d)}$ instead of the scattering amplitude is shown to be a good approximation in calculations for electron scattering from H_2^+ and D_2^+ [85]. The molecular vibrational eigenfunctions $\chi_{i\nu}(\boldsymbol{d})$ and eigenenergies $\varepsilon_{i\nu}$ can be calculated via diagonalisation of the molecular Hamiltonian with the electronic ground-state potential curve $V_{\rm pot}$. In Figure 4.3 radial distribution functions, $|\chi_{i\nu}(d)|^2 d^2$, for the lowest vibrational levels ($\nu = 0, 1$ and 2) are given.

As described in Section 4.2.2, the multi-centre H_2O problem is reduced to a central one by modelling the water molecule as a neon-like atom. In addition, since only single electron transitions are allowed the electronic stopping cross section is simply given by Eq. (2.72).

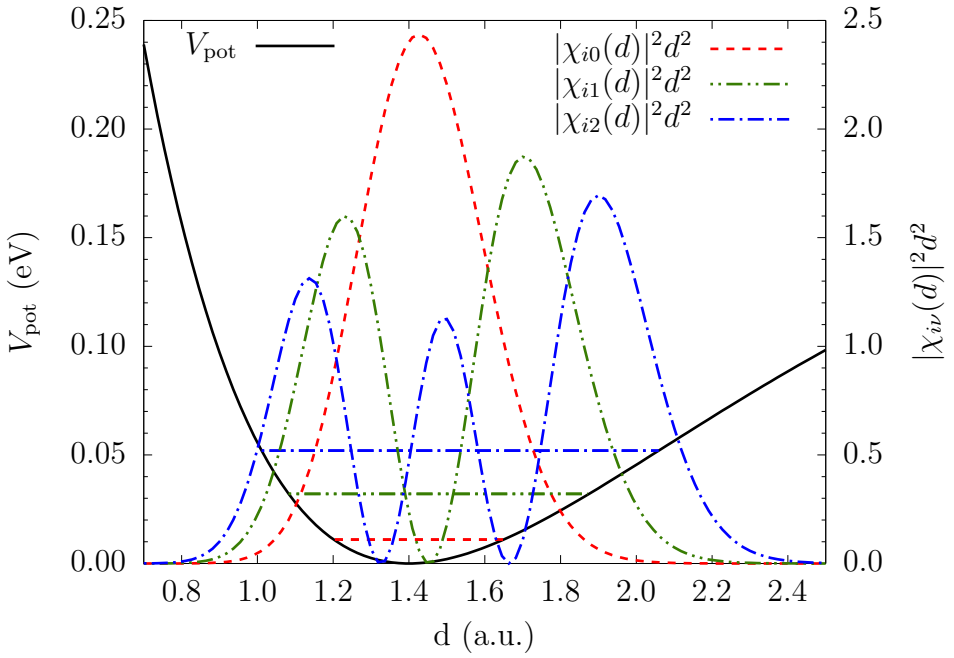

Figure 4.3: Radial distribution functions $|\chi_{i\nu}(d)|^2 d^2$ of the H_2 molecular vibrations with $\nu = 0$, 1, and 2, in a.u.. The potential energy curve and the vibrational energy levels of H_2 are shown in units of eV. Note that the potential energy curve is shifted up by 31.7007 eV which is the ground state energy of H_2 at the mean internuclear separation of 1.4487 a.u..

4.6 Chapter summary

We have presented the theoretical framework for the calculation of stopping powers in antiproton collisions with molecular hydrogen and the water molecule. For H_2 we derive a set of coupled-channel equations for the molecular-orientation-independent parts of the expansion coefficients of the scattering wave function. Orientation averaging is performed analytically to obtain transition probabilities that account for all possible orientations of the target molecule. Details of the electronic, nuclear, and vibrational stopping powers in a coupled-channel approach to antiproton-H_2 collisions have been presented. For H_2O we reduce a multi-centre problem to a central one by describing the water molecule as a pseudo-spherical neon-like atom. Therefore, we use the same model as the one

used for neon, i.e. six p-shell electrons above a frozen Hartree-Fock core with only one-electron excitations from the outer p shell allowed.

In the following chapter results of calculations for the stopping cross section in antiproton collisions with molecular hydrogen and the water molecule will be presented.

Chapter 5

Antiproton stopping in molecular targets

5.1 Introduction

In this chapter calculations of the stopping cross section for antiproton collisions with molecular hydrogen and the water molecule will be presented and compared with existing theoretical and experimental data.

The stopping cross section for antiprotons in a gas of H_2 has been measured by Adamo *et al.* [86] at the CERN LEAR facility. To obtain the stopping cross section they first simultaneously measured the spatial coordinates and annihilation times of antiprotons traveling through a gas of H_2. The measured quantities were then expressed in terms of the stopping cross section with the resulting equations solved numerically using parameters to obtain the best fit to the data. Agnello *et al.* [77] later repeated the experiment using the same technique due to errors in the pressure scale of the original measurements. This led to significantly different results, thus superseding the earlier ones given by Adamo *et al.* [86]. Lodi Rizzini *et al.* [87] later reanalysed the data with emphasis on the Barkas effect [22].

From a theoretical perspective, apart from our CCC calculations [52], the most recent calculations of antiproton stopping in H_2 have been performed by Lühr and Saenz [50]. They used a semiclassical close-coupling approach to the solution of the time-dependent Schrödinger equation. The radial wave function was expanded in a B-spline basis with the H_2 target described using an effective one-electron treatment. Poor agreement with the experiment of Agnello *et al.* [77] was obtained. However good agreement with the original (incorrect) data of Adamo *et al.* [86] was seen. Lühr and Saenz [50] concluded that a two-electron description of H_2 was required to reduce uncertainties in the calculations and also test the accuracy of the latest experimental measurements. The only other H_2 calculations available have been performed by Schiwietz *et al.* [44, 45] using a quasi-atomic generalised AI method which is valid at low energies.

There are a number of calculations for antiproton stopping in atomic hydrogen as discussed in Chapter 3. These are usually compared with the experimental data for its molecular counterpart divided by two. Schiwietz *et al.* [44, 45] performed calculations using atomic-orbital close coupling and distorted-wave Born methods, while Cabrera-Trujillo *et al.* [36] used the electron-nuclear dynamics formalism. Both concluded that disagreement with experiment around and below the stopping maximum was due to neglecting molecular structure effects in their calculations.

In this chapter we present stopping cross section calculations for antiprotons collisions with H_2 and H_2O using the semiclassical time-dependent CCC method, described in Chapter 4. The results presented in this chapter improve upon the current theory of Lühr and Saenz [50] by employing a correlated two-electron multiconfiguration molecular treatment of H_2 and taking into account double ionisation and dissociative ionisation via an independent-event model. In addition, we include vibrational excitation and the nuclear stopping cross sec-

tion. When calculating the dominant electronic stopping cross section we use an analytic orientation-averaging technique to account for all possible orientations of the H_2 molecule and compare this to the average over three orientations. The H_2O target is treated using a neonisation method proposed by Montanari and Miraglia [84], whereby the ten-electron water molecule is described as a dressed Ne-like atom in a pseudo-spherical potential. To our best knowledge there have been no other stopping cross section calculations for the antiproton-H_2O system. Therefore, our calculations should provide a guideline to future experiments on antiproton stopping in H_2O.

It is important to point out that traditionally the antiproton-H_2 stopping cross section has been presented per atom instead of per molecule. In this chapter we present our final results as per molecule and therefore multiply other per-atom results by two before plotting.

5.2 Hydrogen molecule

In this section we present calculations of the stopping cross section for antiproton-molecular hydrogen collisions. Convergence of the stopping cross section for increasing basis size is investigated. Then we present our final calculations compared to existing theories and experiment.

5.2.1 Convergence study

As previously discussed in Chapter 3, it is important to demonstrate convergence in the stopping cross section by increasing the size of the underlying basis used in the expansion of the scattering wave function. This is done to ensure the target space is well represented and the addition of more basis functions will not change the final result. Here we investigate convergence of the analytic orientation-

averaged electronic stopping cross section in terms of the basis parameters $l_{\max}$, the maximum value of orbital angular momentum included in the expansion, and $n_{\max}$, the maximum number of one-electron functions for $l = 0$. The number of one-electron functions for each l is $N_l = n_{\max} - l$. As one would expect, computations for H_2 are significantly more expensive than for He. For this reason we do not bother with frozen-core calculations and move straight to a multiconfiguration approach. In this approach we limit the number of inner electron orbitals included to the $1s$, $2s$, $2p$, $3s$, $3p$, and $3d$ orbitals. Also, for all calculations the exponential fall-off parameter λ_l is chosen to be 2.

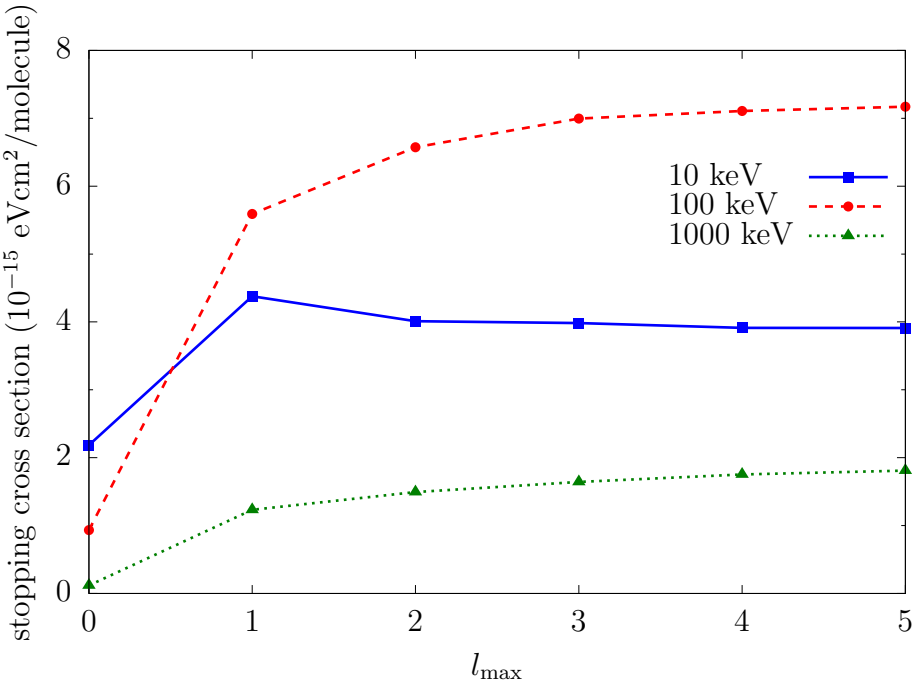

Figure 5.1: Convergence of the electronic stopping cross section for antiprotons incident on molecular hydrogen with increasing $l_{\max}$ for $n_{\max} = 20$ at incident energies of 10 keV, 100 keV, and 1000 keV. Calculations presented here were performed in the multiconfiguration approximation.

Convergence of the electronic stopping cross section has been studied over the whole energy region considered in this work. Here we will give typical examples at antiproton incident energies of 10 keV, 100 keV, and 1000 keV, i.e.

low, intermediate, and high incident energies. First, we fix the basis parameter $n_{\max}$ at some large value and systematically increase $l_{\max}$. Figure 5.1 shows the convergence of the electronic stopping cross section for antiproton-molecular hydrogen collisions with increasing $l_{\max}$, while $n_{\max}$ is fixed at 20. From this figure we can see that at lower incident energies the results converge faster with $l_{\max}$. For instance, at 10 keV an $l_{\max}$ of 4 appears to give sufficient convergence, whereas $l_{\max} = 5$ is required to achieve the convergent results at 100 keV and 1000 keV incident energy. Specifically, the difference between stopping cross section with $l_{\max} = 4$ and $l_{\max} = 5$ at 10 keV, 100 keV, and 1000 keV is 0.01%, 0.88%, and 3.2%, respectively. Next we take a look at convergence of the electronic stopping cross section with increasing $n_{\max}$.

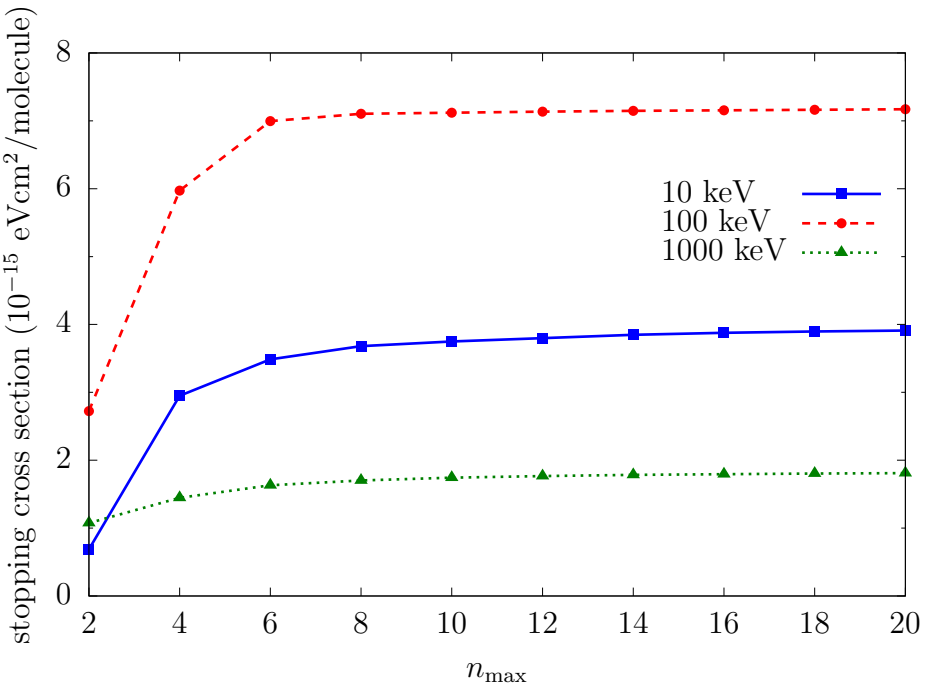

Figure 5.2: Convergence of the electronic stopping cross section for antiprotons incident on molecular hydrogen with increasing $n_{\max}$ for $l_{\max} = 5$ at incident energies of 10 keV, 100 keV, and 1000 keV. Calculations presented here were performed in the multiconfiguration approximation.

Figure 5.2 shows the convergence of the electronic stopping cross section with increasing $n_{\max}$, while $l_{\max}$ is fixed at 5. From the figure we can see that convergence with $n_{\max}$ is similar for all incident energies. The difference between stopping cross section when $n_{\max}$ changes from 18 to 20 at 10 keV, 100 keV, and 1000 keV is 0.36%, 0.10%, and 0.27%, respectively. From Figures 5.1 and 5.2 it can be concluded that a basis with $n_{\max} = 20$ and $l_{\max} = 5$ produces sufficiently convergent results for the electronic stopping cross section. This shows that the stopping cross section requires a larger basis to reach convergence when compared to the total ionisation cross section, which required $n_{\max} = 20$ and $l_{\max} = 4$ [66].

As described in Section 4.5 calculation of the stopping cross section associated with double ionisation and ionisation with excitation requires calculation of antiproton-H_2^+ collisions. Of course such calculations are checked for convergence as well. It was found that basis parameters of $n_{\max} = 20$ and $l_{\max} = 5$ were also sufficient to give convergent results.

5.2.2 Results of calculations

Here we present our final calculations of the antiproton-molecular hydrogen stopping cross section. The convergent basis parameters discussed above result in a total of 843 molecular target states to be used in the solution of the coupled-channel differential equations (4.35) in the multiconfigruation approach. With this model we obtain a two-electron ground state ionisation energy of 1.16497 a.u., which is close to the accurate value of 1.1741 a.u. [88]. Calculations were performed at the mean internuclear separation of H_2, which is 1.4487 a.u. The same internuclear separation was used in the H_2^+ calculations as required by the independent-event model.

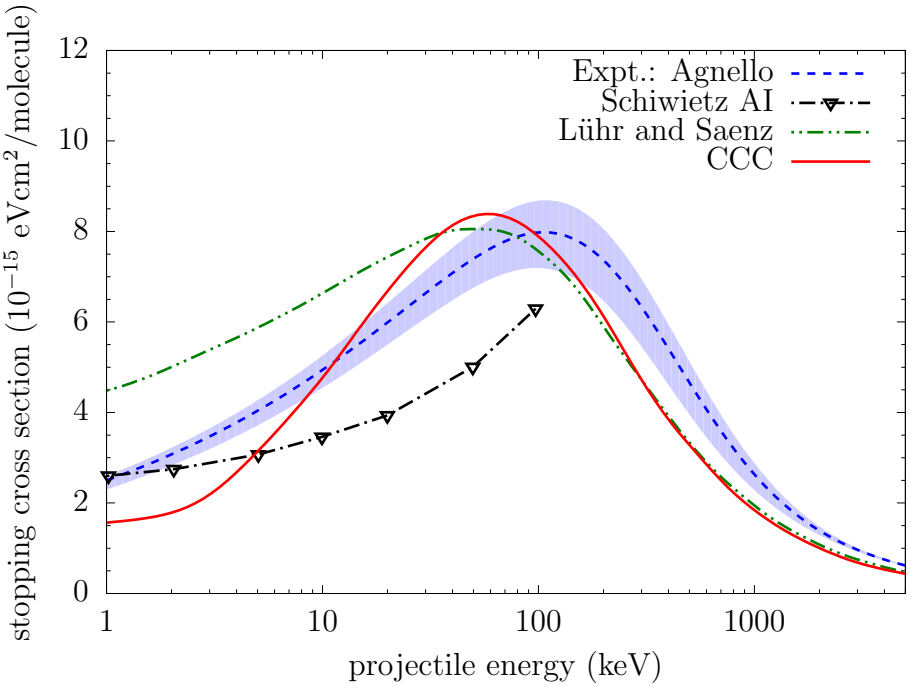

Figure 5.3: Total stopping cross section for antiprotons incident on molecular hydrogen. Included is the experimental data of Agnello *et al.* [77], with the shaded region representing the experimental uncertainty. The CCC results are shown by the solid line. The electronic stopping cross sections of Lühr and Saenz [50] and Schiwietz *et al.* [44, 45] (obtained using the AI method) are also shown. Results previously presented per atom have been multiplied by two.

In Figure 5.3 we present results for the antiproton-H_2 stopping cross section together with the theoretical calculations of Lühr and Saenz [50] and Schiwietz *et al.* [44, 45], as well as the experimental results of Agnello *et al.* [77]. We use an analytic orientation-averaging technique to account for all possible orientations of the molecule. We also take into account double ionisation and dissociative ionisation via the independent-event model. The nuclear and vibrational-excitation contributions are also added, which make a noticeable contribution below about 10 keV, as discussed in more detail later. The CCC results are in good agreement with those of Lühr and Saenz [50] above 150 keV, however, agreement with experimental data is lacking (possible reasons are discussed further below). Note that the calculations of Lühr and Saenz [50] and Schiwietz *et al.* [44, 45]

do not include the nuclear contribution. Adding the latter would increase their results below 10 keV. Additionally, both Lühr and Saenz [50] and Schiwietz *et al.* [44, 45] use an atomic approximation to molecular hydrogen.

Individual contributions to the total stopping cross section are presented in Figure 5.4. First, the figure shows that energy losses from one-electron transitions provide the main contribution to the total stopping cross section. Second, the figure shows that energy losses associated with double-ionisation and dissociative-ionisation processes make a small but important contribution, as does the nuclear stopping cross section. Energy loss to vibrational excitation is

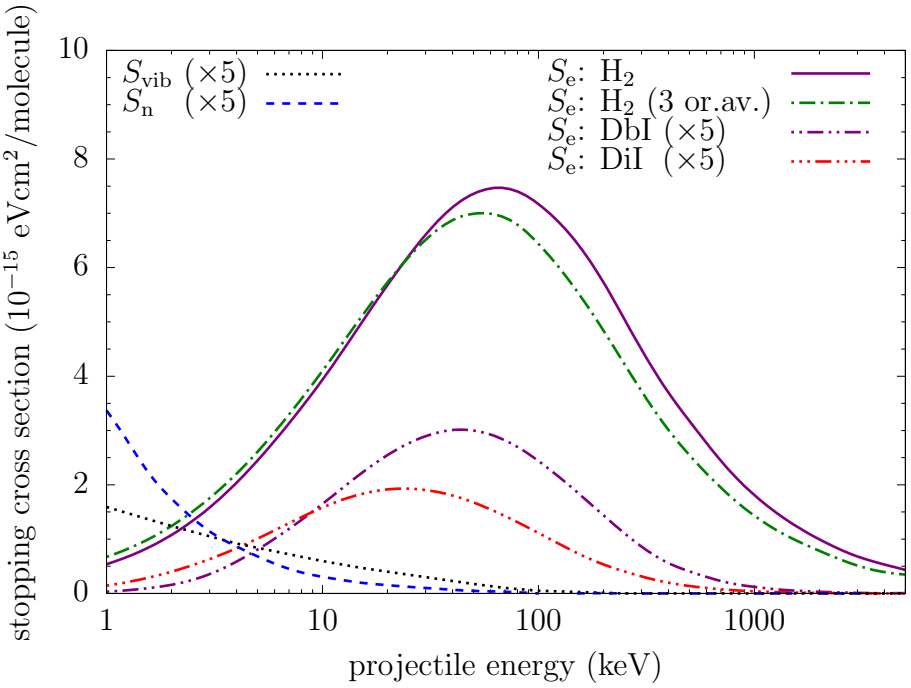

Figure 5.4: Individual contributions to the antiproton-H_2 total stopping cross section. The solid curve labeled "S_e: H_2" is the stopping cross section for the primary electron analytically averaged over all possible molecular orientations. Similarly "S_e: H_2 (3 or.av.)" is for an average over just three perpendicular orientations. "S_e: DbI" and "S_e: DiI" are the stopping cross sections associated with double ionisation and dissociative ionisation (obtained using the analytic orientation-averaging technique). "S_n" is the nuclear stopping cross section and "S_{vib}" is the vibrational-excitation contribution.

shown to make a small contribution at low energies. All these components are multiplied by a factor of 5 to make them visible in comparison with the dominant electronic contribution. The nuclear and vibrational-excitation stopping cross sections make negligible contribution above 10 keV.

Figure 5.4 also demonstrates the improvement the analytic orientation-averaging technique for the target molecule provides over averaging using three orientations. When compared to averaging over three perpendicular orientations, analytic averaging over all possible target orientations significantly increases the stopping cross section near and above the stopping maximum, and slightly reduces it below about 10 keV. The stopping cross sections for each of the three orientations used in Figure 5.4 are presented in Figure 5.5. These three perpendicular orientations of the target molecule are shown in the key of Figure 5.5.

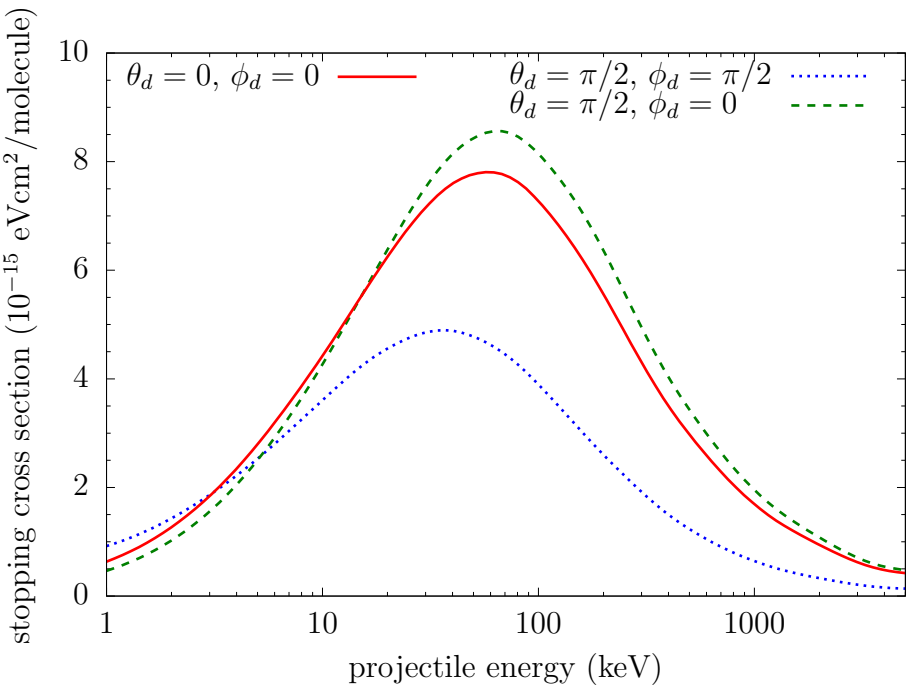

Figure 5.5: Electronic stopping cross sections for one-electron excitations from three main orientations of the H_2 molecule for antiprotons.

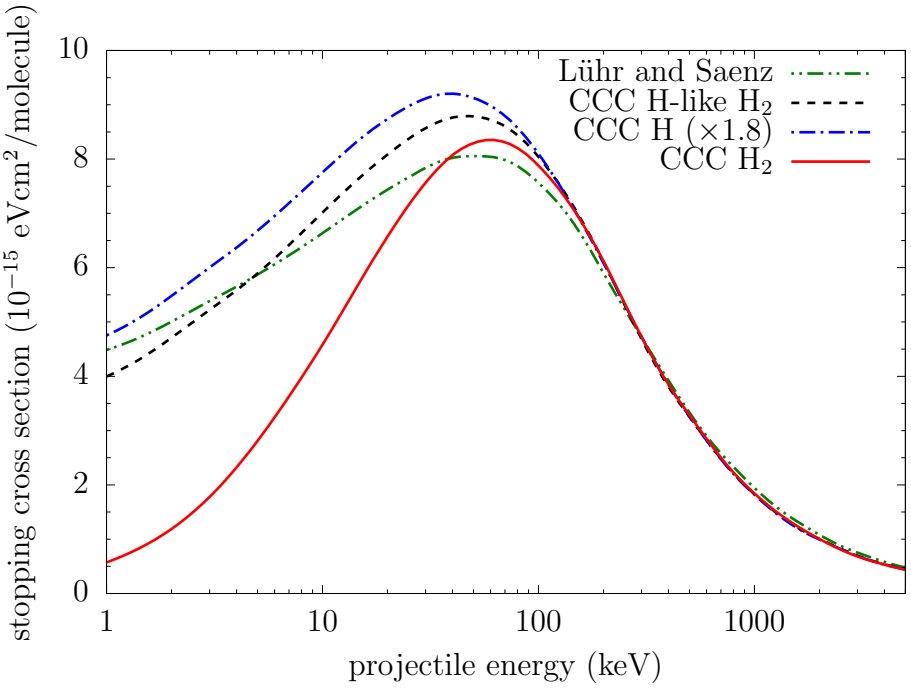

Figure 5.6: Comparison of the electronic stopping cross sections obtained using the full molecular approach and various H-like approximations.

In Figure 5.6 we compare the electronic part of the antiproton-H_2 stopping cross section obtained in the present CCC method with those obtained in various approximate theoretical treatments of the molecular target. We also show results we have obtained using a H-like (single active electron) structure model for H_2. In this model we choose the atomic number Z_{eff} of the hydrogen atom to reproduce the correct one-electron ground state energy of H_2. The results are then multiplied by two to account for both electrons of the molecule. The outcome is in good agreement with our full calculations above 150 keV. We also show the results of Lühr and Saenz [50]. Their calculations were performed using a H-like H_2 structure model, however they introduced a model potential instead of simply using Z_{eff}. After multiplication by two there is good agreement with our calculations above 200 keV. The disagreement at low energies between our full CCC calculations and those using a H-like structure model is attributed to the lack of electron-electron correlation effects in the latter. This demonstrates the

importance of using a proper molecular structure model. Additionally, in Figure 5.6 we show our calculations for atomic hydrogen from Chapter 3 multiplied by 1.8. This factor is determined by fitting to our H_2 results at high energies and demonstrates a slight deviation from Bragg's additivity rule [20] due to bonding effects. With this factor there is agreement with our full molecular calculations above 150 keV.

5.2.3 Discussion of results

We have developed the most comprehensive approach to calculating the stopping cross section of antiprotons in H_2 to date, with the major conclusion that it is important to treat H_2 as a two-electron target. Nevertheless, as can be seen from Figure 5.3 there is still some disagreement between the experiment and calculations. In order to better understand the reason for the disagreement we analyse the situation from the theoretical point of view. We start by mentioning that our theory uses the independent-event model to include the double-ionisation and dissociative-ionisation channels. This model tends to overestimate the double-ionisation and dissociative-ionisation cross sections. However since the contribution of these processes to the total stopping cross section is small they should not have a significant effect on the presented final results.

Secondly, we do not include direct homolytic dissociation of the target. To our best knowledge there are no calculations of this process induced by antiprotons that could be used to estimate its contribution to the energy loss. However, according to Khayrallah [89] electron-impact direct dissociation of H_2 takes place through doubly-excited states of the target. This in turn means that the process is a two-electron one and its probability is significantly smaller than the probability of the single-electron processes. If we assume that antiproton-induced direct

dissociation of H_2 also goes via doubly-excited states, then one can expect that its contribution to the total stopping cross section will be small, possibly similar to the contribution of the dissociative ionisation (see Figure 5.4). As far as direct heterolytic dissociation is concerned, the probability of this happening is even smaller.

It is also important to emphasise that the main reason behind the small stopping cross section obtained in the present calculations at low energies is the strong suppression of the ionisation cross section. This target structure-induced suppression of ionisation has a well-understood theoretical basis [65, 90].

As a cross test of the present results we note that when the internuclear distance in the computer code for H_2 is set to zero our previous He calculations from Chapter 3, which are in better agreement with experiment at low energies than for H_2, are perfectly reproduced. All the above gives us a certain degree of confidence in the reliability of the presented results.

Finally, we would like to make a comment about the experimental method, which we believe may also contribute to the disagreement between the experiment and calculations. The experiment of Agnello *et al.* [77] followed the same procedure as their measurements for helium, as discussed in Chapter 3. To recap, they measured the mean annihilation time $\langle t_a \rangle$ and path length R for antiprotons traveling through a H_2 gas chamber. Both measured quantities are expressed as integrals over functions of the total stopping cross section S as given in Eqs. (3.1) and (3.2). These two relationships are solved simultaneously by making use of a parameterised function for S presented by Andersen and Ziegler [79] for atomic targets. At high energies the function is based on Bethe's formula and is given by $S_h = [(243 - 0.375Z_t)Z_t/E_0]\ln(1 + \gamma/E_0 + 4m_eE_0/m_{\bar{p}}\bar{E})$, where Z_t is the atomic number of the target that Agnello *et al.* [77] have taken to be 1,

m_e and $m_{\bar{p}}$ are the electron and antiproton mass respectively, and $\bar{E}$ is the mean excitation energy of the target. At low energies it is given by $S_l = \alpha E_0^{\beta}$ which is based on the Thomas-Fermi statistical model. In the intermediate energy range the interpolation formula $1/S = 1/S_l + 1/S_h$ is used, which was originally proposed by Varelas and Biersack [80]. The variables α, β, and γ are varied to fit the experimentally measured data for $\langle t_a \rangle$ and R. Agnello *et al.* [77] found these variables to be 1.25, 0.30, and 4×10^5, respectively. The use of such a method for determining the stopping cross section is likely to introduce additional uncertainties on top of the shaded region in Figure 5.3, which is the uncertainty in the experimental measurements. According to Andersen and Ziegler [79] the fitting function described above has an estimated accuracy of 10% at 10 keV and 5% at 500 keV. However in the intermediate energy range the accuracy of the interpolation method is said to be approximately 20%. The restrictions of using a fitting function may be one possible explanation for the disagreement between our calculations and the experimental data.

5.3 Water molecule

Here we present calculations of the electronic stopping cross section for antiproton collisions with H_2O molecules using a spherical neon-like structure model of 6 p-shell electrons above a frozen core. Calculations were performed with basis parameters $N_l = 20 - l$ and λ_l is chosen to be 2. The maximum orbital angular momentum $l_{\max}$ of target states used in calculations was 4. This resulted in the total number of coupled differential equations being 1112.

The present results for H_2O are shown in Figure 5.7. There is no experiment and to our best knowledge there have been no other calculations for the antiproton-H_2O system. However, the demand for calculations of antiprotons

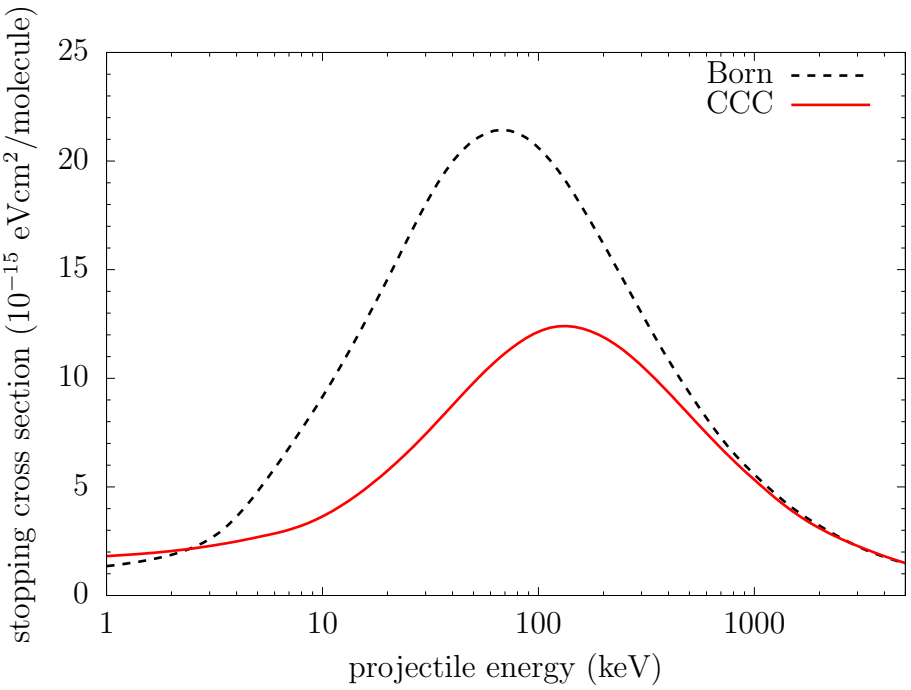

Figure 5.7: Electronic stopping cross section for antiproton collisions with H_2O.

stopping in biologically-important molecules such as water is rapidly increasing due to current research such as the Antiproton Cell Experiment (ACE) [17, 18] at CERN. The ACE aims to fully assess the suitability and effectiveness of antiprotons for cancer therapy. While our calculations for H_2O using a neonisation approximation can not be considered highly accurate, they should still provide a guideline to future experiments on antiproton stopping in water. We note that the presented curve is the stopping cross section associated with the energy losses due to single-electron transitions from the outer p-shell only. It represents the dominant contribution to the stopping cross section. The present Born approximation results are also shown.

5.4 Chapter summary

We have applied the semiclassical CCC method to the calculation of stopping cross sections for antiprotons in the H_2 and H_2O molecules. For H_2 we fully account for the electron-electron correlation and average over all possible orientations of the target using an analytic orientation-averaging technique. Double-ionisation and dissociative-ionisation contributions are also included via an independent-event model. Energy losses through vibrational excitations as well as the nuclear stopping cross section have been included. The presented theoretical results are the most comprehensive and accurate to date. We also presented the stopping cross section for antiprotons in H_2O. For the latter we used a neon-like model of six p-shell electrons above a frozen Hartree-Fock core with only one-electron excitations from the outer p shell allowed.

In the following chapters we shall turn our attention to calculating the stopping cross section for protons colliding with atomic hydrogen. Due to the possibility of rearrangement, whereby the proton can grab an electron and form H, the aforementioned problem is significantly more difficult than its antiproton counterpart because it requires a two-centre expansion of the scattering wave function. Additionally, as the projectile can become a hydrogen atom, one must consider the process of hydrogen collisions with hydrogen to obtain accurate stopping cross sections. In Chapters 6 and 7 we will discuss our theoretical approach to proton-hydrogen and hydrogen-hydrogen collisions, respectively. Then in Chapter 8 we will present the results of calculations.

Chapter 6

Two-centre coupled-channel approach to ion-atom collisions

6.1 Introduction

In this chapter we will present details of our two-centre approach to modelling the collisions of ions with atoms for the purpose of calculating the stopping power. Specifically, we will focus on the collisions of protons with hydrogen. The advantage of a two-centre method is that it allows one to accurately model electron-capture processes. These processes play an important role when calculating the stopping power for systems involving positive ions. Like the single-centre approach (see Chapter 2), we will be using the semiclassical approximation in deriving a set of coupled-channel differential equations, whose solutions give the probability of a scattering event occurring. Furthermore, this will be achieved without the introduction of electron translation factors. The aforementioned method is referred to as the two-centre semiclassical convergent close-coupling approach, or two-centre CCC.

In the semiclassical approximation the target electron is treated fully quantum-mechanically while the motion of the projectile is treated classically. As dis-

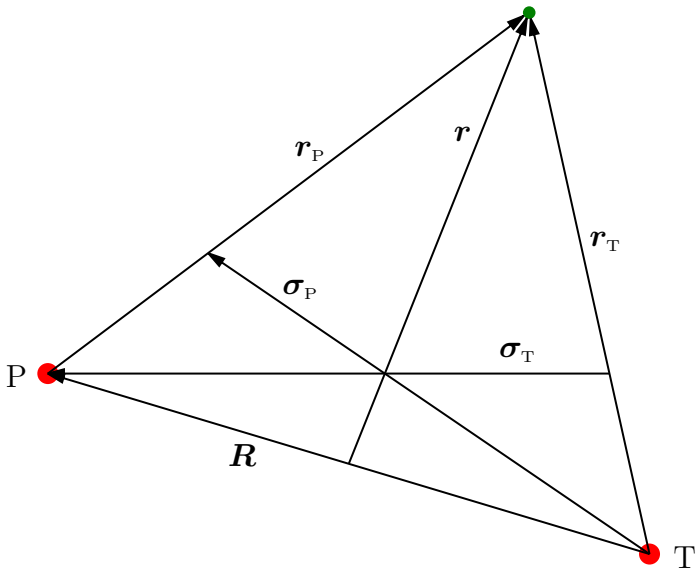

Figure 6.1: Sketch of the Jacobi coordinates used for the proton-hydrogen system. The target nucleus is denoted as T, while P indicates the projectile proton.

cussed in Section 2.1 the projectile is assumed to follow a straight line trajectory, that is

$$\boldsymbol{R}(t) = \boldsymbol{b} + \boldsymbol{v}t, \tag{6.1}$$

where $\boldsymbol{R}$ is the position of the projectile with respect to the target nucleus, $\boldsymbol{v}$ is the velocity of the projectile in the laboratory frame, and $\boldsymbol{b}$ is the impact parameter. In the laboratory frame the target nucleus is at the origin and the $\boldsymbol{v}$ is directed along the z-axis, see Figure 2.1. The position of the projectile along the z-axis is $z = vt$, where t is time and $t = 0$ corresponds to the distance of closest approach.

Furthermore, to describe the proton-hydrogen system we utilise the Jacobi coordinates illustrated in Figure 6.1. Here $\boldsymbol{r}_\mathrm{T}$ is the position of the electron relative to the target proton, while $\boldsymbol{r}_\mathrm{P}$ is the position of the electron relative to the projectile proton. Similarly, $\boldsymbol{\sigma}_\mathrm{T}$ is the position of the projectile proton

relative to the centre-of-mass of the target proton-electron system, while $\boldsymbol{\sigma}_{\mathrm{P}}$ is the position of the centre-of-mass of the projectile proton-electron system relative to the target proton. Finally, $\boldsymbol{r}$ is the position of the electron relative to the centre-of-mass of the two-proton system.

In what follows we will present the theoretical details that allow us to model the collisions of protons with hydrogen. First we will formulate the two-centre couple-channel equations whose solution describes the scattering event. Then we will detail how transition matrix elements are evaluated. Lastly we will discuss the calculation of the stopping power in the two-centre coupled-channel formalism.

6.2 Formulation of the two-centre scattering equations

In the literature, standard derivations of the two-centre coupled-channel equations start from the approximate time-dependent Schrödinger equation for the electronic part of the scattering wave function Φ and rely on the introduction of the so-called "electron translation factors". It is common to expand Φ in terms of target states ψ_α and projectile states ψ_β according to

$$\Phi = \sum_\alpha A_\alpha(t,\boldsymbol{b})\psi_\alpha(\boldsymbol{r}_{\mathrm{T}})e^{-i\epsilon_\alpha t} + \sum_\beta B_\beta(t,\boldsymbol{b})\psi_\beta(\boldsymbol{r}_{\mathrm{P}})e^{-i\epsilon_\beta t}e^{-i(\boldsymbol{v}\cdot\boldsymbol{r}_{\mathrm{T}}+v^2t/2)}, \quad (6.2)$$

where ϵ_α and ϵ_β are the energies of the target and projectile electronic states α and β, respectively, and A_α and B_β are the expansion coefficients that contain all information about the scattering process. The exponential factor $\exp[-i(\boldsymbol{v}\cdot\boldsymbol{r}_{\mathrm{T}} + v^2t/2)]$ in the second term of Eq. (6.2) is referred to as the electron translation factor. In 1958 Bates and McCarroll [91] realised that the conventional expansion of the the electronic part of the wave function does not satisfy the semiclassical time-dependent Schrödinger equation unless an electron translation factor

is introduced to remedy the problem. The problem with this artificial electron translation factor is that there are infinitely many ways of choosing it [38].

However, in this section we will present an alternative derivation of the two-centre coupled-channel equations that does not require the introduction of the electron translation factors. This will be achieved by starting from the exact time-independent Schrödinger equation and using a more general expansion for the total scattering wave function that correctly represents both the target and projectile centres. It is emphasised that we do not use Eq. (6.2) in this derivation.

To proceed with our derivation we recall that the exact nonrelativistic Schrödinger equation for the total scattering wave function Ψ is

$$H\Psi = E\Psi, \tag{6.3}$$

where E is the total energy of the system and H is the full three-body Hamiltonian. The Hamiltonian can be written in the following equivalent forms:

$$H = -\frac{1}{2\mu}\nabla^2_{\boldsymbol{\sigma}_\mathrm{T}} + H_\mathrm{T} + V_\mathrm{P} \tag{6.4}$$

$$= -\frac{1}{2\mu}\nabla^2_{\boldsymbol{\sigma}_\mathrm{P}} + H_\mathrm{P} + V_\mathrm{T}. \tag{6.5}$$

Here μ is the reduced mass of the proton-hydrogen system, H_T and H_P are the target and projectile atom Hamiltonians, V_T is the interaction of the target proton with the projectile atom, and V_P is the interaction of the projectile proton with the target atom. The Hamiltonians H_T and H_P are given by

$$H_\mathrm{T} = -\frac{1}{2}\nabla^2_{\boldsymbol{r}_\mathrm{T}} - \frac{1}{r_\mathrm{T}}, \tag{6.6}$$

and

$$H_\mathrm{P} = -\frac{1}{2}\nabla^2_{\boldsymbol{r}_\mathrm{P}} - \frac{1}{r_\mathrm{P}}, \tag{6.7}$$

while the interactions V_T and V_P are given by

$$V_\mathrm{T} = \frac{1}{R} - \frac{1}{r_\mathrm{T}}, \tag{6.8}$$

and

$$V_{\mathrm{P}} = \frac{1}{R} - \frac{1}{r_{\mathrm{P}}}. \tag{6.9}$$

The two-centre expansion we use for the total scattering wave function is a natural extension of the single-centre one given in Eq. (2.6). The total scattering wave function is expanded in terms of a set of N_{T} target pseudostates ψ_α and N_{P} projectile pseudostates ψ_β according to

$$\Psi = \sum_{\alpha=1}^{N_{\mathrm{T}}} A_\alpha(\boldsymbol{\sigma}_{\mathrm{T}})\psi_\alpha(\boldsymbol{r}_{\mathrm{T}})e^{i\boldsymbol{k}_\alpha\cdot\boldsymbol{\sigma}_{\mathrm{T}}} + \sum_{\beta=1}^{N_{\mathrm{P}}} B_\beta(\boldsymbol{\sigma}_{\mathrm{P}})\psi_\beta(\boldsymbol{r}_{\mathrm{P}})e^{i\boldsymbol{k}_\beta\cdot\boldsymbol{\sigma}_{\mathrm{P}}}, \tag{6.10}$$

where $\boldsymbol{k}_\alpha$ is the relative momentum of the projectile proton and the target atom, and similarly $\boldsymbol{k}_\beta$ is the relative momentum of the target proton and the projectile atom. Hence, the total energy of the system E is given by

$$E = \frac{k_\alpha^2}{2\mu} + \epsilon_\alpha = \frac{k_\beta^2}{2\mu} + \epsilon_\beta. \tag{6.11}$$

Furthermore, the pseudostates ψ_α and ψ_β represent both bound and continuum states, and are constructed to satisfy the conditions

$$\langle\psi_{\alpha'}|H_{\mathrm{T}}|\psi_\alpha\rangle = \epsilon_\alpha\delta_{\alpha'\alpha}, \qquad \langle\psi_{\alpha'}|\psi_\alpha\rangle = \delta_{\alpha'\alpha}, \tag{6.12}$$

and

$$\langle\psi_{\beta'}|H_{\mathrm{P}}|\psi_\beta\rangle = \epsilon_\beta\delta_{\beta'\beta}, \qquad \langle\psi_{\beta'}|\psi_\beta\rangle = \delta_{\beta'\beta}. \tag{6.13}$$

It must be emphasised, that although the pseudostates within each set are orthogonal to each other, a pseudostate from one set is not orthogonal to a pseudostate from the other set.

Substituting our expression for the scattering wave function (6.10) into the

Schrödinger equation (6.3) yields

$$\sum_{\alpha=1}^{N_\mathrm{T}}\left(-\frac{1}{2\mu}\nabla^2_{\boldsymbol{\sigma}_\mathrm{T}}+H_\mathrm{T}+V_\mathrm{P}\right)A_\alpha(\boldsymbol{\sigma}_\mathrm{T})\psi_\alpha(\boldsymbol{r}_\mathrm{T})e^{i\boldsymbol{k}_\alpha\cdot\boldsymbol{\sigma}_\mathrm{T}}$$
$$+\sum_{\beta=1}^{N_\mathrm{P}}\left(-\frac{1}{2\mu}\nabla^2_{\boldsymbol{\sigma}_\mathrm{P}}+H_\mathrm{P}+V_\mathrm{T}\right)B_\beta(\boldsymbol{\sigma}_\mathrm{P})\psi_\beta(\boldsymbol{r}_\mathrm{P})e^{i\boldsymbol{k}_\beta\cdot\boldsymbol{\sigma}_\mathrm{P}}$$
$$=E\sum_{\alpha=1}^{N_\mathrm{T}}A_\alpha(\boldsymbol{\sigma}_\mathrm{T})\psi_\alpha(\boldsymbol{r}_\mathrm{T})e^{i\boldsymbol{k}_\alpha\cdot\boldsymbol{\sigma}_\mathrm{T}}+E\sum_{\beta=1}^{N_\mathrm{P}}B_\beta(\boldsymbol{\sigma}_\mathrm{P})\psi_\beta(\boldsymbol{r}_\mathrm{P})e^{i\boldsymbol{k}_\beta\cdot\boldsymbol{\sigma}_\mathrm{P}}. \tag{6.14}$$

The action of the Laplacian operator in Eq. (6.14) was considered in Chapter 2. It was shown that when applying the semiclassical approximation [see Eqs. (2.11)-(2.16) for details] we get

$$-\frac{1}{2\mu}\nabla^2_{\boldsymbol{\sigma}_\mathrm{T}}A_\alpha(\boldsymbol{\sigma}_\mathrm{T})e^{i\boldsymbol{k}_\alpha\cdot\boldsymbol{\sigma}_\mathrm{T}}\approx\frac{k_\alpha^2}{2\mu}A_\alpha(\boldsymbol{\sigma}_\mathrm{T})e^{i\boldsymbol{k}_\alpha\cdot\boldsymbol{\sigma}_\mathrm{T}}-i\frac{dA_\alpha(\boldsymbol{\sigma}_\mathrm{T})}{dt}e^{i\boldsymbol{k}_\alpha\cdot\boldsymbol{\sigma}_\mathrm{T}}, \tag{6.15}$$

and hence

$$-\frac{1}{2\mu}\nabla^2_{\boldsymbol{\sigma}_\mathrm{P}}B_\beta(\boldsymbol{\sigma}_\mathrm{P})e^{i\boldsymbol{k}_\beta\cdot\boldsymbol{\sigma}_\mathrm{P}}\approx\frac{k_\beta^2}{2\mu}B_\beta(\boldsymbol{\sigma}_\mathrm{P})e^{i\boldsymbol{k}_\beta\cdot\boldsymbol{\sigma}_\mathrm{P}}-i\frac{dB_\beta(\boldsymbol{\sigma}_\mathrm{P})}{dt}e^{i\boldsymbol{k}_\beta\cdot\boldsymbol{\sigma}_\mathrm{P}}. \tag{6.16}$$

Utilising Eqs. (6.15) and (6.16), and considering Eq. (6.11), we can write

$$i\sum_{\alpha=1}^{N_\mathrm{T}}\frac{dA_\alpha(\boldsymbol{\sigma}_\mathrm{T})}{dt}\psi_\alpha(\boldsymbol{r}_\mathrm{T})e^{i\boldsymbol{k}_\alpha\cdot\boldsymbol{\sigma}_\mathrm{T}}+i\sum_{\beta=1}^{N_\mathrm{P}}\frac{dB_\beta(\boldsymbol{\sigma}_\mathrm{P})}{dt}\psi_\beta(\boldsymbol{r}_\mathrm{P})e^{i\boldsymbol{k}_\beta\cdot\boldsymbol{\sigma}_\mathrm{P}}$$
$$=\sum_{\alpha=1}^{N_\mathrm{T}}A_\alpha(\boldsymbol{\sigma}_\mathrm{T})(H_\mathrm{T}+V_\mathrm{P}-\epsilon_\alpha)\psi_\alpha(\boldsymbol{r}_\mathrm{T})e^{i\boldsymbol{k}_\alpha\cdot\boldsymbol{\sigma}_\mathrm{T}}$$
$$+\sum_{\beta=1}^{N_\mathrm{P}}B_\beta(\boldsymbol{\sigma}_\mathrm{P})(H_\mathrm{P}+V_\mathrm{T}-\epsilon_\beta)\psi_\beta(\boldsymbol{r}_\mathrm{P})e^{i\boldsymbol{k}_\beta\cdot\boldsymbol{\sigma}_\mathrm{P}}. \tag{6.17}$$

Now, multiplying Eq. (6.17) on the left by $\psi^*_{\alpha'}(\boldsymbol{r}_\mathrm{T})e^{-i\boldsymbol{k}_{\alpha'}\cdot\boldsymbol{\sigma}_\mathrm{T}}$ and integrating over $\boldsymbol{r}_\mathrm{T}$ we obtain

$$i\sum_{\alpha=1}^{N_\mathrm{T}}\frac{dA_\alpha(\boldsymbol{\sigma}_\mathrm{T})}{dt}\langle\psi_{\alpha'}|\psi_\alpha\rangle e^{i(\boldsymbol{k}_\alpha-\boldsymbol{k}_{\alpha'})\cdot\boldsymbol{\sigma}_\mathrm{T}}+i\sum_{\beta=1}^{N_\mathrm{P}}\frac{dB_\beta(\boldsymbol{\sigma}_\mathrm{P})}{dt}\langle\psi_{\alpha'}|e^{i(\boldsymbol{k}_\beta\cdot\boldsymbol{\sigma}_\mathrm{P}-\boldsymbol{k}_{\alpha'}\cdot\boldsymbol{\sigma}_\mathrm{T})}|\psi_\beta\rangle$$
$$=\sum_{\alpha=1}^{N_\mathrm{T}}A_\alpha(\boldsymbol{\sigma}_\mathrm{T})\langle\psi_{\alpha'}|H_\mathrm{T}+V_\mathrm{P}-\epsilon_\alpha|\psi_\alpha\rangle e^{i(\boldsymbol{k}_\alpha-\boldsymbol{k}_{\alpha'})\cdot\boldsymbol{\sigma}_\mathrm{T}}$$
$$+\sum_{\beta=1}^{N_\mathrm{P}}B_\beta(\boldsymbol{\sigma}_\mathrm{P})\langle\psi_{\alpha'}|e^{i(\boldsymbol{k}_\beta\cdot\boldsymbol{\sigma}_\mathrm{P}-\boldsymbol{k}_{\alpha'}\cdot\boldsymbol{\sigma}_\mathrm{T})}(H_\mathrm{P}+V_\mathrm{T}-\epsilon_\beta)|\psi_\beta\rangle. \tag{6.18}$$

At this point we need to look at the terms in the exponential factors. It has been shown in Chapter 2, Eq. (2.19), that

$$(\boldsymbol{k}_\alpha - \boldsymbol{k}_{\alpha'})\cdot\boldsymbol{\sigma}_{\mathrm{T}} \approx (\epsilon_{\alpha'} - \epsilon_\alpha)t + \boldsymbol{q}_{\alpha\perp}\cdot\boldsymbol{b}, \tag{6.19}$$

where $\boldsymbol{q}_{\alpha\perp}$ is the component of the momentum transfer vector $\boldsymbol{q}_\alpha = \boldsymbol{k}_\alpha - \boldsymbol{k}_{\alpha'}$ that is perpendicular to the z-axis. Now consider the term

$$\boldsymbol{k}_\beta\cdot\boldsymbol{\sigma}_{\mathrm{P}} - \boldsymbol{k}_{\alpha'}\cdot\boldsymbol{\sigma}_{\mathrm{T}}. \tag{6.20}$$

First, we express $\boldsymbol{\sigma}_{\mathrm{T}}$ and $\boldsymbol{\sigma}_{\mathrm{P}}$ in terms of $\boldsymbol{R}$ and $\boldsymbol{r}_{\mathrm{T}}$ according to

$$\boldsymbol{\sigma}_{\mathrm{T}} = \gamma\boldsymbol{r}_{\mathrm{T}} - \boldsymbol{r}_{\mathrm{P}} = \boldsymbol{R} - (1-\gamma)\boldsymbol{r}_{\mathrm{T}}, \tag{6.21}$$

and

$$\boldsymbol{\sigma}_{\mathrm{P}} = \boldsymbol{r}_{\mathrm{T}} - \gamma\boldsymbol{r}_{\mathrm{P}} = \gamma\boldsymbol{R} + (1-\gamma)\boldsymbol{r}_{\mathrm{T}}, \tag{6.22}$$

where γ is the reduced mass of the proton-electron system. We also introduce momentum transfer vectors

$$\boldsymbol{p}_\beta = \gamma\boldsymbol{k}_\beta - \boldsymbol{k}_{\alpha'}, \tag{6.23}$$

and

$$\boldsymbol{p}_{\alpha'} = \boldsymbol{k}_\beta - \gamma\boldsymbol{k}_{\alpha'}. \tag{6.24}$$

This allows us to write

$$\boldsymbol{k}_\beta\cdot\boldsymbol{\sigma}_{\mathrm{P}} - \boldsymbol{k}_{\alpha'}\cdot\boldsymbol{\sigma}_{\mathrm{T}} = \boldsymbol{p}_\beta\cdot\boldsymbol{R} + (\boldsymbol{p}_{\alpha'} - \boldsymbol{p}_\beta)\cdot\boldsymbol{r}_{\mathrm{T}}. \tag{6.25}$$

Furthermore, writing $\boldsymbol{R} = \boldsymbol{z} + \boldsymbol{b}$ and considering the fact that

$$\boldsymbol{p}_{\alpha'} - \boldsymbol{p}_\beta \approx \boldsymbol{v}, \tag{6.26}$$

we can write Eq. (6.25) as

$$\boldsymbol{k}_\beta\cdot\boldsymbol{\sigma}_{\mathrm{P}} - \boldsymbol{k}_{\alpha'}\cdot\boldsymbol{\sigma}_{\mathrm{T}} = p_{\beta\parallel}z + \boldsymbol{p}_{\beta\perp}\cdot\boldsymbol{b} + \boldsymbol{v}\cdot\boldsymbol{r}_{\mathrm{T}}, \tag{6.27}$$

where $\boldsymbol{p}_{\beta\parallel}$ and $\boldsymbol{p}_{\beta\perp}$ are the components of momentum transfer vector $\boldsymbol{p}_\beta$ that are parallel and perpendicular to the z-axis, respectively. In fact,

$$\boldsymbol{p}_{\beta\perp} = \boldsymbol{q}_{\alpha\perp}. \tag{6.28}$$

Additionally, we can express $p_{\beta\parallel}$ as

$$p_{\beta\parallel} = -v/2 + (\epsilon_{\alpha'} - \epsilon_\beta)/v, \tag{6.29}$$

and write Eq. (6.18) as

$$\begin{aligned}
&ie^{i\boldsymbol{q}_{\alpha\perp}\cdot\boldsymbol{b}} \sum_{\alpha=1}^{N_\mathrm{T}} \frac{dA_\alpha(t,\boldsymbol{b})}{dt} \langle\psi_{\alpha'}|\psi_\alpha\rangle e^{i(\epsilon_{\alpha'}-\epsilon_\alpha)t} \\
&+ ie^{i\boldsymbol{p}_{\beta\perp}\cdot\boldsymbol{b}} \sum_{\beta=1}^{N_\mathrm{P}} \frac{dB_\beta(t,\boldsymbol{b})}{dt} \langle\psi_{\alpha'}|e^{i\boldsymbol{v}\cdot\boldsymbol{r}_\mathrm{T}}|\psi_\beta\rangle e^{i(-v^2t/2+(\epsilon_{\alpha'}-\epsilon_\beta)t)} \\
&= e^{i\boldsymbol{q}_{\alpha\perp}\cdot\boldsymbol{b}} \sum_{\alpha=1}^{N_\mathrm{T}} A_\alpha(t,\boldsymbol{b}) \langle\psi_{\alpha'}|H_\mathrm{T} + V_\mathrm{P} - \epsilon_\alpha|\psi_\alpha\rangle e^{i(\epsilon_{\alpha'}-\epsilon_\alpha)t} \\
&\quad + e^{i\boldsymbol{p}_{\beta\perp}\cdot\boldsymbol{b}} \sum_{\beta=1}^{N_\mathrm{P}} B_\beta(t,\boldsymbol{b}) \langle\psi_{\alpha'}|e^{i\boldsymbol{v}\cdot\boldsymbol{r}_\mathrm{T}}(H_\mathrm{P} + V_\mathrm{T} - \epsilon_\beta)|\psi_\beta\rangle e^{i(-v^2t/2+(\epsilon_{\alpha'}-\epsilon_\beta)t)}.
\end{aligned} \tag{6.30}$$

For details on momentum transfer vectors, including Eqs. (6.26) and (6.29), see Appendix A. Finally, taking into account Eqs. (6.12) and (6.28) we arrive at the first set of coupled-channel differential equations

$$\begin{aligned}
&i\frac{dA_{\alpha'}(t,\boldsymbol{b})}{dt} + i\sum_{\beta=1}^{N_\mathrm{P}} \frac{dB_\beta(t,\boldsymbol{b})}{dt} \langle\psi_{\alpha'}|e^{i\boldsymbol{v}\cdot\boldsymbol{r}_\mathrm{T}}|\psi_\beta\rangle e^{i(-v^2t/2+(\epsilon_{\alpha'}-\epsilon_\beta)t)} \\
&= \sum_{\alpha=1}^{N_\mathrm{T}} A_\alpha(t,\boldsymbol{b}) \langle\psi_{\alpha'}|V_\mathrm{P}|\psi_\alpha\rangle e^{i(\epsilon_{\alpha'}-\epsilon_\alpha)t} \\
&\quad + \sum_{\beta=1}^{N_\mathrm{P}} B_\beta(t,\boldsymbol{b}) \langle\psi_{\alpha'}|e^{i\boldsymbol{v}\cdot\boldsymbol{r}_\mathrm{T}}(H_\mathrm{P} + V_\mathrm{T} - \epsilon_\beta)|\psi_\beta\rangle e^{i(-v^2t/2+(\epsilon_{\alpha'}-\epsilon_\beta)t)}, \\
&\alpha' = 1, \ldots, N_\mathrm{T}.
\end{aligned} \tag{6.31}$$

Equation (6.31) couples only half of the expansion coefficients. To couple all expansion coefficients we must obtain a second set of differential equations.

The procedure for this is similar to what has already be shown. Returning to Eq. (6.17), this time we multiply on the left by $\psi^*_{\beta'}(\boldsymbol{r}_\mathrm{P})e^{-i\boldsymbol{k}_{\beta'}\cdot\boldsymbol{\sigma}_\mathrm{P}}$ and integrate over $\boldsymbol{r}_\mathrm{P}$ to obtain

$$\begin{aligned} &i\sum_{\alpha=1}^{N_\mathrm{T}}\frac{dA_\alpha(\boldsymbol{\sigma}_\mathrm{T})}{dt}\langle\psi_{\beta'}|e^{i(\boldsymbol{k}_\alpha\cdot\boldsymbol{\sigma}_\mathrm{T}-\boldsymbol{k}_{\beta'}\cdot\boldsymbol{\sigma}_\mathrm{P})}|\psi_\alpha\rangle + i\sum_{\beta=1}^{N_\mathrm{P}}\frac{dB_\beta(\boldsymbol{\sigma}_\mathrm{P})}{dt}\langle\psi_{\beta'}|\psi_\beta\rangle e^{i(\boldsymbol{k}_\beta-\boldsymbol{k}_{\beta'})\cdot\boldsymbol{\sigma}_\mathrm{P}} \\ &= \sum_{\alpha=1}^{N_\mathrm{T}}A_\alpha(\boldsymbol{\sigma}_\mathrm{T})\langle\psi_{\beta'}|e^{i(\boldsymbol{k}_\alpha\cdot\boldsymbol{\sigma}_\mathrm{T}-\boldsymbol{k}_{\beta'}\cdot\boldsymbol{\sigma}_\mathrm{P})}(H_\mathrm{T}+V_\mathrm{P}-\epsilon_\alpha)|\psi_\alpha\rangle \\ &\quad + \sum_{\beta=1}^{N_\mathrm{P}}B_\beta(\boldsymbol{\sigma}_\mathrm{P})\langle\psi_{\beta'}|H_\mathrm{P}+V_\mathrm{T}-\epsilon_\beta|\psi_\beta\rangle e^{i(\boldsymbol{k}_\beta-\boldsymbol{k}_{\beta'})\cdot\boldsymbol{\sigma}_\mathrm{P}}. \end{aligned} \tag{6.32}$$

Similar to Eq. (6.19), we can write

$$(\boldsymbol{k}_\beta-\boldsymbol{k}_{\beta'})\cdot\boldsymbol{\sigma}_\mathrm{P} \approx (\epsilon_{\beta'}-\epsilon_\beta)t + \boldsymbol{q}_{\beta\perp}\cdot\boldsymbol{b}, \tag{6.33}$$

where $\boldsymbol{q}_{\beta\perp}$ is the component of the momentum transfer vector $\boldsymbol{q}_\beta = \boldsymbol{k}_\beta - \boldsymbol{k}_{\beta'}$ that is perpendicular to the z-axis. Additionally, expressing $\boldsymbol{\sigma}_\mathrm{T}$ and $\boldsymbol{\sigma}_\mathrm{P}$ in terms of $\boldsymbol{R}$ and $\boldsymbol{r}_\mathrm{P}$ according to

$$\boldsymbol{\sigma}_\mathrm{T} = \gamma\boldsymbol{r}_\mathrm{T} - \boldsymbol{r}_\mathrm{P} = \gamma\boldsymbol{R} - (1-\gamma)\boldsymbol{r}_\mathrm{P}, \tag{6.34}$$

and

$$\boldsymbol{\sigma}_\mathrm{P} = \boldsymbol{r}_\mathrm{T} - \gamma\boldsymbol{r}_\mathrm{P} = \boldsymbol{R} + (1-\gamma)\boldsymbol{r}_\mathrm{P}, \tag{6.35}$$

the exponential term $\boldsymbol{k}_\alpha\cdot\boldsymbol{\sigma}_\mathrm{T} - \boldsymbol{k}_{\beta'}\cdot\boldsymbol{\sigma}_\mathrm{P}$ becomes

$$\begin{aligned} \boldsymbol{k}_\alpha\cdot\boldsymbol{\sigma}_\mathrm{T} - \boldsymbol{k}_{\beta'}\cdot\boldsymbol{\sigma}_\mathrm{P} &= \boldsymbol{p}_\alpha\cdot\boldsymbol{R} - (\boldsymbol{p}_{\beta'}-\boldsymbol{p}_\alpha)\cdot\boldsymbol{r}_\mathrm{P} \\ &= p_{\alpha\parallel}z + \boldsymbol{p}_{\alpha\perp}\cdot\boldsymbol{b} - \boldsymbol{v}\cdot\boldsymbol{r}_\mathrm{P}. \end{aligned} \tag{6.36}$$

Here $\boldsymbol{p}_\alpha$ and $\boldsymbol{p}_{\beta'}$ are the momentum transfer vectors

$$\boldsymbol{p}_\alpha = \gamma\boldsymbol{k}_\alpha - \boldsymbol{k}_{\beta'}, \tag{6.37}$$

and

$$\boldsymbol{p}_{\beta'} = \boldsymbol{k}_\alpha - \gamma\boldsymbol{k}_{\beta'}, \tag{6.38}$$

which satisfy

$$\boldsymbol{p}_{\beta'} - \boldsymbol{p}_{\alpha} \approx \boldsymbol{v}. \tag{6.39}$$

Furthermore, $\boldsymbol{p}_{\alpha\parallel}$ and $\boldsymbol{p}_{\alpha\perp}$ are the components of momentum transfer vector $\boldsymbol{p}_{\alpha}$ that are parallel and perpendicular to the z-axis, respectively. Also, $p_{\alpha\parallel}$ can be expressed as

$$p_{\alpha\parallel} = -v/2 + (\epsilon_{\beta'} - \epsilon_{\alpha})/v. \tag{6.40}$$

Again, for details of Eq. (6.40) see Appendix A. Now, considering Eqs. (6.33) and (6.36), we can write Eq. (6.32) as

$$\begin{aligned}
&ie^{i\boldsymbol{p}_{\alpha\perp}\cdot\boldsymbol{b}} \sum_{\alpha=1}^{N_{\mathrm{T}}} \frac{dA_{\alpha}(t,\boldsymbol{b})}{dt} \langle\psi_{\beta'}|e^{-i\boldsymbol{v}\cdot\boldsymbol{r}_{\mathrm{P}}}|\psi_{\alpha}\rangle e^{i(-v^2t/2+(\epsilon_{\beta'}-\epsilon_{\alpha})t)} \\
&+ ie^{i\boldsymbol{q}_{\beta\perp}\cdot\boldsymbol{b}} \sum_{\beta=1}^{N_{\mathrm{P}}} \frac{dB_{\beta}(t,\boldsymbol{b})}{dt} \langle\psi_{\beta'}|\psi_{\beta}\rangle e^{i(\epsilon_{\beta'}-\epsilon_{\beta})t} \\
&= e^{i\boldsymbol{p}_{\alpha\perp}\cdot\boldsymbol{b}} \sum_{\alpha=1}^{N_{\mathrm{T}}} A_{\alpha}(t,\boldsymbol{b}) \langle\psi_{\beta'}|e^{-i\boldsymbol{v}\cdot\boldsymbol{r}_{\mathrm{P}}}(H_{\mathrm{T}} + V_{\mathrm{P}} - \epsilon_{\alpha})|\psi_{\alpha}\rangle e^{i(-v^2t/2+(\epsilon_{\beta'}-\epsilon_{\alpha})t)} \\
&\quad + e^{i\boldsymbol{q}_{\beta\perp}\cdot\boldsymbol{b}} \sum_{\beta=1}^{N_{\mathrm{P}}} B_{\beta}(t,\boldsymbol{b}) \langle\psi_{\beta'}|H_{\mathrm{P}} + V_{\mathrm{T}} - \epsilon_{\beta}|\psi_{\beta}\rangle e^{i(\epsilon_{\beta'}-\epsilon_{\beta})t}.
\end{aligned} \tag{6.41}$$

Finally, taking into account Eq. (6.13) and considering the fact that

$$\boldsymbol{p}_{\alpha\perp} = \boldsymbol{q}_{\beta\perp}, \tag{6.42}$$

we arrive at the second set of coupled-channel differential equations

$$\begin{aligned}
&i \sum_{\alpha=1}^{N_{\mathrm{T}}} \frac{dA_{\alpha}(t,\boldsymbol{b})}{dt} \langle\psi_{\beta'}|e^{-i\boldsymbol{v}\cdot\boldsymbol{r}_{\mathrm{P}}}|\psi_{\alpha}\rangle e^{i(-v^2t/2+(\epsilon_{\beta'}-\epsilon_{\alpha})t)} + i\frac{dB_{\beta'}(t,\boldsymbol{b})}{dt} \\
&= \sum_{\alpha=1}^{N_{\mathrm{T}}} A_{\alpha}(t,\boldsymbol{b}) \langle\psi_{\beta'}|e^{-i\boldsymbol{v}\cdot\boldsymbol{r}_{\mathrm{P}}}(H_{\mathrm{T}} + V_{\mathrm{P}} - \epsilon_{\alpha})|\psi_{\alpha}\rangle e^{i(-v^2t/2+(\epsilon_{\beta'}-\epsilon_{\alpha})t)} \\
&\quad + \sum_{\beta=1}^{N_{\mathrm{P}}} B_{\beta}(t,\boldsymbol{b}) \langle\psi_{\beta'}|V_{\mathrm{T}}|\psi_{\beta}\rangle e^{i(\epsilon_{\beta'}-\epsilon_{\beta})t}, \\
&\beta' = 1, \ldots, N_{\mathrm{P}}.
\end{aligned} \tag{6.43}$$

Bringing Eqs. (6.31) and(6.43) together we obtain the final set of two-centre coupled-channel differential equations that describe proton scattering from hydrogen. That is

$$\begin{cases} i\dot{A}_{\alpha'} + i\sum_{\beta=1}^{N_\mathrm{P}} \dot{B}_\beta \mathcal{K}_{\alpha'\beta} = \sum_{\alpha=1}^{N_\mathrm{T}} A_\alpha \mathcal{D}_{\alpha'\alpha} + \sum_{\beta=1}^{N_\mathrm{P}} B_\beta \mathcal{Q}_{\alpha'\beta}, \\ i\sum_{\alpha=1}^{N_\mathrm{T}} \dot{A}_\alpha \tilde{\mathcal{K}}_{\beta'\alpha} + i\dot{B}_{\beta'} = \sum_{\alpha=1}^{N_\mathrm{T}} A_\alpha \tilde{\mathcal{Q}}_{\beta'\alpha} + \sum_{\beta=1}^{N_\mathrm{P}} B_\beta \tilde{\mathcal{D}}_{\beta'\beta}, \\ \alpha' = 1, \ldots, N_\mathrm{T}, \quad \beta' = 1, \ldots, N_\mathrm{P}, \end{cases} \tag{6.44}$$

where the dots over A and B denote the time derivative. In Eq. (6.44) the direct-scattering matrix elements $\mathcal{D}_{\alpha'\alpha}$ and $\tilde{\mathcal{D}}_{\beta'\beta}$ are

$$\mathcal{D}_{\alpha'\alpha} = e^{i(\epsilon_{\alpha'} - \epsilon_\alpha)t} \int d\boldsymbol{r}_\mathrm{T} \psi^*_{\alpha'}(\boldsymbol{r}_\mathrm{T}) V_\mathrm{P} \psi_\alpha(\boldsymbol{r}_\mathrm{T}) \tag{6.45}$$

and

$$\tilde{\mathcal{D}}_{\beta'\beta} = e^{i(\epsilon_{\beta'} - \epsilon_\beta)t} \int d\boldsymbol{r}_\mathrm{P} \psi^*_{\beta'}(\boldsymbol{r}_\mathrm{P}) V_\mathrm{T} \psi_\beta(\boldsymbol{r}_\mathrm{P}). \tag{6.46}$$

The overlap matrix elements $\mathcal{K}_{\alpha'\beta}$ and $\tilde{\mathcal{K}}_{\beta'\alpha}$ are

$$\mathcal{K}_{\alpha'\beta} = e^{i(-v^2 t/2 + (\epsilon_{\alpha'} - \epsilon_\beta)t)} \int d\boldsymbol{r}_\mathrm{T} \psi^*_{\alpha'}(\boldsymbol{r}_\mathrm{T}) e^{i\boldsymbol{v}\cdot\boldsymbol{r}_\mathrm{T}} \psi_\beta(\boldsymbol{r}_\mathrm{P}) \tag{6.47}$$

and

$$\tilde{\mathcal{K}}_{\beta'\alpha} = e^{i(-v^2 t/2 + (\epsilon_{\beta'} - \epsilon_\alpha)t)} \int d\boldsymbol{r}_\mathrm{P} \psi^*_{\beta'}(\boldsymbol{r}_\mathrm{P}) e^{-i\boldsymbol{v}\cdot\boldsymbol{r}_\mathrm{P}} \psi_\alpha(\boldsymbol{r}_\mathrm{T}), \tag{6.48}$$

and the electron-transfer matrix elements $\mathcal{Q}_{\alpha'\beta}$ and $\tilde{\mathcal{Q}}_{\beta'\alpha}$ are

$$\mathcal{Q}_{\alpha'\beta} = e^{i(-v^2 t/2 + (\epsilon_{\alpha'} - \epsilon_\beta)t)} \int d\boldsymbol{r}_\mathrm{T} \psi^*_{\alpha'}(\boldsymbol{r}_\mathrm{T}) e^{i\boldsymbol{v}\cdot\boldsymbol{r}_\mathrm{T}} (H_\mathrm{P} + V_\mathrm{T} - \epsilon_\beta) \psi_\beta(\boldsymbol{r}_\mathrm{P}) \tag{6.49}$$

and

$$\tilde{\mathcal{Q}}_{\beta'\alpha} = e^{i(-v^2 t/2 + (\epsilon_{\beta'} - \epsilon_\alpha)t)} \int d\boldsymbol{r}_\mathrm{P} \psi^*_{\beta'}(\boldsymbol{r}_\mathrm{P}) e^{-i\boldsymbol{v}\cdot\boldsymbol{r}_\mathrm{P}} (H_\mathrm{T} + V_\mathrm{P} - \epsilon_\alpha) \psi_\alpha(\boldsymbol{r}_\mathrm{T}). \tag{6.50}$$

The system of differential equations (6.44) in a matrix form read as

$$i \begin{pmatrix} \boldsymbol{I} & \boldsymbol{\mathcal{K}} \\ \tilde{\boldsymbol{\mathcal{K}}} & \boldsymbol{I} \end{pmatrix} \begin{pmatrix} \dot{\boldsymbol{A}} \\ \dot{\boldsymbol{B}} \end{pmatrix} = \begin{pmatrix} \boldsymbol{\mathcal{D}} & \boldsymbol{\mathcal{Q}} \\ \tilde{\boldsymbol{\mathcal{Q}}} & \tilde{\boldsymbol{\mathcal{D}}} \end{pmatrix}. \tag{6.51}$$

Equation (6.51) is solved with the initial conditions $A_{\alpha'}(t = -\infty, \boldsymbol{b}) = \delta_{\alpha' i}$ and $B_{\beta'}(t = -\infty, \boldsymbol{b}) = 0$. This implies the target is in the initial state ψ_i. For all calculations we take $i = 1$, i.e. the target is initially in the ground state. The dependence of $A_{\alpha'}$ and $B_{\beta'}$ on the orientation of $\boldsymbol{b}$ can be factored out according to Eq. (2.23). Then the probability for transition from some initial state of the target i into any final target state f or any final projectile state k is given by

$$p_f(b) = |A_f(t = +\infty, b)|^2, \tag{6.52}$$

and

$$p_k(b) = |B_k(t = +\infty, b)|^2, \tag{6.53}$$

where $A_f(t = +\infty, b)$ and $B_k(t = +\infty, b)$ are the probability amplitudes. Equation (6.51) is solved within the region $[-z_{\max}, z_{\max}]$, where parameter $z_{\max}$ is increased until convergent results are obtained.

From Eqs. (6.44)-(6.50) one can see that by using a mathematically more rigorous approach we have obtained the same coupled-channel equations as the standard approaches [38], which is based on plane-wave electron translation factors. Thus there is no need to introduce these factors by hand. The latter appear naturally due the correct treatment of the problem.

6.3 Evaluation of transition matrix elements

In this section we show how transition matrix elements are calculated for proton-hydrogen scattering. Direct-scattering matrix elements $\mathcal{D}_{\alpha'\alpha}$ and $\tilde{\mathcal{D}}_{\beta'\beta}$ are evaluated in spherical coordinates, however it is beneficial to evaluate the overlap matrix elements $\mathcal{K}_{\alpha'\beta}$ and $\tilde{\mathcal{K}}_{\beta'\alpha}$, and the electron-transfer matrix elements $\mathcal{Q}_{\alpha'\beta}$ and $\tilde{\mathcal{Q}}_{\beta'\alpha}$ in prolate spheroidal coordinates, as done in [68]. The hydrogen atom pseudostates used are those described in Section 2.3.1. Hence, they are Laguerre-

based states that are capable of modelling the whole spectrum of the target and projectile atoms.

6.3.1 Direct-scattering matrix elements

The target direct-scattering matrix elements $\mathcal{D}_{\alpha'\alpha}$ are simply those described for antiproton-hydrogen collisions in Section 2.4.1, however the sign of the projectile interaction with the target atom changes. That is

$$\begin{aligned}\mathcal{D}_{\alpha'\alpha}(\boldsymbol{R}) =& e^{i(\epsilon_{\alpha'}-\epsilon_\alpha)t}\int d\boldsymbol{r}_{\mathrm{T}}\psi^*_{\alpha'}(\boldsymbol{r}_{\mathrm{T}})\left(\frac{1}{R}-\frac{1}{|\boldsymbol{R}-\boldsymbol{r}_{\mathrm{T}}|}\right)\psi_\alpha(\boldsymbol{r}_{\mathrm{T}})\\ =& e^{i(\epsilon_{\alpha'}-\epsilon_\alpha)t}\sum_{\lambda\mu}\sqrt{\frac{4\pi(2l_\alpha+1)}{(2l_{\alpha'}+1)(2\lambda+1)}}\,C^{l_{\alpha'}0}_{l_\alpha 0\,\lambda 0}C^{l_{\alpha'}m_{\alpha'}}_{l_\alpha m_\alpha\,\lambda\mu}Y^*_{\lambda\mu}(\hat{\boldsymbol{R}})\\ &\times\int_0^\infty dr_{\mathrm{T}}r_{\mathrm{T}}^2\phi_{n_{\alpha'}l_{\alpha'}}(r_{\mathrm{T}})\phi_{n_\alpha l_\alpha}(r_{\mathrm{T}})\mathcal{U}_\lambda(R,r_{\mathrm{T}}),\end{aligned} \tag{6.54}$$

with

$$\mathcal{U}_\lambda(R,r)=\begin{cases}\dfrac{\delta_{\lambda 0}}{R}-\dfrac{R^\lambda}{r^{\lambda+1}} & \text{if}\quad R\le r,\\[2ex] \dfrac{\delta_{\lambda 0}}{R}-\dfrac{r^\lambda}{R^{\lambda+1}} & \text{if}\quad R>r.\end{cases} \tag{6.55}$$

The projectile direct-scattering matrix elements $\tilde{\mathcal{D}}_{\beta'\beta}$ are given by

$$\tilde{\mathcal{D}}_{\beta'\beta}(\boldsymbol{R}) = e^{i(\epsilon_{\beta'}-\epsilon_\beta)t}\int d\boldsymbol{r}_{\mathrm{P}}\psi^*_{\beta'}(\boldsymbol{r}_{\mathrm{P}})\left(\frac{1}{R}-\frac{1}{|\boldsymbol{R}+\boldsymbol{r}_{\mathrm{P}}|}\right)\psi_\beta(\boldsymbol{r}_{\mathrm{P}}). \tag{6.56}$$

The procedure for evaluating Eq. (6.56) is almost identical to $\mathcal{D}_{\alpha'\alpha}$, however the expansion of target interaction with the projectile atom will contain an extra factor of $(-1)^\lambda$ due to the fact that

$$Y_{\lambda\mu}(-\hat{\boldsymbol{r}}) = (-1)^\lambda Y_{\lambda\mu}(\hat{\boldsymbol{r}}). \tag{6.57}$$

Hence, the interaction potential is expanded according to

$$\frac{1}{R}-\frac{1}{|\boldsymbol{R}+\boldsymbol{r}_{\mathrm{P}}|} = 4\pi\sum_{\lambda\mu}(-1)^\lambda\frac{1}{2\lambda+1}\mathcal{U}_\lambda(R,r_{\mathrm{P}})Y^*_{\lambda\mu}(\hat{\boldsymbol{R}})Y_{\lambda\mu}(\hat{\boldsymbol{r}}_{\mathrm{P}}), \tag{6.58}$$

where $\mathcal{U}_\lambda(R, r_\mathrm{P})$ is given by Eq. (6.55). Therefore, the projectile direct-scattering matrix elements (6.56) are given by

$$\tilde{\mathcal{D}}_{\beta'\beta}(\boldsymbol{R}) = e^{i(\epsilon_{\beta'}-\epsilon_\beta)t} \sum_{\lambda\mu} (-1)^\lambda \sqrt{\frac{4\pi(2l_\beta+1)}{(2l_{\beta'}+1)(2\lambda+1)}}\, C^{l_{\beta'}0}_{l_\beta 0\,\lambda 0} C^{l_{\beta'}m_{\beta'}}_{l_\beta m_\beta\,\lambda\mu} Y^*_{\lambda\mu}(\hat{\boldsymbol{R}}) \times \int_0^\infty dr_\mathrm{P} r_\mathrm{P}^2 \phi_{n_{\beta'}l_{\beta'}}(r_\mathrm{P}) \phi_{n_\beta l_\beta}(r_\mathrm{P}) \mathcal{U}_\lambda(R, r_\mathrm{P}). \tag{6.59}$$

Furthermore, the Clebsch-Gordan coefficient $C^{l_{\beta'}0}_{l_\beta 0\,\lambda 0}$ in Eq. (6.59) implies that $l_{\beta'} + l_\beta + \lambda$ must be even. This means λ has the same parity as $l_{\beta'} + l_\beta$, that is

$$(-1)^\lambda = (-1)^{l_{\beta'}+l_\beta}. \tag{6.60}$$

Therefore, Eq. (6.59) becomes

$$\tilde{\mathcal{D}}_{\beta'\beta}(\boldsymbol{R}) = (-1)^{l_{\beta'}+l_\beta} e^{i(\epsilon_{\beta'}-\epsilon_\beta)t} \sum_{\lambda\mu} \sqrt{\frac{4\pi(2l_\beta+1)}{(2l_{\beta'}+1)(2\lambda+1)}}\, C^{l_{\beta'}0}_{l_\beta 0\,\lambda 0} C^{l_{\beta'}m_{\beta'}}_{l_\beta m_\beta\,\lambda\mu} Y^*_{\lambda\mu}(\hat{\boldsymbol{R}}) \times \int_0^\infty dr_\mathrm{P} r_\mathrm{P}^2 \phi_{n_{\beta'}l_{\beta'}}(r_\mathrm{P}) \phi_{n_\beta l_\beta}(r_\mathrm{P}) \mathcal{U}_\lambda(R, r_\mathrm{P}). \tag{6.61}$$

Comparing Eqs. (6.54) and (6.61) we see that $\tilde{\mathcal{D}}$ is related to $\mathcal{D}$ according to

$$\tilde{\mathcal{D}}_{\beta'\beta} = (-1)^{l_{\beta'}+l_\beta} \mathcal{D}_{\beta'\beta}. \tag{6.62}$$

Additionally, it can be shown that

$$\mathcal{D}_{\alpha\alpha'} = \mathcal{D}^*_{\alpha'\alpha}, \tag{6.63}$$

and

$$\tilde{\mathcal{D}}_{\beta\beta'} = \tilde{\mathcal{D}}^*_{\beta'\beta}. \tag{6.64}$$

The relations (6.62), (6.63), and (6.64) allow us to improve computational efficiency of the CCC code.

6.3.2 Overlap matrix elements

For the evaluation of the overlap matrix elements $\mathcal{K}_{\alpha'\beta}$ and $\tilde{\mathcal{K}}_{\beta'\alpha}$ it is convenient to express them in the rotating molecular frame and then calculate the integrals using prolate spheroidal coordinates with the protons being the two focal points. In the molecular frame the origin of the coordinate system is the midpoint between the two protons and the z'-axis is chosen to be along $\boldsymbol{R}$, as illustrated in Figure 6.2. Coordinates in this frame are denoted with primed variables.

To express $\mathcal{K}_{\alpha'\beta}$ and $\tilde{\mathcal{K}}_{\beta'\alpha}$ in the molecular frame we rotate the angular part of the pseudostates using the Wigner (small) d-matrix $d^l_{mq}(\Theta)$ [76] according to

$$Y_{lm}(\hat{\boldsymbol{r}}) = \sum_q Y_{lq}(\hat{\boldsymbol{r}}')d^l_{mq}(\Theta), \tag{6.65}$$

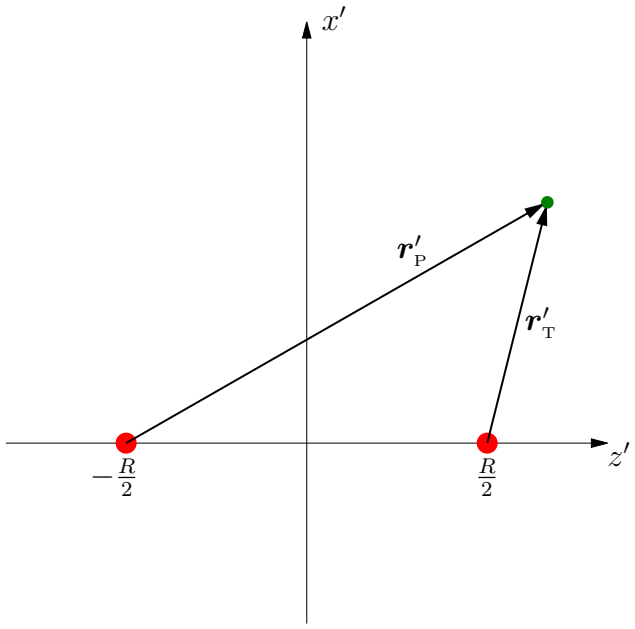

Figure 6.2: Sketch of the rotating molecular-frame coordinate system used for the calculation of overlap and electron-transfer matrix elements in proton-hydrogen collisions. The two protons lie on the z'-axis with the origin of the coordinate system at the midpoint between the protons.

where Θ is the polar angle of $\boldsymbol{R}$ and is given by

$$\Theta = \arccos\left(\frac{z}{R}\right) = \arcsin\left(\frac{b}{R}\right). \tag{6.66}$$

Therefore, in the molecular frame $\mathcal{K}_{\alpha'\beta}$ and $\tilde{\mathcal{K}}_{\beta'\alpha}$ are written as

$$\mathcal{K}_{\alpha'\beta} = e^{i(\epsilon_{\alpha'}-\epsilon_\beta)t}\sum_{q,q'} d^{l_{\alpha'}}_{m_{\alpha'}q'}(\Theta)d^{l_\beta}_{m_\beta q}(\Theta)\int d\boldsymbol{r}'\psi^*_{\alpha'}(\boldsymbol{r}'_{\mathrm{T}})e^{i\boldsymbol{v}'\cdot\boldsymbol{r}'}\psi_\beta(\boldsymbol{r}'_{\mathrm{P}}), \tag{6.67}$$

and

$$\tilde{\mathcal{K}}_{\beta'\alpha} = e^{i(\epsilon_{\beta'}-\epsilon_\alpha)t}\sum_{q,q'} d^{l_{\beta'}}_{m_{\beta'}q'}(\Theta)d^{l_\alpha}_{m_\alpha q}(\Theta)\int d\boldsymbol{r}'\psi^*_{\beta'}(\boldsymbol{r}'_{\mathrm{P}})e^{-i\boldsymbol{v}'\cdot\boldsymbol{r}'}\psi_\alpha(\boldsymbol{r}'_{\mathrm{T}}). \tag{6.68}$$

In Eqs. (6.67) and(6.68) we have changed the integrals over $\boldsymbol{r}_{\mathrm{T}}$ and $\boldsymbol{r}_{\mathrm{P}}$, seen in Eqs. (6.47) and (6.48) respectively, to integrals over $\boldsymbol{r}$ (see Figure 6.1). Additionally, the exponential terms have been expressed in terms of $\boldsymbol{r}$ using the relations

$$\boldsymbol{r}_{\mathrm{T}} = \boldsymbol{r} + \boldsymbol{R}/2, \tag{6.69}$$

and

$$\boldsymbol{r}_{\mathrm{P}} = \boldsymbol{r} - \boldsymbol{R}/2, \tag{6.70}$$

where $\boldsymbol{v}\cdot\boldsymbol{R} = vz = v^2t$.

Now moving to prolate spheroidal coordinates, the cartesian coordinates of the electron (x', y', z') are related to the prolate spheroidal coordinates (η, τ, φ) according to

$$\begin{aligned} x' &= \frac{R}{2}\sqrt{(\eta^2-1)(1-\tau^2)}\cos\varphi, \\ y' &= \frac{R}{2}\sqrt{(\eta^2-1)(1-\tau^2)}\sin\varphi, \\ z' &= \frac{R}{2}\eta\tau, \end{aligned} \tag{6.71}$$

where $1 \leq \eta < \infty$, $-1 \leq \tau \leq 1$, and $0 \leq \varphi \leq 2\pi$. Using Eq. 6.71 we can express r_{T} and r_{P}, as well as the cosine of their polar angles, according to

$$\begin{aligned} r_{\mathrm{T}} &= \sqrt{(z' - R/2)^2 + x'^2} \\ &= \frac{R}{2}(\eta - \tau), \\ r_{\mathrm{P}} &= \sqrt{(z' + R/2)^2 + x'^2} \\ &= \frac{R}{2}(\eta + \tau), \end{aligned} \tag{6.72}$$

and

$$\begin{aligned} \cos\theta'_{r_{\mathrm{T}}} &= \frac{z' - R/2}{r_{\mathrm{T}}} \\ &= \frac{\eta\tau - 1}{\eta - \tau}, \\ \cos\theta'_{r_{\mathrm{P}}} &= \frac{z' + R/2}{r_{\mathrm{P}}} \\ &= \frac{\eta\tau + 1}{\eta + \tau}. \end{aligned} \tag{6.73}$$

In obtaining Eq. (6.72) we set $\varphi = 0$ in x' since r_{T} and r_{P} are independent of φ. Furthermore, to express the dot product $\boldsymbol{v}'\cdot\boldsymbol{r}'$ in spheroidal coordinates we first write r, as well as the cosine and sine of its polar angle, as

$$\begin{aligned} r &= \sqrt{z'^2 + x'^2} \\ &= \frac{R}{2}\sqrt{\eta^2 + \tau^2 - 1}, \\ \cos\theta'_r &= \frac{z'}{r} \\ &= \frac{\eta\tau}{\sqrt{\eta^2 + \tau^2 - 1}}, \\ \sin\theta'_r &= \frac{x'}{r} \\ &= \frac{\sqrt{(\eta^2 - 1)(1 - \tau^2)}}{\sqrt{\eta^2 + \tau^2 - 1}}. \end{aligned} \tag{6.74}$$

Then considering that the polar angle of $\boldsymbol{v}'$ is given by Eq. (6.66), the dot product of $\boldsymbol{v}'$ and $\boldsymbol{r}'$ is given by

$$\begin{aligned}\boldsymbol{v}'\cdot\boldsymbol{r}' &= vr\left(\sin\theta'_v\sin\theta'_r\cos\varphi+\cos\theta'_v\cos\theta'_r\right)\\ &= \frac{vb}{2}\sqrt{(\eta^2-1)(1-\tau^2)}\cos\varphi+\frac{vz}{2}\eta\tau.\end{aligned} \tag{6.75}$$

Concentrating on $\mathcal{K}_{\alpha'\beta}$, we first express the pseudostates ψ according to Eq. (2.25) with the spherical harmonics written as

$$Y_{lm}(\theta,\phi)=\sqrt{\frac{(2l+1)}{4\pi}\frac{(l-m)!}{(l+m)!}}P_l^m(\cos\theta)e^{im\phi}, \tag{6.76}$$

where P_l^m are the associated Legendre polynomials. Then substituting Eqs. (6.72), (6.73), and (6.75) into (6.67) we obtain

$$\begin{aligned}\mathcal{K}_{\alpha'\beta} =& e^{i(\epsilon_{\alpha'}-\epsilon_\beta)t}\frac{R^3}{32\pi^2}\sqrt{(2l_{\alpha'}+1)(2l_\beta+1)}\\ &\times\sum_{q',q}d^{l_{\alpha'}}_{m_{\alpha'}q'}(\Theta)d^{l_\beta}_{m_\beta q}(\Theta)\sqrt{\frac{(l_{\alpha'}-q')!(l_\beta-q)!}{(l_{\alpha'}+q')!(l_\beta+q)!}}\\ &\times\int_1^\infty d\eta\int_{-1}^1 d\tau(\eta^2-\tau^2)e^{i\frac{vz}{2}\eta\tau}\phi_{n_{\alpha'}l_{\alpha'}}\left(\frac{R(\eta-\tau)}{2}\right)\phi_{n_\beta l_\beta}\left(\frac{R(\eta+\tau)}{2}\right)\\ &\times P^{q'}_{l_{\alpha'}}\left(\frac{\eta\tau-1}{\eta-\tau}\right)P^q_{l_\beta}\left(\frac{\eta\tau+1}{\eta+\tau}\right)\int_0^{2\pi}d\varphi e^{i\frac{vb}{2}\sqrt{(\eta^2-1)(1-\tau^2)}\cos\varphi}e^{i(m_\beta-m_{\alpha'})\varphi}.\end{aligned} \tag{6.77}$$

Note that in spheroidal coordinates the Jacobian is given by $R^3(\eta^2-\tau^2)/8$. Integration over φ can be taken if we use the relation

$$\int_0^{2\pi}e^{ix\cos\varphi}e^{im\varphi}d\varphi=2\pi i^m J_m(x), \tag{6.78}$$

where J_m is the Bessel function of the first kind. Therefore, Eq. (6.77) becomes

$$\begin{aligned}\mathcal{K}_{\alpha'\beta} =& e^{i(\epsilon_{\alpha'}-\epsilon_\beta)t}\frac{R^3}{16\pi}\sqrt{(2l_{\alpha'}+1)(2l_\beta+1)} \\ &\times \sum_{q,q'} i^{q-q'} d^{l_{\alpha'}}_{m_{\alpha'}q'}(\Theta) d^{l_\beta}_{m_\beta q}(\Theta)\sqrt{\frac{(l_{\alpha'}-q')!(l_\beta-q)!}{(l_{\alpha'}+q')!(l_\beta+q)!}} \\ &\times \int_1^\infty d\eta \int_{-1}^1 d\tau(\eta^2-\tau^2) e^{i\frac{vz}{2}\eta\tau}\phi_{n_{\alpha'}l_{\alpha'}}\left(\frac{R(\eta-\tau)}{2}\right)\phi_{n_\beta l_\beta}\left(\frac{R(\eta+\tau)}{2}\right) \\ &\times P^{q'}_{l_{\alpha'}}\left(\frac{\eta\tau-1}{\eta-\tau}\right) P^{q}_{l_\beta}\left(\frac{\eta\tau+1}{\eta+\tau}\right) J_{q-q'}\left(\frac{vb}{2}\sqrt{(\eta^2-1)(1-\tau^2)}\right). \end{aligned} \tag{6.79}$$

Following the same procedure, $\tilde{\mathcal{K}}_{\beta'\alpha}$ can be expressed as

$$\begin{aligned}\tilde{\mathcal{K}}_{\beta'\alpha} =& e^{i(\epsilon_{\beta'}-\epsilon_\alpha)t}\frac{R^3}{16\pi}\sqrt{(2l_{\beta'}+1)(2l_\alpha+1)} \\ &\times \sum_{q,q'} (-i)^{q-q'} d^{l_{\beta'}}_{m_{\beta'}q'}(\Theta) d^{l_\alpha}_{m_\alpha q}(\Theta)\sqrt{\frac{(l_{\beta'}-q')!(l_\alpha-q)!}{(l_{\beta'}+q')!(l_\alpha+q)!}} \\ &\times \int_1^\infty d\eta \int_{-1}^1 d\tau(\eta^2-\tau^2) e^{-i\frac{vz}{2}\eta\tau}\phi_{n_{\beta'}l_{\beta'}}\left(\frac{R(\eta+\tau)}{2}\right)\phi_{n_\alpha l_\alpha}\left(\frac{R(\eta-\tau)}{2}\right) \\ &\times P^{q'}_{l_{\beta'}}\left(\frac{\eta\tau+1}{\eta+\tau}\right) P^{q}_{l_\alpha}\left(\frac{\eta\tau-1}{\eta-\tau}\right) J_{q-q'}\left(\frac{vb}{2}\sqrt{(\eta^2-1)(1-\tau^2)}\right), \end{aligned} \tag{6.80}$$

where we have used the fact that

$$J_m(-x) = (-1)^m J_m(x). \tag{6.81}$$

The remaining integrals over η and τ are evaluated numerically using Gauss-Laguerre and Gauss-Legendre quadratures, respectively.

Finally, comparing Eqs. (6.80) and (6.79) we see that $\tilde{\mathcal{K}}$ is related to $\mathcal{K}$ according to

$$\tilde{\mathcal{K}}_{\beta'\alpha} = \mathcal{K}^*_{\alpha\beta'}. \tag{6.82}$$

6.3.3 Electron-transfer matrix elements

The electron-transfer matrix elements $\mathcal{Q}_{\alpha'\beta}$ and $\tilde{\mathcal{Q}}_{\beta'\alpha}$ are evaluated in the same way as the overlap matrix elements. That is, they are first expressed in the

rotating molecular frame and then calculated using prolate spheroidal coordinates. Following Section 6.3.2 we express $\mathcal{Q}_{\alpha'\beta}$ and $\tilde{\mathcal{Q}}_{\beta'\alpha}$ in the molecular frame according to

$$\mathcal{Q}_{\alpha'\beta} = e^{i(\epsilon_{\alpha'}-\epsilon_\beta)t}\int d\boldsymbol{r}\psi^*_{\alpha'}(\boldsymbol{r}_{\rm T})e^{i\boldsymbol{v}\cdot\boldsymbol{r}}(H_{\rm P}+V_{\rm T}-\epsilon_\beta)\psi_\beta(\boldsymbol{r}_{\rm P}), \tag{6.83}$$

and

$$\tilde{\mathcal{Q}}_{\beta'\alpha} = e^{i(\epsilon_{\beta'}-\epsilon_\alpha)t}\int d\boldsymbol{r}\psi^*_{\beta'}(\boldsymbol{r}_{\rm P})e^{-i\boldsymbol{v}\cdot\boldsymbol{r}}(H_{\rm T}+V_{\rm P}-\epsilon_\alpha)\psi_\alpha(\boldsymbol{r}_{\rm T}). \tag{6.84}$$

Concentrating first on $\mathcal{Q}_{\alpha'\beta}$, we write $V_{\rm T}$ as given in Eq. (6.8) and then split $\mathcal{Q}_{\alpha'\beta}$ into three terms according to

$$\mathcal{Q}_{\alpha'\beta} = \left(\frac{1}{R}-\epsilon_\beta\right)\mathcal{K}_{\alpha'\beta}+\mathcal{X}_{\alpha'\beta}+\mathcal{Z}_{\alpha'\beta}. \tag{6.85}$$

Here $\mathcal{K}_{\alpha'\beta}$ are the overlap matrix elements, which are given by Eq. (6.79), and $\mathcal{X}_{\alpha'\beta}$ and $\mathcal{Z}_{\alpha'\beta}$ are given by

$$\mathcal{X}_{\alpha'\beta} = e^{i(\epsilon_{\alpha'}-\epsilon_\beta)t}\sum_{q,q'} d^{l_{\alpha'}}_{m_{\alpha'}q'}(\Theta)d^{l_\beta}_{m_\beta q}(\Theta)\int d\boldsymbol{r}'\psi^*_{\alpha'}(\boldsymbol{r}'_{\rm T})e^{i\boldsymbol{v}'\cdot\boldsymbol{r}'}\frac{1}{r_{\rm T}}\psi_\beta(\boldsymbol{r}'_{\rm P}), \tag{6.86}$$

and

$$\mathcal{Z}_{\alpha'\beta} = e^{i(\epsilon_{\alpha'}-\epsilon_\beta)t}\sum_{q,q'} d^{l_{\alpha'}}_{m_{\alpha'}q'}(\Theta)d^{l_\beta}_{m_\beta q}(\Theta)\int d\boldsymbol{r}'\psi^*_{\alpha'}(\boldsymbol{r}'_{\rm T})e^{i\boldsymbol{v}'\cdot\boldsymbol{r}'}H_{\rm P}\psi_\beta(\boldsymbol{r}'_{\rm P}). \tag{6.87}$$

Expressing $\mathcal{X}_{\alpha'\beta}$ in spheroidal coordinates is trivial as it is simply the expression for $\mathcal{K}_{\alpha'\beta}$, Eq. (6.79), multiplied by $1/r_{\rm T}$. Writing $1/r_{\rm T}$ according to Eq. (6.72) we obtain

$$\begin{aligned}\mathcal{X}_{\alpha'\beta} =& e^{i(\epsilon_{\alpha'}-\epsilon_\beta)t}\frac{R^2}{8\pi}\sqrt{(2l_{\alpha'}+1)(2l_\beta+1)}\\
&\times\sum_{q,q'} i^{q-q'}d^{l_{\alpha'}}_{m_{\alpha'}q'}(\Theta)d^{l_\beta}_{m_\beta q}(\Theta)\sqrt{\frac{(l_{\alpha'}-q')!(l_\beta-q)!}{(l_{\alpha'}+q')!(l_\beta+q)!}}\\
&\times\int_1^\infty d\eta\int_{-1}^1 d\tau(\eta+\tau)e^{i\frac{vz}{2}\eta\tau}\phi_{n_{\alpha'}l_{\alpha'}}\left(\frac{R(\eta-\tau)}{2}\right)\phi_{n_\beta l_\beta}\left(\frac{R(\eta+\tau)}{2}\right)\\
&\times P^{q'}_{l_{\alpha'}}\left(\frac{\eta\tau-1}{\eta-\tau}\right)P^{q}_{l_\beta}\left(\frac{\eta\tau+1}{\eta+\tau}\right)J_{q-q'}\left(\frac{vb}{2}\sqrt{(\eta^2-1)(1-\tau^2)}\right).\end{aligned} \tag{6.88}$$

To express $\mathcal{Z}_{\alpha'\beta}$ in spheroidal coordinates we first write the projectile atom Hamiltonian $H_{\rm P}$ acting on the pseudostate ψ_β in the form

$$H_{\rm P}\psi_\beta(\boldsymbol{r}'_{\rm P}) = \Xi_{n_\beta l_\beta}(r'_{\rm P})Y_{l_\beta q}(\hat{\boldsymbol{r}}'_{\rm P}), \tag{6.89}$$

where the function Ξ_{nl} will be discussed below. Then the expression for $\mathcal{Z}_{\alpha'\beta}$ in spheroidal coordinates is simply $\mathcal{K}_{\alpha'\beta}$ with $\phi_{n_\beta l_\beta}$ replaced with $\Xi_{n_\beta l_\beta}$. That is

$$\begin{aligned}\mathcal{Z}_{\alpha'\beta} =& e^{i(\epsilon_{\alpha'}-\epsilon_\beta)t}\frac{R^3}{16\pi}\sqrt{(2l_{\alpha'}+1)(2l_\beta+1)} \\ &\times\sum_{q,q'} i^{q-q'} d^{l_{\alpha'}}_{m_{\alpha'}q'}(\Theta)d^{l_\beta}_{m_\beta q}(\Theta)\sqrt{\frac{(l_{\alpha'}-q')!(l_\beta-q)!}{(l_{\alpha'}+q')!(l_\beta+q)!}} \\ &\times\int_1^\infty d\eta\int_{-1}^1 d\tau(\eta^2-\tau^2)e^{i\frac{vz}{2}\eta\tau}\phi_{n_{\alpha'}l_{\alpha'}}\left(\frac{R(\eta-\tau)}{2}\right)\Xi_{n_\beta l_\beta}\left(\frac{R(\eta+\tau)}{2}\right) \\ &\times P^{q'}_{l_{\alpha'}}\left(\frac{\eta\tau-1}{\eta-\tau}\right)P^{q}_{l_\beta}\left(\frac{\eta\tau+1}{\eta+\tau}\right)J_{q-q'}\left(\frac{vb}{2}\sqrt{(\eta^2-1)(1-\tau^2)}\right).\end{aligned} \tag{6.90}$$

Similarly, $\tilde{\mathcal{Q}}_{\beta'\alpha}$ can be written as

$$\tilde{\mathcal{Q}}_{\beta'\alpha} = \left(\frac{1}{R}-\epsilon_\alpha\right)\tilde{\mathcal{K}}_{\beta'\alpha} + \tilde{\mathcal{X}}_{\beta'\alpha} + \tilde{\mathcal{Z}}_{\beta'\alpha}, \tag{6.91}$$

where $\tilde{\mathcal{K}}_{\beta'\alpha}$ is given by Eq. (6.80), and $\tilde{\mathcal{X}}_{\beta'\alpha}$ and $\tilde{\mathcal{Z}}_{\beta'\alpha}$ are given by

$$\begin{aligned}\tilde{\mathcal{X}}_{\beta'\alpha} =& e^{i(\epsilon_{\beta'}-\epsilon_\alpha)t}\sum_{q,q'} d^{l_{\beta'}}_{m_{\beta'}q'}(\Theta)d^{l_\alpha}_{m_\alpha q}(\Theta)\int d\boldsymbol{r}'\psi^*_{\beta'}(\boldsymbol{r}'_{\rm P})e^{-i\boldsymbol{v}'\cdot\boldsymbol{r}'}\frac{1}{r_{\rm P}}\psi_\alpha(\boldsymbol{r}'_{\rm T}) \\ =& e^{i(\epsilon_{\beta'}-\epsilon_\alpha)t}\frac{R^2}{8\pi}\sqrt{(2l_{\beta'}+1)(2l_\alpha+1)} \\ &\times\sum_{q,q'}(-i)^{q-q'} d^{l_{\beta'}}_{m_{\beta'}q'}(\Theta)d^{l_\alpha}_{m_\alpha q}(\Theta)\sqrt{\frac{(l_{\beta'}-q')!(l_\alpha-q)!}{(l_{\beta'}+q')!(l_\alpha+q)!}} \\ &\times\int_1^\infty d\eta\int_{-1}^1 d\tau(\eta-\tau)e^{-i\frac{vz}{2}\eta\tau}\phi_{n_{\beta'}l_{\beta'}}\left(\frac{R(\eta+\tau)}{2}\right)\phi_{n_\alpha l_\alpha}\left(\frac{R(\eta-\tau)}{2}\right) \\ &\times P^{q'}_{l_{\beta'}}\left(\frac{\eta\tau+1}{\eta+\tau}\right)P^{q}_{l_\alpha}\left(\frac{\eta\tau-1}{\eta-\tau}\right)J_{q-q'}\left(\frac{vb}{2}\sqrt{(\eta^2-1)(1-\tau^2)}\right),\end{aligned} \tag{6.92}$$

$$\begin{aligned}\tilde{\mathcal{Z}}_{\beta'\alpha} =& e^{i(\epsilon_{\beta'}-\epsilon_\alpha)t}\sum_{q,q'} d^{l_{\beta'}}_{m_{\beta'}q'}(\Theta)d^{l_\alpha}_{m_\alpha q}(\Theta)\int d\boldsymbol{r}'\psi^*_{\beta'}(\boldsymbol{r}'_{\mathrm{P}})e^{-i\boldsymbol{v}'\cdot\boldsymbol{r}'}H_{\mathrm{T}}\psi_\alpha(\boldsymbol{r}'_{\mathrm{T}})\\ =& e^{i(\epsilon_{\beta'}-\epsilon_\alpha)t}\frac{R^3}{16\pi}\sqrt{(2l_{\beta'}+1)(2l_\alpha+1)}\\ &\times\sum_{q,q'}(-i)^{q-q'}d^{l_{\beta'}}_{m_{\beta'}q'}(\Theta)d^{l_\alpha}_{m_\alpha q}(\Theta)\sqrt{\frac{(l_{\beta'}-q')!(l_\alpha-q)!}{(l_{\beta'}+q')!(l_\alpha+q)!}}\\ &\times\int_1^\infty d\eta\int_{-1}^1 d\tau(\eta^2-\tau^2)e^{-i\frac{vz}{2}\eta\tau}\phi_{n_{\beta'}l_{\beta'}}\left(\frac{R(\eta+\tau)}{2}\right)\Xi_{n_\alpha l_\alpha}\left(\frac{R(\eta-\tau)}{2}\right)\\ &\times P^{q'}_{l_{\beta'}}\left(\frac{\eta\tau+1}{\eta+\tau}\right)P^{q}_{l_\alpha}\left(\frac{\eta\tau-1}{\eta-\tau}\right)J_{q-q'}\left(\frac{vb}{2}\sqrt{(\eta^2-1)(1-\tau^2)}\right).\end{aligned}\tag{6.93}$$

Returning to Eq. (6.89), we will now define the function $\Xi_{nl}(r)$. We start by considering the action of the hydrogen atom Hamiltonian on a pseudostate, which is given by

$$\left(-\frac{1}{2}\nabla^2_{\boldsymbol{r}}-\frac{1}{r}\right)\psi_{nlm}(\boldsymbol{r}).\tag{6.94}$$

After separating the radial and angular parts of ψ according to

$$\psi_{nlm}(\boldsymbol{r})=\sum_k B^l_{nk}\mathcal{R}_{kl}(r)Y_{lm}(\hat{\boldsymbol{r}}),\tag{6.95}$$

Eq. (6.94) can be expressed as

$$\sum_k B^l_{nk}\left(-\frac{1}{2}\nabla^2_{\boldsymbol{r}}-\frac{1}{r}\right)\mathcal{R}_{kl}(r)Y_{lm}(\hat{\boldsymbol{r}}).\tag{6.96}$$

Here B^l_{nk} are the expansion coefficients described in Section 2.3.1 and $\mathcal{R}_{kl}$ are the radial functions

$$\mathcal{R}_{kl}(r)=\xi_{kl}(r)/r,\tag{6.97}$$

where ξ_{kl} are the Laguerre basis functions, defined by Eq. (2.27). The action of the Laplacian $\nabla^2_{\boldsymbol{r}}$ in Eq. (6.96) can be written as

$$\nabla^2_{\boldsymbol{r}}\mathcal{R}_{kl}(r)Y_{lm}(\hat{\boldsymbol{r}})=Y_{lm}(\hat{\boldsymbol{r}})\nabla^2_{\boldsymbol{r}}\mathcal{R}_{kl}(r)+\mathcal{R}_{kl}(r)\nabla^2_{\boldsymbol{r}}Y_{lm}(\hat{\boldsymbol{r}}),\tag{6.98}$$

where

$$\nabla^2_{\boldsymbol{r}}\mathcal{R}_{kl}(r)=\frac{1}{r}\frac{d^2}{dr^2}\xi_{kl}(r),\tag{6.99}$$

and

$$\nabla^2_{\boldsymbol{r}} Y_{lm}(\hat{\boldsymbol{r}}) = -\frac{l(l+1)}{r^2} Y_{lm}(\hat{\boldsymbol{r}}). \tag{6.100}$$

Therefore Eq. (6.96) can be expressed as

$$\sum_k B^l_{nk} \Lambda_{kl}(r) Y_{lm}(\hat{\boldsymbol{r}}), \tag{6.101}$$

where

$$\Lambda_{kl}(r) = -\frac{1}{2}\left(\frac{1}{r}\frac{d^2}{dr^2}\xi_{kl}(r) - \frac{l(l+1)}{r^2}\mathcal{R}(r)\right) - \frac{1}{r}\mathcal{R}(r). \tag{6.102}$$

Furthermore, taking the second derivative of the Laguerre functions ξ_{kl} we obtain

$$\begin{aligned}\frac{d^2}{dr^2}\xi_{kl}(r) = &\left(\frac{\lambda_l(k-1)!}{(2l+1+k)!}\right)^{1/2} \lambda^2(\lambda_l r)^l \exp(-\lambda_l r/2)\Big(\lambda r L^{2l+4}_{k-3}(\lambda_l r) \\ &+ (\lambda r - 2l - 2) L^{2l+3}_{k-2}(\lambda_l r) + \left(\frac{l(l+1)}{\lambda r} - (l+1) + \frac{\lambda r}{4}\right) L^{2l+2}_{k-1}(\lambda_l r)\Big).\end{aligned} \tag{6.103}$$

Equation (6.103) can be simplified if we use the relation

$$L^a_n(x) = \frac{a+1-x}{n} L^{a+1}_{n-1}(x) - \frac{x}{n} L^{a+2}_{n-2}(x). \tag{6.104}$$

With $n = k-1$, $a = 2l+2$, and $x = \lambda r$ we can write

$$\lambda r L^{2l+4}_{k-3}(\lambda r) = (2l+3-\lambda r) L^{2l+3}_{k-2}(\lambda r) - (k-1) L^{2l+2}_{k-1}(\lambda r), \tag{6.105}$$

and therefore Eq. (6.103) becomes

$$\begin{aligned}\frac{\partial^2}{\partial r^2}\xi_{kl}(r) = &\left(\frac{\lambda_l(k-1)!}{(2l+1+k)!}\right)^{1/2} \lambda^2(\lambda_l r)^l \exp(-\lambda_l r/2) L^{2l+3}_{k-2}(\lambda_l r) \\ &+ \left(\frac{l(l+1)}{r^2} - \frac{\lambda(k+l)}{r} + \frac{\lambda^2}{4}\right)\xi_{kl}(r).\end{aligned} \tag{6.106}$$

Substituting Eq. (6.106) into (6.102) we obtain the final expression for Λ_{kl} and hence Ξ_{nl}. That is

$$\Xi_{nl}(r) = \sum_k B^l_{nk} \Lambda_{kl}(r), \tag{6.107}$$

where

$$\begin{aligned}\Lambda_{kl}(r) = &-\frac{\lambda^2}{2r}\left(\frac{\lambda_l(k-1)!}{(2l+1+k)!}\right)^{1/2} (\lambda r)^l e^{-\lambda_l r/2} L^{2l+3}_{k-2}(\lambda_l r) \\ &- \frac{1}{2}\left(\frac{\lambda^2}{4} - \frac{\lambda(k+l)}{r} + \frac{2}{r}\right)\mathcal{R}(r).\end{aligned} \tag{6.108}$$

6.4 Stopping power

In this section we discuss the stopping cross section formula and how it should appear in the two-centre coupled-channel approach presented in this chapter. The stopping cross section is related to the stopping power by the density of target atoms in the stopping medium as shown in Eq. (2.69).

Due to the possibility of electron capture the incident proton can grab an electron and form a hydrogen atom. This newly formed hydrogen atom will continue interacting with the stopping medium, losing energy and potentially losing and gaining electrons many times. For this reason all possible charge states of the projectile must be considered when calculating the total stopping cross section for protons incident on atomic hydrogen. The total stopping cross section for the proton-hydrogen system is therefore given by

$$S(E_0) = f^{\mathrm{H}^+} S^{\mathrm{H}^+} + f^{\mathrm{H}^0} S^{\mathrm{H}^0}, \tag{6.109}$$

where S^{H^+} is the stopping cross sections for a beam consisting entirely of protons (positive charge), S^{H^0} is the stopping cross sections for a beam consisting entirely of hydrogen atoms (neutral charge), and f^{H^+} and f^{H^0} are the positive and neutral charge-state fractions of the beam, respectively. In this work we neglect the negative charge state as the probability of H^- formation is insignificant. The charge-state fractions f^{H^+} and f^{H^0} are calculated from the total electron-capture cross section σ_{c} in proton-hydrogen collisions and the total electron-loss cross section σ_{l} in hydrogen-hydrogen collisions according to

$$f^{\mathrm{H}^+} = \sigma_{\mathrm{l}}/(\sigma_{\mathrm{c}} + \sigma_{\mathrm{l}}), \tag{6.110}$$

and

$$f^{\mathrm{H}^0} = \sigma_{\mathrm{c}}/(\sigma_{\mathrm{c}} + \sigma_{\mathrm{l}}). \tag{6.111}$$

This highlights the importance of having a two-centre approach that can provide accurate electron-capture cross sections. Further details on σ_{c} and σ_{l} are given below. Additionally, in this work we consider only the electronic part of the stopping cross section as we are interested in incident energies above 10 keV where the nuclear part is insignificant. However, if one is interested in incident energies below 10 keV, calculation of the nuclear part is trivial and is given by Eq. (2.77).

The positive-charge-state electronic stopping cross section $S_{\mathrm{e}}^{\mathrm{H}^+}$ is the result of three possible energy-loss processes in the proton-hydrogen collision system. These are excitation and ionisation of the target, and capture of the target electron to a bound state of the projectile. The stopping cross section is therefore written as

$$S_{\mathrm{e}}^{\mathrm{H}^+}(E_0) = \sum_{f=1}^{\infty}(\epsilon_f - \epsilon_i)\sigma_{fi} + \int_0^{E_0+\epsilon_i}(\epsilon-\epsilon_i)\frac{d\sigma}{d\epsilon}d\epsilon + \sum_{k=1}^{\infty}(\epsilon_k - \epsilon_i + v^2/2)\sigma_{ki}, \quad (6.112)$$

where ϵ_i is the energy of the initial state of the target i, σ_{fi} is the cross section for excitation to a state f of energy ϵ_f, $d\sigma/d\epsilon$ is the single-differential cross section for ionisation of the electron with energy ϵ, and σ_{ki} is the cross section for electron capture to a state k of energy ϵ_k. Additionally, the $v^2/2$ term represents the kinetic energy of an electron travelling with the speed of the incident proton after being captured.

To accurately model electron-capture processes we use the two-centre coupled-channel approach with pseudostates centred on both the target and projectile described in Section 6.2. For the calculation of the stopping cross section we only include the continuum pseudostates on the target centre, i.e. we drop the positive-energy pseudostates from the projectile centre and keep only the negative-energy ones. This is due to ambiguities in the calculation of the single-differential cross section in a two-centre approach with continuum states on both

centres. Such issues have been explored in [73]. With this model the first two terms in Eq. (6.112) that represent excitation and ionisation become a single sum over N_{T} negative- and positive-energy target-centred pseudostates, while the third term becomes a sum over N_{P} negative-energy projectile-centred pseudostates. Thus we obtain

$$S_{\mathrm{e}}^{\mathrm{H}^+} \approx \sum_{f=1}^{N_{\mathrm{T}}} (\epsilon_f - \epsilon_i)\sigma_{fi} + \sum_{k=1}^{N_{\mathrm{P}}} (\epsilon_k - \epsilon_i + v^2/2)\sigma_{ki}. \tag{6.113}$$

Here the cross sections for direct transitions σ_{fi} and rearrangement transitions σ_{ki} are obtained by integration of the transition probabilities (6.52) and (6.53) over the impact parameter according to

$$\sigma_{fi} = 2\pi \int_0^\infty p_{fi}(b) b db, \tag{6.114}$$

and

$$\sigma_{ki} = 2\pi \int_0^\infty p_{ki}(b) b db. \tag{6.115}$$

Furthermore, the total electron-capture cross section σ_{c}, which is required for the calculation of the charge-state fractions (6.110) and (6.111), is the sum of all electron-capture cross sections (6.115), i.e.

$$\sigma_{\mathrm{c}} = \sum_{k=1}^{N_{\mathrm{P}}} \sigma_{ki}. \tag{6.116}$$

The neutral-charge-state electronic stopping cross section $S_{\mathrm{e}}^{\mathrm{H}^0}$ is the result of many possible energy-loss processes in the hydrogen-hydrogen collision system. These are excitation or ionisation of either the target or projectile, simultaneous excitation or ionisation of both the target and projectile, and excitation of either the target or projectile with ionisation of the other. Including all these terms

the stopping cross section is written as

$$\begin{aligned} S_{\mathrm{e}}^{\mathrm{H}^0} =& 2\sum_{f=1}^{\infty}(\epsilon_f-\epsilon_i)\sigma_{fi}+\sum_{f\neq i}^{\infty}\sum_{k\neq i}^{\infty}(\epsilon_f-\epsilon_i+\epsilon_k-\epsilon_i)\sigma_{fi,ki} \\ &+2\int_0^{E_0+\epsilon_i}(\epsilon-\epsilon_i)\frac{d\sigma}{d\epsilon}d\epsilon+\int_0^{E_0+\epsilon_i}\int_0^{E_0+\epsilon_i}(\epsilon-\epsilon_i+\epsilon'-\epsilon_i)\frac{d\sigma}{d\epsilon d\epsilon'}d\epsilon d\epsilon' \\ &+2\sum_{f\neq i}^{\infty}\int_0^{E_0+\epsilon_i}(\epsilon_f-\epsilon_i+\epsilon-\epsilon_i)\frac{d\sigma_{fi}}{d\epsilon}d\epsilon, \end{aligned} \tag{6.117}$$

where ϵ_i is the ground state energy of the hydrogen atom, σ_{fi} is the cross section for excitation of one hydrogen atom to a state f of energy ϵ_f while the other remains in the ground state, $\sigma_{fi,ki}$ is the cross section for excitation of both hydrogen atoms, one to a state f of energy ϵ_f and the other to a state k of energy ϵ_k, $d\sigma/d\epsilon$ is the differential cross section for ionisation of one hydrogen atom to an energy ϵ while the other remains in the ground state, $d\sigma/d\epsilon d\epsilon'$ is the differential cross section for ionisation of both hydrogen atoms, one with energy ϵ and the other with energy ϵ', and $d\sigma_{fi}/d\epsilon$ is the differential cross section for ionisation of one hydrogen atom to an energy ϵ while the other is excited to a state f of energy ϵ_f. Additionally, the factor of 2 in the first, third, and last terms of Eq. (6.117) is due to the symmetry of the system.

Furthermore, the total electron-loss cross section σ_{l}, which is required for the calculation of the charge-state fractions (6.110) and (6.111), is the sum of all cross sections corresponding to ionisation of the target atom. Therefore, it is the sum of the total single-ionisation cross section σ_{si}, total double-ionisation cross section σ_{di}, and total ionisation-with-excitation cross section σ_{ie}, that is

$$\sigma_{\mathrm{l}}=\sigma_{\mathrm{si}}+\sigma_{\mathrm{di}}+\sigma_{\mathrm{ie}}. \tag{6.118}$$

The method used for calculating the cross sections required to obtain the neutral-charge-state electronic stopping cross section and the total electron-loss cross section is described in Chapter 7.

6.5 Chapter summary

The theoretical framework of the two-centre semiclassical convergent close-coupling approach to proton-hydrogen collisions has been presented. Starting from the exact Schrödinger equation and using a more general expansion for the total scattering wave function we have derived the standard two-centre coupled-channel scattering equations without the introduction of electron translation factors. Direct-scattering matrix elements are evaluated in spherical coordinates while overlap and electron-transfer matrix elements are evaluated in prolate spheroidal coordinates. The electronic stopping cross section in a two-centre coupled-channel approach to proton-hydrogen collisions has been discussed. Not only does it require the calculation of proton-hydrogen scattering but it also requires the calculation of hydrogen-hydrogen scattering.

Chapter 7

Theory of hydrogen-hydrogen collisions for stopping power calculations

7.1 Introduction

In this chapter we will present details of our theoretical approach to modelling the collision of two hydrogen atoms for the purpose of calculating the stopping power. These calculations are necessary if one wishes to obtain the total stopping cross section for proton collisions with hydrogen, as discussed in Section 6.4. When a hydrogen atom collides with another hydrogen atom there are many different processes that can occur, with some being more difficult to calculate than others. The possible processes that can occur are:

- Excitation or ionisation of one atom while the other remains in the ground state:

$$\mathrm{H}(1s) + \mathrm{H}(1s) \rightarrow \mathrm{H}(1s) + \mathrm{H}(nlm),$$
$$\mathrm{H}(1s) + \mathrm{H}(1s) \rightarrow \mathrm{H}(1s) + \mathrm{H}^{+} + \mathrm{e}^{-}.$$

- Simultaneous excitation or ionisation of both atoms:

$$\mathrm{H}(1s) + \mathrm{H}(1s) \rightarrow \mathrm{H}(nlm) + \mathrm{H}(n'l'm'),$$
$$\mathrm{H}(1s) + \mathrm{H}(1s) \rightarrow \mathrm{H}^+ + \mathrm{e}^- + \mathrm{H}^+ + \mathrm{e}^-.$$

- Ionisation of one atom with excitation of the other:

$$\mathrm{H}(1s) + \mathrm{H}(1s) \rightarrow \mathrm{H}(nlm) + \mathrm{H}^+ + \mathrm{e}^-.$$

Below we will describe two methods that are used to solve the hydrogen-hydrogen scattering problem. The first method is the FBA, which has previously been applied to H-H collisions by Bates and Griffing [27–29]. Although the Born approximation does not take into account the coupling between channels, it has the benefit that all energy-loss processes can be calculated relatively easily. The second method is a single-centre coupled-channel approach. Unlike the Born approximation, this method does take into account the coupling between channels. However, since it is a single-centre approach, we assume that one atom remains in the ground state, meaning only energy losses associated with single-electron excitation and ionisation are included. Although we have developed a two-centre approach to the three-body proton-hydrogen collision system, presented in Chapter 6, extension of the method to the four-body problem of hydrogen-hydrogen collisions is complicated and still under development.

For collisions of hydrogen with hydrogen we use the coordinate system illustrated in Figure 7.1, where $\boldsymbol{r}$ is the position of the target electron relative to the target nucleus (T), $\boldsymbol{r}'$ is the position of the projectile electron relative to the projectile nucleus (P), and $\boldsymbol{R}$ is the position of P relative to T.

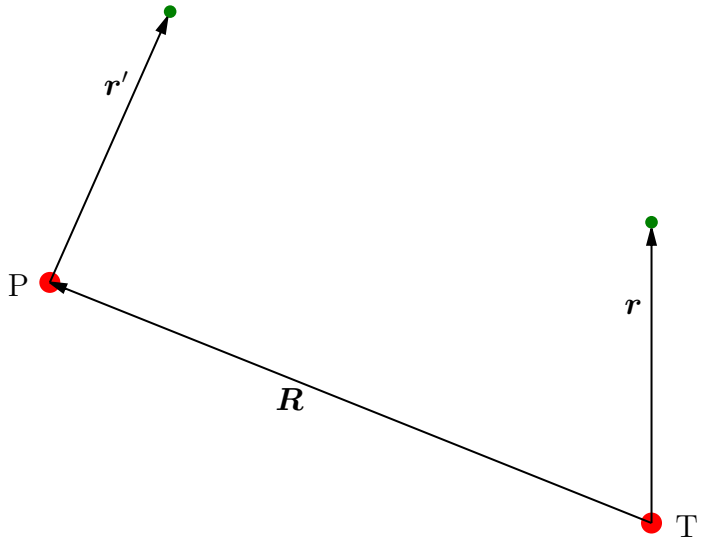

Figure 7.1: Coordinates used for a system of two hydrogen atoms. The projectile and target nuclei are denoted as P and T, respectively.

In what follows we will first present the theoretical details of the Born approximation, including derivation of analytic formulas for the transition amplitudes. Then we will outline the single-centre coupled-channel theory. Details of the stopping power in both the Born approximation and coupled-channel approach will be discussed. It should be noted that the cross sections for symmetric processes are equal.

7.2 Born approximation

7.2.1 Transition amplitude

In the Born approximation the transition amplitude for the scattering process

$$\mathrm{H}(1s) + \mathrm{H}(1s) \rightarrow \mathrm{H}(\alpha) + \mathrm{H}(\beta)$$

is given by

$$T_{\alpha,\beta} = \iiint d\boldsymbol{r}d\boldsymbol{r}'d\boldsymbol{R}\,\psi_{1s}(\boldsymbol{r})\psi^*_{\alpha}(\boldsymbol{r})\psi_{1s}(\boldsymbol{r}')\psi^*_{\beta}(\boldsymbol{r}')e^{i\boldsymbol{K}\cdot\boldsymbol{R}} \times\left(\frac{1}{R}-\frac{1}{|\boldsymbol{R}+\boldsymbol{r}'|}-\frac{1}{|\boldsymbol{R}-\boldsymbol{r}|}+\frac{1}{|\boldsymbol{R}+\boldsymbol{r}'-\boldsymbol{r}|}\right). \tag{7.1}$$

Here $\boldsymbol{K}=\boldsymbol{k}_i-\boldsymbol{k}_f$ is the momentum transfer vector, where $\boldsymbol{k}_i$ and $\boldsymbol{k}_f$ are the initial and final momenta of the projectile, respectively. In the Born approximation we will choose $\boldsymbol{K}$ to be along the z-axis. Additionally, α and β represent the final states of the target and projectile atoms, respectively. If the final state of the target is a bound state then $\alpha=n_\alpha l_\alpha m_\alpha$, where n, l, and m are the principal, orbital, and magnetic quantum numbers, and $\psi_\alpha=\psi_{n_\alpha l_\alpha m_\alpha}$ is an eigenstate wave function of the hydrogen atom. On the other-hand, if the final state of the target is a continuum state then we use the momentum of the ejected electron $\boldsymbol{k}_\mathrm{e}$ as the channel index, i.e. $\alpha=\boldsymbol{k}_\mathrm{e}$, and $\psi_\alpha=\psi^-_{\boldsymbol{k}_\mathrm{e}}$ is the two-body Coulomb wave function (see below). Similarly, if the final state of the projectile is a bound state then $\beta=n_\beta l_\beta m_\beta$, and if it is a continuum state then $\beta=\boldsymbol{k}'_\mathrm{e}$.

One benefit of the Born approximation is that Eq. (7.1) can be evaluated completely analytically. We start by writing the Coulomb potential $1/r$ as the Fourier transform of its momentum-space representation according to

$$\frac{1}{r}=(2\pi)^{-3}\int d\boldsymbol{k}\frac{4\pi}{k^2}e^{-i\boldsymbol{k}\cdot\boldsymbol{r}}. \tag{7.2}$$

Now substituting Eq. (7.2) into (7.1) we obtain

$$\begin{aligned} T_{\alpha,\beta} &= (2\pi)^{-3}\iiiint d\boldsymbol{r}d\boldsymbol{r}'d\boldsymbol{R}d\boldsymbol{k}\,\psi_{1s}(\boldsymbol{r})\psi^*_{\alpha}(\boldsymbol{r})\psi_{1s}(\boldsymbol{r}')\psi^*_{\beta}(\boldsymbol{r}')e^{i\boldsymbol{K}\cdot\boldsymbol{R}} \\ &\quad\times\frac{4\pi}{k^2}\left(e^{-i\boldsymbol{k}\cdot\boldsymbol{R}}-e^{-i\boldsymbol{k}\cdot(\boldsymbol{R}+\boldsymbol{r}')}-e^{-i\boldsymbol{k}\cdot(\boldsymbol{R}-\boldsymbol{r})}+e^{-i\boldsymbol{k}\cdot(\boldsymbol{R}+\boldsymbol{r}'-\boldsymbol{r})}\right) \\ &= (2\pi)^{-3}\iiiint d\boldsymbol{r}d\boldsymbol{r}'d\boldsymbol{R}d\boldsymbol{k}\,\psi_{1s}(\boldsymbol{r})\psi^*_{\alpha}(\boldsymbol{r})\psi_{1s}(\boldsymbol{r}')\psi^*_{\beta}(\boldsymbol{r}')e^{i(\boldsymbol{K}-\boldsymbol{k})\cdot\boldsymbol{R}} \\ &\quad\times\frac{4\pi}{k^2}\left(1-e^{i\boldsymbol{k}\cdot\boldsymbol{r}}\right)\left(1-e^{-i\boldsymbol{k}\cdot\boldsymbol{r}'}\right). \end{aligned} \tag{7.3}$$

Integration over $\boldsymbol{R}$ can be performed using the relation

$$\int d\boldsymbol{r} e^{i(\boldsymbol{k}-\boldsymbol{k}')\cdot\boldsymbol{r}} = (2\pi)^3\delta(\boldsymbol{k}-\boldsymbol{k}'), \tag{7.4}$$

where $\delta(\boldsymbol{k}-\boldsymbol{k}')$ is the Dirac-delta function. Therefore, Eq. (7.3) becomes

$$\begin{aligned} T_{\alpha,\beta} = \iiint d\boldsymbol{r}d\boldsymbol{r}'d\boldsymbol{k}\,\psi_{1s}(\boldsymbol{r})\psi^*_\alpha(\boldsymbol{r})\psi_{1s}(\boldsymbol{r}')\psi^*_\beta(\boldsymbol{r}')\delta(\boldsymbol{K}-\boldsymbol{k}) \\ \times \frac{4\pi}{k^2}\left(1-e^{i\boldsymbol{k}\cdot\boldsymbol{r}}\right)\left(1-e^{-i\boldsymbol{k}\cdot\boldsymbol{r}'}\right). \end{aligned} \tag{7.5}$$

Furthermore, considering the relation

$$\int d\boldsymbol{k} f(\boldsymbol{k})\delta(\boldsymbol{k}-\boldsymbol{k}') = f(\boldsymbol{k}'), \tag{7.6}$$

integration over $\boldsymbol{k}$ can be performed to obtain

$$T_{\alpha,\beta} = \frac{4\pi}{K^2}\int d\boldsymbol{r}\,\psi_{1s}(\boldsymbol{r})\psi^*_\alpha(\boldsymbol{r})\left(1-e^{i\boldsymbol{K}\cdot\boldsymbol{r}}\right)\int d\boldsymbol{r}'\psi_{1s}(\boldsymbol{r}')\psi^*_\beta(\boldsymbol{r}')\left(1-e^{-i\boldsymbol{K}\cdot\boldsymbol{r}'}\right). \tag{7.7}$$

Lastly, taking into account the orthogonality of the wave functions, the transition amplitude becomes

$$T_{\alpha,\beta} = \frac{4\pi}{K^2}\left(\delta_{\alpha,1s}-\mathcal{F}_\alpha(\boldsymbol{K})\right)\left(\delta_{\beta,1s}-\mathcal{F}_\beta(-\boldsymbol{K})\right), \tag{7.8}$$

where

$$\mathcal{F}_\gamma(\boldsymbol{K}) = \int d\boldsymbol{r}\psi_{1s}(\boldsymbol{r})\psi^*_\gamma(\boldsymbol{r})e^{i\boldsymbol{K}\cdot\boldsymbol{r}}. \tag{7.9}$$

The function $\mathcal{F}_\gamma$ will be referred to as the individual-atom amplitude. It can be determined analytically for both excitation and ionisation processes, as will be shown in the following sections.

7.2.2 Evaluation of excitation amplitudes

Here we discuss how the individual-atom amplitudes $\mathcal{F}$ for transitions to bound states are evaluated. As stated, we choose $\boldsymbol{K}$ to be aligned along the z-axis. This results in non-zero amplitudes only when the change in magnetic quantum

number is equal to zero. Since we are interested in the case where both atoms are initially in the ground state, only final states with $m = 0$ need to be considered. Specifically, in this work we will consider transitions to states with $n \leq 8$ and $l \leq 3$. For excitation transitions both the initial- and final-state wave functions are obtained from the general expression for the wave functions of the hydrogen atom. That is

$$\psi_{nlm}(\boldsymbol{r}) = R_{nl}(r)Y_{lm}(\hat{\boldsymbol{r}}), \tag{7.10}$$

where R_{nl} are the radial functions

$$R_{nl}(r) = \sqrt{\left(\frac{2}{n}\right)^3 \frac{(n-l-1)!}{2n(n+l)!}} e^{-r/n} \left(\frac{2r}{n}\right)^l L_{n-l-1}^{2l+1}\left(\frac{2r}{n}\right) \tag{7.11}$$

and Y_{lm} are the spherical harmonics

$$Y_{lm}(\theta,\phi) = \sqrt{\frac{(2l+1)}{4\pi}\frac{(l-m)!}{(l+m)!}} P_l^m(\cos\theta)e^{im\phi}. \tag{7.12}$$

Here L_{n-l-1}^{2l+1} and P_l^m are the the associated Laguerre polynomials and Legendre polynomials, respectively. Utilising the above expressions, Eq. (7.9) becomes

$$\mathcal{F}_{nl}(\boldsymbol{K}) = \int d\boldsymbol{r} R_{10}(r)\frac{1}{\sqrt{4\pi}} R_{nl}(r)Y_{l0}^*(\hat{\boldsymbol{r}})e^{i\boldsymbol{K}\cdot\boldsymbol{r}}. \tag{7.13}$$

The plane wave is expanded according to [76]

$$e^{i\boldsymbol{K}\cdot\boldsymbol{r}} = 4\pi \sum_{l'm'} i^{l'} j_{l'}(Kr)Y_{l'm'}^*(\hat{\boldsymbol{K}})Y_{l'm'}(\hat{\boldsymbol{r}}), \tag{7.14}$$

where j_l is the spherical Bessel function of the first kind. Substituting Eq. (7.14) into Eq. (7.13) and considering the orthogonality of spherical harmonics (2.54), integration over $\hat{\boldsymbol{r}}$ can be performed, which gives

$$\mathcal{F}_{nl}(\boldsymbol{K}) = i^l\sqrt{4\pi}\, Y_{l0}^*(\hat{\boldsymbol{K}}) \int_0^\infty r^2 dr R_{10}(r)R_{nl}(r)j_l(Kr). \tag{7.15}$$

Since $\boldsymbol{K}$ is aligned along the z-axis

$$Y_{l0}^*(\hat{\boldsymbol{K}}) = \sqrt{\frac{2l+1}{4\pi}}, \tag{7.16}$$

and therefore Eq. (7.15) becomes

$$\mathcal{F}_{nl}(K) = i^l \sqrt{2l+1} \int_0^\infty r^2 dr R_{10}(r) R_{nl}(r) j_l(Kr). \tag{7.17}$$

The remaining expression can be evaluated analytically using Mathematica for all transitions. As mentioned above, we calculated the amplitudes for transitions to states with $n \leq 8$ and $l \leq 3$. The amplitudes were previously calculated by Bates and Griffing [27] for transitions up to the $3d$ state only. As an example, the $1s$, $2s$, and $2p$ individual-atom amplitudes are given by

$$\mathcal{F}_{1s}(K) = \frac{16}{(4+K^2)^2}, \tag{7.18}$$

$$\mathcal{F}_{2s}(K) = \frac{256\sqrt{2}K^2}{(9+4K^2)^3}, \tag{7.19}$$

and

$$\mathcal{F}_{2p}(K) = i\,\frac{384\sqrt{2}K}{(9+4K^2)^3}. \tag{7.20}$$

These amplitudes can be used to calculate single- and double-excitation processes. For transitions involving ionisation of one or both of the atoms we need to evaluate $\mathcal{F}$ when the final state is the Coulomb wave function.

7.2.3 Evaluation of ionisation amplitudes

For transitions to continuum states we take the final-state wave function to be the two-body Coulomb wave function

$$\psi^-_{\boldsymbol{k}_\mathrm{e}}(\boldsymbol{r}) = (2\pi)^{-3/2} e^{-\pi\eta/2} \Gamma(1-i\eta) e^{i\boldsymbol{k}_\mathrm{e}\cdot\boldsymbol{r}} {}_1F_1(i\eta; 1; -ik_\mathrm{e} r - i\boldsymbol{k}_\mathrm{e}\cdot\boldsymbol{r}), \tag{7.21}$$

where Γ is the Gamma function, ${}_1F_1$ is the confluent hypergeometric function, and η is the Sommerfeld parameter, which for hydrogen is given by

$$\eta = -1/k_\mathrm{e}. \tag{7.22}$$

To evaluate individual-atom amplitudes we first note that $\mathcal{F}_{\boldsymbol{k}_\mathrm{e}}$ is the Fourier transform of

$$(2\pi)^{3/2}\psi_{1s}(\boldsymbol{r})\psi^{-*}_{\boldsymbol{k}_\mathrm{e}}(\boldsymbol{r}). \tag{7.23}$$

It was shown in Refs. [92, 93] that the Fourier transform of the Coulomb wave function $\tilde{\psi}^{-}_{\boldsymbol{k}_\mathrm{e}}$ is calculated according to

$$\begin{aligned}\tilde{\psi}^{-}_{\boldsymbol{k}_\mathrm{e}}(\boldsymbol{k}) =& \lim_{\nu\to 0}(2\pi)^{-3/2}\int d\boldsymbol{r}\psi^{-}_{\boldsymbol{k}_\mathrm{e}}(\boldsymbol{r})e^{i\boldsymbol{k}\cdot\boldsymbol{r}-\nu r}\\ =& -\lim_{\nu\to 0}\frac{\partial}{\partial\nu}\left(\frac{4\pi}{(2\pi)^3}e^{-\pi\eta/2}\Gamma(1-i\eta)\frac{\left[k^2-(k_\mathrm{e}-i\nu)^2\right]^{-i\eta}}{\left[(\boldsymbol{k}_\mathrm{e}-\boldsymbol{k})^2+\nu^2\right]^{1-i\eta}}\right).\end{aligned} \tag{7.24}$$

Therefore, since $\psi_{1s}=e^{-r}/\sqrt{\pi}$, we can utilise Eq. (7.24) to write $\mathcal{F}_{\boldsymbol{k}_\mathrm{e}}$ as

$$\begin{aligned}\mathcal{F}_{\boldsymbol{k}_\mathrm{e}}(\boldsymbol{K}) =& -\frac{(2\pi)^{3/2}}{\sqrt{\pi}}\frac{\partial}{\partial\nu}\left(\frac{4\pi}{(2\pi)^3}e^{-\pi\eta/2}\Gamma(1+i\eta)\frac{\left[K^2-(k_\mathrm{e}+i\nu)^2\right]^{i\eta}}{\left[(\boldsymbol{k}_\mathrm{e}+\boldsymbol{K})^2+\nu^2\right]^{1+i\eta}}\right)\Bigg|_{\nu=1}\\ =& \frac{2\sqrt{2}}{\pi}e^{-\pi\eta/2}\Gamma(1+i\eta)\frac{\left[K^2-(k_\mathrm{e}+i)^2\right]^{i\eta}}{\left[(\boldsymbol{k}_\mathrm{e}+\boldsymbol{K})^2+1\right]^{1+i\eta}}\\ &\times\left(\frac{(1+i\eta)[K^2-(k_\mathrm{e}+i)^2]+(1-i\eta)[(\boldsymbol{k}_\mathrm{e}+\boldsymbol{K})^2+1]}{[(\boldsymbol{k}_\mathrm{e}+\boldsymbol{K})^2+1][K^2-(k_\mathrm{e}+i)^2]}\right).\end{aligned} \tag{7.25}$$

With $\boldsymbol{K}$ directed along the z-axis Eq. (7.25) becomes

$$\begin{aligned}\mathcal{F}_{\boldsymbol{k}_\mathrm{e}}(\pm\boldsymbol{K}) =& \frac{4\sqrt{2}}{\pi}e^{\pi/(2k_\mathrm{e})}\Gamma(1-i/k_\mathrm{e})\frac{\left[K^2-(k_\mathrm{e}+i)^2\right]^{-i/k_\mathrm{e}}}{\left[K^2+k_\mathrm{e}^2\pm 2Kk_\mathrm{e}\cos\theta_{k_\mathrm{e}}+1\right]^{1-i/k_\mathrm{e}}}\\ &\times\frac{K\left[K\pm\cos\theta_{k_\mathrm{e}}(k_\mathrm{e}+i)\right]}{[K^2+k_\mathrm{e}^2\pm 2Kk_\mathrm{e}\cos\theta_{k_\mathrm{e}}+1][K^2-(k_\mathrm{e}+i)^2]},\end{aligned} \tag{7.26}$$

where θ_{k_e} is the polar angle of the ejected electron and Eq. (7.22) is used for η. The above amplitude can be used to calculate single- and double-ionisation processes. Also, when it is used in combination with the excitation amplitudes presented in Section 7.2.2 ionisation-with-excitation processes can be calculated.

Additionally, since we are interested in the cross section it will be useful to define the modulus squared of $\mathcal{F}_{\boldsymbol{k}_\mathrm{e}}$. Using the relationships

$$|\Gamma(1-i/k_\mathrm{e})|^2=\frac{\pi}{k_\mathrm{e}}\mathrm{csch}(\pi/k_\mathrm{e}), \tag{7.27}$$

and

$$\left|\left[K^2-(k_\mathrm{e}+i)^2\right]^{-i/k_\mathrm{e}}\right|^2 = e^{2\mathrm{Arg}[K^2-(k_\mathrm{e}+i)^2]/k_\mathrm{e}}, \tag{7.28}$$

we may write $|\mathcal{F}_{\boldsymbol{k}_\mathrm{e}}|^2$ as

$$\begin{aligned}|\mathcal{F}_{\boldsymbol{k}_\mathrm{e}}(\pm\boldsymbol{K})|^2 =& \frac{2^5}{\pi}\frac{1}{k_\mathrm{e}}\mathrm{csch}(\pi/k_\mathrm{e})e^{(\pi+2\mathrm{Arg}[K^2-(k_\mathrm{e}+i)^2])/k_\mathrm{e}} \\ &\times \frac{K^2\left[(K\pm k_\mathrm{e}\cos\theta_{k_\mathrm{e}})^2+\cos^2\theta_{k_\mathrm{e}}\right]}{[K^2+k_\mathrm{e}^2\pm 2Kk_\mathrm{e}\cos\theta_{k_\mathrm{e}}+1]^4[(K^2-k_\mathrm{e}^2+1)^2+4k_\mathrm{e}^2]},\end{aligned} \tag{7.29}$$

where $\mathrm{Arg}(z)$ is the principal argument of z. Furthermore, as we are not interested in cross sections that are differential in the angle of the electron it will prove useful to evaluate the integral of Eq. (7.29) over $\Omega_{\boldsymbol{k}_\mathrm{e}}$. First, let's define the function

$$\mathcal{I}_{k_\mathrm{e}}(\boldsymbol{K}) = \int d\Omega_{\boldsymbol{k}_\mathrm{e}}\,|\mathcal{F}_{\boldsymbol{k}_\mathrm{e}}(\boldsymbol{K})|^2\,. \tag{7.30}$$

Integration over $\cos\theta_{k_\mathrm{e}}$ is performed according to

$$\int_{-1}^{1} dz \frac{[(K\pm k_\mathrm{e}z)^2+z^2]}{[K^2+k_\mathrm{e}^2\pm 2Kk_\mathrm{e}z+1]^4} = \frac{2\left[K^2+\frac{1}{3}(k_\mathrm{e}^2+1)\right]}{[(K^2-k_\mathrm{e}^2+1)^2+4k_\mathrm{e}^2]^2}. \tag{7.31}$$

Therefore, we obtain the expression

$$\mathcal{I}_{k_\mathrm{e}}(\boldsymbol{K}) = 2^7\mathrm{csch}(\pi/k_\mathrm{e})e^{(\pi+2\mathrm{Arg}[K^2-(k_\mathrm{e}+i)^2])/k_\mathrm{e}}\frac{K^2\left[K^2+\frac{1}{3}(k_\mathrm{e}^2+1)\right]}{k_\mathrm{e}\left[(K^2-k_\mathrm{e}^2+1)^2+4k_\mathrm{e}^2\right]^3}. \tag{7.32}$$

7.2.4 Stopping power

Details of the stopping cross section for hydrogen-hydrogen collisions has been presented in Section 6.4. To obtain the stopping cross section the scattering cross sections for single excitation, double excitation, single ionisation, double ionisation, and ionisation with excitation must be calculated. Here we show how these scattering cross sections are obtained from the Born transition amplitudes described above.

Firstly, the single excitation cross section, in which one atom is excited to state $\alpha = n_\alpha l_\alpha$ while the other remains in the ground state, is calculated according to

$$\sigma_{n_\alpha l_\alpha} = \frac{\mu^2}{2\pi k_i^2} \int |T_{n_\alpha l_\alpha, 1s}|^2 K dK. \tag{7.33}$$

Secondly, the double-excitation cross section, in which one atom is excited to state $\alpha = n_\alpha l_\alpha$ and the other is excited to state $\beta = n_\beta l_\beta$, is calculated according to

$$\sigma_{n_\alpha l_\alpha, n_\beta l_\beta} = \frac{\mu^2}{2\pi k_i^2} \int |T_{n_\alpha l_\alpha, n_\beta l_\beta}|^2 K dK. \tag{7.34}$$

Thirdly, the differential cross section for single ionisation, in which one atom is ionised with energy $\epsilon = k_\mathrm{e}^2/2$ while the other remains in the ground state, is calculated as

$$\frac{d\sigma}{d\epsilon} = k_\mathrm{e} \frac{\mu^2}{2\pi k_i^2} \iint |T_{\boldsymbol{k}_\mathrm{e}, 1s}|^2 K dK d\Omega_{\boldsymbol{k}_\mathrm{e}}. \tag{7.35}$$

Fourthly, the differential cross section for ionisation with excitation, in which one atom is ionised with energy $\epsilon = k_\mathrm{e}^2/2$ and the other is excited to state $\alpha = n_\alpha l_\alpha$, is calculated as

$$\frac{d\sigma_{n_\alpha l_\alpha}}{d\epsilon} = k_\mathrm{e} \frac{\mu^2}{2\pi k_i^2} \iint |T_{n_\alpha l_\alpha, \boldsymbol{k}_\mathrm{e}}|^2 K dK d\Omega_{\boldsymbol{k}_\mathrm{e}}. \tag{7.36}$$

Lastly, the differential cross section for double ionisation, in which one atom is ionised with energy $\epsilon = k_\mathrm{e}^2/2$ and the other is ionised with energy $\epsilon' = {k'_\mathrm{e}}^2/2$, is calculated according to

$$\frac{d\sigma}{d\epsilon d\epsilon'} = k_\mathrm{e} k'_\mathrm{e} \frac{\mu^2}{2\pi k_i^2} \iiint |T_{\boldsymbol{k}_\mathrm{e}, \boldsymbol{k}'_\mathrm{e}}|^2 K dK d\Omega_{\boldsymbol{k}_\mathrm{e}} \Omega_{\boldsymbol{k}'_\mathrm{e}}. \tag{7.37}$$

In Eqs. (7.33)-(7.37), the integrals over K range from $K_\mathrm{min} = k_i - k_f$ to $K_\mathrm{max} = k_i + k_f$ and are evaluated numerically. The final momentum of the projectile k_f is obtained from the energy-conservation law and depends on the final states of the atoms. Also, the integrals over $\Omega_{\boldsymbol{k}_\mathrm{e}}$ are evaluated analytically as described in Section 7.2.3.

Furthermore, as discussed in Section 6.4 the total electron-loss cross section is required for the calculation of the charge-state fractions (6.110) and (6.111). In turn, the latter are required for the calculation of the total stopping cross section in proton-hydrogen collisions. The total electron-loss cross section is the sum of the total single-ionisation cross section $\sigma_{\rm si}$, total double-ionisation cross section $\sigma_{\rm di}$, and total ionisation-with-excitation cross section $\sigma_{\rm ie}$, as shown in Eq. (6.118). These cross sections are calculated according to

$$\sigma_{\rm si} = \int_0^{E_0+\epsilon_{1s}} \frac{d\sigma}{d\epsilon} d\epsilon, \tag{7.38}$$

$$\sigma_{\rm di} = \int_0^{E_0+\epsilon_{1s}} \int_0^{E_0+\epsilon_{1s}} \frac{d\sigma}{d\epsilon d\epsilon'} d\epsilon d\epsilon', \tag{7.39}$$

and

$$\sigma_{\rm ie} = \sum_{n_\alpha, l_\alpha} \int_0^{E_0+\epsilon_{1s}} \frac{d\sigma_{n_\alpha l_\alpha}}{d\epsilon} d\epsilon, \tag{7.40}$$

where E_0 is the incident energy of the projectile.

It is noted that calculation of scattering cross sections for all transitions has been performed and excellent agreement with the results of Bates and Griffing [27–29] is obtained when the same number of states is used.

7.3 Single-centre coupled-channel approach

In this section we present the details of the single-centre coupled-channel approach used to model the collisions of hydrogen with hydrogen. The method is referred to as the convergent close-coupling approach. However, as stated, in this model we assume the projectile atom remains fixed in the ground state throughout the collision. Again we use the semiclassical approximation, treating the target electron fully quantum-mechanically and the motion of the projectile classically. It is assumed the projectile follows the straight-line trajectory described by Eq. (2.1), that is $\boldsymbol{R}(t) = \boldsymbol{b} + \boldsymbol{v}t$.

With the projectile atom fixed in the ground state the total scattering wave function is expanded in terms of a complete set of N target pseudostates ψ_α according to

$$\Psi = \sum_{\alpha=1}^{N} A_\alpha(\boldsymbol{\sigma})\psi_\alpha(\boldsymbol{r})\psi_{1s}(\boldsymbol{r'})e^{i\boldsymbol{k}_\alpha\cdot\boldsymbol{\sigma}}, \tag{7.41}$$

where α denotes the target electronic state, $\boldsymbol{\sigma}$ is the relative position of the projectile and target centre-of-mass, $\boldsymbol{k}_\alpha$ is the projectile-target relative momentum in channel α, and A_α are the expansion coefficients that contain all information about the scattering process. The pseudostates ψ_α are those described in Section 2.3.1, that is they are Laguerre-based pseudostates that model both bound and continuum states of the target.

7.3.1 Scattering equations

The set of single-centre coupled-channel differential equations that describe the scattering system are obtained in the same way as in Section (2.2), therefore the procedure will not be repeated.

Briefly, the total scattering wave function (7.41) satisfies the Schrödinger equation

$$H\Psi = E\Psi, \tag{7.42}$$

where the total energy of the system E is given by

$$E = \frac{k_\alpha^2}{2\mu} + \epsilon_\alpha + \epsilon_{1s}, \tag{7.43}$$

and the total Hamiltonian H is written as

$$H = -\frac{1}{2\mu}\nabla_{\boldsymbol{\sigma}}^2 + H_{\mathrm{T}} + H_{\mathrm{P}} + V, \tag{7.44}$$

where μ is the reduced mass of the hydrogen-hydrogen system. Here H_{T} and H_{P} are the target and projectile Hamiltonians

$$H_{\mathrm{T}} = -\frac{1}{2}\nabla_{\boldsymbol{r}}^2 - \frac{1}{r}, \tag{7.45}$$

and

$$H_{\mathrm{P}} = -\frac{1}{2}\nabla_{\boldsymbol{r}'}^2 - \frac{1}{r'}. \tag{7.46}$$

Also, V is the projectile-target interaction, which is given by

$$V = \frac{1}{R} - \frac{1}{|\boldsymbol{R} - \boldsymbol{r}|} - \frac{1}{|\boldsymbol{R} + \boldsymbol{r}'|} + \frac{1}{|\boldsymbol{R} + \boldsymbol{r}' - \boldsymbol{r}|}. \tag{7.47}$$

Substituting the scattering wave function (7.41) into the Schrödinger equation (7.42) and following Section 2.2 we will arrive at the final set of coupled-channel differential equations

$$i\frac{dA_{\alpha'}(t,\boldsymbol{b})}{dt} = \sum_{\alpha=1}^{N} A_\alpha(t,\boldsymbol{b})\langle\psi_{\alpha'}\psi_{1s}|V(\boldsymbol{r},\boldsymbol{R})|\psi_{1s}\psi_\alpha\rangle e^{i(\epsilon_{\alpha'}-\epsilon_\alpha)t}; \quad \alpha' = 1,\ldots,N. \tag{7.48}$$

Equation (7.48) is solved with the condition that the target is initially in the ground state, i.e. $A_{\alpha'}(t = -\infty, \boldsymbol{b}) = \delta_{\alpha' 1}$. The dependence of $A_{\alpha'}$ on the orientation of $\boldsymbol{b}$ can be factored out according to Eq. (2.23). Therefore, the probability for transition of the target into some final state f is

$$p_f(b) = |A_f(t = +\infty, b)|^2, \tag{7.49}$$

where $A_f(t = +\infty, b)$ is the probability amplitude. Additionally, due to the symmetry of the system the probability of the target transitioning to a state f while the projectile remains in the ground state is equal to the probability of the projectile transitioning to a state f while the target remains in the ground state.

7.3.2 Evaluation of transition matrix elements

The transition matrix elements are defined as

$$\begin{aligned} V_{\alpha'\alpha}(\boldsymbol{R}) =& \langle \psi_{\alpha'}\psi_{1s}|V(\boldsymbol{r},\boldsymbol{r}',\boldsymbol{R})|\psi_{1s}\psi_{\alpha}\rangle \\ =& \iint d\boldsymbol{r}d\boldsymbol{r}'\psi^*_{\alpha'}(\boldsymbol{r})\psi_{\alpha}(\boldsymbol{r})\psi^*_{1s}(\boldsymbol{r}')\psi_{1s}(\boldsymbol{r}') \\ & \times\left(\frac{1}{R}-\frac{1}{|\boldsymbol{R}-\boldsymbol{r}|}-\frac{1}{|\boldsymbol{R}+\boldsymbol{r}'|}+\frac{1}{|\boldsymbol{R}+\boldsymbol{r}'-\boldsymbol{r}|}\right). \end{aligned} \tag{7.50}$$

To evaluate Eq. (7.50) we first write $V_{\alpha'\alpha}$ in the form

$$V_{\alpha'\alpha}(\boldsymbol{R}) = \int d\boldsymbol{r}\psi^*_{\alpha'}(\boldsymbol{r})\psi_{\alpha}(\boldsymbol{r})\mathcal{V}(\boldsymbol{r},\boldsymbol{R}), \tag{7.51}$$

where $\mathcal{V}$ is the effective potential

$$\mathcal{V}(\boldsymbol{r},\boldsymbol{R}) = \int d\boldsymbol{r}'\psi^*_{1s}(\boldsymbol{r}')\psi_{1s}(\boldsymbol{r}')\left(\frac{1}{R}-\frac{1}{|\boldsymbol{R}-\boldsymbol{r}|}-\frac{1}{|\boldsymbol{R}+\boldsymbol{r}'|}+\frac{1}{|\boldsymbol{R}+\boldsymbol{r}'-\boldsymbol{r}|}\right). \tag{7.52}$$

With $V_{\alpha'\alpha}$ now in the form of Eq. (7.51) we take a similar approach to that presented in Section 2.4.1 for the evaluation of antiproton-hydrogen transition matrix elements. That is, we start by expanding $\mathcal{V}$ in partial waves according to

$$\mathcal{V}(\boldsymbol{r},\boldsymbol{R}) = 4\pi\sum_{\lambda\mu}\mathcal{U}_{\lambda}(r,R)Y^*_{\lambda\mu}(\hat{\boldsymbol{R}})Y_{\lambda\mu}(\hat{\boldsymbol{r}}), \tag{7.53}$$

where $\mathcal{U}_{\lambda}$ is a radial function that will be defined below. Inserting our expression for the hydrogen pseudostates (2.25) and the expansion (7.53) into Eq. (7.51) we obtain

$$\begin{aligned} V_{\alpha'\alpha}(\boldsymbol{R}) =& \sum_{\lambda\mu}Y^*_{\lambda\mu}(\hat{\boldsymbol{R}})\int_0^{\infty}drr^2\phi_{n_{\alpha'}l_{\alpha'}}(r)\phi_{n_{\alpha}l_{\alpha}}(r)\mathcal{U}_{\lambda}(r,R) \\ & \times\int d\hat{\boldsymbol{r}}Y^*_{l_{\alpha'}m_{\alpha'}}(\hat{\boldsymbol{r}})Y_{l_{\alpha}m_{\alpha}}(\hat{\boldsymbol{r}})Y_{\lambda\mu}(\hat{\boldsymbol{r}}). \end{aligned} \tag{7.54}$$

The angular integration is performed using Eq. (2.49), and therefore Eq. (7.54) reduces to

$$V_{\alpha'\alpha}(\boldsymbol{R}) = \sqrt{\frac{4\pi(2l_\alpha+1)}{(2l_{\alpha'}+1)}}\sum_{\lambda\mu}\sqrt{(2\lambda+1)}C^{l_{\alpha'}0}_{l_\alpha 0\lambda 0}C^{l_{\alpha'}m_{\alpha'}}_{l_\alpha m_\alpha\lambda\mu}Y^*_{\lambda\mu}(\widehat{\boldsymbol{R}}) \times \int_0^\infty dr r^2\phi_{n_{\alpha'}l_{\alpha'}}(r)\phi_{n_\alpha l_\alpha}(r)\mathcal{U}_\lambda(r,R). \tag{7.55}$$

The remaining radial integral is evaluated using Simpson's rule and λ and μ are limited by the Clebsch-Gordan coefficients.

We now turn our attention to the radial function $\mathcal{U}_\lambda$. To find an expression for $\mathcal{U}_\lambda$ we must first evaluate the effective potential $\mathcal{V}$. Considering the orthonormality of the hydrogen wave functions, one can write Eq. (7.52) as

$$\mathcal{V}(\boldsymbol{r},\boldsymbol{R}) = \frac{1}{R} - \frac{1}{|\boldsymbol{R}-\boldsymbol{r}|} - \int d\boldsymbol{r}'\frac{\psi^*_{1s}(\boldsymbol{r}')\psi_{1s}(\boldsymbol{r}')}{|\boldsymbol{R}+\boldsymbol{r}'|} + \int d\boldsymbol{r}'\frac{\psi^*_{1s}(\boldsymbol{r}')\psi_{1s}(\boldsymbol{r}')}{|\boldsymbol{R}-\boldsymbol{r}+\boldsymbol{r}'|}. \tag{7.56}$$

We now consider the general integral

$$I = \int d\boldsymbol{r}'\frac{\psi^*_{1s}(\boldsymbol{r}')\psi_{1s}(\boldsymbol{r}')}{|\boldsymbol{X}+\boldsymbol{r}'|}, \tag{7.57}$$

where $\boldsymbol{X}$ can be either $\boldsymbol{R}$ or $\boldsymbol{R}-\boldsymbol{r}$. Inserting the $1s$ hydrogen wave function $\psi_{1s} = e^{-2r}/\sqrt{\pi}$ into Eq. (7.57) and expanding $1/|\boldsymbol{X}+\boldsymbol{r}'|$ in a similar manner to Eq. (2.46), we obtain

$$I = 4\sum_{lm}\frac{(-1)^l}{2l+1}Y^*_{lm}(\hat{\boldsymbol{X}})\int d\boldsymbol{r}' e^{-2r'}U_l(X,r')Y_{lm}(\hat{\boldsymbol{r}}'), \tag{7.58}$$

where

$$U_l(X,r') = \begin{cases} \dfrac{X^l}{r'^{l+1}} & \text{if } X \le r', \\ \dfrac{r'^l}{X^{l+1}} & \text{if } X > r'. \end{cases} \tag{7.59}$$

Angular integration is performed using the relation

$$\int d\hat{\boldsymbol{r}}Y_{lm}(\hat{\boldsymbol{r}}) = \sqrt{4\pi}\delta_{l0}\delta_{m0}. \tag{7.60}$$

As a result Eq. (7.58) becomes

$$I = 4\int_0^\infty dr' r'^2 e^{-2r'} U_l(X, r'). \tag{7.61}$$

Inserting Eq. (7.59) into (7.61) and splitting the integrand, the final expression for I is

$$\begin{aligned} I &= 4\left(\frac{1}{X}\int_0^X dr' r'^2 e^{-2r'} + \int_X^\infty dr' r'^2 e^{-2r'}\frac{1}{r'}\right) \\ &= \frac{1}{X} - \frac{e^{-2X}}{X}(1+X). \end{aligned} \tag{7.62}$$

Finally, utilising Eq. (7.62) with $X = R$ and $X = |\boldsymbol{R} - \boldsymbol{r}|$, we obtain

$$\mathcal{V}(\boldsymbol{r}, \boldsymbol{R}) = \frac{e^{-2R}}{R}(1+R) - \frac{e^{-2|\boldsymbol{R}-\boldsymbol{r}|}}{|\boldsymbol{R}-\boldsymbol{r}|}(1+|\boldsymbol{R}-\boldsymbol{r}|). \tag{7.63}$$

Having evaluated $\mathcal{V}$ we can now move on to determining $\mathcal{U}_\lambda$. For this we start from the expansion [76]

$$\frac{e^{ikr}}{r} = 4\pi ik \sum_{lm} j_l(kr_1) h_l^{(1)}(kr_2) Y_{lm}^*(\hat{\boldsymbol{r}}_1) Y_{lm}(\hat{\boldsymbol{r}}_2), \tag{7.64}$$

where $r = |\boldsymbol{r}_1 - \boldsymbol{r}_2|$ and $r_1 < r_2$. Also, j_l and $h_l^{(1)}$ and the spherical Bessel and spherical Hankel functions of the first kind, respectively. Taking $k = 2i$ in Eq. (7.64) we obtain

$$\frac{e^{-2r}}{r} = -8\pi \sum_{lm} j_l(2ir_1) h_l^{(1)}(2ir_2) Y_{lm}^*(\hat{\boldsymbol{r}}_1) Y_{lm}(\hat{\boldsymbol{r}}_2). \tag{7.65}$$

Additionally, we can write

$$e^{-2r} = -i\frac{\partial}{\partial k}\frac{e^{ikr}}{r}\bigg|_{k=2i}, \tag{7.66}$$

where the derivative of Eq. (7.64) with respect to k is given by

$$\begin{aligned} \frac{\partial}{\partial k}\frac{e^{ikr}}{r} = 4\pi i \sum_{lm} \Big[& j_l(kr_1)\big((2l+1)h_l^{(1)}(kr_2) - kr_2 h_{l+1}^{(1)}(kr_2)\big) \\ & - kr_1 j_{l+1}(kr_1) h_l^{(1)}(kr_2)\Big] Y_{lm}^*(\hat{\boldsymbol{r}}_1) Y_{lm}(\hat{\boldsymbol{r}}_2). \end{aligned} \tag{7.67}$$

Therefore, we obtain the expansion

$$e^{-2r} = 4\pi \sum_{lm} \Big[j_l(2ir_1)\big((2l+1)h_l^{(1)}(2ir_2) - 2ir_2 h_{l+1}^{(1)}(2ir_2)\big) - 2ir_1 j_{l+1}(2ir_1)h_l^{(1)}(2ir_2)\Big] Y_{lm}^*(\hat{\boldsymbol{r}}_1)Y_{lm}(\hat{\boldsymbol{r}}_2). \tag{7.68}$$

To avoid the need for complex arithmetic we write the spherical Bessel and spherical Hankel functions, j_l and $h_l^{(1)}$, in terms of the modified spherical Bessel functions of the first and second kind, i_l and k_l, respectively. That is,

$$j_l(ix) = i^l i_l(x), \tag{7.69}$$

and

$$h_l^{(1)}(ix) = -i^{-l}k_l(x). \tag{7.70}$$

Therefore, Eqs. (7.65) and (7.68) become

$$\frac{e^{-2r}}{r} = 8\pi \sum_{lm} i_l(2r_1)k_l(2r_2)Y_{lm}^*(\hat{\boldsymbol{r}}_1)Y_{lm}(\hat{\boldsymbol{r}}_2), \tag{7.71}$$

and

$$e^{-2r} = 4\pi \sum_{lm} \Big[i_l(2r_1)\big(2r_2 k_{l+1}(2r_2) - (2l+1)k_l(2r_2)\big) - 2r_1 i_{l+1}(2r_1)k_l(2r_2)\Big] Y_{lm}^*(\hat{\boldsymbol{r}}_1)Y_{lm}(\hat{\boldsymbol{r}}_2). \tag{7.72}$$

Lastly, summing Eqs. (7.71) and (7.72), we obtain the expansion

$$\frac{e^{-2r}}{r}(1+r) = 4\pi \sum_{lm} \Big[i_l(2r_1)\big(2r_2 k_{l+1}(2r_2) - (2l-1)k_l(2r_2)\big) - 2r_1 i_{l+1}(2r_1)k_l(2r_2)\Big] Y_{lm}^*(\hat{\boldsymbol{r}}_1)Y_{lm}(\hat{\boldsymbol{r}}_2). \tag{7.73}$$

We state again that $r = |\boldsymbol{r}_1 - \boldsymbol{r}_2|$ and $r_1 < r_2$. Finally, comparing Eq. (7.73) to

(7.53) and (7.63) we see that $\mathcal{U}_\lambda$ can be written according to

$$\mathcal{U}_\lambda(r,R) = \delta_{\lambda 0}\frac{e^{-2R}}{R}(1+R) - \begin{cases} \big[i_\lambda(2R)\big(2rk_{\lambda+1}(2r) - (2\lambda-1)k_\lambda(2r)\big) \\ \quad -2Ri_{\lambda+1}(2R)k_\lambda(2r)\big] & \text{if } R \leq r, \\ \big[i_\lambda(2r)\big(2Rk_{\lambda+1}(2R) - (2\lambda-1)k_\lambda(2R)\big) \\ \quad -2ri_{\lambda+1}(2r)k_\lambda(2R)\big] & \text{if } R > r. \end{cases} \tag{7.74}$$

7.3.3 Stopping power

Details of the stopping cross section for hydrogen-hydrogen collisions has been presented in Section 6.4. Here we show how it is calculated in the single-centre coupled-channel approach described above.

In our single-centre model one atom is fixed in the ground state meaning only energy losses due one-electron processes can be accounted for. The first and third terms of Eq. (6.117) represent the stopping cross section associated with single excitation and ionisation, respectively. Therefore, the single-centre stopping cross section for hydrogen-hydrogen collisions $\bar{S}_{\rm e}^{\rm H^0}$ is written as

$$\bar{S}_{\rm e}^{\rm H^0} = 2\sum_{f=1}^{\infty}(\epsilon_f - \epsilon_i)\sigma_{fi} + 2\int_0^{E_0+\epsilon_i}(\epsilon-\epsilon_i)\frac{d\sigma}{d\epsilon}d\epsilon. \tag{7.75}$$

As discussed in the previous chapters, since we discretise the continuum the sum and integral in Eq. (7.75) become a single sum over N negative- and positive-energy pseudostates. Therefore, the stopping cross section in a single-centre coupled-channel approach is

$$\bar{S}_{\rm e}^{\rm H^0} = 2\sum_{f=1}^{N}(\epsilon_f - \epsilon_i)\sigma_{fi}. \tag{7.76}$$

Here the transition cross section σ_{fi} is obtained by integration of the transition

probability (7.49) over the impact parameter, that is

$$\sigma_{fi} = 2\pi \int_0^\infty p_{fi}(b) b db. \tag{7.77}$$

Furthermore, the total single-ionisation cross section $\sigma_{\rm si}$, required for the calculation of the total electron-loss cross section (6.118) and the charge-state fractions (6.110) and (6.111), is calculated according to

$$\sigma_{\rm si} = \sum_{f,\epsilon_f>0}^{N} \sigma_{fi}. \tag{7.78}$$

When using the single-centre coupled-channel approach it can be useful to include two-electron processes that are calculated using the Born approximation.

7.4 Chapter summary

Details of the Born approximation and the single-centre semiclassical convergent close-coupling approach to modelling hydrogen-hydrogen collisions have been presented. In the Born approximation analytic expressions for excitation and ionisation transition amplitudes have been derived. This approach allows one to calculate both one- and two-electron processes. In the single-centre coupled-channel method we assume one atom to be fixed in the ground state. Therefore only one-electron processes can be accounted for. Details of calculating the stopping cross section in both approaches have also been presented.

In the following chapter results of stopping cross section calculations for proton and atomic hydrogen collisions with hydrogen atoms will be presented. The hydrogen-hydrogen stopping cross section will be combined with the proton-hydrogen one to yield the total stopping cross section for a beam of protons passing through hydrogen.

Chapter 8

Proton stopping in hydrogen

8.1 Introduction

In this chapter calculations of the stopping cross section for proton and hydrogen collisions with atomic hydrogen will be presented. The two stopping cross sections will be combined to yield the total stopping cross section for protons travelling through hydrogen. Results of calculations will be compared to existing theoretical and experimental data.

There is currently no experimental data for proton stopping in atomic hydrogen. For this reason theoretical calculations are usually compared to experimental measurements involving a molecular hydrogen target. Measurements of the stopping cross section for protons passing through a H_2 gas, which cover the range from 10 keV to 2 MeV, have been performed by Reynolds *et al.* [94], Reiter *et al.* [95], and Golser and Semrad [96].

The first theoretical study of proton stopping in atomic hydrogen was performed by Dalgarno and Griffing [24]. They applied the FBA to calculate the proton-hydrogen and hydrogen-hydrogen stopping cross sections. Rearrangement processes in the case of proton-hydrogen scattering and two-electron pro-

cesses in the case of hydrogen-hydrogen scattering were included. The results were combined by weighting each contribution by its charge-state fraction to obtain the total stopping cross section. Agreement with the experimental data for proton-H_2 was obtained above 120 keV, however their calculations underestimated the data at low energies. This discrepancy was attributed to the failure of the Bragg additivity rule in the proton-hydrogen fraction.

Schiwietz [39] performed single-centre coupled-channel AO calculations for the proton fraction of the beam. They used the FBA calculations for the hydrogen fraction (including only single-excitation and single-ionisation processes) and the experimental H_2 charge-state fractions of Allison [97] to obtain the total stopping cross section. Agreement with the calculations of Dalgarno and Griffing [24] above 125 keV was obtained. Also, agreement with experiment within 5% was obtained at low and high energies, however results underestimated the experiment by 10-15% at intermediate energies. It was suggested that the deterioration was due to an inaccurate ionisation cross section in hydrogen-hydrogen collisions as electron-electron correlations were neglected.

Schiwietz and Grande [40] further developed the aforementioned work of Schiwietz [39] by replacing the single-centre AO results below 30 keV with two-centre (AO+) ones, which included electron capture. The result was a significant reduction in the proton-hydrogen stopping cross section in this region. Additionally, a screened potential was used to perform AO calculations for hydrogen-hydrogen collisions, including only single excitation and single ionisation. Continuing to use the experimental H_2 charge-state fractions, these authors achieved 5% agreement with the H_2 stopping-power experiments over the whole energy range from 10 keV to 500 keV.

Fainstein *et al.* [32] used the CDW-EIS model to calculate the stopping cross

section for protons impinging on atomic hydrogen. When combined with the FBA hydrogen-hydrogen results of Dalgarno and Griffing [24] good agreement with experiment was obtained above 70 keV. Disagreement with the experiment below 70 keV was attributed to the usage of the FBA in the hydrogen-hydrogen channel. Agreement with all previous calculations was obtained above 125 keV, however, different results were obtained below this.

In this chapter we present stopping cross section calculations for proton and hydrogen collision with atomic hydrogen. The stopping cross sections from both the positive and neutral charge-states of the projectile will be combined to yield the total stopping cross section for protons passing through hydrogen. For the proton fraction we use the two-centre time-dependent CCC method, described in Chapter 6. These calculations improve upon the work of Schiwietz and Grande [40] by employing a two-centre approach over the whole energy region considered as well as by including more target and projectile states in the expansion of the scattering wave function. For the hydrogen fraction we use two approaches, the first is the FBA and the second is the single-centre time-dependent CCC method. Both are described in Chapter 7. The Born approximation allows one to include the one-electron processes of single excitation and ionisation and the two-electron processes of double excitation, double ionisation, and ionisation with excitation. These calculations improve upon those of Dalgarno and Griffing [24] by including excitations up to the $n = 8$ shell. In the single-centre CCC approach we are only able to model one-electron processes, however coupling between channels is included.

8.2 Proton-hydrogen stopping cross section

In this section we present calculations of the stopping cross section for proton-hydrogen collisions. Convergence of the stopping cross section for increasing basis size is investigated. Then we present our final calculations compared to existing theories. The Barkas effect is also investigated.

8.2.1 Convergence studies

As previously discussed in Chapter 3, it is important to demonstrate convergence in the stopping cross section by increasing the size of the underlying basis used in the expansion of the scattering wave function. Here we investigate convergence of the electronic stopping cross section in terms of the basis parameters $l_{\max}$, the maximum value of orbital angular momentum included in the expansion, and $n_{\max}$, the maximum number of basis functions for $l = 0$, at incident energies of 10 keV, 100 keV, and 1000 keV. The number of basis functions for each l is $N_l = n_{\max} - l$. For proton-hydrogen scattering we use a two-centre expansion, this means the scattering wave function is expanded in terms of both target and projectile states. For the target we use all states generated with the parameters $l_{\max}$ and $n_{\max}$, however, for the projectile we only use bound states. That is, we only use states with a negative energy that are generated with the basis parameters $l_{\max}$ and $n_{\max}$. This way the continuum of the target and both the target and projectile discrete states are accurately represented, while the ambiguity associated with calculating the single-differential cross section when continuum states are placed on both centres is eliminated. Also, in all calculations the basis function exponential fall-off parameter λ_l is chosen to be 2 for all l, which is optimal for the ground state.

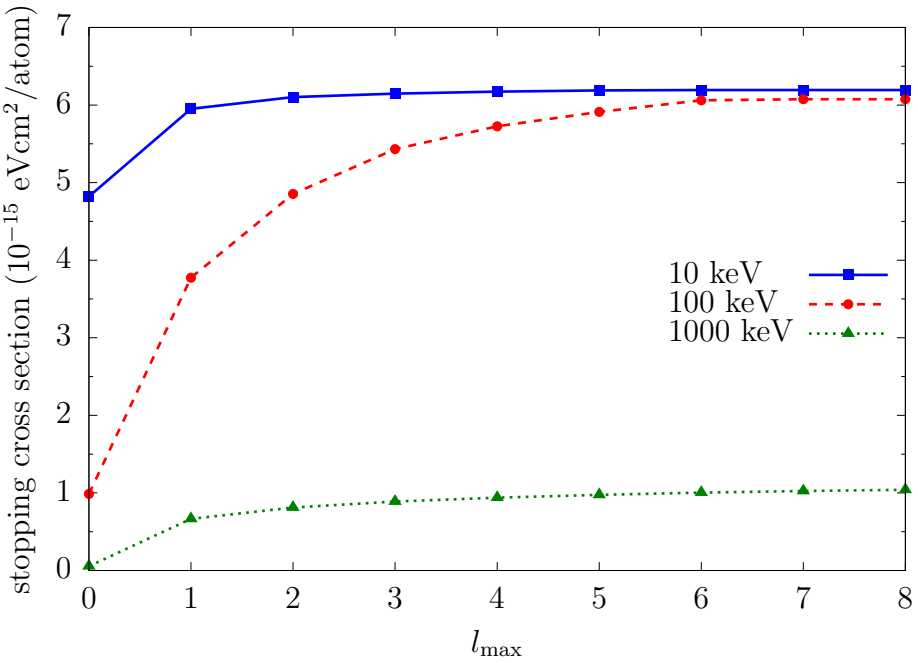

Figure 8.1: Convergence of the electronic stopping cross section for protons incident on hydrogen with increasing $l_{\max}$ for $n_{\max} = 30$ at incident energies of 10 keV, 100 keV, and 1000 keV.

Convergence is studied in the same way described in Section 3.2.1. First, we fix the basis parameter $n_{\max}$ at some large value and systematically increase $l_{\max}$. Figure 8.1 shows the convergence of the electronic stopping cross section for proton-hydrogen collisions with increasing $l_{\max}$, while $n_{\max}$ is fixed at 30. From this figure we see that convergence with increasing $l_{\max}$ is faster at lower incident energies. At 10 keV, 100 keV, and 1000 keV incident energies the stopping cross section has converged to within 0.08%, 0.23%, and 1.4%, respectively.

Now we investigate convergence of the electronic stopping cross section with increasing $n_{\max}$. Figure 8.2 shows the convergence of the electronic stopping cross section with increasing $n_{\max}$, while $l_{\max}$ is fixed at 8. From the figure we see that at 10 keV convergence is achieved with an $n_{\max}$ as low as 10, whereas at 1000 keV the stopping cross section gradually increases up until $n_{\max} = 30$. Based on the difference between the last two data points, the stopping cross

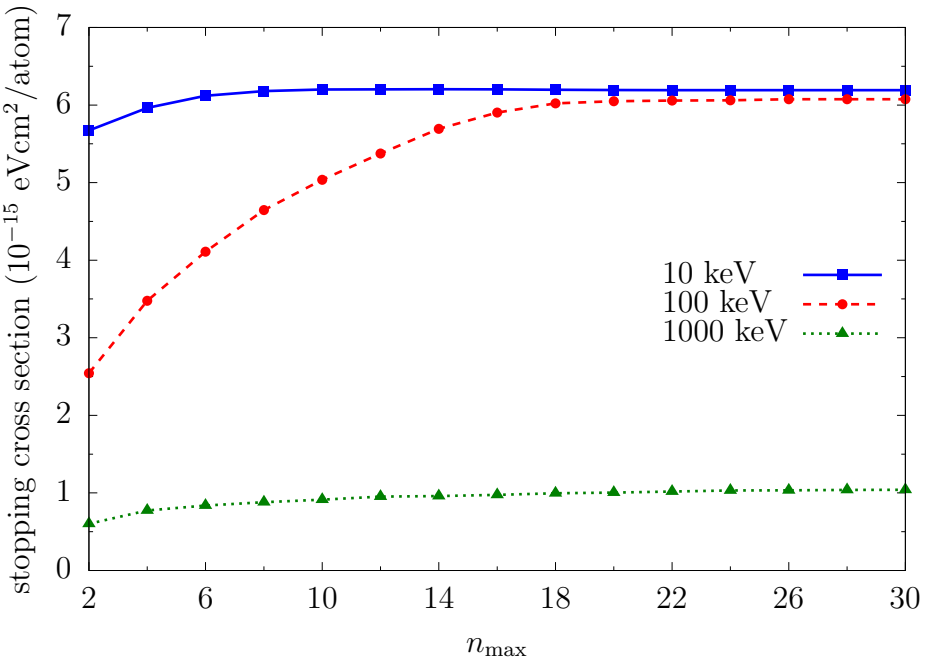

Figure 8.2: Convergence of the electronic stopping cross section for protons incident on hydrogen with increasing $n_{\max}$ for $l_{\max} = 8$ at incident energies of 10 keV, 100 keV, and 1000 keV.

section has converged to within 0.05%, 0.23%, and 0.19% at 10 keV, 100 keV, and 1000 keV incident energies, respectively. From Figures 8.1 and 8.2 it can be concluded that a basis with $n_{\max} = 30$ and $l_{\max} = 8$ produces sufficiently convergent results for the electronic stopping cross section.

8.2.2 Results of calculations

The convergent basis parameters discussed above result in a total of 1896 target states and 159 projectile states to be used in the solution of the coupled-channel differential equations (6.44).

In Figure 8.3 we present our result for the proton-hydrogen electronic stopping cross section together with the calculations of Dalgarno and Griffing [24], Schiwietz [39], Schiwietz and Grande [40], and Fainstein *et al.* [32]. We use

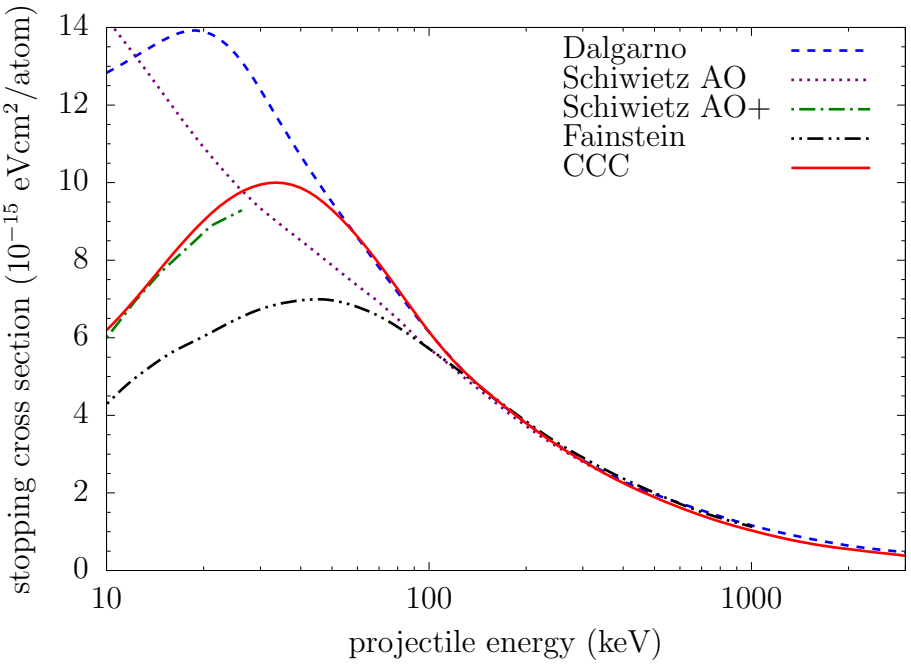

Figure 8.3: Electronic stopping cross section for protons incident on hydrogen. The two-centre CCC calculations are compared with the results of Dalgarno and Griffing [24], Schiwietz [39] (AO), Schiwietz and Grande [40] (AO+), and Fainstein *et al.* [32].

the two-centre CCC approach, meaning energy losses due to electron-capture processes are explicitly included, as well as energy losses due to excitation and ionisation. The CCC results are in good agreement with the FBA calculation of Dalgarno and Griffing [24] above 50 keV. They are also in good agreement with the AO calculations of Schiwietz [39] and the CDW-EIS calculations of Fainstein *et al.* [32] above 130 keV. Furthermore, in the lower energy region we obtain reasonable agreement with the two-centre AO+ calculations of Schiwietz and Grande [40]. The fact that the AO+ results are slightly lower than the CCC ones above 15 keV is likely to be due to the inclusion of more target and projectile states in our calculations compared to those of Schiwietz and Grande [40]. In addition, comparing the single-centre AO calculations of Schiwietz [39] to the two-centre CCC and AO+ calculations we see that the explicit

inclusion of electron-capture channels results in a significant difference in the proton-hydrogen electronic stopping cross section below 100 keV.

Individual contributions to the stopping cross section are presented in Figure 8.4. This figure demonstrates that below 35 keV energy loss due to momentum transfer to the electron during electron capture is the dominant contribution to the stopping cross section, whereas above 35 keV the dominant contribution is due to ionisation. Additionally, it shows that energy losses associated with excitation of the target make a substantial contribution over the whole energy region, while electron-capture processes make a significant contribution only below 60 keV.

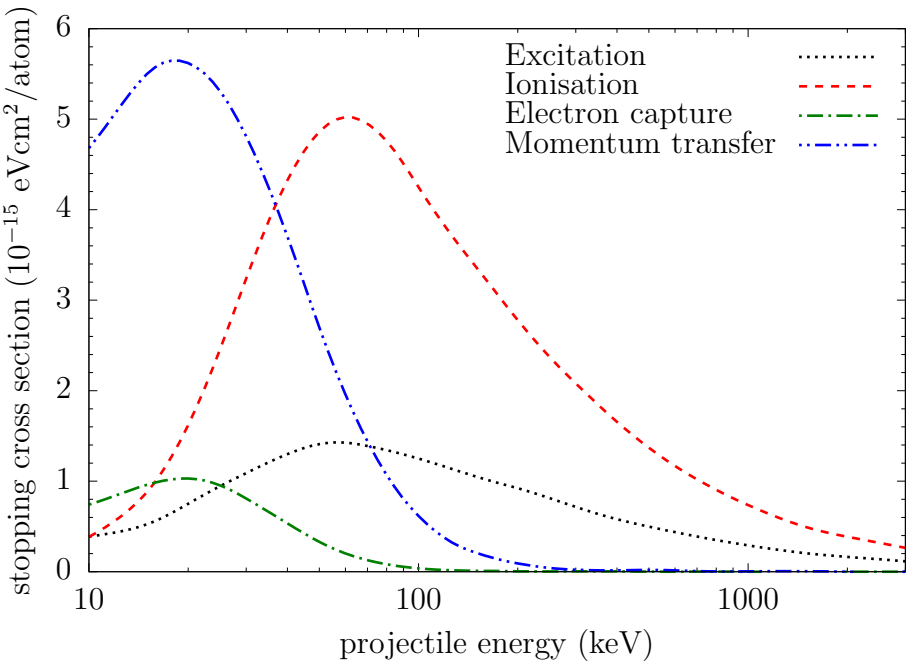

Figure 8.4: Individual contributions to the proton-hydrogen electronic stopping cross section. The curves labelled "Excitation" and "Ionisation" are the stopping cross sections associated with excitation and ionisation of the target atom, respectively. The curves labelled "Electron capture" and "Momentum transfer" are the stopping cross sections associated with electron capture and the momentum transferred to the electron during electron capture, respectively.

8.2.3 Barkas effect

Before moving on to results for the hydrogen-hydrogen stopping cross section, we shall take a brief detour to consider the Barkas effect in relation to our calculations for the antiproton-hydrogen and proton-hydrogen stopping cross sections.

As discussed in Section 1.2, the first formula for calculating the stopping cross section, which was obtained by Bethe [19], is proportional to the square of the projectile charge. Therefore, it predicts no difference in the stopping cross section of a charged particle penetrating matter when compared to its antiparticle. However, in 1963 Barkas *et al.* [22] experimentally observed a difference in the ranges of positive and negative Σ hyperons and predicted that slow negative hyperons lose energy at a lower rate than do positive particles of the same velocity. This difference in the stopping cross section between positively- and negatively-charged particles has become know as the Barkas effect and has since been the subject of many further studies.

Based on our calculations of the antiproton-hydrogen and proton-hydrogen stopping cross sections presented in Sections 3.2.2 and 8.2.2, respectively, we can draw some conclusions in relation to the Barkas effect. Comparison between the two stopping cross sections is shown in Figure 8.5a. It can be seen that the two stopping cross section are approximately the same above 1 MeV incident energy, however, below this the proton stopping cross section is larger. This is consistent with the the statement of Barkas *et al.* [22] that the negatively-charged particle loses energy at a lower rate. In addition, the figure shows that the peak of the stopping cross section for protons is more pronounced. It should be emphasised that the proton-hydrogen stopping cross section shown in Figure 8.5a is that of the positive charge state only. Furthermore, in Figure 8.5b the relative stopping

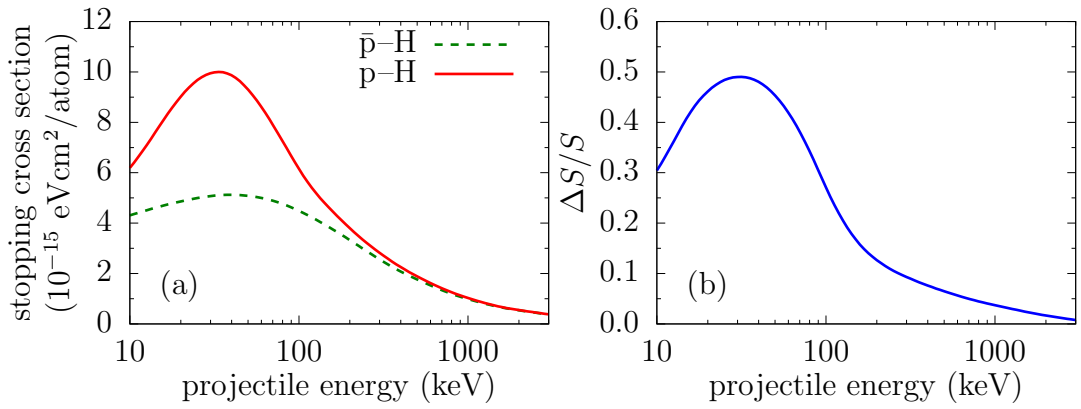

Figure 8.5: The Barkas effect. (a) Comparison of calculated stopping cross section for proton and antiproton collisions with hydrogen. (b) Relative stopping cross section for proton and antiproton collisions with hydrogen, $\Delta S/S = (S^{\mathrm{p}} - S^{\bar{\mathrm{p}}})/S^{\mathrm{p}}$.

cross section, $\Delta S/S = (S^{\mathrm{p}} - S^{\bar{\mathrm{p}}})/S^{\mathrm{p}}$, is presented. This quantity is useful for analysing the Barkas effect. From the figure we see that the significance of the Barkas effect peaks at 30 keV incident energy.

8.3 Hydrogen-hydrogen stopping cross section

In this section we present calculations of the stopping cross section for hydrogen-hydrogen collisions. For the single-centre CCC calculations convergence with increasing basis size is investigated. For the Born calculations convergence of the stopping cross section for increasing number of excited states is investigated. Then we present our final calculations in comparison with existing theories.

8.3.1 Convergence studies

As discussed above in Section 8.2.1, it is important to demonstrate convergence in the stopping cross section by increasing the size of the basis used in the expansion of the scattering wave function. Here we investigate convergence of

the CCC electronic stopping cross section in terms of the basis parameters $l_{\max}$ and $n_{\max}$ (see Section 8.2.1 for description) at incident energies of 10 keV, 100 keV, and 1000 keV. In all calculations the exponential fall-off parameter λ_l of the basis functions is chosen to be 4 for all l.

First, we fix the basis parameter $n_{\max}$ at some large value and systematically increase $l_{\max}$. Figure 8.6 shows the convergence of the electronic stopping cross section for hydrogen-hydrogen collisions with increasing $l_{\max}$, while $n_{\max}$ is fixed at 30. From this figure we can see that large values of orbital angular momentum are required to achieve convergence at all incident energies. This is the result of using a single-centre approach to the two-centre problem. At 10 keV, 100 keV, and 1000 keV incident energies the stopping cross section has converged to within 0.17%, 0.07%, and 1.4%, respectively.

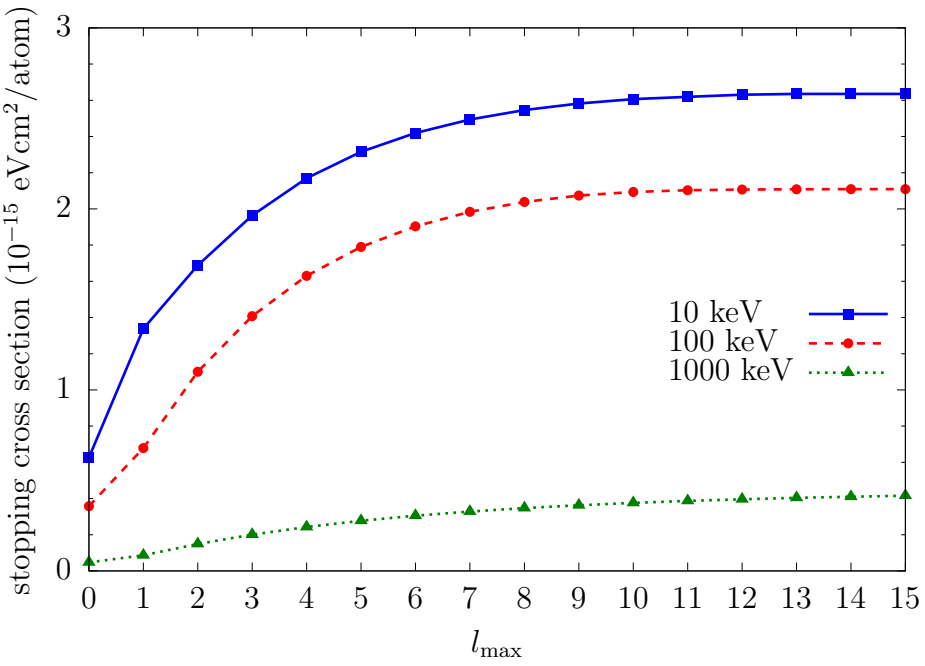

Figure 8.6: Convergence of the CCC electronic stopping cross section for hydrogen incident on hydrogen with increasing $l_{\max}$ for $n_{\max} = 30$ at incident energies of 10 keV, 100 keV, and 1000 keV.

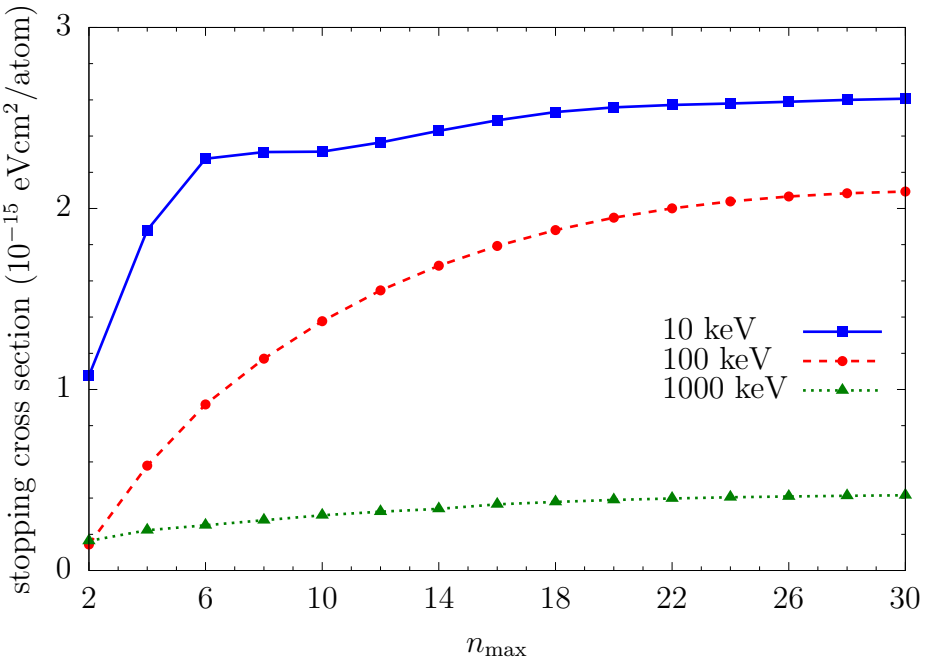

Figure 8.7: Convergence of the CCC electronic stopping cross section for hydrogen incident on hydrogen with increasing $n_{\max}$ for $l_{\max} = 15$ at incident energies of 10 keV, 100 keV, and 1000 keV.

Next we investigate convergence of the electronic stopping cross section with increasing $n_{\max}$. Figure 8.7 shows the convergence of the electronic stopping cross section with increasing $n_{\max}$, while $l_{\max}$ is fixed at 15. From the figure we can see that convergence with $n_{\max}$ is similar for all incident energies, i.e. it gradually increases before reaching convergence. The difference between stopping cross section when $n_{\max}$ changes from 28 to 30 at 10 keV, 100 keV, and 1000 keV is 0.26%, 0.65%, and 0.70%, respectively. From Figures 8.6 and 8.7 it can be concluded that a basis with $n_{\max} = 30$ and $l_{\max} = 15$ produces sufficiently convergent results for the electronic stopping cross section.

Now convergence in the Born approach will be investigated. In this instance we are interested in determining the number of excited states that should be included in calculations. Therefore, we will be focusing on convergence of the total stopping cross section due to excitation. Specifically, the latter is the sum of

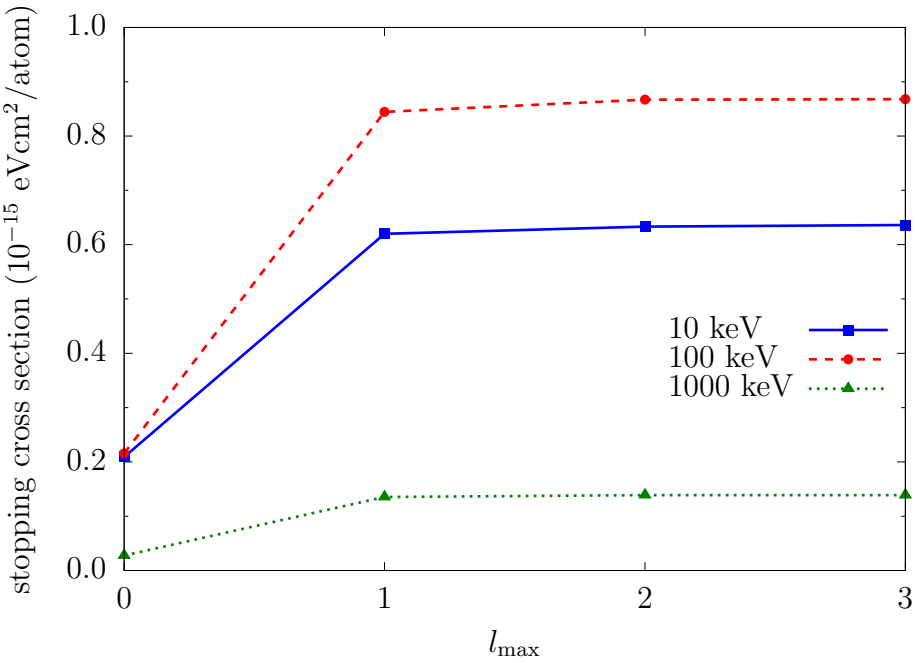

Figure 8.8: Convergence of the total stopping cross section due to excitation for hydrogen incident on hydrogen with increasing $l_{\max}$ for $n_{\max} = 8$ at incident energies of 10 keV, 100 keV, and 1000 keV, calculated using the Born approximation.

the stopping cross sections due to single excitation, double excitation, and ionisation with excitation. Furthermore, the parameter $l_{\max}$ will now represent the maximum orbital quantum number and $n_{\max}$ the maximum principal quantum number of bound states included in calculations.

Figure 8.8 shows convergence of the total stopping cross section due to excitation for increasing $l_{\max}$, while $n_{\max}$ is fixed at 8. From the figure we can see that the stopping cross section increases sharply between $l_{\max} = 0$ and $l_{\max} = 1$ before rapidly reaching convergence. The difference between stopping cross section with $l_{\max} = 2$ and $l_{\max} = 3$ at 10 keV, 100 keV, and 1000 keV is 0.45%, 0.09%, and 0.07%, respectively. Next we take a look at convergence of the total excitation stopping cross section with increasing $n_{\max}$.

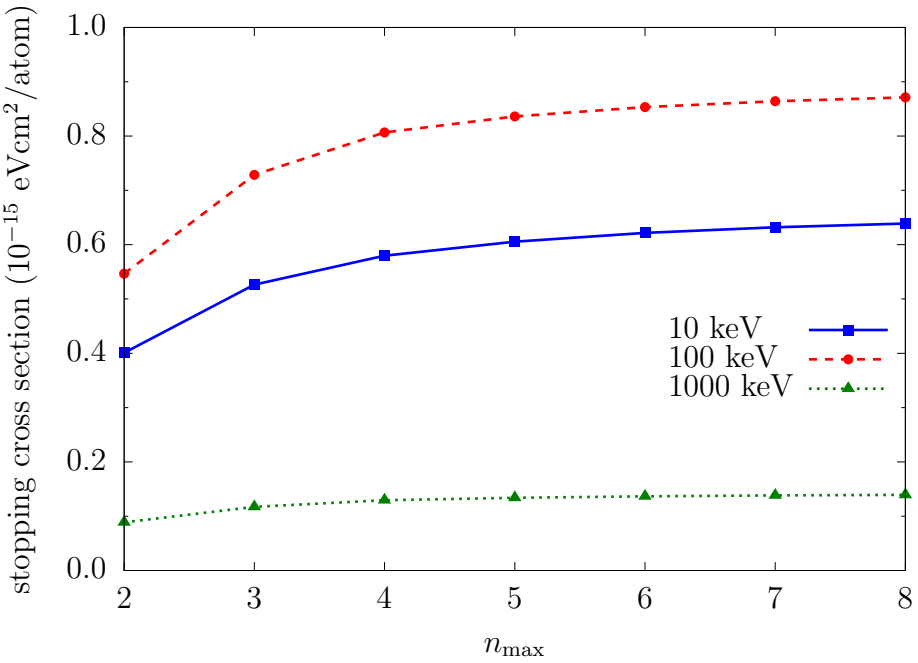

Figure 8.9: Convergence of the total stopping cross section due to excitation for hydrogen incident on hydrogen with increasing $n_{\max}$ for $l_{\max} = 3$ at incident energies of 10 keV, 100 keV, and 1000 keV, calculated using the Born approximation.

Figure 8.9 shows convergence of the total stopping cross section due to excitation for increasing $n_{\max}$, while $l_{\max}$ is fixed at 3 (except for $n_{\max} \leq 3$, where $l_{\max} = n_{\max} - 1$). From the figure we can see that at all incident energies, as $n_{\max}$ is increased, the stopping cross section gradually increases before reaching convergence. At 10 keV, 100 keV, and 1000 keV incident energies the stopping cross section has converged to within 1.1%, 0.84%, and 0.80%, respectively. From Figures 8.8 and 8.9 it can be concluded that the inclusion of excited states up to $n_{\max} = 8$ and $l_{\max} = 3$ produces sufficiently convergent results.

8.3.2 Results of calculations

In CCC calculations the convergent basis parameters discussed above result in a total of 5080 target states used in the solution of the coupled-channel differential

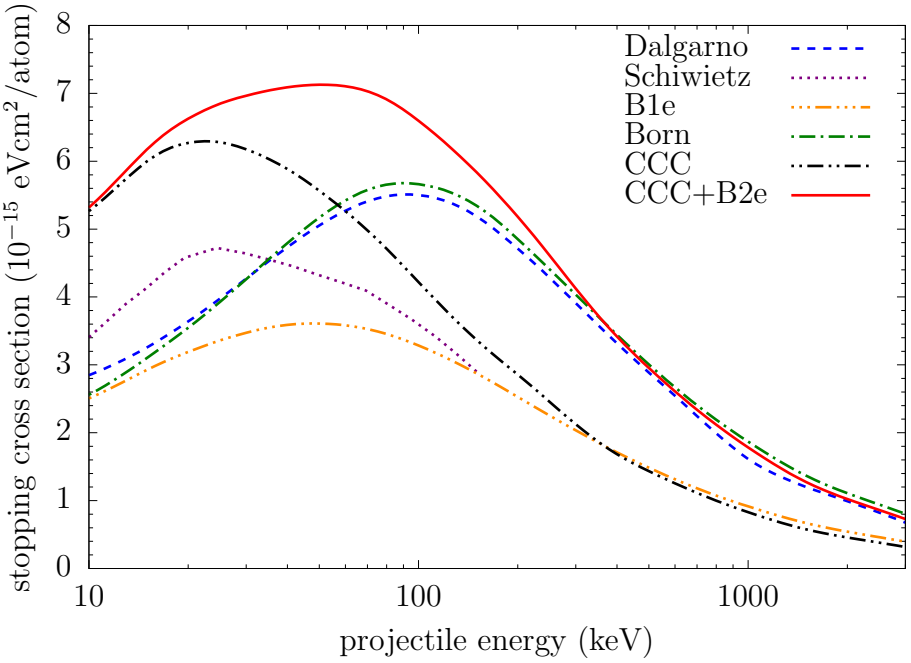

Figure 8.10: Electronic stopping cross section for hydrogen incident on hydrogen. Calculations are compared with those of Dalgarno and Griffing [24], and Schiwietz and Grande [40]. The results labelled as "CCC" and "B1e" include one-electron processes only, while "CCC+B2e" and "Born" results include one- and two-electron processes (see text for details).

equations (7.48). Furthermore, in the Born calculations we include excitations to all states for which $n \leq 8$ and $l \leq 3$.

In Figure 8.10 we present our results for the hydrogen-hydrogen electronic stopping cross section together with the calculations of Dalgarno and Griffing [24], and Schiwietz and Grande [40]. The CCC calculations include energy losses due to single excitation and single ionisation, whereas the Born results include energy losses due to single and double excitation and ionisation as well as ionisation with excitation. Additionally, we present the Born calculations for one-electron processes only (labelled B1e) and the CCC results that include two-electron processes calculated using the Born approach (labelled CCC+B2e). First, we note that the CCC results are in agreement with the B1e results at high

energies where the latter is considered accurate. Specifically, good agreement is seen above 300 keV. However, at lower energies, below 200 keV, the coupling between channels in the CCC approach results in a significantly larger stopping cross section when compared to the B1e results. In this energy region CCC calculations are much larger than the AO calculations of Schiwietz and Grande [40] as well, although both methods are based on a similar approach. It could be that the results of Schiwietz and Grande [40] did not have a sufficient number of states as the CCC calculations include a much larger number of target states. Turning to the Born results we see a small but systematic disagreement with the FBA calculations of Dalgarno and Griffing [24] above 40 keV. This is due to the fact that we include excitation to all states with $n \leq 8$ and $l \leq 3$, whereas Dalgarno and Griffing [24] include excitations up to the $n = 3$ shell only. This statement has been verified by performing calculations that include the same number of states as Dalgarno and Griffing [24]. On the other hand, below 20 keV the FBA calculations of Dalgarno and Griffing [24] are slightly higher as they have included an estimated contribution to the stopping cross section due to H^- formation. Lastly, comparing our calculations that include one-electron processes (CCC & B1e) to those that include one- and two-electron processes (CCC+B2e & Born) we see that double excitation, double ionisation, and ionisation with excitation make a substantial contribution to the stopping cross section above 20 keV (discussed in more detail below). As such, the CCC+B2e calculation is considered our most accurate result.

The aforementioned statement can be validated by considering the total cross section for electron loss by the projectile as there is experimental data to compare with. Since the stopping cross section is dominated by ionisation processes (as shown below), this may prove useful in assessing the accuracy of the hydrogen-hydrogen stopping cross section. In Figure 8.11 we present

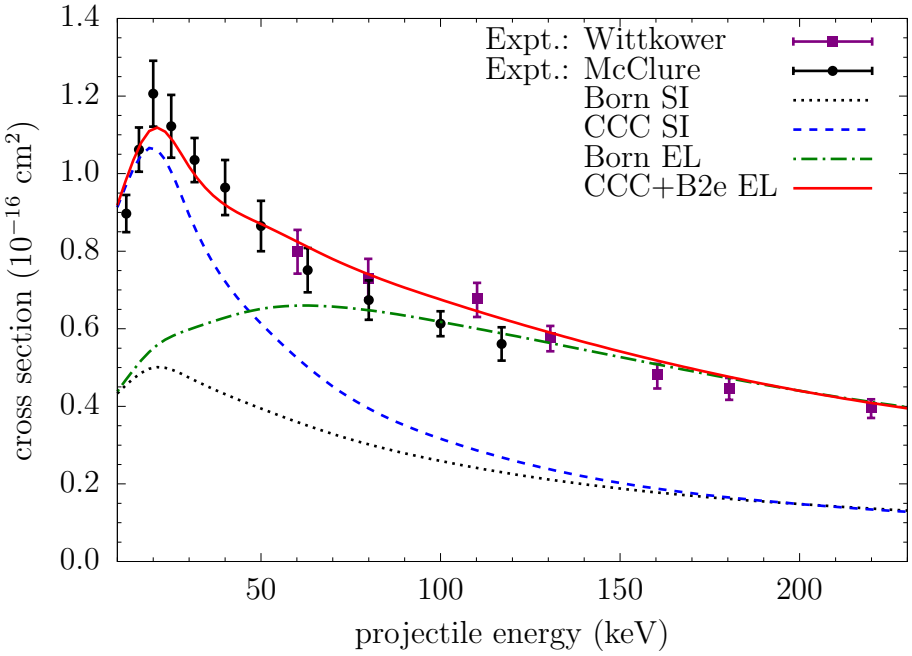

Figure 8.11: Total cross section for electron loss by the projectile in hydrogen collisions with hydrogen. The CCC+B2e calculations (see text for details) are compared to the experimental data of Wittkower *et al.* [98] and McClure [99]. Also shown are the Born calculations for total electron loss (Born EL), as well as the Born and CCC calculations for single ionisation only, labelled "Born SI" and "CCC SI", respectively.

our CCC+B2e calculation for the total electron-loss cross section compared to the experimental data of Wittkower *et al.* [98] and McClure [99]. Also shown are the Born calculations for the total electron-loss cross section (Born EL), as well as the Born and single-centre CCC calculations for the single-ionisation cross section (denoted as Born SI and CCC SI, respectively). The CCC+B2e results are in good agreement with the experimental data over the whole energy region considered. On the other hand, the Born EL calculations significantly underestimate experiment below 70 keV projectile energy. This illustrates the benefit of using a coupled-channel approach for the one-electron processes, as is done presently. This becomes evident when we compare the CCC SI and Born SI calculations, where the latter significantly underestimates the former below

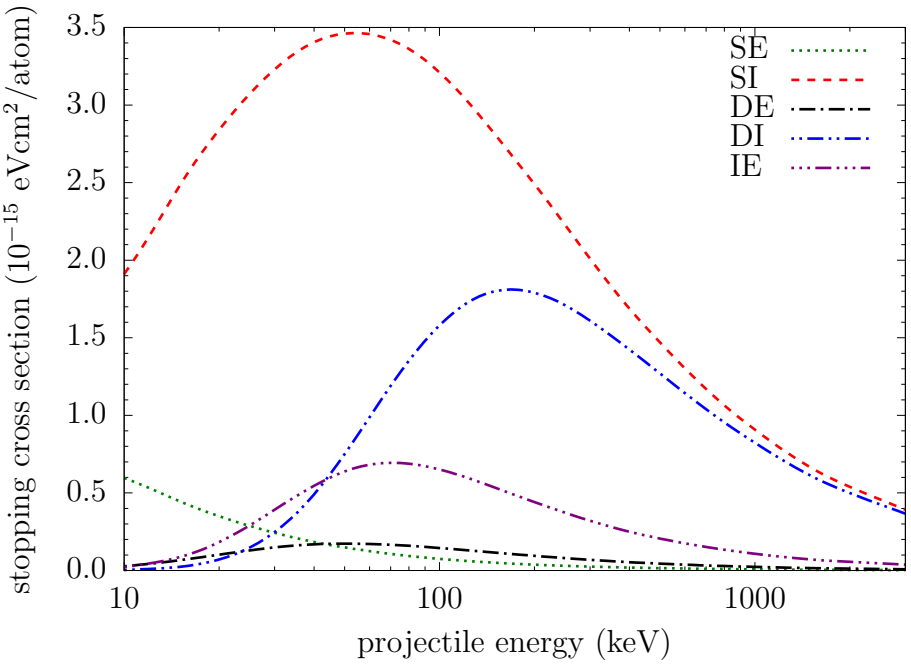

Figure 8.12: Individual contributions to the hydrogen-hydrogen electronic stopping cross section calculated in the Born approximation. The curves labelled "SE" and "SI" are the stopping cross sections associated with single excitation and ionisation, respectively. While the curves labelled "DE" and "DI" are the stopping cross sections associated with double excitation and ionisation, respectively. Also, "IE" is the stopping cross section due to ionisation with excitation.

100 keV. Furthermore, the importance of including the two-electron processes becomes apparent when two models that include one-electron processes only, i.e. CCC SI and Born SI, are compared to those that include both one- and two-electron processes, i.e. CCC+B2e EL and Born EL. As can been seen, the CCC SI calculations underestimate experiment above 20 keV projectile energy and the Born SI calculations underestimate experiment at all projectile energies considered.

Individual contributions to the Born stopping cross section are presented in Figure 8.12. This figure demonstrates that at high incident energies the stopping cross section is dominated by single- and double-ionisation processes, each making an almost equal contribution. In the intermediate energy region, energy

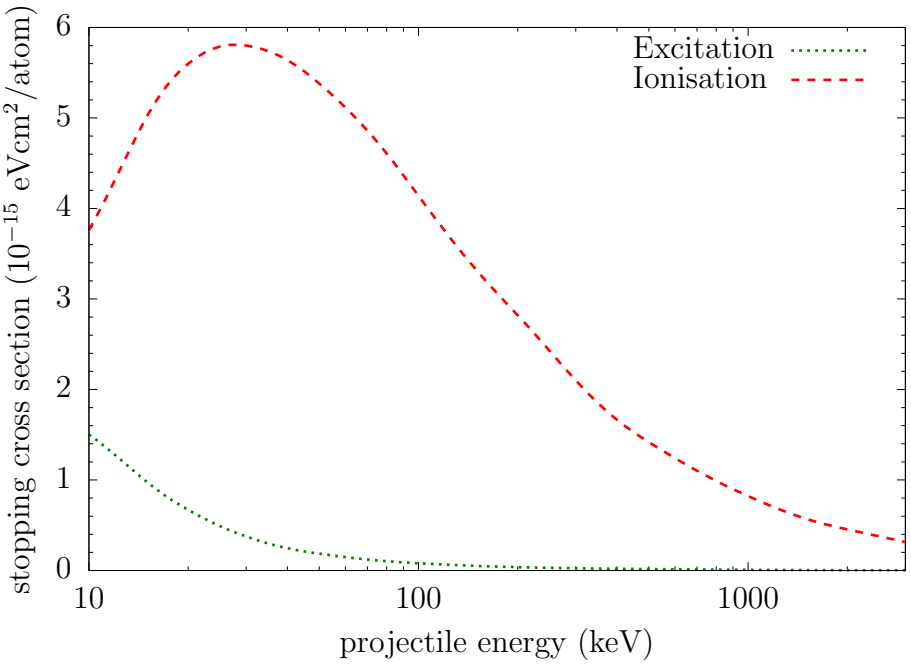

Figure 8.13: Individual contributions to the hydrogen-hydrogen electronic stopping cross section calculated with the CCC method. The curves labelled "Excitaiton" and "Ionisation" are the stopping cross sections associated with single excitation and ionisation, respectively.

losses due to single ionisation are the main contribution to the stopping cross section, while double ionisation and ionisation with excitation make a smaller but still significant addition. Double excitation also makes relatively small but important contribution in this region. Lastly, at lower incident energies the contribution from single-excitation processes increases and becomes significant, however, single ionisation remains dominant.

The same but for the CCC stopping cross section are presented in Figure 8.13. The figure shows that energy losses due to ionisation dominate the stopping cross section at all incident energies considered, while energy losses due to excitation make a significant contribution only below 50 keV.

8.4 Total stopping cross section

As discussed in Section 6.4, the total stopping cross section for protons passing through hydrogen is calculated by summing the proton-hydrogen and hydrogen-hydrogen stopping cross sections (presented in Sections 8.2 and 8.3, respectively) weighted by their respective charge-state fractions. It should be made clear that for the hydrogen-hydrogen stopping cross section we use the CCC+B2e result. Subsequently, the hydrogen-hydrogen total electron-loss cross section, which is required for the calculation of charge-state fractions, is the sum of the single-ionisation cross that is calculated in the single-centre CCC approach and the double-ionisation and ionisation-with-excitation cross sections that are calculated using the Born approximation.

In Figure 8.14 we present our results for the positive (f^{H^+}) and neutral (f^{H^0}) charge-state fractions for a beam of protons passing through hydrogen. They are displayed alongside the calculations of Dalgarno and Griffing [24] and Fainstein *et al.* [32], as well as the experimental data of Allison [97] (which was used in the calculation of the total stopping cross section by Schiwietz [39] and Schiwietz and Grande [40]). We obtain good agreement with Dalgarno and Griffing [24] above 40 keV projectile energy and with Fainstein *et al.* [32] above 150 keV. Furthermore, although the experimental data of Allison [97] were measured for a molecular hydrogen target, we obtain reasonable agreement with the latter over the whole energy range. Additionally, from Figure 8.14 we can make some statements about the composition of the beam passing through the target. Firstly, above 200 keV projectile energy the beam is comprised almost entirely of protons. As the projectile energy falls the proportion of hydrogen begins to rise, reaching 50% of the beam composition at 50 keV. Below 50 keV hydrogen atoms make up the majority of the beam, reaching 90% of the beam

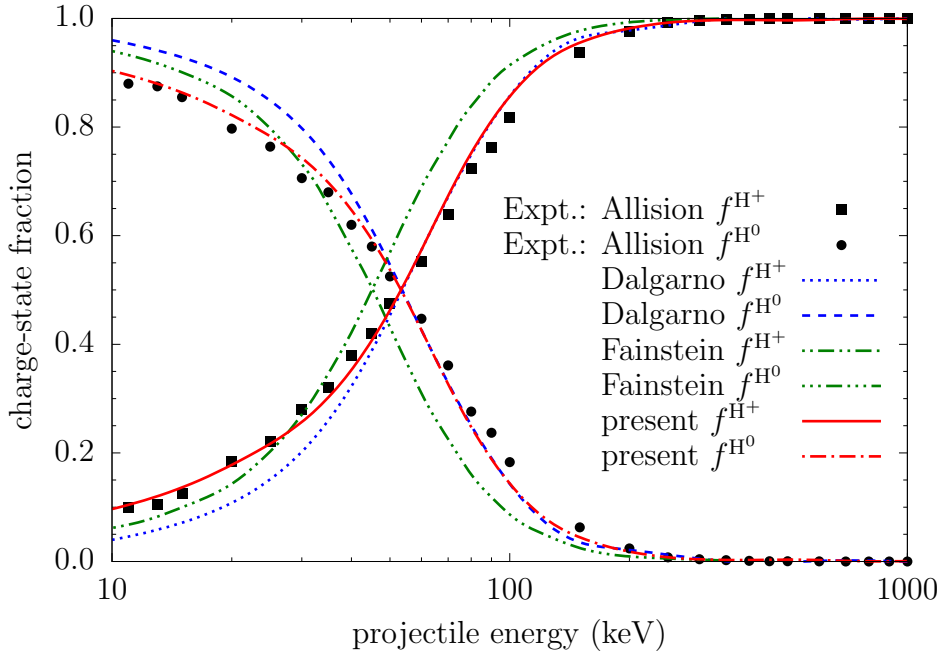

Figure 8.14: Positive (f^{H^+}) and neutral (f^{H^0}) charge-state fractions for protons passing through hydrogen. The present results are compared to those of Dalgarno and Griffing [24], and Fainstein *et al.* [32]. The experimental data of Allison [97], which were measured for a molecular hydrogen target, are also shown.

composition at 10 keV.

In Figure 8.15 we present our results for the total electronic stopping cross section for protons passing through hydrogen together with the theoretical calculations of Dalgarno and Griffing [24], Schiwietz [39], Schiwietz and Grande [40], and Fainstein *et al.* [32]. Also shown are the experimental results of Reynolds *et al.* [94], Reiter *et al.* [95], and Golser and Semrad [96] for protons passing through molecular hydrogen divided by two, i.e. the results are given per atom as originally presented. Good agreement with the calculations of Dalgarno and Griffing [24] is seen above 100 keV projectile energy, while agreement with the calculations of Schiwietz [39], Schiwietz and Grande [40], and Fainstein *et al.* [32] is obtained above 125 keV. Furthermore, there is good agreement with the

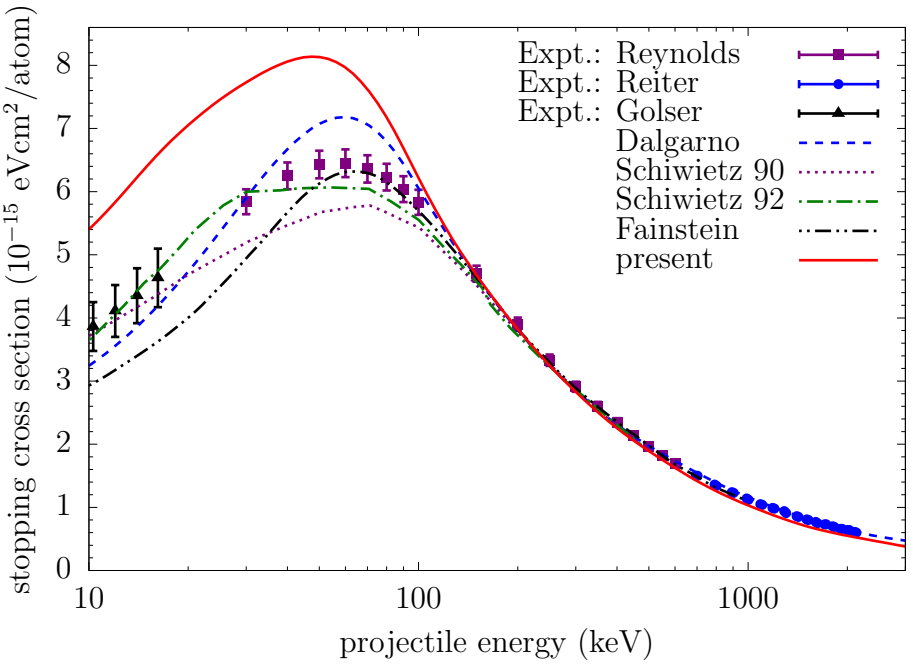

Figure 8.15: Total electronic stopping cross section for protons passing through hydrogen. The present results have been obtained using the two-centre CCC method for the positive charge-state contribution and the CCC+B2e (see text for details) method for the neutral charge-state contribution. Also shown are the theoretical calculations of Dalgarno and Griffing [24], Schiwietz [39], Schiwietz and Grande [40], and Fainstein *et al.* [32]. The experimental data of Reynolds *et al.* [94], Reiter *et al.* [95], and Golser and Semrad [96] for protons passing through molecular hydrogen are shown as well.

experimental data above 150 keV. This demonstrates that the Bragg additivity rule, according to which H_2 is an aggregate of two independent hydrogen atoms, is acceptable above the aforementioned projectile energy. On the other hand, our calculations are significantly above other theoretical estimates and the H_2 experimental data below 100 keV. This fact will be discussed in more detail below. Noticeably, in this region there are substantial deviations between all theoretical approaches. These deviations cannot be attributed to either the positive or neutral charge-state contributions, since there are large deviations between theories in both cases, as seen in Figures 8.3 and 8.10. We can, however, emphasise that our calculations for the positive charge-state contribution

are the most sophisticated and accurate as we employ a large two-centre expansion of the scattering wave function, which explicitly includes electron-capture channels. Also, for the neutral charge-state contribution our approach produces the most accurate projectile total electron-loss cross section.

We conclude by discussing our calculations for atomic hydrogen in comparison to the experimental measurements for molecular hydrogen below 100 keV projectile energy. As can be seen in Figure 8.15 there is a significant difference between the two results. This demonstrates that Bragg's additivity rule is not valid in this region and, hence, the stopping cross for protons passing through molecular hydrogen can not be represented as twice the stopping cross section for protons passing through atomic hydrogen. This fact was previously demonstrated in Chapter 5, specifically in Figure 5.6, where a significant difference between the calculated antiproton-atomic hydrogen and antiproton-molecular hydrogen stopping cross sections below the maximum was also observed. Therefore, although some theoretical calculations for atomic hydrogen showed good agreement with experimental data for molecular hydrogen and the authors claimed this to be a positive aspect of their approach, we emphasise that agreement between the two should not be expected. To further support this statement we can estimate how might experimental data for the proton-atomic hydrogen stopping cross section look like based on the proton-molecular hydrogen stopping cross section data. To achieve this we scale the proton-H_2 stopping cross section data of Reynolds *et al.* [94], Reiter *et al.* [95], and Golser and Semrad [96] by the ratio between the proton-hydrogen and proton-H_2 total ionisation cross sections. Ionisation is a dominant energy-loss process and therefore the ratio between the atomic- and molecular-hydrogen ionisation cross sections can provide a reasonable estimate of the ratio between the atomic- and molecular-hydrogen stopping cross sections. For the ratio between the atomic- and molecular-hydrogen total

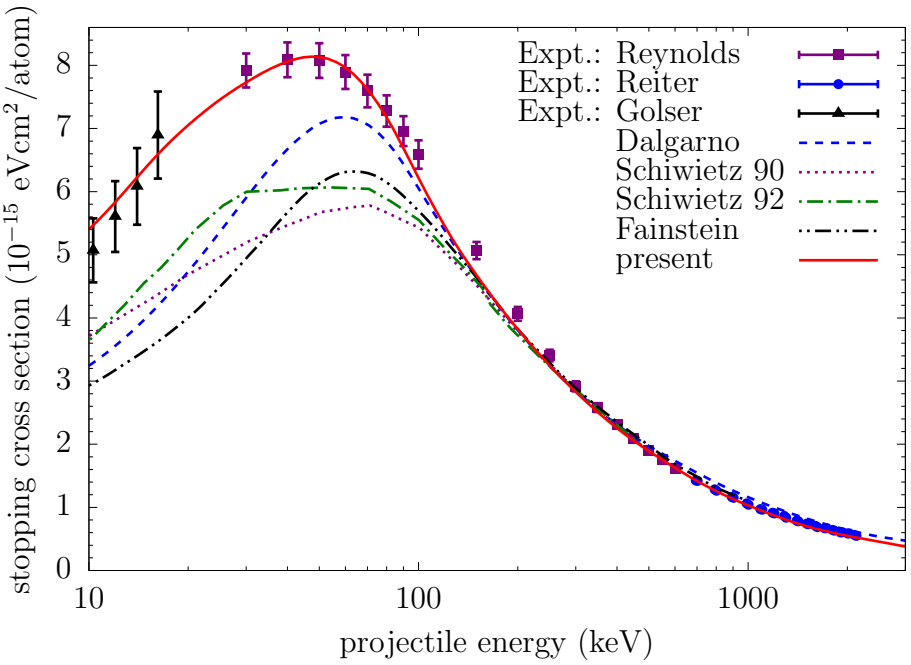

Figure 8.16: Total electronic stopping cross section for protons passing through hydrogen. Our present calculations are shown alongside the calculations of Dalgarno and Griffing [24], Schiwietz [39], Schiwietz and Grande [40], and Fainstein *et al.* [32]. Also shown is the experimental data of Reynolds *et al.* [94], Reiter *et al.* [95], and Golser and Semrad [96] for a molecular hydrogen target that has been scaled by the ratio between the atomic- and molecular-hydrogen total ionisation cross sections to provide an estimate of experimental data for an atomic target (see text for details).

ionisation cross sections we use the experimental result of Shah and Gilbody [100]. These authors give the ratio from 38 keV to 1.5 MeV. At 1.5 MeV the ratio has plateued and therefore above this the ratio is taken to be constant. Below 38 keV we calculate the ratio based on the measurements of Shah *et al.* [101] for the atomic target and the measurements of Afrosimov *et al.* [102] for the molecular target. In Figure 8.16 we present the same theoretical calculations for the proton-hydrogen total electronic stopping cross section from Figure 8.15 alongside the scaled experimental data of Reynolds *et al.* [94], Reiter *et al.* [95], and Golser and Semrad [96]. With the aforementioned scaling of experimental data we obtain excellent agreement over the whole energy range.

8.5 Chapter summary

We have calculated the total electronic stopping cross section for protons passing through hydrogen. Both the positive and neutral charge-states of the projectile are accounted for. For proton-hydrogen collisions we use the two-centre CCC approach. This allows us to explicitly include energy losses due to electron capture, as well as the excitation and ionisation processes. For hydrogen-hydrogen collisions we include energy losses due to single-electron excitation and ionisation, double excitation and ionisation, and simultaneous ionisation with excitation. Specifically, the single-centre CCC approach is used for the calculation of the one-electron processes, while the Born approximation is used for the calculation of the two-electron processes. The aforementioned approaches are also applied to the calculation of the charge-state fractions. These are then used to combine the proton-hydrogen and hydrogen-hydrogen stopping cross sections to yield the total stopping cross section for protons passing through hydrogen.

Chapter 9

Conclusion and outlook

In this final chapter of the thesis we shall draw conclusions from the present study. We also discuss some potential future directions that this work can take.

9.1 Conclusion

The present thesis was devoted to the study of energy-loss processes in ion-atom collision. Stopping cross sections were calculated using the convergent close-coupling method for the first time. We started from the simplest antiproton-hydrogen system, before moving to more complicated targets and then to proton projectiles.

The single-centre CCC method was applied to the calculation of stopping cross sections in antiproton collisions with the atomic targets of hydrogen, helium, neon, argon, krypton, and xenon. Results for the antiproton-hydrogen stopping cross section are in agreement with existing theories. This fact was used to validate our approach to calculating the stopping cross section. For the helium target our calculations are the first to use a multiconfiguration description of the atom, which fully accounts for electron-electron correlations. It was found that the results of this approach improved upon other calculations

that employed a hydrogen-like model of the helium atom. Therefore, it can be concluded that the electron-electron correlations must be accounted for if one wishes to obtain accurate stopping cross sections for helium atoms. Also, our calculations for the other noble gasses are the first results for these targets.

The stopping cross section for antiproton collisions with molecules was also calculated using the single-centre CCC approach. Specifically, the hydrogen and water molecules were considered. Calculations for H_2 are the first to employ an accurate molecular structure model and consider energy losses due to vibrational excitations. Also, all possible orientations of the molecule were accounted for via an analytic orientation-averaging technique. The obtained results are significantly different in comparison to methods that employ an atomic model of the molecule around and below the maximum of the stopping cross section. From this we can conclude that an accurate molecular structure model should be used when calculating the H_2 stopping cross section. Furthermore, from this observation we can also conclude that Bragg's additivity rule is not valid, particularly at the lower energies. That is, the stopping cross section for molecular hydrogen is not equal to twice the stopping cross section for atomic hydrogen. In addition, the conclusion can be drawn that all orientations of the molecule must be taken into account, not just one or even an average over a small number, for example three orientations. To our best knowledge, the results for the water molecule are the first calculations performed for this target.

Moving to proton projectiles, the total stopping cross section for protons passing through hydrogen was calculated. Due to the possibility of electron capture both the positive and neutral charge states of the projectile were considered. To model proton-hydrogen collisions the two-centre CCC method was used. By starting from the exact Schrödinger equation and using a more general expansion for the scattering wave function we were able to demonstrate that

the two-centre scattering equations can be derived without introducing electron translation factors. By comparing the results of our two-centre calculations to other single-centre calculations we conclude that singe-centre approaches cannot produced accurate stopping cross sections at low and intermediate incident energies. To model hydrogen-hydrogen collisions the single-centre CCC method was used for the calculation of one-electron processes and the Born approximation was used for the calculation of two-electron processes. This is the first time the CCC method has been applied to collisions involving two atoms. From the results of these calculations it can be concluded that the coupling between channels plays an important role in the calculation of one-electron processes. It can also be concluded that two-electron processes make a significant contribution to the stopping cross section. In addition, this hybrid approach to modelling hydrogen-hydrogen collisions appears to give reasonable results. The calculations for the positive and neutral charge states of the projectile were combined by utilising calculated charge-state fractions to yield the total stopping cross section for protons passing through atomic hydrogen. From analysing the results of our calculations and experimental data for molecular hydrogen we can conclude that around and below the stopping maximum the stopping cross for protons passing through molecular hydrogen can not be represented as twice the stopping cross section for protons passing through atomic hydrogen, further echoing conclusions drawn in relation to antiproton-H_2 calculations. In addition, although some theoretical calculations for atomic hydrogen have attempted to obtain good agreement with experimental data for molecular hydrogen, we emphasise that agreement between the two should not be expected.

Lastly, additional conclusions can be drawn by considering the results of multiple chapters, which have not been discussed in any single chapter. First, achieving convergence in the stopping cross section generally required a larger

basis for the expansion of the scattering wave function in comparison to scattering cross sections, such as the total ionisation cross section. This can be explained by the fact that the cross section for excitation to a high-energy continuum state is small and so does not contribute to the total ionisation cross section. However, the energy required to excite the target to this state is large and, therefore, makes a noticeable contribution to the stopping cross section [see Eq. (2.72)]. Hence, a larger basis was required to accurately model the high-energy continuum. In fact, due to the increased demand for computational resources that stems from the requirement for a large basis, achieving convergence in the stopping cross section was one of the challenges faced in this work.

9.2 Outlook

Based on the results presented in this thesis the outlook for future applications of the convergent close-cloupling method to the study of energy-loss processes in ion-atom and ion-molecule collisions is very bright. In fact, there are many paths that can be taken at this point, here we shall briefly discuss just a few potential projects.

The next logical step would be to extend the two-centre CCC method for heavy projectiles to multi-electron targets such as helium and molecular hydrogen. Helium is the simplest two-electron target and there is a substantial set of experimental data [94–96, 103–105] to compare with. This would allow for a continued test of the theory. Furthermore, calculations for proton stopping in molecular hydrogen would allow for comparison to experiment without the need for scaling to approximate an atomic hydrogen target (as done in Section 8.4). Such calculations would be useful to highlight the difference between the stopping cross sections of atomic and molecular hydrogen for protons, as done in

this thesis for antiprotons.

Due to the electron-capture process in proton scattering, calculations for hydrogen atom projectiles are also required to obtain the total stopping cross section for protons penetrating matter. Therefore, the development of a more sophisticated approach to treating collisions involving a hydrogen projectile would be an important next step. The current approach treats one-electron processes using the single-centre CCC method and two-electron processes using the Born approximation. This approach appears to be reasonably successful in the case of hydrogen-hydrogen scattering, however, it will prove useful to develop a coupled-channel approach that can calculate both one- and two-electron processes.

There are also problems that the current method could be applied to that require little or no extra development. For example, the problem of muon stopping in helium and molecular hydrogen. As their is no electron-capture channels, the existing single-centre CCC approach could be utilised. There is also experimental data [106, 107] to compare with. In addition, problems such as helium-ion stopping in hydrogen are also of great interest [95, 96, 104, 108, 109] and could be easily tackled with the existing method.

Lastly, in relation to the broader goal of this project, which is to provide accurate stopping power data for use in hadron therapy, calculations for proton stopping in water should be of the highest priority. Water is the most biologically-relevant molecule and H_2O stopping pawer data is heavily relied on in radiation dose simulations. This work will require significant efforts to be devoted to the development of an accurate structure model for the water molecule. Following this, other biologically-relevant molecules, such as DNA bases, can be considered.

Appendix A

Momentum transfer vectors

In this appendix we consider the momentum transfer vectors $\boldsymbol{q}_\alpha$, $\boldsymbol{q}_\beta$, $\boldsymbol{p}_\alpha$, $\boldsymbol{p}_\beta$, $\boldsymbol{p}_{\alpha'}$, and $\boldsymbol{p}_{\beta'}$ that were introduced in Chapters 2 and 6. First let's consider the momentum transfer vector $\boldsymbol{q}_\alpha$, which is given by

$$\boldsymbol{q}_\alpha = \boldsymbol{k}_\alpha - \boldsymbol{k}_{\alpha'}. \tag{A.1}$$

With $\boldsymbol{k}_\alpha$ directed along the z-axis we can write $\boldsymbol{q}_\alpha$ in cartesian coordinates as

$$\boldsymbol{q}_\alpha = -k_{\alpha' x}\hat{\boldsymbol{x}} - k_{\alpha' y}\hat{\boldsymbol{y}} + (k_\alpha - k_{\alpha'}\cos\theta)\hat{\boldsymbol{z}}, \tag{A.2}$$

where $k_{\alpha' x}$ and $k_{\alpha' y}$ are the x and y components of $\boldsymbol{k}_{\alpha'}$ respectively, and θ is the polar angle of $\boldsymbol{k}_{\alpha'}$, i.e the scattering angle. Expressing $\boldsymbol{q}_\alpha$ in terms of its components that are perpendicular and parallel to the z-axis, Eq. (A.2) becomes

$$\boldsymbol{q}_\alpha = \boldsymbol{q}_{\alpha\perp} + q_{\alpha\parallel}\hat{\boldsymbol{z}}, \tag{A.3}$$

where the component perpendicular to the z-axis $\boldsymbol{q}_{\alpha\perp}$ is given by

$$\boldsymbol{q}_{\alpha\perp} = -k_{\alpha' x}\hat{\boldsymbol{x}} - k_{\alpha' y}\hat{\boldsymbol{y}}, \tag{A.4}$$

and the component parallel to the z-axis $q_{\alpha\parallel}$ can be approximated as

$$q_{\alpha\parallel} \approx k_\alpha - k_{\alpha'}. \tag{A.5}$$

In obtaining Eq. (A.5) we have assumed the projectile primarily scatters in the forward direction and therefore apply a small angle approximation, that is $\cos\theta \approx 1$. Furthermore, from energy conservation we can write

$$\frac{k_\alpha^2}{2\mu} + \epsilon_\alpha = \frac{k_{\alpha'}^2}{2\mu} + \epsilon_{\alpha'}, \tag{A.6}$$

where μ is the reduced mass of the proton-hydrogen system, that is

$$\mu = \frac{M(M+1)}{2M+1}, \tag{A.7}$$

where M is the proton mass. Rearranging Eq. (A.6) we can write

$$k_\alpha - k_{\alpha'} = \frac{2\mu\Delta\epsilon_{\alpha'\alpha}}{k_\alpha + k_{\alpha'}}, \tag{A.8}$$

where $\Delta\epsilon_{\alpha'\alpha} = \epsilon_{\alpha'} - \epsilon_\alpha$. On the right-hand side of Eq. (A.8) we use the approximation

$$k_{\alpha'} \approx k_\alpha = \mu v. \tag{A.9}$$

Then we can express $q_{\alpha\parallel}$ according to

$$q_{\alpha\parallel} = \frac{\Delta\epsilon_{\alpha'\alpha}}{v}. \tag{A.10}$$

Similarly, the momentum transfer vector $\boldsymbol{q}_\beta = \boldsymbol{k}_\beta - \boldsymbol{k}_{\beta'}$ can be written as

$$\boldsymbol{q}_\beta = \boldsymbol{q}_{\beta\perp} + q_{\beta\parallel}\hat{\boldsymbol{z}}, \tag{A.11}$$

where the perpendicular and parallel components of $\boldsymbol{q}_\beta$ are given by

$$\boldsymbol{q}_{\beta\perp} = -k_{\beta' x}\hat{\boldsymbol{x}} - k_{\beta' y}\hat{\boldsymbol{y}}, \tag{A.12}$$

and

$$q_{\beta\parallel} = \frac{\Delta\epsilon_{\beta'\beta}}{v}. \tag{A.13}$$

Here $\Delta\epsilon_{\beta'\beta} = \epsilon_{\beta'} - \epsilon_\beta$.

Now let's consider the momentum transfer vectors $\boldsymbol{p}_\alpha$ and $\boldsymbol{p}_{\beta'}$, which are given by

$$\boldsymbol{p}_\alpha = \gamma \boldsymbol{k}_\alpha - \boldsymbol{k}_{\beta'} \tag{A.14}$$

and

$$\boldsymbol{p}_{\beta'} = \boldsymbol{k}_\alpha - \gamma \boldsymbol{k}_{\beta'}. \tag{A.15}$$

Here γ is the reduced mass of the proton-electron system, that is

$$\gamma = \frac{M}{M+1}. \tag{A.16}$$

Following the ideas used above, we write $\boldsymbol{p}_\alpha$ and $\boldsymbol{p}_{\beta'}$ in terms of their components that are perpendicular and parallel to the z-axis as

$$\boldsymbol{p}_\alpha = \boldsymbol{p}_{\alpha\perp} + p_{\alpha\parallel}\hat{\boldsymbol{z}} \tag{A.17}$$

and

$$\boldsymbol{p}_{\beta'} = \boldsymbol{p}_{\beta'\perp} + p_{\beta'\parallel}\hat{\boldsymbol{z}}. \tag{A.18}$$

The perpendicular and parallel components of $\boldsymbol{p}_\alpha$ are

$$\boldsymbol{p}_{\alpha\perp} = -k_{\beta' x}\hat{\boldsymbol{x}} - k_{\beta' y}\hat{\boldsymbol{y}} \tag{A.19}$$

and

$$p_{\alpha\parallel} = \gamma k_\alpha - k_{\beta'}, \tag{A.20}$$

and the perpendicular and parallel components of $\boldsymbol{p}_{\beta'}$ are

$$\boldsymbol{p}_{\beta'\perp} = -\gamma k_{\beta' x}\hat{\boldsymbol{x}} - \gamma k_{\beta' y}\hat{\boldsymbol{y}} \tag{A.21}$$

and

$$p_{\beta'\parallel} = k_\alpha - \gamma k_{\beta'}. \tag{A.22}$$

Again, we can express energy conservation according to

$$\frac{k_\alpha^2}{2\mu} + \epsilon_\alpha = \frac{k_{\beta'}^2}{2\mu} + \epsilon_{\beta'}, \tag{A.23}$$

and then rearrange for $k_{\beta'}$ to obtain

$$k_{\beta'} = k_\alpha \sqrt{1 - \frac{2\mu\Delta\epsilon_{\beta'\alpha}}{k_\alpha^2}}, \tag{A.24}$$

where $\Delta\epsilon_{\beta'\alpha} = \epsilon_{\beta'} - \epsilon_\alpha$. Considering the series expansion

$$(1+x)^\eta = \sum_{\lambda=0}^{\infty} \binom{\eta}{\lambda} x^\lambda, \tag{A.25}$$

where $\binom{\eta}{\lambda}$ is the binomial coefficient, we can express the square root in Eq. A.24 as

$$\left(1 - \frac{2\mu\Delta\epsilon_{\beta'\alpha}}{k_\alpha^2}\right)^{1/2} = 1 - \frac{1}{2}\left(\frac{2\mu\Delta\epsilon_{\beta'\alpha}}{k_\alpha^2}\right) - \frac{1}{8}\left(\frac{2\mu\Delta\epsilon_{\beta'\alpha}}{k_\alpha^2}\right)^2 - \dots \tag{A.26}$$

Additionally, since $k_\alpha \gg 2\mu\Delta\epsilon_{\beta'\alpha}$ we keep only the first two terms of Eq. (A.26) and write Eq. (A.24) as

$$k_{\beta'} \approx k_\alpha \left(1 - \frac{\mu\Delta\epsilon_{\beta'\alpha}}{k_\alpha^2}\right). \tag{A.27}$$

Substituting Eq. (A.27) into (A.20) and (A.22), we obtain

$$p_{\alpha\parallel} = \gamma k_\alpha - k_\alpha \left(1 - \frac{\mu\Delta\epsilon_{\beta'\alpha}}{k_\alpha^2}\right), \tag{A.28}$$

and

$$p_{\beta'\parallel} = k_\alpha - \gamma k_\alpha \left(1 - \frac{\mu\Delta\epsilon_{\beta'\alpha}}{k_\alpha^2}\right). \tag{A.29}$$

Furthermore, considering the fact that $M_\mathrm{p} \propto 10^3$ we can make the following approximations:

$$1 - \gamma = \frac{1}{M+1} \approx \frac{1}{M}, \tag{A.30}$$

$$\gamma = \frac{M}{M+1} \approx 1, \tag{A.31}$$

and

$$\mu = \frac{M(M+1)}{2M+1} \approx \frac{M}{2}. \tag{A.32}$$

With these approximations and writing $k_\alpha = \mu v$ we can express $p_{\alpha\|}$ and $p_{\beta'\|}$ as

$$p_{\alpha\|} = -\frac{v}{2} + \frac{\Delta\epsilon_{\beta'\alpha}}{v} \tag{A.33}$$

and

$$p_{\beta'\|} = \frac{v}{2} + \frac{\Delta\epsilon_{\beta'\alpha}}{v}. \tag{A.34}$$

Similarly, the momentum transfer vectors $\boldsymbol{p}_\beta = \gamma\boldsymbol{k}_\beta - \boldsymbol{k}_{\alpha'}$ and $\boldsymbol{p}_{\alpha'} = \boldsymbol{k}_\beta - \gamma\boldsymbol{k}_{\alpha'}$ can be written as

$$\boldsymbol{p}_\beta = \boldsymbol{p}_{\beta\perp} + p_{\beta\|}\hat{\boldsymbol{z}} \tag{A.35}$$

and

$$\boldsymbol{p}_{\alpha'} = \boldsymbol{p}_{\alpha'\perp} + p_{\alpha'\|}\hat{\boldsymbol{z}}, \tag{A.36}$$

The perpendicular and parallel components of $\boldsymbol{p}_\beta$ are

$$\boldsymbol{p}_{\beta\perp} = -k_{\alpha' x}\hat{\boldsymbol{x}} - k_{\alpha' y}\hat{\boldsymbol{y}} \tag{A.37}$$

and

$$p_{\beta\|} = -\frac{v}{2} + \frac{\Delta\epsilon_{\alpha'\beta}}{v}, \tag{A.38}$$

and the perpendicular and parallel components of $\boldsymbol{p}_{\alpha'}$ are

$$\boldsymbol{p}_{\alpha'\perp} = -\gamma k_{\alpha' x}\hat{\boldsymbol{x}} - \gamma k_{\alpha' y}\hat{\boldsymbol{y}}, \tag{A.39}$$

and

$$p_{\alpha'\|} = \frac{v}{2} + \frac{\Delta\epsilon_{\alpha'\beta}}{v}. \tag{A.40}$$

Here $\Delta\epsilon_{\alpha'\beta} = \epsilon_{\alpha'} - \epsilon_\beta$.

Lastly, comparing Eq. (A.19) to (A.12) and (A.37) to (A.4) we see that

$$\boldsymbol{p}_{\alpha\perp} = \boldsymbol{q}_{\beta\perp}, \tag{A.41}$$

and

$$\boldsymbol{p}_{\beta\perp} = \boldsymbol{q}_{\alpha\perp}. \tag{A.42}$$

Also, considering the fact that the velocity of the projectile is approximately constant throughout the collision, that is

$$\boldsymbol{k}_{\beta} \approx \boldsymbol{k}_{\beta'} \approx \boldsymbol{k}_{\alpha'} \approx \boldsymbol{k}_{\alpha} = \mu \boldsymbol{v}, \tag{A.43}$$

we can obtain the following expressions:

$$\boldsymbol{p}_{\beta'} - \boldsymbol{p}_{\alpha} = (1-\gamma)\boldsymbol{k}_{\alpha} + (1-\gamma)\boldsymbol{k}_{\beta'} \approx \boldsymbol{v} \tag{A.44}$$

and

$$\boldsymbol{p}_{\alpha'} - \boldsymbol{p}_{\beta} = (1-\gamma)\boldsymbol{k}_{\beta} + (1-\gamma)\boldsymbol{k}_{\alpha'} \approx \boldsymbol{v}. \tag{A.45}$$

Here we have applied Eqs. (A.30) and (A.32).

Abbreviations

Abbreviation	Description
ACE	Antiproton Cell Experiment
AI	Adiabatic Ionisation
AO	Atomic Orbital
BF	Body-Frame
CCC	Convergent Close-Coupling
CDW-EIS	Continuum-Distorted-Wave Eikonal-Initial-State
CI	Configuration-Interaction
DI	Double Ionisation
DW	Distorted Wave
EL	Electron Loss
END	Electron-Nuclear Dynamics
FBA	First Born Approximation
FC	Frozen-Core
IE	Ionisation with Excitation
LEAR	Low-Energy Antiproton Ring
LET	Linear Energy Transfer
MC	Multiconfiguration
SI	Single Ionisation

List of Figures

Bibliography

[1] E. Rutherford, Philos. Mag. **21**, 669 (1911).

[2] P. Sigmund, *Particle Penetration and Radiation Effects: General Aspects and Stopping of Swift Point Charges*, Springer Series in Solid-State Sciences, Vol. 151 (Springer Berlin Heidelberg, 2006).

[3] J. W. Wilson, J. Miller, A. Konradi, and F. A. Cucinotta, eds., *Shielding Strategies for Human Space Exploration*, NASA conference publication 3360 (Langley Research Center; Hampton, VA United States, 1997).

[4] Dž. Belkić, *Theory of Heavy Ion Collision Physics in Hadron Therapy*, Advances in Quantum Chemistry, Vol. 65 (Elsevier, Amsterdam, 2014).

[5] W. H. Bragg, Philos. Mag. **8**, 719 (1904).

[6] R. R. Wilson, Radiology **47**, 487 (1946).

[7] J. W. Boldeman and R. Banati, J. Proc. R. Soc. N.S.W. **144**, 58 (2011).

[8] J. Hansen, "Proton therapy: The new weapon of choice against cancer is coming to Australia," The Daily Telegraph (20/9/2014), Accessed: July, 2018.

[9] S. Agostinelli *et al.* (Geant4 Collaboration), Nucl. Instrum. Methods Phys. Res. A **506**, 250 (2003).

[10] J. Allison *et al.* (Geant4 Collaboration), Nucl. Instrum. Methods Phys. Res. A **835**, 186 (2016).

[11] M. A. Bernal *et al.* (Geant4-DNA Collaboration), Phys. Med. **31**, 861 (2015).

[12] A. Ferrari, P. R. Sala, A. Fassò, and J. Ranft, *FLUKA: A multi-particle transport code*, CERN Yellow Reports: Monographs (CERN, Geneva, 2005).

[13] G. Battistoni *et al.* (FLUKA Collaboration), Ann. Nucl. Energy **82**, 10 (2015).

[14] N. Bassler, D. C. Hansen, A. Lühr, B. Thomsen, J. B. Petersen, and N. Sobolevsky, J. Phys. Conf. Ser. **489**, 012004 (2014).

[15] V. T. Taasti, H. Knudsen, M. H. Holzscheiter, N. Sobolevsky, B. Thomsen, and N. Bassler, Nucl. Instrum. Methods Phys. Res. B **347**, 65 (2015).

[16] L. Gray and T. E. Kalogeropoulos, Radiat. Res. **97**, 246 (1984).

[17] M. H. Holzscheiter *et al.* (ACE Collaboration), Radiother. Oncol. **81**, 233 (2006).

[18] N. Bassler *et al.* (ACE Collaboration), Radiother. Oncol. **86**, 14 (2008).

[19] H. Bethe, Ann. Phys. **397**, 325 (1930).

[20] W. H. Bragg and R. Kleeman, Philos. Mag. **10**, 318 (1905).

[21] F. Bloch, Ann. Phys. **408**, 285 (1933).

[22] W. H. Barkas, J. N. Dyer, and H. H. Heckman, Phys. Rev. Lett. **11**, 26 (1963).

[23] H. Bichsel, Phys. Rev. A **65**, 052709 (2002).

[24] A. Dalgarno and G. W. Griffing, Proc. R. Soc. A **232**, 423 (1955).

[25] D. R. Bates and A. Dalgarno, Proc. Phys. Soc. A **65**, 919 (1952).

[26] D. R. Bates and A. Dalgarno, Proc. Phys. Soc. A **66**, 972 (1953).

[27] D. R. Bates and G. W. Griffing, Proc. Phys. Soc. A **66**, 961 (1953).

[28] D. R. Bates and G. W. Griffing, Proc. Phys. Soc. A **67**, 663 (1954).

[29] D. R. Bates and G. W. Griffing, Proc. Phys. Soc. A **68**, 90 (1955).

[30] D. S. F. Crothers and J. F. McCann, J. Phys. B **16**, 3229 (1983).

[31] P. D. Fainstein, V. H. Ponce, and R. D. Rivarola, J. Phys. B **24**, 3091 (1991).

[32] P. D. Fainstein, V. H. Ponce, and A. E. Martinez, Phys. Rev. A **47**, 3055 (1993).

[33] E. Deumens, A. Diz, R. Longo, and Y. Öhrn, Rev. Mod. Phys. **66**, 917 (1994).

[34] R. Cabrera-Trujillo, J. R. Sabin, Y. Öhrn, and E. Deumens, Phys. Rev. Lett. **84**, 5300 (2000).

[35] R. Cabrera-Trujillo, E. Deumens, Y. Öhrn, and J. R. Sabin, Nucl. Instrum. Methods Phys. Res. B **168**, 484 (2000).

[36] R. Cabrera-Trujillo, J. R. Sabin, Y. Öhrn, and E. Deumens, Phys. Rev. A **71**, 012901 (2005).

[37] R. Cabrera-Trujillo, Plasma Sources Sci. Technol. **19**, 034006 (2010).

[38] B. H. Bransden and M. R. C. McDowell, *Charge Exchange and the Theory of Ion-Atom Collisions* (Clarendon Press, Oxford, 1992).

[39] G. Schiwietz, Phys. Rev. A **42**, 296 (1990).

[40] G. Schiwietz and P. L. Grande, Nucl. Instrum. Methods Phys. Res. B **69**, 10 (1992).

[41] P. L. Grande and G. Schiwietz, Phys. Rev. A **44**, 2984 (1991).

[42] P. L. Grande and G. Schiwietz, Phys. Rev. A **47**, 1119 (1993).

[43] P. L. Grande and G. Schiwietz, Nucl. Instrum. Methods Phys. Res. B **132**, 264 (1997).

[44] G. Schiwietz, U. Wille, R. Díez Muiño, P. D. Fainstein, and P. L. Grande, Nucl. Instrum. Methods Phys. Res. B **115**, 106 (1996).

[45] G. Schiwietz, U. Wille, R. Díez Muiño, P. D. Fainstein, and P. L. Grande, J. Phys. B **29**, 307 (1996).

[46] A. Lühr and A. Saenz, Phys. Rev. A **77**, 052713 (2008).

[47] A. Lühr and A. Saenz, Phys. Rev. A **78**, 032708 (2008).

[48] A. Lühr and A. Saenz, Phys. Rev. A **80**, 022705 (2009).

[49] A. Lühr and A. Saenz, Phys. Rev. A **81**, 010701 (2010).

[50] A. Lühr and A. Saenz, Phys. Rev. A **79**, 042901 (2009).

[51] J. J. Bailey, A. S. Kadyrov, I. B. Abdurakhmanov, D. V. Fursa, and I. Bray, Phys. Rev. A **92**, 022707 (2015).

[52] J. J. Bailey, A. S. Kadyrov, I. B. Abdurakhmanov, D. V. Fursa, and I. Bray, Phys. Rev. A **92**, 052711 (2015).

[53] J. J. Bailey, A. S. Kadyrov, I. B. Abdurakhmanov, D. V. Fursa, and I. Bray, Phys. Med. **32**, 1827 (2016).

[54] J. J. Bailey, A. S. Kadyrov, I. B. Abdurakhmanov, and I. Bray, J. Phys. Conf. Ser. **777**, 012010 (2017).

[55] I. Bray and A. T. Stelbovics, Phys. Rev. A **46**, 6995 (1992).

[56] I. Bray and A. T. Stelbovics, Phys. Rev. Lett. **70**, 746 (1993).

[57] I. Bray, Phys. Rev. A **49**, 1066 (1994).

[58] D. V. Fursa and I. Bray, Phys. Rev. A **52**, 1279 (1995).

[59] A. S. Kadyrov and I. Bray, Phys. Rev. A **66**, 012710 (2002).

[60] A. S. Kadyrov and I. Bray, J. Phys. B **49**, 222002 (2016).

[61] A. S. Kadyrov, I. Bray, M. Charlton, and I. I. Fabrikant, Nat. Commun. **8**, 1544 (2017).

[62] I. B. Abdurakhmanov, A. S. Kadyrov, I. Bray, and A. T. Stelbovics, J. Phys. B **44**, 075204 (2011).

[63] I. B. Abdurakhmanov, A. S. Kadyrov, I. Bray, and A. T. Stelbovics, J. Phys. B **44**, 165203 (2011).

[64] I. B. Abdurakhmanov, A. S. Kadyrov, D. V. Fursa, I. Bray, and A. T. Stelbovics, Phys. Rev. A **84**, 062708 (2011).

[65] I. B. Abdurakhmanov, A. S. Kadyrov, D. V. Fursa, and I. Bray, Phys. Rev. Lett. **111**, 173201 (2013).

[66] I. B. Abdurakhmanov, A. S. Kadyrov, D. V. Fursa, S. K. Avazbaev, and I. Bray, Phys. Rev. A **89**, 042706 (2014).

[67] I. B. Abdurakhmanov, A. S. Kadyrov, D. V. Fursa, S. K. Avazbaev, J. J. Bailey, and I. Bray, Phys. Rev. A **91**, 022712 (2015).

[68] I. B. Abdurakhmanov, A. S. Kadyrov, S. K. Avazbaev, and I. Bray, J. Phys. B **49**, 115203 (2016).

[69] I. B. Abdurakhmanov, A. S. Kadyrov, and I. Bray, J. Phys. B **49**, 03LT01 (2016).

[70] S. K. Avazbaev, A. S. Kadyrov, I. B. Abdurakhmanov, D. V. Fursa, and I. Bray, Phys. Rev. A **93**, 022710 (2016).

[71] I. B. Abdurakhmanov, A. S. Kadyrov, and I. Bray, Phys. Rev. A **94**, 022703 (2016).

[72] I. B. Abdurakhmanov, A. S. Kadyrov, I. Bray, and K. Bartschat, Phys. Rev. A **96**, 022702 (2017).

[73] I. B. Abdurakhmanov, J. J. Bailey, A. S. Kadyrov, and I. Bray, Phys. Rev. A **97**, 032707 (2018).

[74] M. R. C. McDowell and J. P. Coleman, *Introduction to the theory of ion-atom collisions* (North-Holland Pub. Co., Amsterdam, 1970).

[75] D. V. Fursa and I. Bray, New J. Phys. **14**, 035002 (2012).

[76] D. A. Varshalovich, A. N. Moskalev, and V. K. Khersonskii, *Quantum Theory of Angular Momentum* (World Scientific, 1988).

[77] M. Agnello *et al.* (OBELIX Collaboration), Phys. Rev. Lett. **74**, 371 (1995).

[78] E. Lodi Rizzini *et al.* (OBELIX Collaboration), Phys. Lett. B **599**, 190 (2004).

[79] H. H. Andersen and J. F. Ziegler, *Hydrogen: Stopping Powers and Ranges in All Elements*, The Stopping and Ranges of Ions in Matter, Vol. 3 (Pergamon Press, 1977).

[80] C. Varelas and J. Biersack, Nucl. Instrum. Methods **79**, 213 (1970).

[81] L. H. Andersen, P. Hvelplund, H. Knudsen, S. P. Møller, J. O. P. Pedersen, S. Tang-Petersen, E. Uggerhøj, K. Elsener, and E. Morenzoni, Phys. Rev. A **41**, 6536 (1990).

[82] P. Hvelplund, H. Knudsen, U. Mikkelsen, E. Morenzoni, S. P. Møller, E. Uggerhøj, and T. Worm, J. Phys. B **27**, 925 (1994).

[83] H. Knudsen, H. P. E. Kristiansen, H. D. Thomsen, U. I. Uggerhøj, T. Ichioka, S. P. Møller, C. A. Hunniford, R. W. McCullough, M. Charlton, N. Kuroda *et al.*, Nucl. Instrum. Methods Phys. Res. B **267**, 244 (2009).

[84] C. C. Montanari and J. E. Miraglia, J. Phys. B **47**, 015201 (2014).

[85] M. O. Abdellahi El Ghazaly, J. Jureta, X. Urbain, and P. Defrance, J. Phys. B **37**, 2467 (2004).

[86] A. Adamo *et al.* (OBELIX Collaboration), Phys. Rev. A **47**, 4517 (1993).

[87] E. Lodi Rizzini *et al.* (OBELIX Collaboration), Phys. Rev. Lett. **89**, 183201 (2002).

[88] T. E. Sharp, At. Data Nucl. Data Tables **2**, 119 (1970).

[89] G. A. Khayrallah, Phys. Rev. A **13**, 1989 (1976).

[90] T. Kirchner and H. Knudsen, J. Phys. B **44**, 122001 (2011).

[91] D. R. Bates and R. McCarroll, Proc. R. Soc. A **245**, 175 (1958).

[92] E. Guth and C. J. Mullin, Phys. Rev. **83**, 667 (1951).

[93] H. van Haeringen, *Charged-Particle Interactions: Theory and Formulas* (Coulomb Press Leyden, Leiden, 1985).

[94] H. K. Reynolds, D. N. F. Dunbar, W. A. Wenzel, and W. Whaling, Phys. Rev. **92**, 742 (1953).

[95] G. Reiter, N. Kniest, E. Pfaff, and G. Clausnitzer, Nucl. Instrum. Methods Phys. Res. B **44**, 399 (1990).

[96] R. Golser and D. Semrad, Nucl. Instrum. Methods Phys. Res. B **69**, 18 (1992).

[97] S. K. Allison, Rev. Mod. Phys. **30**, 1137 (1958).

[98] A. B. Wittkower, G. Levy, and H. B. Gilbody, Proc. Phys. Soc. **91**, 306 (1967).

[99] G. W. McClure, Phys. Rev. **166**, 22 (1968).

[100] M. B. Shah and H. B. Gilbody, J. Phys. B **15**, 3441 (1982).

[101] M. B. Shah, D. S. Elliott, and H. B. Gilbody, J. Phys. B **20**, 2481 (1987).

[102] V. V. Afrosimov, G. A. Leĭko, Yu. A. Mamaev, and M. N. Panov, Sov. Phys. JETP **29**, 648 (1969).

[103] J. A. Phillips, Phys. Rev. **90**, 532 (1953).

[104] P. K. Weyl, Phys. Rev. **91**, 289 (1953).

[105] J. T. Park and E. J. Zimmerman, Phys. Rev. **131**, 1611 (1963).

[106] F. Kottmann, in *Proc. 2nd Int. Symp. Muon and Pion Interactions with Matter* (JINR, Dubna, 1987) p. 268.

[107] P. Hauser, F. Kottmann, C. Lüchinger, and R. Schaeren, in *Muonic atoms and molecules*, edited by L. A. Schaller and C. Petitjean (Birkhäuser, Basel, 1993) p. 235.

[108] S. K. Allison and S. D. Warshaw, Rev. Mod. Phys. **25**, 779 (1953).

[109] R. A. Langley, Phys. Rev. B **12**, 3575 (1975).